Steady-State Multiplicity and Transient Behaviour within a Lumped-Parameter Solid Oxide Fuel Cell

by

Harvind Arjun Rai

A thesis submitted to
The University of Birmingham
for the degree of
Doctor of Philosophy

School of Mathematics
The University of Birmingham
September 2016

Abstract

In this thesis, the existence of multiple steady-state solutions within a planar, zero-dimensional Solid Oxide Fuel Cell (SOFC) is investigated. The model presented here is a development of a previous SOFC model by Bavarian and Soroush (2012), where the heat-transfer coefficients are no longer assumed to be constant, and momentum conservation is considered within the gas channels. The aim is to not only give a more accurate representation as to the location and size of any multiplicity regions within the SOFC, but to also show the existence of more than one operating region via transient calculations.

The steady-state behaviour of a Solid Oxide Fuel Cell is investigated for three modes of operation: (i) constant external load; (ii) Potentiostatic (constant voltage); (iii) Galvanostatic (constant current). For each mode of operation, the constant parameter is treated as the bifurcation parameter. Any multiplicity region within a Solid Oxide Fuel Cell can be shown by the existence of a hysteresis loop in the profile of any parameter for a region of bifurcation parameter values. For the first two modes of operation, up to three steady-state solutions exists: two stable and one unstable.

The main focus is on the first mode of operation. Besides the existence of any multiplicity regions, the effect of the model modifications on the amount of heat produced and removed from the SOFC will also be investigated. There will also be a look into a few non-dimensional parameters to gain a further understanding of the dominant dynamics within both gas flows, and how they affect cell performance. The effects of the different

inlet parameters on SOFC performance will also be investigated, along with multiplicity regions for each of the parameters considered.

The dynamic model is also considered for a Solid Oxide Fuel Cell operating under a constant external load. The different time-scales relevant to this model is investigated to highlight the multi-time-scale nature of the SOFC system. The transient behaviour of the SOFC is investigated for changes in value of the external load resistance R_{load}. The external load resistance is expressed in terms of the tanh function, and is defined in such a way such that R_{load} changes smoothly from one value to another at around 100 seconds. Using this expression of R_{load}, the evolution of different SOFC parameters with time is investigated, as well as the transient behaviour of the SOFC during ignition and extinction. The results show that there is at least two different operating regimes within a Solid Oxide Fuel Cell. The transient behaviour of the SOFC operating at a point along the unstable steady-state branch is also covered.

Acknowledgements

I like to thank my supervisor Dr David Leppinen for his continuous guidance. A special thanks is also given to the organisers of the Joint European Summer School for Fuel Cells, Electrolyser and Battery technologies (JESS) in Crete in 2014, and people from the chemical engineering department for helping me to solidify my background knowledge of fuel cells.

I would also like to give thanks to my colleagues in the mathematics department (including those from both offices that I have worked in) past and present for mainly non-work related aspects, and a thanks to my family for letting me stay in the house. A final thanks goes to the University of Birmingham for funding this PhD.

Contents

Nomenclature

(*Unless otherwise stated in the text*)

Symbols

C - Concentration (mol/m^3)

$C_{\mathrm{p,cell}}$ - Specific Heat Capacity of the cell (J/(kg·K))

C_{p} - Molar Heat Capacity (J/(mol·K))

$C_{\mathrm{p}}^{\mathrm{S}}$ - Specific Heat Capacity (J/(kg·K))

d_j - Thickness of cell component "j" (j=An, Cat, Ele) (m)

$\mathrm{d}r_i/\mathrm{d}t$ - Rate of change of molar number per unit area r_i (mol/(m^2·s))

D - Diffusion coefficient (m^2/s)

D_{eff} - Effective diffusion coefficient (m^2/s)

$D_{i,m}$ - Binary diffusion coefficient of fluid "i" within fluid "m" (m^2/s)

D_K - Knudsen diffusion coefficient (m^2/s)

E - Open Circuit Voltage (OCV) (V)

E_{act} - Activation Energy (J/mol)

E_0 - Standard Electrode Potential (V)

F - Faraday's constant ($= 96,485$ C/mol)

$\Delta^r G$ - Gibbs free energy of the electrochemical reaction (J/mol)

$\Delta^r G_p$ - Total free energy change at constant pressure (J/mol)

h - Heat-transfer coefficient (W/(m^2·K))

h^j - Height of gas channel "j" (j=fuel, air) (m)

H - Enthalpy (J/mol)

ΔH_{R} - Net enthalpy flux into the cell (J/(m^2·s))

$\Delta^r H$ - Net enthalpy produced from the electrochemical reaction (J/mol)

i - Surface current density (A/m^2)

i_0 - Exchange current density (A/m^2)

i_l - Limiting current density (A/m^2)

I - Cell Current (A)

j^{r} - Molar flux into the reaction zone per unit area (mol/(m^2·s))

j^{s} - Molar flux into the cell surface per unit area (mol/(m^2·s))

k - Thermal conductivity (W/(m·K))

k^{r} - Reaction rate constant (mol/(m^2·s))

L - Cell Length (m)

M - Molar mass (kg/mol)

n^{el} - Number of electrons transferred in the electrochemical reaction

$\dot{N}$ - Molar flow rate (mol/s)

Nu - Nusselt number

p - Pressure (Pa)

p_i - Partial pressure of "i-th" chemical species (Pa)

p_0 - Standard atmospheric pressure (=1 atm)

P - Surface power density (W/m^2)

Pe - Péclet number

Pr - Prandtl number

Q_{P} - Heat Production (W)

Q_{R} - Heat Removal (W)

R - Universal Gas Constant (= 8.3144 J/(mol $\cdot$ K))

R_i - Consumption/production rate of "i-th" chemical species (mol/s)

R_{load} - External load resistance (Ω)

Re - Reynolds number

S - Entropy (J/(mol·K))

$\Delta^r S$ - Net entropy produced from the electrochemical reactions (J/(mol·K))

$\Delta^r S_p$ - Net entropy at constant pressure (J/(mol·K))

T - Temperature (K)

T_{Adv} - Advection time-scale (s)

T_{Cond} - Conduction time-scale (s)

T_{Conv} - Convection time-scale (s)

T_{Diff} - Diffusion time-scale (s)

T_{Re} - Cell Reactant consumption time-scale (s)

u - Velocity (m/s)

U_f - Fuel utilisation

V - Voltage (V)

W - Cell Width (m)

y - Mole fraction

Greek Letters

α - Thermal diffusivity (m^2/s)

β_i - Coefficient for specific resistivity of electrolyte ($(\Omega \cdot \text{m})^{-1}$)

β_{ii} - Coefficient for specific resistivity of electrolyte (K)

γ - Pre-exponential kinetic factor (A/m^2)

δ_j - Pore mean radius of electrode "j" (m)

Δ_j - Thickness of the diffusion layer in electrode "j" (m)

ε - Porosity of the electrode

η_{act} - Activation Polarisation (V)

η_{conc} - Concentration Polarisation (V)

η_{el} - Electrical efficiency

η_{Ohm} - Ohmic Polarisation (V)

η_{rev} - Reversible efficiency

η_{Thm} - Thermodynamic efficiency

η_{Vol} - Voltage efficiency

θ - Transfer reaction coefficient

θ_{b} - Transfer reaction coefficient of the backward reaction

θ_{f} - Transfer reaction coefficient of the forward reaction

μ - Dynamic viscosity (Pa· s)

ν - Atomic Diffusion Volume (cm^3/mol)

ν^{S} - Stoichiometric coefficient of reaction

ρ_{cell} - Density of the cell (kg/m^3)

ρ^j - Specific Resistivity of cell component "j" (j=An, Cat, Ele) (Ω·m)

τ - Tortuosity of the electrode

ω - Constant present in the equation for R_{load} in chapter 7 (s)

Subscripts and Superscripts

air - Air flow/Air Channel

An - Anode

b - Bulk gas flow (within gas channels)

Cat - Cathode

Cell - Solid Cell component (PEN structure)

Ele - Electrolyte

fuel - Fuel flow/Fuel Channel

H - Heat transfer (Péclet number)

H_2 - Hydrogen

H_2O - Water

in - Inlet

M - Mass transfer (Péclet number)

Mh - Mass transfer (Péclet number: Advection across length, diffusion across height of channel)

ML - Mass transfer (Péclet number: Advection and diffusion across the channel length)

out - Outlet

O_2 - Oxygen

OCV - Open Circuit Voltage

OX - Oxidised

tpb/TPB - Triple phase boundary

Chapter 1

A background to Solid Oxide Fuel Cells

1.1 Introduction to Fuel Cells

Fuel Cells are electrochemical devices which convert the chemical energy of a fuel (Hydrogen) combined with Oxygen into electricity (and possibly heat as a by-product) via electrochemical (and chemical) reactions. They consist of two electrodes: an **Anode** and a **Cathode**, with an **electrolyte** in-between, plus an external circuit to allow transport of electrons from one electrode to another, as well as supplying electricity to a device (see figure 1.1). The electrode-electrolyte structure is commonly known as the PEN structure (Positive electrode (Cathode)-Electrolyte-Negative electrode (Anode)). Fuel Cells work similar to batteries with one important exception: a fuel cell will continue to run if it has a constant supply of fuel and air, while batteries need to be recharged after a certain amount of time. The electrochemical reactions usually occur near the electrode/electrolyte interface, and the electrolyte in-between allows the transport of ions/protons from one electrode to the other to participate in the electrochemical reactions.

The concept of a FC goes back as far as the early 19th century thanks to Sir Humphrey

Davy [1], who created a simple fuel cell based upon the reaction of Carbon with water to produce Hydrogen and Carbon Monoxide. The actual principle of a fuel cell was discovered in the 19th century by Christian Friedrich Schönbein and Sir William Grove [2]. The latter developed what is known as the "Grove Cell", a wet-cell battery which is based on reversing the electrolysis of water to extract the Hydrogen needed for the fuel cell [3]. There is some debate as to which of the two actually discovered that principle, with [4] stating that it was Grove, and [5] stating it was Schönbein based on letter exchanges between the two. Further improvements were made to the electrodes used by Grove by Ludwig Mond and Carl Langer in 1889 [6], and the first fuel cell invented for practical use was made in 1896 by William W. Jacques [6]. The fuel cell produced was used for a coal-fired power station, operated between 400-500°C, and achieved efficiencies between 2.6-15%.

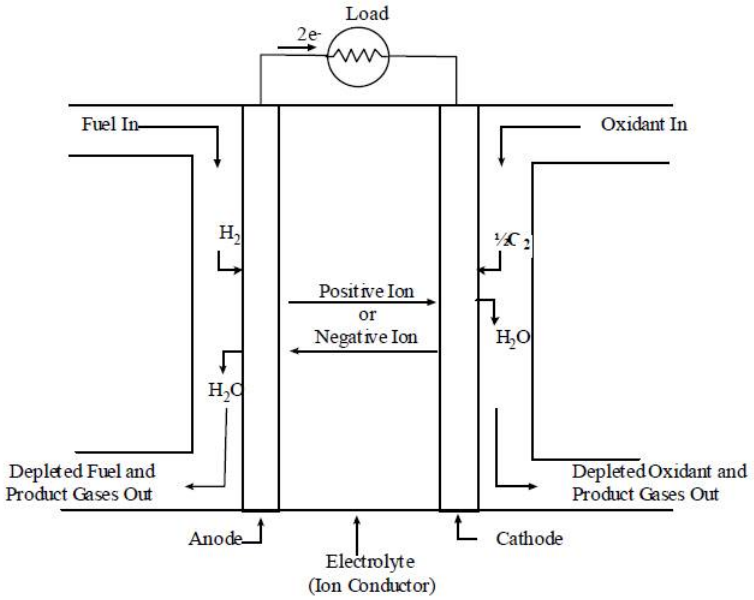

Figure 1.1: A schematic of a general fuel cell powered by Hydrogen and Oxygen (taken from [7]). Hydrogen and Oxygen enter their respective electrodes to participate in the electrochemical reaction. The material of the electrolyte determines whether positive or negative ions transport through the electrolyte. Any water produced from the electrochemical reactions exits the fuel cell, while the electrons pass through an external circuit.

	PEFC	AFC	PAFC	MCFC	SOFC
Electrolyte	Hydrated Polymeric Ion Exchange Membranes	Mobilized or Immobilized Potassium Hydroxide in asbestos matrix	Immobilized Liquid Phosphoric Acid in SiC	Immobilized Liquid Molten Carbonate in $LiAlO_2$	Perovskites (Ceramics)
Electrodes	Carbon	Transition metals	Carbon	Nickel and Nickel Oxide	Perovskite and perovskite / metal cermet
Catalyst	Platinum	Platinum	Platinum	Electrode material	Electrode material
Interconnect	Carbon or metal	Metal	Graphite	Stainless steel or Nickel	Nickel, ceramic, or steel
Operating Temperature	40 – 80 °C	65°C – 220 °C	205 °C	650 °C	600-1000 °C
Charge Carrier	H^+	OH^-	H^+	$CO3^=$	$O^=$
External Reformer for hydrocarbon fuels	Yes	Yes	Yes	No, for some fuels	No, for some fuels and cell designs
External shift conversion of CO to hydrogen	Yes, plus purification to remove trace CO	Yes, plus purification to remove CO and CO_2	Yes	No	No
Prime Cell Components	Carbon-based	Carbon-based	Graphite-based	Stainless-based	Ceramic
Product Water Management	Evaporative	Evaporative	Evaporative	Gaseous Product	Gaseous Product
Product Heat Management	Process Gas + Liquid Cooling Medium	Process Gas + Electrolyte Circulation	Process Gas + Liquid cooling medium or steam generation	Internal Reforming + Process Gas	Internal Reforming + Process Gas

Figure 1.2: A comparison table showing the different properties of five different fuel cells (taken from [7]). The first four rows cover the material of the main cell components, including any additional catalysts used. The sixth row describes what charge is carried through the electrolyte of each fuel cell. The seventh row describes whether the fuel cell needs an external reformer to extract Hydrogen from hydrocarbon-based fuels. The eighth row covers whether the fuel cell needs an external shift converter to remove any carbon monoxide (and dioxide) from the fuel. The ninth row describes the general material used for the prime cell components. The final two rows describes the state of any water and heat produced within the fuel cell.

Since then, research from the 1920s onwards has led to the development of a wide selection of fuel cells, and they are split into two categories: **Low-Temperature** FCs and **High Temperature** FCs. Low-temperature FCs include **Alkaline Fuel Cells** (AFCs), **Phosphoric Acid Fuel Cells** (PAFCs), and **Proton-Exchange Membrane Fuel Cells** (PEMFCs), while high-temperature FCs include **Molten-Carbonate Fuel Cells** (MCFCs) and **Solid Oxide Fuel Cells** (SOFCs).

1.2 Other Fuel Cells

1.2.1 Proton-Exchange Membrane Fuel Cells (PEMFCs)

A proton-exchange membrane fuel cell is a low temperature fuel cell with an electrolyte that allows the transport of positive Hydrogen ions from the anode to the cathode, as shown in figure 1.3. Developed in the 1950s by two GE scientists Thomas Grubb and Leonard Niedrach (along with the availability of Teflon) [2], a PEMFC has an ion exchange membrane, made from a water-based, acidic polymer membrane (e.g. fluorinated sulphonic acid polymer) [7].

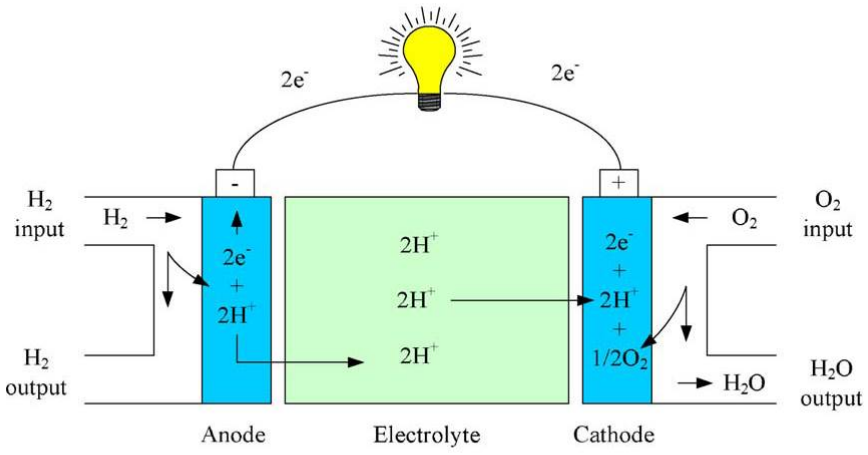

Figure 1.3: A schematic of a Proton-Exchange Membrane Fuel Cell (taken from [2]).

The operating temperature of a PEMFC is around 60-80°C, so the electrodes contain a heavy loading of platinum, which acts as a catalyst for the electrochemical reactions given in (1.1) and (1.2). Both electrodes are Carbon based, with carbon/metal interconnects [7]. Pt is useful in separating the electrons from the Hydrogen molecules in reduction reaction (1.1) in the anode,

$$\mathrm{H_2} \rightarrow 2\mathrm{H^+} + 2e^-. \tag{1.1}$$

The electrons flow through the external circuit into the cathode, and the ions through the electrolyte into the cathode to participate in the oxidation reaction (1.2),

$$\frac{1}{2}\mathrm{O_2} + 2\mathrm{H^+} + 2e^- \rightarrow \mathrm{H_2O}, \tag{1.2}$$

where the water produced in the cathode leaves the cell.

Water management is very important in a PEMFC. The membrane has to stay hydrated, so the water produced must not evaporate faster than it is made (which is possible due to the low operating temperature) [7]. The low operating temperature also means that the fuel cell can only be fuelled by pure Hydrogen, or Hydrogen with low levels of Carbon Monoxide (CO). PEMFCs cannot tolerate even small traces of sulphur (along with Carbon Monoxide and ammonia), and are at risk of being permanently damaged if there is any trace of these chemical compounds in the fuel flow [7]. This means that hydrocarbon-based fuels require the use of an external fuel reformer to extract the Hydrogen, which makes the process more complicated, as well as costly [7]. Also, platinum is an expensive choice of catalyst, and it is not as good a catalyst in the oxidation reaction (1.2) in the cathode as it is in the reduction reaction (1.1) in the anode.

However, due to the low operating temperature of a PEMFC, it does have a quick start-up time, especially in comparison with high temperature fuel cells (including SOFCs). This makes it useful for portable and transportation systems [8], including replacing

rechargeable batteries and automotive uses, especially with the rise in Fuel Cell Vehicles (FCV) in recent years from hybrid buses in London (part of the London Hydrogen Project) [9, 10], to cars like the Hyundai ix35 fuel cell car [11, 12] and the soon-to-be released Toyota Mirai[1] [13, 14]. Also, the low operating temperature means that the handling, assembly and tightness of these cells are less complex than in other cells [2]. They are compact (hence its use in portable systems), have a simple mechanical design, and the use of exotic materials is not required [7].

1.2.2 Alkaline Fuel Cells (AFCs)

Alkaline Fuel Cells (AFCs) is a low-temperature fuel cell that has an electrolyte made from a molten alkaline mixture of Potassium Hydroxide (KOH), making it a liquid electrolyte. AFCs were developed in the 1930s by British Scientist Francis Thomas Bacon, and has the distinction of being the first modern fuel cell (*i.e.* a fuel cell to be powered by Hydrogen and Oxygen) ever to be produced [2]. Eventually, a model was demonstrated in 1959, and its patent was acquired by Pratt and Whitney. It went on to be used in the NASA Apollo missions in the 1960s [2]. The AFC can use a wide range of electro-catalysts (mainly transition metals) [7], and its electrolyte conducts hydroxide ions (OH^-) from the reduction reaction in the cathode

$$O_2 + 2H_2O + 4e^- \rightarrow 4OH^-. \tag{1.3}$$

The hydroxide ions react with Hydrogen molecules in the oxidation reaction in the anode to produce water (some of which diffuses into the cathode [15][p127]), and electrons, which flow through an external circuit to the cathode. The oxidation reaction

$$2H_2 + 4OH^- \rightarrow 4H_2O + 4e^-. \tag{1.4}$$

[1] In Europe, starting in September 2015. True as of 4th August, 2015

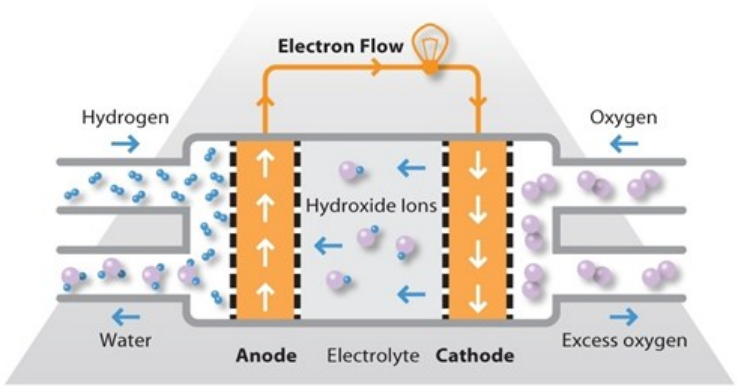

Figure 1.4: A schematic of an Alkaline Fuel Cell (taken from [16]).

The operating temperature of a AFC is between 65-220°C depending on the concentration of KOH in the electrolyte [7]. This low operating temperature means that it has a quick start-up time, just like PEMFCs [2]. They also have low weight and volume, just like PEMFCs, but their main advantage is that it can use a wide variety of electro-catalysts, giving it excellent performance on hydrogen and oxygen compared to other FCs [7]. However, unlike PEMFCs, it does have a liquid electrolyte, making it more difficult to handle. It requires a evacuation of the water treatment complex [2], and it has a high intolerance to impurities, including Carbon Dioxide (CO_2), in which a very small amount is present in air. This means that it is more difficult to use them for terrestrial applications (especially with the rise of PEMFCs) [2]. Therefore, it is primarily used in extra-terrestrial applications.

1.2.3 Phosphoric Acid Fuel Cells (PAFCs)

Phosphoric Acid Fuel Cells (PAFCs) were developed in 1961 by G.V. Elmore and H.A. Tanner in their work entitled *Intermediate Temperature Fuel Cells* [2]. The operating temperature is around 150-220°C. The electrolyte is made up from liquid Phosphoric acid in Silicon Carbide (SiC), with carbon based electrodes and graphite interconnects

[7].

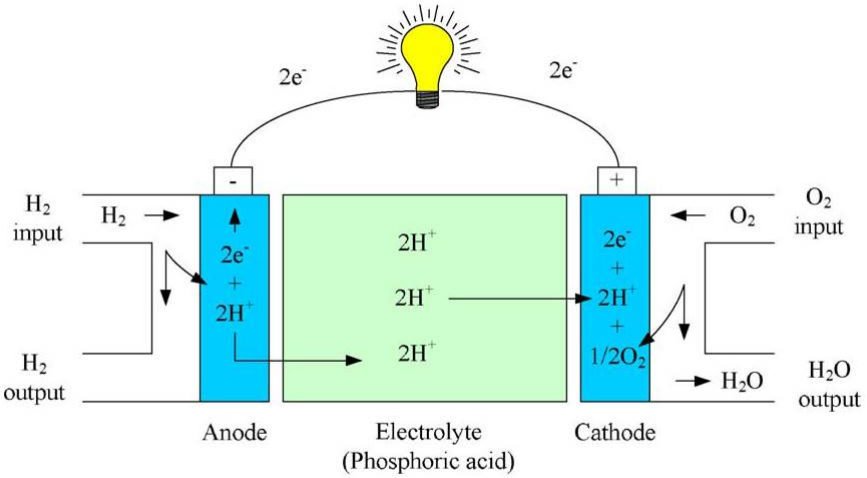

Figure 1.5: A schematic of a Phosphoric Acid Fuel Cell (taken from [2]).

Like PEMFC, the electrolyte is a conductor of Hydrogen protons, which are obtained from the anode-based reduction reaction of Hydrogen

$$2\mathrm{H}_2 \rightarrow 4\mathrm{H}^+ + 4e^-. \tag{1.5}$$

The protons travel through the electrolyte into the cathode, participating the oxidation reaction

$$\mathrm{O}_2 + 4\mathrm{H}^+ + 4e^- \rightarrow 2\mathrm{H}_2\mathrm{O}, \tag{1.6}$$

where the water exits the cell. PAFCs are mainly used for stationary applications, and are widely used commercially [2], especially as they can use waste heat for co-generation [2]. They are also tolerant to certain levels of CO_2 unlike AFCs, and the electrolyte has stable characteristics [2]. Operating temperatures are still low enough that common materials can be used, however, due to the corrosive nature of Phosphoric acid, expensive materials are required in the stack [7]. They are also intolerant to significant levels of CO, although

not as badly as the other two low-temperature fuel cells in this section [7]. They also require external fuel reformers, and unlike the other two fuel cells in this section, they are quite heavy [2].

1.2.4 Molten-Carbonate Fuel Cells (MCFCs)

The origins of Molten-Carbonate Fuel Cells (MCFCs) go back as far as the 1920s [2] (the first MCFC being built by Emil Baur in 1921). Further work was done in the future by H.J. Broers and J.A.A. Ketelaar [2], who created a fuel cell that uses a mixture of lithium, sodium and potassium carbonate in a porous disc of magnesium oxide. The electrolyte in a MCFC is made from a combination of alkali carbonates, like liquid molten carbonate in $LiAlO_2$ [7], or molten carbonate with potassium. The operating temperature is above 600°C (around 650°C), which means that additional expensive catalysts like platinum are not needed. Instead, the catalyst for the electrochemical reactions can be found in the material of the electrode itself, which contain Nickel (Ni)/Nickel Oxide (NiO) [7]. Also, due to the high operating temperatures, the fuel cell is less prone to poisoning from impurities such as CO or CO_2, making it fuel flexible. In fact, the flow on the cathode side is a combination of oxygen and carbon dioxide. The electrolyte is a good conductor of carbonate ions (CO_3^{2-}), which are transferred from the cathode to the anode. The carbonate ions are originated from the cathode-side reduction reaction

$$\frac{1}{2}O_2 + CO_2 + 2e^- \rightarrow CO_3^{2-}. \tag{1.7}$$

Once transferred to the anode, they take part in the oxidation reaction

$$H_2 + CO_3^{2-} \rightarrow H_2O + CO_2 + 2e^-, \tag{1.8}$$

where the water produced leaves the cell, and the carbon dioxide is recycled to be used in reaction (1.7) (see figure 1.6).

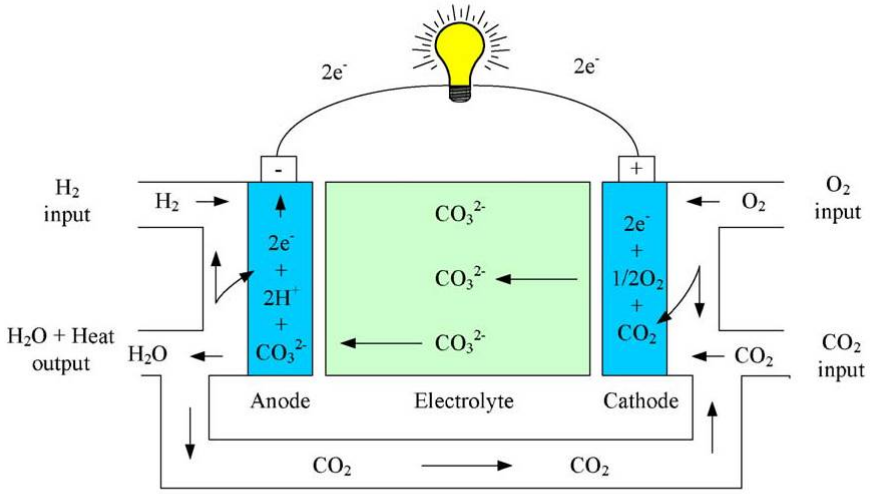

Figure 1.6: A schematic of a Molten-Carbonate Fuel Cell (taken from [2]).

Due to its high operating temperatures, the electrochemical reactions activate more quickly and easily (resulting in higher power densities), and more heat is available from the cell. The higher temperatures can be useful in extracting Hydrogen from other substances within the cell. Also, the temperature of the gases exiting the cell is higher, making it a good source of heat as well as electricity. This means that it can be used as a Combined Heat and Power (CHP) system for buildings. The main disadvantage however stems from the electrolyte, which not only can dissolve the nickel oxide in the cathode [2], but is also mobile (as it is in liquid form), which requires the use of nickel and high-grade stainless steel as hardware for the cell [7]. Also, the starting time is longer in comparison to low-temperature fuel cells because of the time needed for the cell to heat up to the required operating temperature. Its main applications are stationary, including power plants [2] and marine applications [2, 7].

1.3 An introduction to Solid Oxide Fuel Cells

1.3.1 Brief History of SOFCs

A Solid Oxide Fuel Cell (SOFC) is a high-temperature fuel cell whose solid electrolyte is made from ceramic-based materials like yttria-stabilised zirconia (YSZ), which is a good ionic conductor. The discovery of stabilised zirconia as an ionic conductor was made by Walther Nernst in the late 1890s [17]. Nernst designed a light bulb (known as the *Nernst Lamp*) with a filament made up of a combination of 85% zirconia, and 15% yttria (which was known as the *Nernst Mass*) [18, pp 24-25]. Although it did have its problems, it was eventually recognised that this particular filament design did act as a conductor of oxide ions (by Wagner in 1942 [19]), and with the platinum contacts acting as electrodes, the Nernst lamps essentially became an example of what would be the first solid electrolyte fuel cell.

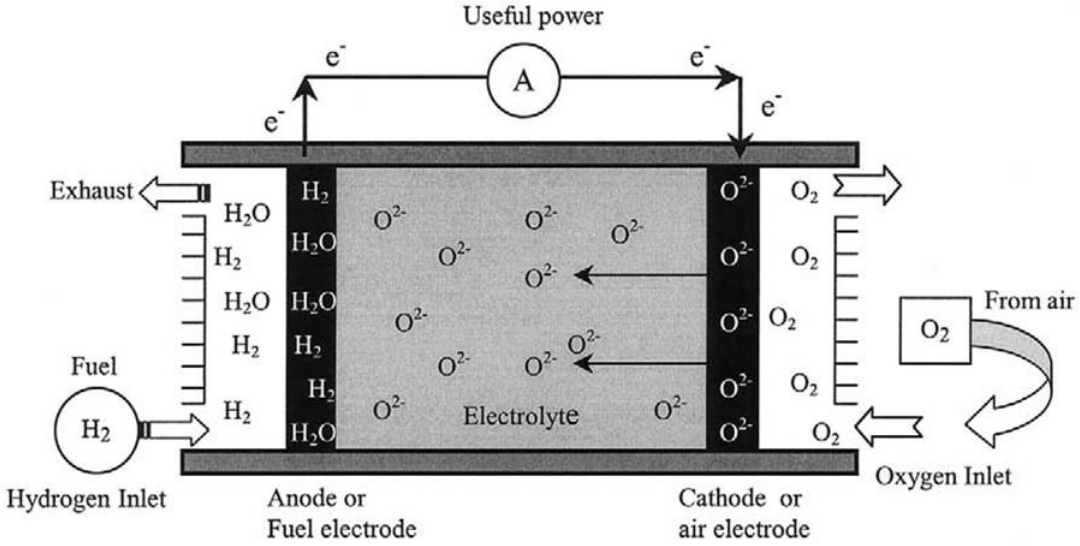

Figure 1.7: A schematic of a Solid Oxide Fuel Cell (taken from [1]).

The first conceptual SOFC with a zirconia ceramic acting as the electrolyte was made by Emil Baur and Hans Preis in 1937 [20], along with other choices for ceramics including those containing tungsten oxide and cerium oxide. However, there were problems with this fuel cell including the material for the cathode, and the resistivity of the electrolyte [18, p 28]. Progress in fuel cells with ceramic-based electrolytes containing a mixture of zirconium and yttrium was not really made until the late 1950s, started off by investigations on metal/metal oxide systems by Kiukkola and Wagner in 1957, using CaO-stabilised ZrO_2 as a solid electrolyte [21]. This stimulated further research into solid state electrochemistry using solid electrolytes (a short summary of which can be found in [22], and a more detailed one in [18, pp 31-44]), and this eventually led to the publication of what would be the design of the cathode air-supported tubular SOFC by R Ruka, J. Weissbart and scientists at Westinghouse [23]. Since then, most of the research has been dedicated into finding the optimal material for the other cell components (see section 1.5) [18, pp 32-44],[22]. As for fuel cell configuration, SOFC design has moved away from air-supported SOFCs (where air is injected through a metal tube located inside the tubular cell) towards tubular SOFCs without the injection tube (late 1970s), and more commonly, planar SOFC configurations (1980s and 1990s) [18, p 42]. These different configurations are described in section 1.4, and they are used for a wide variety of applications due to the large power density range achievable by SOFCs (section 1.7).

1.3.2 Operating parameters and cell reactions

A SOFC operates in the region of 600-1000°C [18, p 1], depending on the material composition of the cell components, especially the solid electrolyte (see section 1.5, [24]). The amount of power generated from a SOFC can range from below 1 kW to the multi-MW range, making it useful for a wide variety of applications (section 1.7). The YSZ electrolyte is a good conductor of oxide ions, which travel from the cathode to the anode.

The oxide ions are formed from the reduction reaction of oxygen molecules in the cathode

$$\frac{1}{2}O_2 + 2e^- \rightarrow O^{2-}. \tag{1.9}$$

These ions travel to the anode to oxidise hydrogen molecules in the oxidation reaction

$$H_2 + O^{2-} \rightarrow H_2O + 2e^-, \tag{1.10}$$

where the water leaves the cell, and the electrons pass through the external circuit to the cathode to participate in (1.9). Hence the overall cell reaction is

$$\frac{1}{2}O_2 + H_2 \rightarrow H_2O. \tag{1.11}$$

The electrochemical reactions take place in a region near, or at the electrode/electrolyte interface known as the **Triple Phase Boundary** (TPB). The TPB is a combination of molecules from the gas flow (hydrogen or oxygen), ionic conducting sites (oxide ions) and electronic conducting sites (electrons), as shown in the schematic of the TPB in the anode in figure 1.8.

Due to the high operating temperatures of SOFCs, it does tolerate other compounds, including carbon monoxide, which can also be oxidised on the anode side in the electrochemical reaction

$$CO + O^{2-} \rightarrow CO_2 + 2e^-. \tag{1.12}$$

The temperatures are also high enough to break down hydrocarbons, so more natural fuels like Methane can be used as fuel for the SOFC. Due to the materials contained in the anode (Nickel), the methane is broken down on the surface of the anode in the

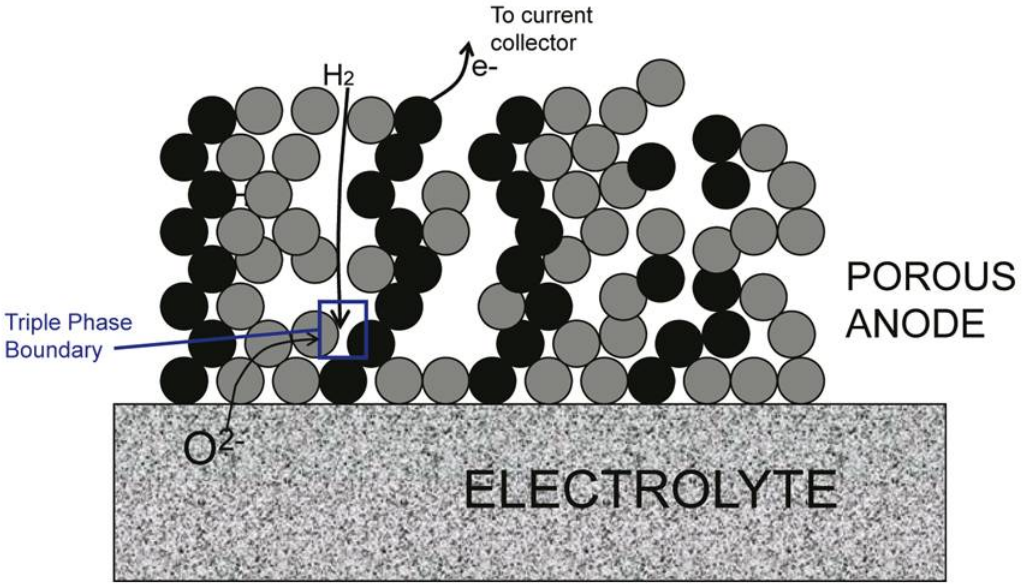

Figure 1.8: A schematic of the porous anode and the solid electrolyte, with the location of the TPB inside the small blue square (taken from [25, p 61]). Inside the small blue square, the hydrogen occupying the gaps between the oxide ions (grey) and the electrons (black) in the porous electrode, reacts with the oxide ions to produce water and electrons.

endothermic steam-reforming reaction

$$CH_4 + H_2O \rightarrow 3H_2 + CO, \tag{1.13}$$

which along with the exothermic water gas-shift reaction

$$CO + H_2O \rightarrow H_2 + CO_2, \tag{1.14}$$

allows the extraction of extra hydrogen from methane, while converting any carbon monoxide into carbon dioxide.

The theoretical, reversible voltage E of a SOFC (also known as the open circuit voltage

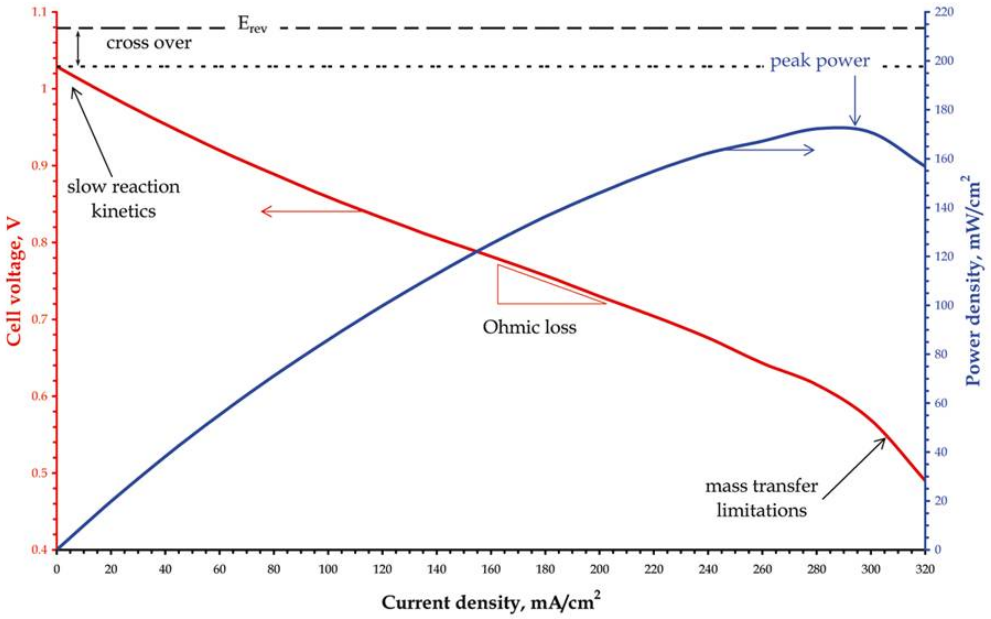

Figure 1.9: A graph showing the I-V (red) and P-I (blue) profiles of a SOFC (taken from [25, p 5]). The difference between the actual voltage and the open circuit potential of a SOFC due to the polarizations that occur within the cell are shown.

(OCV)), is described by the **Nernst Equation**

$$E = E_0 - \frac{RT}{n^{el}F} \log\left(\frac{p_{\mathrm{H_2O}}}{p_{\mathrm{H_2}}}\sqrt{\frac{p_0}{p_{\mathrm{O_2}}}}\right), \tag{1.15}$$

where E_0 represents the standard electrode potential, T represents the temperature of the fuel cell (in K), R is the universal gas constant, F is the Faraday constant, n^{el} represents the number of electrons transferred in the electrochemical reactions (= 2 according to (1.9) and (1.10)), and p_i ($i = \mathrm{H_2}, \mathrm{H_2O}, \mathrm{O_2}$) represents the partial pressure of the chemical species (measured in Pa) with p_0 representing standard atmospheric pressure (1 atm = 1.013×10^5 Pa). At standard conditions (*i.e.* $p_i = 1$ atm and $T = 298.15$ K), the reversible cell potential is solely described by the standard electrode potential, which is a function of temperature only. The optimal theoretical voltage produced by a fuel cell is around 1.229 V [7],[25, p 4], but it varies depending on the fuel cell and how E_0 is

approximated.

In reality, the cell voltage is not reversible. The actual cell voltage falls below the open circuit voltage due to the existence of any cracks and fissures in the electrolyte causing electrons to leak into the electrolyte, and due to certain cell overpotentials, or polarisations [25, p 5]. These polarizations include Activation, Ohmic and Concentration polarisations, and is represented in figure 1.9 by the area between the OCV and the actual cell voltage. Activation polarisation is the voltage loss due to a delay in the activation of the electrochemical reactions. This is due to the number of steps which need to be taken within the reaction zones of the electrodes before the electrochemical reactions are activated. These effects are more prominent at very low current density values as shown in figure 1.9. Ohmic polarisation is the voltage loss due to electric resistivity in the electrodes, and ionic resistivity in the electrolyte. These effects occur all throughout the V-I profile in figure 1.9. Concentration polarisation is the voltage loss due to mass transfer limitations within the electrode, where not enough Hydrogen (and Oxygen) is entering the TPB to participate in the electrochemical reactions. These occur at high current density values as shown by the late drop in voltage and power density near the end of the graph in figure 1.9. The derivation of the open circuit voltage, and the cell polarisations will be explained in more detail in chapter 3.

1.4 Layout of a Solid Oxide Fuel Cell

1.4.1 Planar

Figure 1.10 shows a schematic of a typical planar SOFC layout. It consists of all the cell components including the interconnect, and can easily be stacked on top of or alongside each other in the form of a stack to obtain the highest power density available. The interconnects are located either side of the PEN structure with the gas channels located in the slots in-between the electrode and the interconnect on both sides.

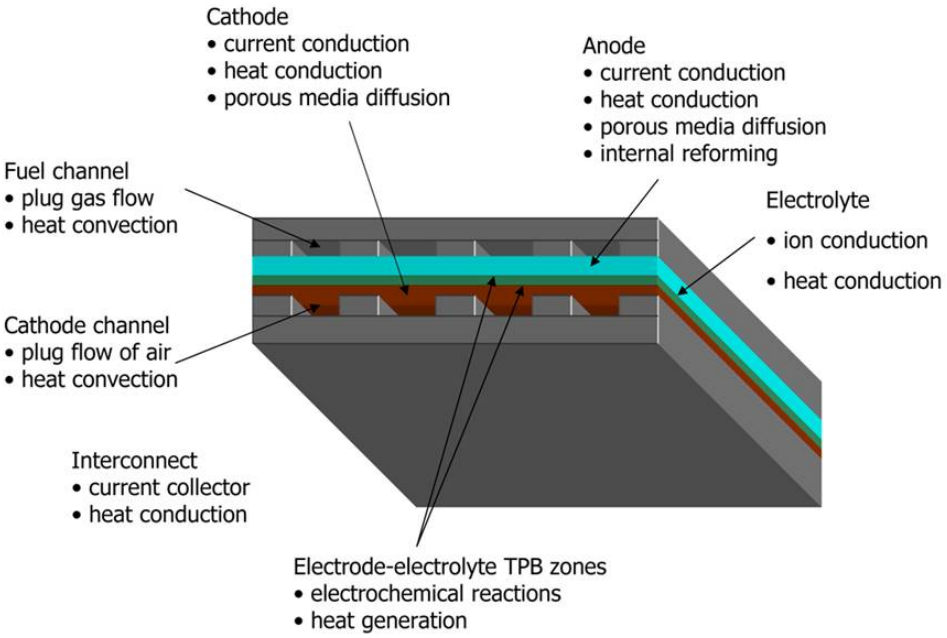

Figure 1.10: A schematic of a planar SOFC with a description of each component of the fuel cell (taken from [25, p. 6]).

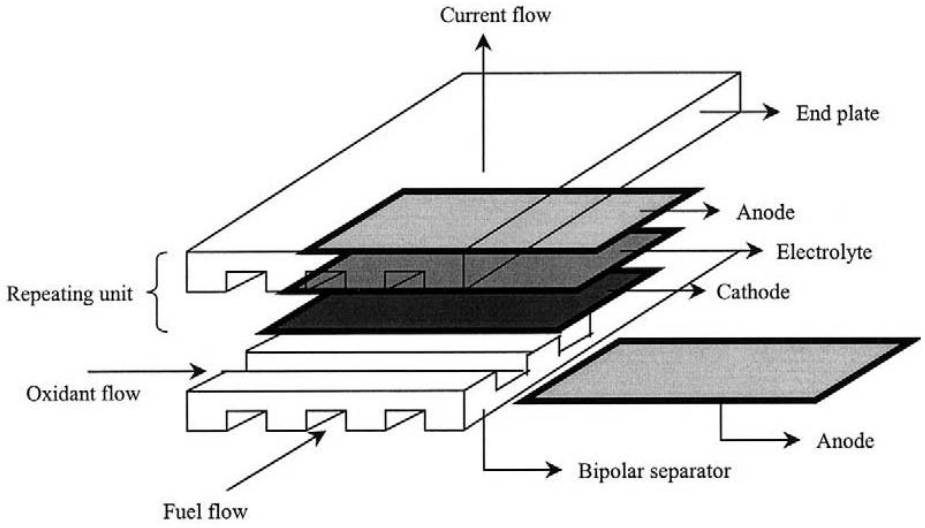

Figure 1.11: A schematic of a planar SOFC with a cross-flow arrangement where the oxidant flow is flowing width-wise and the fuel flow is flowing lengthwise (taken from [1]).

The main design requirements of a planar SOFC include good electrical and electrochemical performance, good thermal management, and high mechanical/structural integrity [18, pp 198-199]. To enable good electrical performance, the Ohmic polarization losses have to be small. The interconnects in a planar SOFC are built so that electrons can be easily transported to and from the PEN structure and across other cells in the stack, which results in a short and direct current path between cells. As the gas channel slots are inserted within the interconnect, there is sufficient contact area between the electrodes and the interconnect, enabling good electrical contact. All of this ensures that Ohmic polarization losses are small. The mechanical stresses imposed on the cell and the whole stack, especially the interconnect, have to be small, so the interconnect has certain requirements in terms of composition (see subsection 1.5.4).

The flow arrangement of the planar SOFC configuration in figure 1.10 can be either co- or counter-flow. There are quite a few different flow arrangements for planar SOFC configurations. The planar SOFC in figure 1.11 has a cross-flow arrangement, where the fuel and air flow travel perpendicularly to each other. Other flow arrangements include Z-flow, Serpentine, Radial and Spiral flow [18, pp. 199-201]. The stack design also requires the use of manifolds (external or internal to the structure) to route gases from a supply point to the cell, and to also remove waste gases [18, p. 201]. There are also a variety of planar SOFC configurations, either self-supporting or external supporting, each with their own benefits and drawbacks [18, pp. 202-205]. In a self-supporting SOFC, one of the main cell components (anode, cathode or electrolyte) acts as the main structural support of the fuel cell. Since the 1980s, attention has shifted towards anode-supported SOFCs [22] so that the cell becomes more conductive, especially with thinner electrolytes. In an external supporting SOFC, the main structural support comes from an external component away from the PEN structure, either from the interconnect or a porous substrate. [18, p. 205]. The main advantage of this layout is that it is more capable of producing high power

densities due to a shorter and direct current path across the stack components. However, to prevent corrosion of the interconnect over time and premature fuel mixing, high temperature sealants are often necessary for application at the interconnect, which can be very costly in terms of overall fuel cell design [18, p. 208]. The materials required for these sealants are usually insulating glass or glass ceramics, which contain highly volatile earth-based materials [25, p. 7]. Due to the high cost and volatility of these sealants, some designs aim to avoid sealing altogether.

1.4.2 Tubular

The PEN in a tubular SOFC (figure 1.12) represents a solid tube, where the interior layer is the cathode, the exterior layer is the anode, the layer in the middle is the electrolyte and the interconnect located at the top of the tube, running along the length of the cell. The air flows inside the tube in contact with the cathode layer and the fuel flow surrounds the outer surface area of the tube. The location of the interconnect at the top of the tube results in a longer current path, which means that it has the disadvantage of lower power densities in comparison to the flat-planar SOFCs [18, p. 217]. To combat this problem, high power density designs consisting of flattened tubes can be developed to reduce the current path and increase the power density [18, pp. 217-218]. The main advantage of the tubular SOFC layout is that unlike planar SOFCs, tubular SOFCs can be manufactured without the use of expensive sealants [18, p. 217], saving money, although they are mainly suitable for stationary applications [18, p. 217]. Another advantage of this is its enhanced tolerance for high thermal stresses [25, p. 6], meaning that the cathode can be made thinner, reducing Ohmic resistance.

The tubular SOFC in figure 1.12 represents a large diameter tubular SOFC design. Plenty of research has also been focused towards micro-tubular SOFC designs [18, p. 219-225],[27]. They have two major advantages over large diameter SOFCs in that they

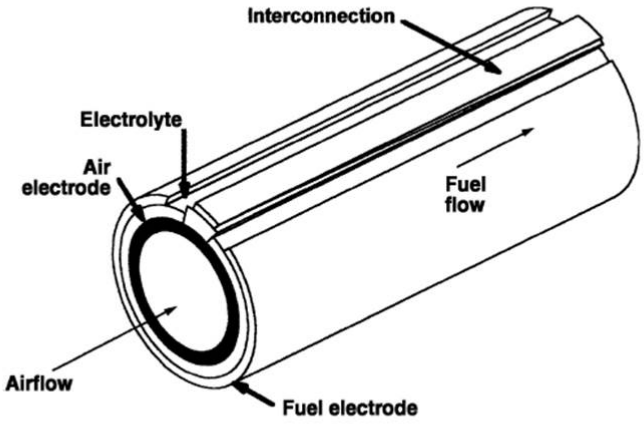

Figure 1.12: A schematic of a typical tubular SOFC (taken from [26]). Air flows inside the cell, fuel around the outer surface of the cell, and the interconnect is located at the top of the cell.

achieve higher volumetric power densities, and they have an even higher thermal shock resistance (despite the increased thermal stability of large diameter tubular SOFCs in comparison to its planar counterpart) [18, p. 219]. The design of the micro-tubular SOFC is similar to a large diameter SOFC, except in length scales, where the electrolyte acts as a support for the electrodes, the diameter is typically around 2 mm, and the length is around 10-20 cm [18, p. 219]. A review of micro-tubular SOFCs and their stacks can be found in [27].

1.5 Materials of cell components

1.5.1 Anode

The anode materials must have the following capabilities:

- It must be a Mixed Ionic and Electronic Conductor (MIEC) (*i.e.* it must allow the transport of oxide ions and electrons within the component);

- Sufficiently porous (for ease of transport of hydrogen molecules from the bulk flow to the reaction zone);
- Chemically compatible with the electrolyte (ionic conductor) and interconnect (electronic conductor);
- It must be stable in highly reducing atmospheres (*i.e.* when oxidation is prevented by the removal of oxygen in the fuel cell and any other oxidizing gases/vapours) exhibiting oxygen partial pressures as low as 10^{-20}atm [25, p. 8];
- It must catalyse the electrochemical reaction (1.10), as well as the reforming reaction (1.13) and its associated water-gas shift reaction (1.14) in the case where hydrocarbons are present in the fuel;
- It must resist coking (*i.e.* the blockage of pores in the anode) due to gas phase carbon deposition [25, p. 8].

The material mainly used for purely hydrogen-fed SOFCs include yttria-stabilised zirconia, along with around 30-50 mol-% Nickel Oxide (NiO) cermets (with the nickel oxide being reduced to Nickel prior to operation) [25, p. 8]. This material for the anode is suited to applications with YSZ based electrolytes, especially as it is a Mixed Ionic-Electronic Conductor (MIEC). Nickel, besides being a good electronic conductor, also acts as a good catalyst for the oxidation reaction (1.10), and for the steam-reforming reaction (1.13).
The main risk with Nickel based cermets, especially with the existence of carbon monoxide and methane in the fuel, is that there is the risk of carbon deposition on the anode according to the *Boudouard Reaction*

$$2\mathrm{CO} \leftrightarrow \mathrm{CO_2} + \mathrm{C}, \tag{1.16}$$

and the methane decomposition reaction

$$CH_4 \leftrightarrow 2H_2 + C, \tag{1.17}$$

which may result in coking in the cell [25, 18]. It is also has some sensitivities with Sulphur [18]. To try and prevent this, lower operating temperatures are considered, plus additional and alternative materials have been considered, including a layer of yttria-doped ceria (CYO) between the electrolyte and the Ni/YSZ cermet [24], and replacing Nickel-based cermets with Copper-base cermets (Cu) [24], or Cu-Ni based alloys [25] as Copper is not only a good electronic conductor, but is also less sensitive to sulphur impurities and very useful as a catalyst for the steam-reforming reaction (1.13) [24]. Copper/Cobalt (Co) based alloys have also been looked at, and are apparently more tolerant to carbon [24]. These are all examples of metal-ceria based systems. Oxide mineral systems have been looked at as alternatives, including perovskites, pyrochlores and spinels [24], although there is still difficulty in finding a type that is as good as Nickel in terms of catalytic activity for both the oxidation reaction (1.10) and the steam-reforming reaction (1.13), as well as being a good MIEC.

1.5.2 Cathode

The cathode materials must have the following capabilities:

- High electronic and ionic conductor (*i.e.* mixed ionic electronic conductor (MIEC))due to presence of electrons and oxygen ions (from (1.9));
- Sufficient porosity for gas phase transport;
- Must be catalytically active towards the reduction reaction (1.9);
- Must be chemically compatible with other cell components (electrolyte, interconnect, sealant (if needed));

- Must have dimensional and thermodynamic stability in oxidizing atmospheres.

The main cathode-based materials are perovskite-structured ceramic electrode materials [1, p. 445]. The most common perovskite used as cathode material is strontium-doped lanthanum magnetite (LSM) [25, 24], due to its good electrical conductivity, good catalytic activity for the reduction reaction (1.9), good thermal stability and is compatible with a variety of possible electrolyte materials, especially with regards to the transfer of oxide ions to the electrolyte. For lower temperature (Intermediate-temperature) SOFCs, A-site-doped lanthanum ferrite perovskites (LSF) (including Strontium-doped lanthanum ferrite perovskites) are considered [24], as well as cobaltites (Cobalt including perovskites) where doped ceria is used as the electrolyte/barrier layer to deal with the high thermal expansion coefficient of cobalt [24]. Other materials considered as cathode materials include K_2NiF_4 structures due to the high diffusivity of oxide ions [24], and ordered double perovskites [24].

1.5.3 Electrolyte

The material for the solid electrolyte must have the following capabilities:

- Must be solely an ionic conductor (only oxygen ions can travel through the electrolyte towards the anode to participate in (1.10));
- Sufficiently strong to provide structural support;
- Gas tight;
- Must be as thin as possible not to compromise on required conductivity;
- Must be thermodynamically stable in oxidising and reducing environments (related to reactions (1.9) and (1.10));

- Should have high mechanical strength and toughness to withstand dynamic, mechanical and thermal loads;
- Must be chemically compatible with anode and cathode materials.

The main material of choice is YSZ with its conductivity based on oxide ions (in this case, YSZ containing 8 mol-% Y_2O_3) [25, p. 8]. This meets the required criteria above, especially for temperatures between 700-800°C [24]. Scandia-doped zirconia (ScSZ) is one of the main choices for intermediate-temperature SOFCs [24]. Other choices for electrolyte material include *Bismuth Oxide* electrolytes (stabilised), which does have a higher conductivity, but not as stable with regards to reduction to bismuth metal under anode conditions (compatibility with the anode) [24]; ceria-based electrolytes like Gd- and Sm-stabilised ceria electrolytes which, along with ScSZ, is more suitable for intermediate-temperature SOFCs, and is compatible with cathodes made with cobalt containing perovskite oxides [24]; Perovskite related systems, LAMOX and rare-earth apatites are also considered [24].

1.5.4 Interconnect

The interconnect material must have the following capabilities:

- Must be solely a good electronic conductor (to enable transport of electrons from one fuel cell to another in a stack). Must not allow transport of chemical species;
- Chemically compatible with electrode materials [28];
- The thermal expansion coefficient must match well with the thermal expansion coefficient of all the other cell components [18, p177];
- Must have adequate stability in both oxidising and reducing atmospheres (especially as it has to deal to oxygen on one side and fuel on the other) [28];
- No reactions are allowed to occur.

- In the case of planar SOFCs, it (bipolar plate) must be dense (to provide structural support), have high mechanical strength and toughness, and be able to be easily fabricated [28].

Interconnects are made of either Ceramic-based materials such as Lanthanum and Yttrium Chromites [18, pp. 174-180], or they can be metallic [18, pp. 181-186]. For tubular SOFCs, interconnects are made of Mg-doped lanthanum chromites (LSMC) [25, p. 9]. These materials are also used for some planar designs. The main problem with ceramic-based interconnects is their sensitivity to oxygen partial pressures, and the cost of ceramic-based interconnects [28]. The bipolar plates/interconnects of planar SOFCs on the other hand are mainly metallic [25, p. 9],[28] (such as engineered Cr-based alloys and ferritic stainless steels [18, p. 185]), with protective layers of perovskites on it to prevent cathode poisoning from Cr species evaporating from the plate metallic surface (the most volatile being chromium acid) [18, p. 187]. The other problem with metallic interconnects is the formation of oxide scales, especially with the interaction of the interconnect with the ceramic-based cell components [18, p. 187], but certain perovskite-based materials on the whole provides good protection for the metallic interconnects [18, pp. 187-189].

1.6 Benefits and Limitations

SOFCs have noticeable benefits, including high efficiency levels (around 60%), especially in comparison with other fuel cells [29], good reliability and the capability to produce high power densities. Their high operating temperatures mean that not only is internal reforming inside the cell is possible (including the breakdown of hydrocarbons), which gives SOFCs fuel flexibility, but reactant activity (*i.e.* increasing current density and reducing polarizations) is increased [1]. SOFCs can use a variety of catalysts to initiate the electrochemical and chemical reactions (see section 1.5). Also, the temperatures of the exit gases are higher, making SOFCs a good source of heat as well as electricity. This

makes them useful as Combined Heat and Power systems (CHP), where heat is given off as a by-product. Also, at low enough costs, they could be used as hybrid/gas-turbine cycles [30].

However, there are also very noticeable limitations to SOFCs that need to be taken account of. Higher operating temperatures results in a longer start-up time, and it is very sensitive to temperature changes [1, 31]. Also, high temperatures result in corrosion of components, decreasing the lifetime of the cell (especially under thermal cycling conditions), and requiring the use of high-cost alloys and sealants to protect certain components like the interconnect [31, 32].

1.7 Applications of Solid Oxide Fuel Cells

Solid Oxide Fuel Cells have the potential to be used in a wide variety of applications for both stationary and mobile:

- Small portable devices including a thermally integrated 20 W portable system concept which includes a SOFC operating on jet fuels, and a 500 W battery-charging system in which the SOFC operates on logistic fuels [30]. There are quite a few companies that develop portable SOFC systems for military applications, including Protonex [33];

- Small power systems (around a few kilowatts), including a 5 kW small power system for stationary applications as well as for automobile auxiliary power units [30]. The main developer of SOFC-APU units is Delphi [34]. Projects including Callux in Germany [35], and the ENE farm project in Japan [36] have developed stand-alone fuel cell systems for households, including boilers and water tank units;

- Distributed generation power plants (between 100-500 kW [30]) in the form of Combined Heat and Power systems (CHP), where the by-product heat generated from

the fuel cell can be used to provide heat to a certain location. There are various forms of CHP fuel cell systems, from stand-alone to network (*i.e* individual buildings to a group of buildings linked to each other), heat load following or electrical load following, and fixed heat-to-power ratio to variable heat-to-power ratio [37]. One particular example is Bloom Energy. Based in California, USA, they have SOFC power distributors which can generate over 200 kW of power, and can be fuelled using natural gas [38];

- Multi-MW systems such as a SOFC-GT (Gas Turbine) hybrid system [30]. Companies like Fuel Cell Energy Solutions [39] can develop MW-SOFC systems which can be used for grid generation.

A list of all the major fuel cell manufacturers (including SOFC) can be found in [40][2].

1.8 Summary

A introduction to fuel cells and Solid Oxide Fuel Cells was made in this chapter. Fuel cells are electrochemical devices that produce electricity (and heat) via electrochemical conversion of Hydrogen and Oxygen, making it a more cleaner and efficient way to produce electricity compared to using fossil fuels. The principle of fuel cells was discovered by either Grove or Schönbein in the 1830s, and from the first invention of a fuel cell for practical purposes by Jacques in the 1890s, there is a core group of around five fuel cells with varying operating temperatures. Low-temperature fuel cells like PEMFCs and AFCs have very quick start-up time, and can be used for a wide variety of mobile applications. But the low operating temperatures makes them on the whole susceptible to poisoning by certain contaminants like sulphur dioxide, carbon monoxide and even carbon dioxide. This is not much of a problem for higher temperature fuel cells, which can take in more natural fuels including hydrocarbons. It also has the added benefit of providing

[2]All websites referenced in this section true as of 15th August, 2015.

heat along with electricity in a combined heat-and-power system (CHP), but there is the problem of longer start-up times, and corrosion of cell components over time due to the high operating temperature, especially for SOFCs.

Building on work on solid electrolytes by Nernst and Wagner, plus work in the 1930s by Baur and Preis, the first commercial SOFC was made by Siemens-Westinghouse in the early 1960s. Since then, most of the research has been concentrated towards finding the optimal materials for the components of the SOFC. Unlike MCFC, SOFCs can operate on a wide temperature range (including temperatures less than 600°C depending on materials used). The voltage produced by the cell once a current is drawn is affected by any cracks/fissures in the electrolyte, and polarizations within the cell due to the resistivity of the electrodes and the electrolyte, the delay in start-up of the electrochemical reactions, and the eventual lack of hydrogen consumed in relation to water produced for higher current density values.

There are two main SOFC design layouts: planar and tubular. Planar SOFCs have gas channels inserted into the interconnect, increasing the surface area of the interconnect allowing a larger transport of electrons to and from the cell. These are placed on top and alongside each other in the form of stacks to obtain as much power as possible. Planar SOFCs have the advantage of high power densities, especially due to its short current path. But expensive sealants for the interconnect are required to prevent serious corrosion of cell components. Tubular SOFCs have higher tolerance of high thermal stresses, and do not require the use of expensive catalysts, but the location of the interconnect at the top of the cell does increase the current path, reducing power density. Flattened tubes have been considered, but the focus is now on micro-tubular designs.

Both electrodes are Mixed Ionic and Electronic Conductors (MIEC), and are sufficiently porous to allow the transport of hydrogen, water and oxygen molecules into/out of the electrodes. Materials for the anode include Nickel-based cermets, like Nickel mixed with

yttria-stabilised zirconia (YSZ), which is a good ionic conductor, and Nickel mixed with Copper based cermets which is a good catalyst for the steam-reforming reaction. Materials for the cathode include perovskite-based materials like strontium-doped lanthanum magnetite (LSM). Electrolytes must be solely ionic conductors to allow transport of oxide ions from the cathode to the anode, as well as being compatible with both electrodes. The main material is YSZ, although there are alternatives which have higher conductivities, but they are either not as stable as YSZ, or they are more suitable for intermediate-temperature SOFCs. Interconnects on the other hand must be solely electronic conductors, not participate in any reactions, be compatible with both electrodes, and have high mechanical strength. The main materials are ceramic-based interconnects and metallic interconnects, but (especially for planar SOFCs), they require the use of sealants to prevent long-term corrosion and formation of oxide scales.

The benefits of SOFCs align with the benefits of high-temperature fuel cells, that being higher efficiencies and power densities in comparison with other fuel cells, fuel flexibility due to its ability to break down hydrocarbons (thanks to its higher operating temperatures), and solely in the case of SOFC, the wide variety of applications of SOFCs (mobile and stationary), ranging from small portable devices to transport and auxiliary power units, and from providing heat and electricity for households to mini power plants and electrical grids. The main disadvantages include the start-up time of SOFCs, and the durability of cell components over time as a result of the high operating temperatures.

Chapter 2

Literature Review

2.1 Introduction

In this chapter, we will review some of the literature covered in this thesis. This chapter starts off by covering introductory texts to Solid Oxide Fuel Cells, review papers covering most of the work done in steady-state and dynamic SOFC modelling so far, and papers looking into how the different dynamics and aspects of a Solid Oxide Fuel Cell are modelled mathematically. Next, the work done on the existence of multiple steady-states within a Solid Oxide Fuel Cell will be covered, followed by an overview of some of the work done on general steady-state behaviour within a Solid Oxide Fuel Cell. The work covering the dynamic behaviour of the SOFC, including transient behaviour will also be covered in this chapter. This chapter ends with a conclusion, stating how this thesis aims to move beyond the work covered in this chapter.

2.2 Introductionary texts and Review papers

A good introduction into Solid Oxide Fuel Cells, how they work, thermodynamics, mathematical modelling and solution approaches is given by K. Kendall and S. Singhal [18], and R. Bove and S. Ubertini [25]. The history of SOFCs, as well as fuel cells in general is given by Andujar and Segura [2], while a more focused historical insight into SOFCs is

given in [1] and [22]. Applications of SOFCs are covered in a paper by Minh [30], while a complete list of fuel cell manufacturers can be found in the fuel cell industry and patent review by Blue Vine [40].

In terms of research into Solid Oxide Fuel Cells, there are two review papers which give a good insight into SOFC research and some of the issues which need addressing in terms of progression in SOFC research development: one by Bavarian et al. [41], and the other by Huang et al. [42]. [41] gives a comprehensive review into the recent research done in terms of mathematical modelling of SOFCs and PEMFCs. For both SOFC and PEMFC modelling, a comprehensive list is given of the dimensions of the model, whether it is steady-state or transient, and what the model accounts for along with a reference. A brief description of these papers is also given. A review of the work done into steady-state behaviour of both SOFCs and PEMFCs is given, including multiple steady-states as well as dynamic behaviour, sample studies and control studies.

The second review paper [42] mainly focuses on the research of the dynamic behaviour and control of Solid Oxide Fuel Cells. This paper covers briefly the history of solid oxide fuel cells, the main components and governing equations of SOFCs, the dynamic modelling of SOFCs, and SOFC control. For the dynamic modelling section, this paper goes through different aspects of dynamic modelling including dynamic modelling in electrodes (including Source of energy, activation, concentration and ohmic losses), flow channels, modelling of temperature dynamics, and goes through the work done by researchers in those areas. Validation of these dynamic models are then discussed, including the difficulties face by researchers in conducting direct experiments to validate their models. After a short analysis and summary of the main sources of dynamic modelling, this paper goes on to discuss other development and applications of dynamic models, reviewing different dynamic models used by researchers to describe certain dynamics of SOFCs (i.e. temperature dynamics, polarization, flow rates, etc.), finishing off with a review of what are

the main issues regarding the dynamic modelling of SOFCs are. Two of the main issues regarding dynamic modelling of SOFCs are the dynamic effects of various geometries (i.e. the effects of dynamic performance of a tubular SOFC compared to a planar SOFC), and control-relevant dynamic models. Here, [42] mentions that one of the main bottlenecks to SOFC development is the temperature gradient and hot spots which cause cell damage. This in turn could lead to the existence of multiple steady-states within the SOFC, which is what is being covered in this thesis.

As for papers which give a comprehensive review of how SOFCs are mathematically modelled, there are two main papers. The first paper is by Bove and Ubertini [43], and the second paper is from [44]. The first paper is a detailed summary of the mathematical modelling chapter in [25] from the same authors. [43] presents a complete, three-dimensional, time dependent SOFC model, that considers all the phenomena that occurs for all the different SOFC components (gas channels, electrodes, electrolyte and interconnect). The model presented in [43] is independent of cell geometry. The reactions considered include the Red-ox reactions in the TPBs (electrochemical reactions involving Hydrogen and Oxygen), the shift reforming reaction, and the associated water-gas-shift reaction. For the gas channels, the mass, momentum and energy conservation equations are considered in their complete form. In the electrodes, current, ionic and electronic conservation is considered, where the Butler-Volmer equation is defined. In some cases, the TPB is located at the electrode/electrolyte interface. Energy and mass conservation is also considered in the electrodes, where mass transfer is dominated by diffusion. Three different expressions for the diffusion coefficient are covered. Momentum conservation within the electrodes (if considered), is described using Darcy's law. Within the electrolyte, ionic, current and energy conservation is considered, and electronic, current and energy conservation is considered for the interconnect. The paper also covers the different methods that can be used to discretise the equations (finite difference, finite volume and finite element), approaches

to finding a solution to the problem in 3D, 2D, 1D , 0D and multi-dimensional forms, and Boundary Conditions applied to each component (internal and external). The boundary conditions applied to each cell component are usually source/sink terms in which, depending on the problem, can be incorporated straight into the conservation equations. This paper is useful as an introduction to how SOFCs are modelled mathematically, and the different approaches that can be taken. But, it lacks some detail in how certain dynamics and parameters are defined, and the different derivations considered by certain authors. This is covered more thoroughly by Hajimolana et al. in [44]. Just like [43], it presents a complete set of equations for each component of the SOFC. Unlike [43], it takes into account the different geometries of the SOFC, namely the planar and tubular configurations, and presents the equations for both geometries. Also, unlike [43], it delves deeper into certain dynamics that affect the performance of the SOFC, namely the different polarisations and how they are defined, and also presents different derivations used for certain parameters such as the heat-transfer coefficient, the diffusion coefficient, radiation, approximations for the pressure gradient, and reaction rates for the reforming and shift reactions. It is a more thorough review of how the different dynamics are modelled for each component according to how it has been modelled in literature. However, it does miss out the current conservation equations within the electrodes, electrolyte and the interconnect. Despite this, it builds on [43] by giving an insight as to how different equations and terms/parameters within these equations are modelled by different authors.

2.3 Steady-State Multiplicity

The earliest work on the existence of multiple steady-states in a Solid Oxide Fuel Cell (SOFC) was done by Debenedetti and Vayenas in 1983 [45], where they set up a mathematical model describing the steady-state behaviour of a high-temperature SOFC. Two different fuels were considered (Hydrogen and Carbon Monoxide), and the model con-

sisted of six equations describing the material balance of Oxygen and the fuel, an energy balance equation, reversible cell voltage, actual cell voltage, and the coupling of the actual cell voltage with cell current by Ohm's law where an external load is considered. Specific resistivity of the electrolyte was defined to be inversely proportional to the cell temperature. The gas mixtures in the anode and cathode channels were assumed to be well-mixed, and the fuel cell is assumed to be isothermal. The equations describing the material balances of Oxygen and the fuel, cell temperature, reversible and actual cell voltages and cell current were non-dimensionalised into four algebraic equations describing the material balances of Oxygen and the fuel, the energy balance and the electron balance in the fuel cell. The oxygen feed rate in the fuel cell was controlled by fixing the air feed ratio at a desired level. In terms of steady-state behaviour, it shares similar qualitative characteristics to a chemical Continuous Stirred Tank Reactor (CSTR).

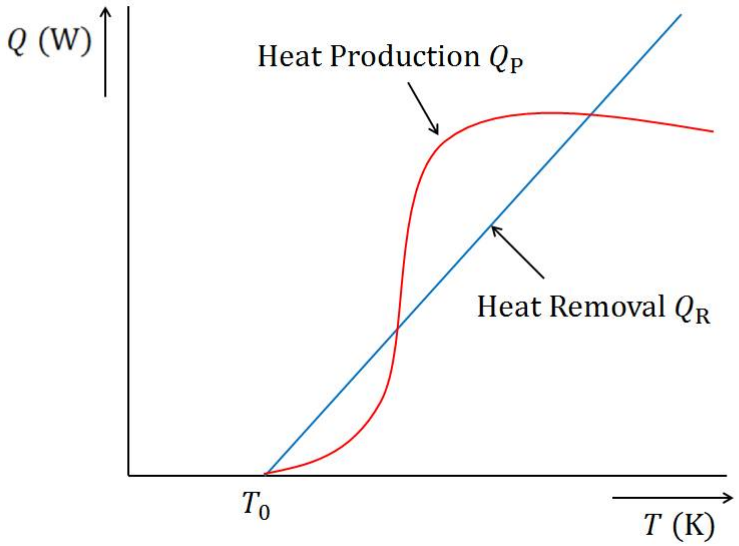

Figure 2.1: A schematic diagram showing heat balance in a mixed reactor. Q represents heat, T represents the temperature of the reactor, and T_0 represents the inlet temperature. The blue curve Q_R represents the amount of heat removed from the reactor, and the red curve Q_P represents the amount of heat produced within the reactor. The number of steady-state solutions can be represented by the number of intersections between the two curves.

van Heerden in 1956 [46] showed that in a continuous exothermic process, a **continuous mixed reactor** can exhibit up to **three steady-states**. Two of these states are stable: one with low temperature and a low degree of conversion, the other with a higher temperature and almost complete conversion. The remaining steady-state in-between those two stable steady-states is unstable. The main reason for the existence of more than one solution is due to the exponential dependency of the reaction rate on temperature, where an Arrhenius expression is used to describe the reaction rate. By considering the material and heat balance inside the mixed reactor, he showed that the number of steady-state solutions is equivalent to the number of intersections of the heat production curve with the heat removal curve with increasing temperature (see figure 2.1). Heat production within the mixed reactor is due to the heat produced from the reaction and results in an S-shaped curve due to an initial exponential increase in the amount of heat produced due to the reaction, followed by an eventual decrease due to almost complete conversion. Heat removal is due to the difference between heat coming into the cell and heat going out, and is represented by a straight diagonal line intersecting the initial temperature value on the x-axis.

As for a SOFC, heat generation within a fuel cell is also affected by the electrical energy produced by the fuel cell, while heat removal is similar to a chemical CSTR shown in [46]. In [45], the heat production and heat removal terms are dimensionless. Despite the slight differences in heat production, qualitatively, the shape of the heat production curve in a fuel cell is very similar to the heat production curve in a CSTR, hence the possibility of the existence of more than one steady-state within a SOFC. Electrolyte conductivity plays a big part in the existence of an ignited steady state, which can be maintained depending on the ratio of the external cell area to the electrolyte area (see figure 2.2). Increasing the ratio increases the amount of heat removed from the fuel cell (powered by Carbon Monoxide) in comparison to the heat produced, hence only one unignited steady-state

solution exists at a low temperature value.

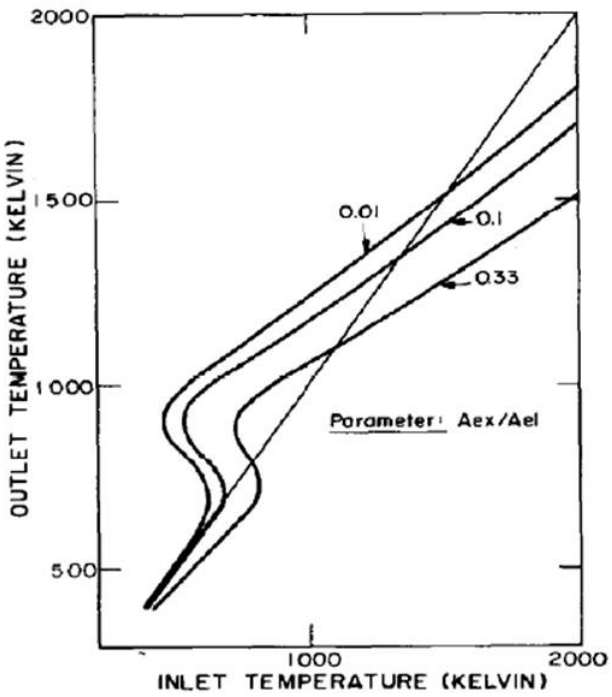

Figure 2.2: The influence of cell geometry on steady-state multiplicity of a SOFC fuelled by Hydrogen, with a constant air feed ratio operation in [45]. A_{ex} represents the external cell surface area, A_{el} represents the electrolyte area. The ratio of A_{ex} to A_{el} is not much more than 0.3. Decreasing this ratio helps the cell to maintain an ignited steady-state, as shown by the intersection of the heat removal curve (straight line) with the heat production curve at higher values of the outlet temperature.

For a constant air feed ratio operation (powered by Hydrogen), decreasing the ratio lifts the heat production curve which also results in the existence of only one steady-state solution, but this time at a higher temperature value. Steady-state multiplicity can also be removed from the fuel cell by increasing the air feed rate (as well as decreasing the external load resistance and increasing the air feed temperature), resulting in one steady-state solution at a high temperature value.

In 2006, Mangold et al. [47] investigated the existence of multiple steady-states within a planar SOFC for three modes of operation: (i) **Constant External Load**; (ii) **Potentiostatic** (constant voltage); (iii) **Galvanostatic** (constant current). Two separate

models were considered: one a simple lumped-parameter model consisting of only four equations taking account of cell temperature, voltage drop in the electrolyte and the reaction kinetics within the anode and the cathode (described by the activation polarization terms); the other a more detailed, spatial model also taking account of mole balances within a fuel cell, energy balances within the gas flows, diffusion within the electrodes (based on convective mass transfer), open circuit voltage, and charge balances within the electrodes.

For a cell operating under a constant external load, cell voltage and cell current are coupled by Ohm's law. The external load resistance component represents the part of the circuit that consumes electrical power. The other two modes of operation are more suitable for testing cell stacks, observing how they perform as the cell components degrade over time. Heat production in the cell is a net difference between the net enthalpy fluxes of Hydrogen, Oxygen and Water going into the cell and the amount of power per unit area dissipated from the cell into the external circuit. This net difference represents the energy liberated from the electrochemical reactions. Heat removal is due to forced convection either side of the cell by the fuel and air flows either side of the cell. For each of the three modes of operation, the constant parameter is treated as the bifurcation parameter. Any steady-state multiplicity within the cell (including location of ignition and extinction points) can be shown by the existence of a hysteresis loop in the constant parameter versus cell temperature profile. This is backed up by the number of intersections between the heat production and heat removal curves for values of the bifurcation parameter where more than one solution exists. For a constant external load and potentiostatic operation, up to three steady-states are observed for the lumped parameter model.

The main reason for this is due to the inverse, non-linear relationship between electrolyte conductivity and temperature, which increases with increasing temperature (due to a decrease in load resistance and cell voltage). This leads to an increase in cell current, and

since the consumption/production rates of hydrogen, oxygen and water are described in terms of the current density, the reaction kinetics intensify, leading to the formation of a hot spot within a SOFC. If the cell voltage or load resistance is reduced low enough, the cell temperature shoots up to a new, ignited steady-state[1]. This was highlighted in their previous paper [48] back in 2004. In [48], a one-dimensional high temperature fuel cell model was considered, and the model only consisted of equations describing energy conservation of the cell, activation polarisation in the electrodes, Ohmic polarisation and a relation between current density and the total current (similar to the lumped-parameter model in [47]). Working with a non-dimensionalised form of the model, it is shown that via phase plane and bifurcation analysis that complex spatial temperature and current density patterns are observed for both the potentiostatic and galvanostatic cases, which could lead to hot spots. The work done in [48] is more theoretical than any of the other works considered in this section.

The rise in the operating temperature after ignition is greater for the potentiostatic case than it is for the case of a constant external load (see figure 2.3), hence a larger multiplicity region. As for the galvanostatic case, a constant cell current removes any non-linearity associated with the reaction kinetics. This more linear behaviour between electrolyte conductivity and temperature means that no multiple steady-states exist for that case. Regions where multiple steady-states exist was investigated for different values of the heat transfer coefficient. Increasing the heat transfer coefficient increases the amount of heat removed by the fuel cell by convection, resulting in a steeper heat removal curve which in turn results in a larger multiple steady-state region for lower values of cell voltage. To ensure that no multiple steady states exist, inlet cell temperatures are increased to ensure that less heat is removed by convection, leading to a more gradual rise in temperature.

[1]For the lumped parameter model in [47] (plus future works in this section), the location of the hot spot within the SOFC is not a major concern. Since the temperature of the whole cell component shoots up towards a new steady-state solution on another steady-state branch once a hot spot is formed anywhere within the SOFC, the hot spot is assumed to cover the whole cell component.

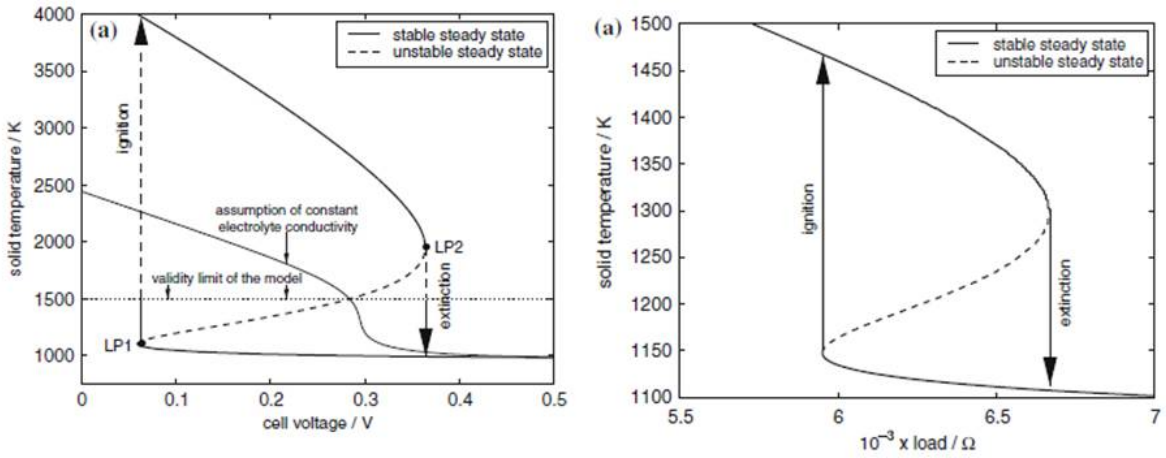

Figure 2.3: Two theoretical profiles showing how changing the value of the bifurcation parameter (Cell voltage on the L.H.S. and Load Resistance on the R.H.S.) affects the operating cell temperature in [47]. For certain values of both bifurcation parameters, up to three steady-state solutions for cell temperature exist. The multiplicity region in both profiles is expressed in terms of a limit-cycle, hysteresis style loop with the existence of an ignition and extinction state. On the profile on the L.H.S. there is an alternative profile where electrolyte conductivity is assumed to be constant, highlighting how important electrolyte conductivity is to the existence of multiple steady-states.

For the potentiostatic case, if the heat-transfer coefficient is increased, the gas inlet temperatures have to be increased further to remove any steady-state multiplicity within the fuel cell. However, the temperatures in the ignited state are way beyond the reasonable operating temperature of a SOFC, so an increase in the heat transfer coefficient increases the region of the cell voltage that the cell can operate within (as long as the cell voltage is not too low).

For the more detailed, spatially distributed model, it has been observed that up to five steady-states may exist for the potentiostatic operation, and three steady states for the galvanostatic operation (see figure 2.4), due to the additional degrees of freedom in the spatially distributed model. These equations were solved using the method of lines. The reason for the existence of multiple steady-states under a galvanostatic operation is that

the interaction between the heat produced by the electrochemical reaction and the temperature dependence of electrolyte conductivity may narrow down the charge transport through the electrolyte to a small portion of the electrode (as charge transport is considered in the more detailed model), leading to the formation of a hot spot. The importance of the temperature dependence of the electrolyte conductivity was confirmed by a dynamic analysis where the transient behaviour over the length of the cell in response to a change in current was observed for a temperature-independent electrolyte conductivity, and for a temperature-dependent electrolyte conductivity. For increasing time, there was a larger spike in temperature near the cell inlet for the case of a temperature-dependent electrolyte conductivity then for the case of a temperature-independent electrolyte conductivity.

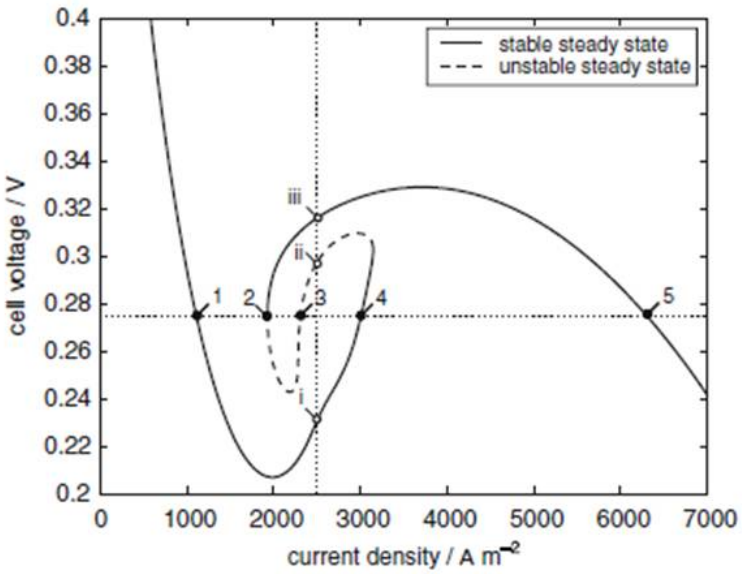

Figure 2.4: The Cell Voltage vs Average Current Density profile based on the more detailed spatially distributed model (from [47]). It shows that for certain values of the cell voltage, upto five steady-state solutions exist (three stable, two unstable), as denoted by the dashed line running lengthwise. Even for a SOFC operating under a galvanostatic operation, upto three steady-state solutions may exist, as shown by the dashed line running vertically.

Continuing the work done in [47], Bavarian and Soroush [49] also investigated steady-state multiplicity in a planar SOFC with a more detailed lumped-parameter model than the

one by Mangold et al. Their model accounted for mass transport and diffusion within the electrodes, the energy balance within the cell, mass balances in the gas channels of the whole gas flow as well as individual gas species, and the energy balance of the gas flow. Voltage within the cell was affected by ohmic, activation and concentration polarizations. Similar to the work done in [47], steady-state multiplicity within the SOFC was investigated under the case of a constant external load (where cell voltage and cell current are coupled by Ohm's law), the potentiostatic case, and the galvanostatic case. For both the constant external load case and the potentiostatic case, the qualitative behaviour of the graphs are similar, but there are differences in the results produced.

Under a constant external load, no multiple steady-states exist when gas inlet temperatures are 980 K compared to the graph in [47], where multiple steady-states exist in a very small region of the load resistance. In fact, multiple steady-states exist for lower inlet gas temperatures due to the role convection (*i.e.* heat loss) plays with regards to existence and size of multiplicity regions. Multiplicity regions are also considered in this case for different values of the heat-transfer coefficient. Just like the potentiostatic case in [47], increasing the heat-transfer coefficient increases the amount of heat removed by convection, leading to larger multiple steady-state regions for lower values of load resistance. Steady-state multiplicity can be removed by increasing the inlet gas temperatures. There is also a three-dimensional graph showing the multiplicity region disappearing from the cell temperature profile for increasing inlet gas flow temperatures. However, the effects of the inlet fuel temperature and the inlet air temperature on SOFC performance have not been investigated separately. So a more thorough parametric analysis of both inlet gas flow temperatures is needed to investigate their individual effects on the operating cell temperature, along with separate multiplicity regions.

The existence of multiple steady-states in a SOFC under a constant external load were also investigated for changes in inlet velocities and changes in inlet molar flow rates for

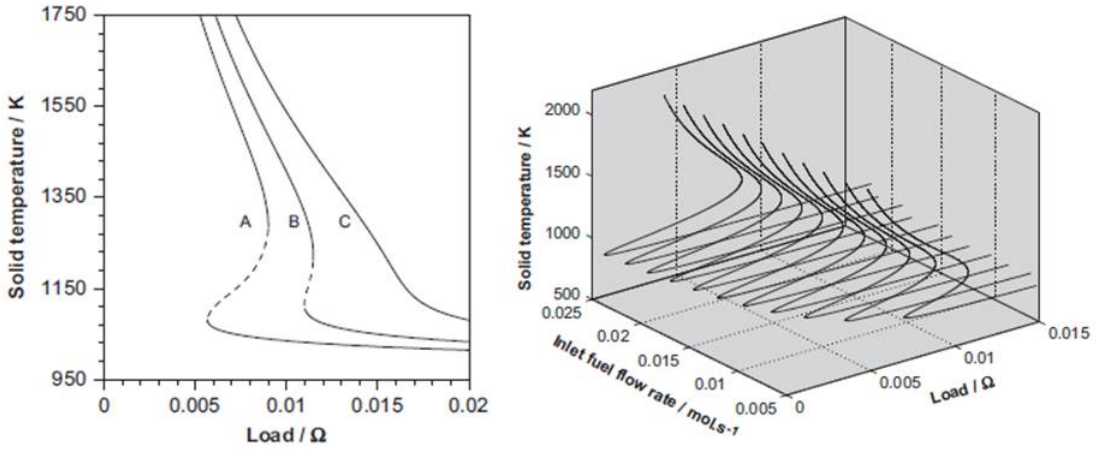

Figure 2.5: Cell Temperature vs Load Resistance profiles for changes in gas flow velocities (L.H.S.) and inlet molar flow rates (R.H.S.) (from [49]). On the L.H.S. profile, increasing the gas flow velocity leads to the profile shown in A, while decreasing the gas flow velocities leads to the profile in C. As for the R.H.S. profile, increasing the inlet fuel molar flow rate leads to larger multiplicity regions. Increasing either gas flow velocity, or the inlet fuel molar flow rate leads to a increase in the size of the multiplicity region located at lower values of the load resistance.

the fuel and air flow separately. An increase in inlet velocity of the gas flows increases the amount of heat removed by convection, increasing the multiplicity region for lower values of load resistance, resulting in a larger ignition state. A decrease in inlet velocities has exactly the reverse effect, such that if they are lowered enough, no multiple steady-states exist. However, similar to inlet gas temperatures, more work is needed to determine which of the two inlet gas flow velocities has a bigger impact on SOFC performance. Also, there are no multiplicity regions to show how the multiplicity region disappears, plus visual representation of the multiplicity region disappearing for lower inlet gas flow velocities.
A change in the fuel molar flow rate has a larger impact on the size of the multiplicity region than a change in the air molar flow rate, and an increase in the fuel molar flow rate results in much larger multiplicity regions for lower values of load resistance, and much larger ignition states the higher the molar flow rate is increased. The only thing that is

missing is the multiplicity regions associated with changes in the inlet molar flow rate. Looking at figure 2.5, we can see the comparison between the work done to investigate the behaviour of the SOFC for changes in the inlet gas flow velocities, and the behaviour of the SOFC for changes in the inlet fuel molar flow rate.

Heat production and heat removal curves were also looked at against cell temperature, as well as the fuel temperature, air temperature and mole fractions of hydrogen, oxygen and water in the triple phase boundary (TPB). There is a linear relationship between the gas flow temperatures and cell temperature (the rise in fuel temperature is much greater than the rise in air temperature). As for the TPB mole fractions, at higher temperatures, more Hydrogen is consumed which is equivalent to a higher conversion rate on the second stable steady state curve.

For the potentiostatic case, the graphs obtained were qualitatively similar to those obtained in [47]. But for inlet gas temperatures of 980 K, the multiplicity range is shifted towards higher values of the cell voltage, and the rise in cell voltage along the ignited steady-state is smaller for lower values of the cell voltage. As for the multiplicity regions, increasing the value of the heat transfer coefficient only shifts the region towards lower values of the cell voltage, but not higher values of the gas inlet temperatures. The galvanostatic case, just like in [47] (when the lumped-parameter model is considered), only has one steady-state due to the removal of the majority of the non-linearity in the model associated with making the cell current constant.

In comparison to the more simpler lumped-parameter model in [47], the multiplicity regions in the more detailed model in [49] are shifted towards higher values of the load resistance and cell voltage, and in the case of a constant external load, lower gas inlet temperatures. Since the gas flow temperatures are no longer constant, and increase with rising cell temperature, the amount of heat removed by convection goes down since the gap between the operating cell temperature and the gas flow temperature is not as big

as in [47]. The amount of heat produced by the cell also is higher than the amount of heat produced in [47] since the enthalpies of Hydrogen and Oxygen increase with rising fuel and air temperatures respectively. However, since the heat-transfer coefficients are still assumed to be constant, it does not fully take into account the effect of velocity and concentration on the amount of heat removed from the cell due to convection. Therefore, for this thesis, there will be an expression for the heat-transfer coefficient based on an approximation of the Nusselt number (subsection 3.3.3).

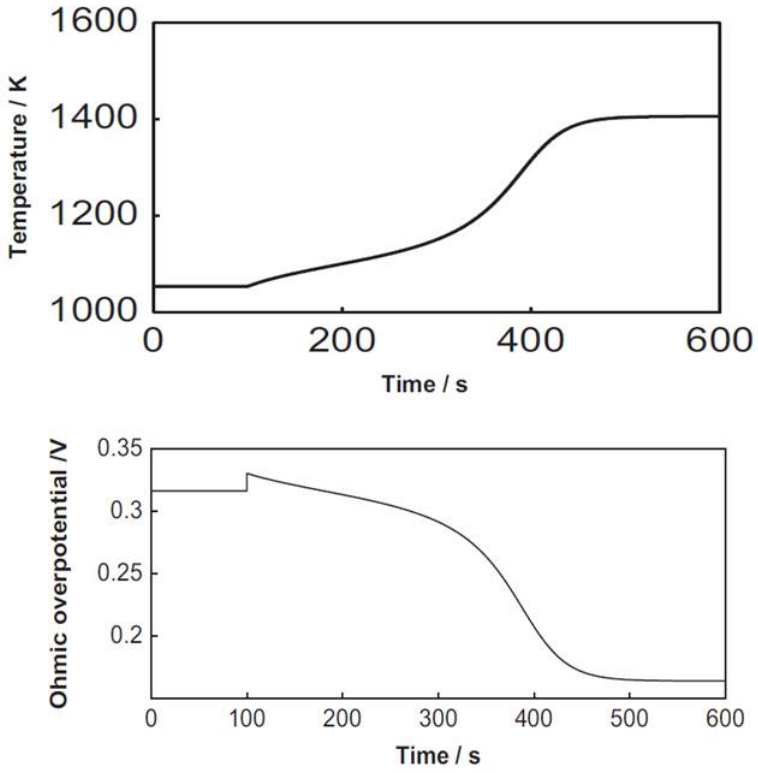

Figure 2.6: Transient behaviour of the operating cell temperature (top) and the Ohmic overpotential (bottom) after the load resistance changes from 0.014 Ω to 0.01 Ω after 100 s (from [49]). The steady-state solution at $R_{\text{load}} = 0.014$ Ω lies along the lower stable steady-state branch, while the new steady-state solution after the change in R_{load} lies on the ignited steady-state branch. Around 300 s, cell temperature gradually moves up towards its new, ignited steady-state solution as the decrease in the Ohmic overpotential (or increase in conductivity) leads to the formation of a hot spot, causing the cell to ignite and operate at higher than expected operating temperature.

Transient behaviour of the cell was also investigated due to changes in the load resistance after 100 seconds: one where the load resistance drops from 10 Ω to 5 Ω, the other where the load resistance drops from 0.014 Ω to 0.01 Ω. For the first case, the cell parameters (including cell temperature) reach a new steady-state which lies along the same unignited steady-state curve. However, for the latter case, since the cell is operating at the ignited state at 0.01 Ω in comparison to 0.014 Ω, the rise in temperature after the reduction in load resistance is larger than the first case, and it takes longer for the parameters to reach the new, ignited steady-states. The transient results show the difference between the transient behaviour of a cell operating along the same steady-state branch, and the transient behaviour of the cell during the ignition phase. However, it is not fully verified that the SOFC is actually operating at a different steady-state regime. To do this, another step-change is needed for the external load resistance (a step-increase, but not larger than the extinction point) to show that it operates on a different regime. This will be rectified in this thesis.

Since that paper was published, Bavarian and Soroush have gone on to look at the existence of multiple steady-states in in a proton-conducting SOFC [50], and a Co-ionic SOFC (along with Benziger and Kevrekidis) [51, 52]. In [50], steady-state multiplicity is considered in a Solid Oxide Fuel Cell with a proton-conducting electrolyte that allows the transport of Hydrogen protons from the Anode to the Cathode rather than Oxygen ions. The main advantages of proton-conducting SOFCs compared to normal SOFCs according to [50] is that the operational temperature is lower, which reduces the cost of operation, and reduces start-up time. The equations are modified to suit the SOFC in question, but the dynamics considered in the model are more or less the same as in [49]. For the electrochemical model, the polarisation terms are defined in the same way as in [49] (with exception of the transfer rate coefficients of the Butler-Volmer equation (subsection 3.2.2)). The only main difference is the specific resistivity of the electrolyte, which

is different due to the material used for the electrolyte. The cell temperature equation is modelled in the same way, where critically the heat-transfer coefficients are still assumed to be constant. Mass and energy conservation are considered for both gas flows (velocity is still assumed constant), and they are modelled in the same way, as well as the concentration of Hydrogen, Water and Oxygen in the TPBs. The only main differences are that Water is now produced in the Cathode, and that since Hydrogen protons, Oxygen and Water molecules exist in the Cathode, the diffusion coefficients are re-defined using the Wilke formula, and the binary-diffusion coefficients by the Chapman-Enskog formula.
The V-I curve for the model at a constant temperature is validated with experimental results, and the graph shows a good fit. In terms of results, the steady-state profiles of parameters such as the mole fractions of individual gas species, gas flow temperatures, and power density for decreasing values of the external load resistance are considered. The change in the profile for the operating cell temperature (plus the multiplicity region) is shown for changing values of the inlet gas flow temperatures, and the inlet molar flow rates, which are assumed to be of the same value. These additional profiles are also considered for the other two modes of operation. Only one steady-state solution exists for the galvanostatic case. Also, there is a comparison between the anode-supported proton-conducting SOFC with the electrolyte-supported SOFC. Nothing is shown of the effect the gas flow velocities have on multiple steady-state behaviour. The main problem with this model, just like the model in [49] is that the heat-transfer coefficient still does not take into account the effect of velocity and concentration on convection. There still is not an accurate representation of the amount of heat that is actually removed in the SOFC. The lack of derivation for the heat-transfer coefficient is rectified in [52], where a Nusselt number approximation was used for a laminar, forced external flow over a flat, parallel plate of length L. The SOFC considered in [52] is a co-ionic conducting SOFC, where the electrolyte is made of materials which enable it to conduct Hydrogen protons and

Oxygen ions. This means that there are four electrochemical reactions to consider, and an increase in the number of equations to the model due to the extra reaction kinetics that need to be accounted for. The way in which the dynamics are modelled in [52] are very similar to how they are modelled in [49] and [50]. But, at least convective effects are better taken into account in this paper. And since the heat-transfer coefficients are no longer assumed to be constant, there is only one multiplicity region associated with the change in value of any inlet parameter.

As for results, the cases considered are similar to the cases considered in [50]. For steady-state behaviour, another case is considered where the power density is assumed to be a constant bifurcation parameter as well. Unlike [50], the transient behaviour of the SOFC is also considered for step-changes in the external load resistance along the lower, un-ignited steady-state branch as well as the transient behaviour of the SOFC during extinction. These step-changes take place after 500 seconds. For a co-ionic conducting SOFC, it takes around 6000 seconds for the SOFC to settle at a new steady-state along the un-ignited steady-state branch after extinction. This has not been fully verified though by raising the external load resistance back to its original value to see whether it goes back to its original steady-state or not. The behaviour of this SOFC during ignition is not considered.

Experimental work validating in the existence of multiple steady-states within Solid Oxide Fuel Cells is lacking. The closest we have come to experimental validation comes from J. Sands [53] who investigated non-linear oscillatory dynamics within a Solid Oxide Fuel Cell. The theoretical work in which the experimental work in [53] is based on can be found in [54] and [55]. The model considered varies differently from the rest of the mathematical models considered in this chapter. It only consists of three ODEs covering mass conservation of Methane, Hydrogen and Water within the anode. The concentrations of each of the three individual gas components is affected by the reaction rates of

the electrochemical and steam-reforming reactions, and diffusion within the anode.

These equations are non-dimensionalised, where they are reduced to two non-dimensional ODEs covering mass conservation for Methane and Hydrogen only. The non-dimensional ODE for Water is reduced to an algebraic expression, which is substituted to the non-dimensional ODEs for Methane and Hydrogen. Two cases are considered: one where fuel stream humidification is ignored [54], and the other where it is considered [55]. Using phase plane analysis, it is shown that oscillations arise in the SOFC due to the presence of Hopf bifurcations in the dynamical system for both cases. For the second case, it is shown that hysteresis effects occur in the SOFC where fuel stream humidification is considered, which highlight the existence of more than one steady-state within the SOFC. The regions in the phase plane diagram where oscillations occur are validated via numerical integration of the non-dimensional ODEs using the MATLAB solver *ode23s* in those regions. The experimental work done in [53] shows the cell current struggling to stay at a single steady-state value, either shifting from one steady-state value to another, or reaching a state where it oscillates for increasing time. A micro-tubular SOFC and a tubular SOFC operating under a constant cell voltage were considered.

Even though the work is very mathematical, the main problem with this model is that all the dynamics considered is concentrated to within one electrode. A lot of other dynamics, including cell temperature, polarisation losses (including Ohmic), gas flow temperatures, velocity and pressure are not considered in the model. This model is much more simplified than the lumped-parameter model in [47], making it good for additional mathematical analysis, but not so good for obtaining a full picture into the operation of a real-life SOFC. Except for [45], all the equations in the other papers that cover steady-state multiplicity within a Solid Oxide Fuel Cell are left in dimensional form. Except for the spatially distributed model in [47], the models considered are lumped-parameter models. Transitioning from a lumped-parameter model to a one-dimensional model is not difficult, but

more work needs to be done for the lumped-parameter model to take account of the effects of the heat-transfer coefficient and velocity on steady-state performance. Once the results are obtained for a more developed model, a more mathematical approach can be taken via non-dimensionalising the equations (see section 8.2). Also, more work needs to be done to verify the existence of more than one operating regime within a Solid Oxide Fuel Cell when considering the transient behaviour of the SOFC during ignition and extinction.

2.4 General Steady-State Behaviour

As regards to other work done in the area of steady-state behaviour of SOFCs, in 2004, Aguiar et al. [56] looked at the development of an anode-supported, intermediate temperature, direct internal reforming, solid oxide fuel cell stack for steady-state behaviour. The SOFCs were of a planar configuration, and modelled in 1D. In the model, mass balances are considered where the two main electrochemical reactions are considered along with the reforming reaction and the associated water-gas shift reaction. Energy balances are considered for both gas flows as well as the interconnect and PEN section. The electrochemical model takes account of the theoretical open circuit voltage, the actual voltage, and the different polarisations within the cell (Ohmic, activation and concentration). The equations for these processes are only considered in steady-state form and individual gas flows are neglected. The model was solved using the finite difference method. Cell voltage and power density, which were measured as a function of the current density, were compared at different temperature levels (for a fully reformed mixture) and different fuel utilisation levels. For lower temperatures, the highest obtainable voltage in the SOFC is achieved at lower current densities, where the power density curve peak is at its lowest which represents a downside in the attempt to lower operating temperatures. As for fuel utilisation levels, while the power density peak increases with higher fuel utilisation levels, the voltage drops more dramatically for increasing fuel utilisation levels thanks to

the increasing influence of the concentration polarization. The effects of the different polarization to the cell voltage were also investigated, with the major source of loss coming from the cathode polarization at the optimum voltage level (around 0.7 V). Mole fractions of the chemical species of the fuel flow, predicted voltage and current density levels, potential losses, and temperature of the gas-flow and solid-state profiles were investigated for a co- and counter-flow SOFC with the same operating conditions. For the counter-flow case, all the methane is converted within the first 20% of the cell length, resulting in a steeper temperature gradient (after reaching its peak), which could result in damage to the ceramic components of the cell, whereas the methane conversion in a co-flow case is more gradual and the temperatures rise after the first 30% of the cell length. But, the counter-flow SOFC achieves a higher cell temperature, which in turn results in a higher terminal voltage, power density level, and better fuel utilisation levels. Temperature, voltage, current density and potential losses were also investigated for changes in some of the operating conditions. It can be seen that SOFC performance is greatly affected by temperatures, fuel composition, gas flow rates and current density.

In 2005, Iora et al. [57] presented two dynamic 1D models of a direct internal-reforming, intermediate temperature ($\sim$ 1023K) Solid Oxide Fuel Cell. One where the flow properties such as pressure, gas stream densities, heat capacities, thermal conductivities, and viscosity, as well as gas velocities are taken as constant throughout the system, based on inlet conditions, and the other where we consider the variation of those properties. These models are known as the Constant Properties Model (CPM) and the Variable Properties model (VPM). Here, the mass balances, energy balances, PEN and Interconnect temperatures, as well as the momentum balances are considered. For the mass and energy balances, the steam reforming reaction (1.13) and the associated water-gas shift reaction (1.14) are considered along with the electrochemical reactions (1.9) and (1.10). All the mathematical equations relevant to this model are included and presented clearly

along with the relevant boundary conditions. The initial conditions are given when the equations of motion are in steady-state. The system of partial differential equations are solved by an application of the method of lines, where a finite-difference method is used, and is a mixed system of differential and algebraic equations (DAE) of index 2. The equations are solved in non-dimensional form. The results show that there is a good correlation between the two models for most dynamic properties except for current density near the end of the cell where there is a slight drop due to mass transfer limitations. The peak in the CPM version is bigger than the peak for VPM. There is also a bit of a gap between the two models for transient cell voltage and fuel exit temperature. The VPM is seen to be the more preferable model for higher current densities despite the increase in number of calculations in comparison to the CPM. Also, besides voltage and fuel exit temperature, there is no insight into the transient behaviour of any of the other variables. In 2004, Campanari and Iora [58] looked at finite volume model of a 1D tubular solid oxide fuel cell. In the electrochemical model, voltage dynamics are considered where the cell voltage is modelled using the Nernst potential while taking account of certain polarizations, including ohmic, activation and diffusion polarization, as well as the number of moles of hydrogen, oxygen and water consumed/produced. The model also looks at the reforming and shift reactions, including the methane reaction rate, mole number change of hydrogen, methane and carbon monoxide, and the equilibrium constant of the shift reaction. Heat transfer dynamics are also considered, including heat of the pre-heated air in the injection tube and the cathode side air channel, heat of the solid cell, and heat of the fuel. The electrochemical model is calculated one section at a time, and the thermal model generating $4 \times n$ equations with $4 \times n$ unknown temperatures. These equations are solved using the Gauss-Seidel method. In terms of results, all the main temperatures, chemical compositions, polarization profiles, and the relation between current density and the reversible voltage are considered. Sensitivity analysis of these results are also given,

highlighting the effect of different polarization losses on cell performance, as well as the effect of the Nusselt number, different methane reforming rates, and the effect of different meshing on the model.

From these papers, it is possible to obtain a combination of steady-state profiles describing certain variables over the length of the cell via computational means and some dynamic analysis as well, mainly regarding cell voltage and temperature after a change in the load (*i.e* current density).

2.5 Dynamic Behaviour

Some of the earliest work on transient modelling in SOFCs was made by Elmar Achenbach in 1994/95 [59, 60]. In [59], a three-dimensional planar SOFC model was considered with different flow configurations, and with a fuel flow consisting of hydrogen, methane, carbon monoxide, carbon dioxide and water. The oxidation of carbon monoxide was considered along with the reduction reaction (1.9) and the oxidation reaction (1.10). Other reactions considered were the steam reforming reaction (1.13), the shift reaction (1.14), and two decomposition reactions of methane and carbon monoxide. Mass balances of the gas flows, energy balance of the solid cell, and reaction kinetics of the three electrochemical reactions, plus the additional chemical and decomposition reactions were taken into account. The molar distribution of the different chemical species, and the distribution of cell voltage, current density and temperature all across the the cell was considered for different flow configurations (co-, counter-, and cross-flow) and in a stack. Also considered was the dynamic behaviour of the cell after a change in the load (current density) after a certain amount of time. It was noticed that a rise/drop in current density causes an almost instant drop/rise in cell voltage due to the slow response of cell temperature to rise/drop towards a new steady-state (mainly due to the specific heat capacity of the solid cell structure, and the reaction of the electrochemical and chemical reactions to the

change in the load). After the initial drop/rise, the cell voltage rises/drops towards a new steady-state value. This work was continued in [60] in 1995.

In 1999, Hall and Colclaser [61] developed a computer model simulating the transient behaviour of a tubular solid oxide fuel cell. The electrochemical and thermal model were taken into account where the transient behaviour of the cell voltage, maximum temperature and minimum temperature were investigated after a step change in current density. The behaviour of cell voltage after a step change in current density was very similar to [59], but the cell voltage tends to a steady-state value closer to the original steady-state value before the change, and it takes a lot longer to reach a new steady-state.

In 2000, Padullés [62] developed a SOFC plant dynamic model for a power systems simulation (PSS) commercial software package. The dynamics in this model are expressed in a Laplace transform domain. In this model, all the gasses were assumed ideal, the temperature is assumed to be constant at all times and is not investigated, the only source of potential loss is ohmic at moderate cell currents, and pressure along the channels are assumed uniform. Molar flows, partial pressures, and cell voltage were taken into account. The main focus on this paper was voltage and power output from the fuel cell stack against current density for certain molar flow values of hydrogen, and different fuel utilisation levels to determine operation levels, and limits of the plant. This model works at its best when fuel utilisation is between 70-90%, but loses synchronism with the network if the cell voltage drops beyond a certain point, affecting the accuracy of this model. Cell voltage transient behaviour was also looked at when load changes was applied after a certain amount of time. This is a good basic model for power simulation and checking its operational limits, but since it does not take cell temperature into account, accuracy over the voltage values may be questionable.

In 2004, Sedghisigarchi and Feliachi [63] developed a lumped-parameter (0D), non-linear dynamic model of a Solid Oxide Fuel Cell that could be used for dynamic and transient

stability studies. This model accounted for the electrochemical model and the component material balance equations where molar flows are taken into account, the thermal model where cell temperature is taken into account, and the cell voltage where sources of potential losses occur due to activation, concentration and ohmic polarizations. The stack is fed by hydrogen and air only, uniform gas distribution is assumed, and there is no heat transfer between cells. The set of equations in this model is set in the Laplace transform domain, and only dynamic and transient behaviour for the stack voltage and temperature is considered after step changes in current density and fuel flow step change. Output stack voltage response for short-time intervals were also investigated, one with or without temperature variations, and one with or without species dynamics consideration. One such model which has been developed in 1D form to describe the dynamic and transient behaviour of the cell in real time was developed by Cheddie and Denver in 2007 [64]. This model accounts for all transport and electrochemical phenomena, and the planar 1D SOFC model is split up into three control volumes (CV): one containing the anode-side interconnect and fuel channel integrated into one CV, one containing the PEN section, and one containing the cathode-side interconnect and air channel integrated together. The fuel flow consists of hydrogen only. For the electrochemical model, ohmic and activation polarization is considered, while the average PEN partial pressure of any chemical species can be determined using Fick's law. As for the transport model, conservation of mass and momentum of the fluid flow is considered at the channel domains (where Darcy friction with the wall channels is considered), temperature of the PEN and interconnects are considered (along with heat generation and entropy change), and the mass fraction of the individual chemical species is considered. The equations for the transport model are written in partial differential equation form taking account of time and position. The length of the SOFC is split up into 21 equally spaced discretised nodes from start to finish, and at each node, these equations are solved explicitly using a 4-th order Runge-Kutta

method in MATLAB. This greatly reduces the number of computations in comparison with iterative procedures. The results include a look into solution accuracy and computational times versus the number of nodes to determine the minimum number of nodes (21 in this case) required to ensure solution accuracy (at the smallest time-step possible). Anode and cathode outlet temperatures were investigated to help determine the smallest number of nodes needed. This model is then validated against a fully resolved model (3D model, solved using a finite element mesh) for the same set of operating conditions and geometric parameters (with cell voltage investigated after a change in loading conditions). The results show that despite an error around the order of 1%, the fully resolved model requires computational times of at least 2-3 s for a 1D domain, much larger than the time used in this model. Therefore accuracy is not severely compromised by the simplifications made in this model. Dynamic behaviour of the outlet anode and cathode temperatures and the maximum PEN temperatures subject to a load change was also investigated for constant and temperature dependent specific heat capacities. Variable specific heat capacities (where it is updated at every node) results in higher temperatures (as the potentials and overpotentials are also affected by the changes). A parametric analysis is also made, looking at the breakdown of steady-state cell parameters for various inlet conditions, and an investigation is made into the pumping power required to overcome Darcy friction on the walls of the flow channel. Overall, this is a very bold attempt to create a 1D model for real-time simulation where a set of PDE equations (along with a few assumptions) can be solved using an explicit 4-th order Runge-Kutta method without resorting to iterative methods, and the errors induced by the simplifications are very small.

In 2005, Qi, Huang and Chuang looked at the effects of diffusion and the dynamic behaviour of voltage/inherent impedance in a 1D model of a tubular solid oxide fuel cell [65]. Diffusion in the fuel cell is modelled using Fick's law for bi-molecular diffusion and the 1D mass transport equation. Using Laplace's transform, mass flux conditions on the cell

surface and the electrode-electrolyte interface/triple phase boundary, and the ideal gas law, diffusion in the fuel cell can be described by six sub-equations: 3 modelling the mass flux into the cell surface of Hydrogen, Water and Oxygen, and 3 modelling the partial pressures of Hydrogen, Water and Oxygen at the triple phase boundary, with the binary diffusion coefficients based on Fuller's correlation [66]. Voltage in the fuel cell is described by the Nernst equation, taking account of activation polarization in the cell, whereas inherent impedance is described by 3 resistance processes (ohmic, ionic and charge-transfer) and 2 capacitance processes (both charge-transfer). The behaviour of inherent impedance in the fuel cell can be described using an equivalent RC circuit where the equation for the charge-transfer voltage can be described using Kirchhoff's current laws at a node. All the equations modelling diffusion and inherent impedance are written in the form of first-order ODEs with respect to time. The results focus on changes to voltage, current and mass flux into the cell surface after step changes to the air pressure, load resistance, hydrogen partial pressure, thickness of diffusion layer (*i.e.* electrodes), and temperature. Later on in 2005, Qi and Huang (along with Luo) wrote another paper focusing on the effect of transport dynamics in a finite Control Volume (CV) section of a 1D tubular solid oxide fuel cell [67]. Carrying on from the work done on the effects of diffusion and voltage/inherent impedance of a SOFC [65], dynamics such as heat transfer/energy, mass transfer and momentum are looked at for five different control-volume sections: (i) the PEN structure; (ii) Fuel Channel; (iii) Air Channel; (iv) Injection tube; (v) Air flow inside the injection tube.

For the SOFC CV, along with diffusion and inherent impedance, heat transfer dynamics are considered. The dynamics considered include convection, radiation, enthalpy fluxes, electrical energy and heat from the reforming reaction. In the fuel channel CV, the reaction rates of the reforming and shift reactions are considered (with the reforming reaction rate determined experimentally from Ahmed and Foger [68]), along with mass transfer

dynamics, heat transfer dynamics and the momentum balance. Mass transfer dynamics, heat transfer dynamics and momentum balance are also considered for the air channel CV. As no reactions take place in and around the injection tube, only the heat transfer dynamics are considered for both the injection tube CV and the air flow in the injection tube CV. Just like in [67], the equations modelling these dynamics are expressed as a system of first-order ODEs with respect to time and solved using MATLAB. The changes in voltage, current, fuel temperature, pressure and velocity, cell temperature and mole fractions are investigated when subject to step changes to the load resistance, fuel temperature, fuel pressure and fuel velocity. Plenty of information is given about the fuel flow, where temperature changes increases the speed of the reforming reaction and velocity has an impact on the heat-transfer coefficient, but not enough information is given about the air flow, especially the air temperature profile.

Based on work done in the previous two papers [65],[67], Qi, Huang and Luo combined what they had done in another paper looking at a complete 1D dynamic model of a tubular SOFC where internal reforming (of methane) is considered [69]. Dynamic properties such as open circuit voltage, current density, mass flux, energy balances, mass balances, and flow velocities are considered for the whole length of the fuel cell. Unlike most models of SOFCs where computational methods like the finite difference method or finite element method are used, this model, which is a system of a mixture of PDEs and ODEs is converted to a system of control relevant first-order ODEs via transform methods applied to the diffusion-based equations, and the gas-flow based conservation equations.

The effects of voltage, inherent impedance and diffusion comes from the work done by Qi, Huang, and Chuang [65], with the inherent impedance equations slightly modified to take account of the equivalent circuit of the whole fuel cell as opposed to just a section. The changes in the cell and injection tube temperature is based on work done by Qi, Huang and Luo [67]. The transport dynamics of the fuel and air flow (*i.e.* concentration,

temperature, and velocity) are modelled using conservation equations. Using certain assumptions, including the fluid being incompressible and neglecting velocity dynamics, as well as solving the fuel and air velocity by adding up the mole fraction equations for both the fuel and air flow respectively, these equations can be transformed into first-order time derivative ODEs via analytical approximations (Laplace's transform and the inverse Laplace transform): one taking account of a linear approximation of velocity, and another taking account of an alternative approximation of the fuel velocity based on an approximation of the reforming reaction rate. From this, there is a system of 25 first-order time-derivative ODEs which is solved using MATLAB/Simulink. Here, it is possible to obtain a full dynamic model of all the variables in the SOFC combined with the steady-state dynamics as shown by the 3-D graphs in the paper, but the graphs are not very clear when it comes to transient dynamics after a step change of one of the input variables after a certain amount of time.

2.6 Summary

In this chapter, a review of the literature relevant to the work done in this thesis was made. There are at least two books dedicated towards the introduction of Solid Oxide Fuel Cells for people interested in reading up on it, plus a few other papers. In terms of review papers, [41] offers a more comprehensive review of most of the work done towards SOFCs for steady-state modelling, dynamic modelling, and control studies. The other review paper [42] is more focused towards dynamic modelling and control studies, but it does raise a few issues that needs to be addressed. One of those issues is that there are not enough control relevant dynamic models (which need to be at least one-dimensional) that can capture all the relevant dynamics including potential issues that can arise in SOFC operation, including the formation of hot spots. Even though the model presented here is a zero-dimensional model rather than a one-dimensional model, it will be verified

that hot spot formation can occur in a Solid Oxide Fuel Cell via transient calculations in chapter 7.

As for review papers that cover how SOFCs are modelled mathematically, [43] offers a more concise summary of all the different equations that are considered for each component of the SOFC, as well as modelling approaches and boundary conditions. However, [44] does give more information about the derivation of certain coefficients that crop up in certain equations. It gives the reader a better idea of how the equations look like for different configurations, and it is better related to how SOFCs are modelled in various literature. It gives you a slightly easier insight into how different dynamics in different components are modelled.

One noticeable aspect of the literature review is that there is a lot more literature related to the dynamic and transient behaviour of a cell compared to the steady-state multiplicity of a SOFC. In terms of steady-state multiplicity within a SOFC, [45] showed that a SOFC behaves very similarly to a CSTR, and may exhibit multiple steady-state behaviour similar to multiple steady-states within a tank reactor (as shown in [46]), due to the non-linear relationship of the reaction rate with the cell temperature (and conductivity). It is the only major piece of work in that section where the equations are non-dimensionalised. The number of steady-state solutions is determined by looking at the number of intersections between the non-dimensionalised heat production term, and the non-dimensionalised heat removal term. However, there is nothing regarding the existence of multiple steady-states within a Solid Oxide Fuel Cell for non-isothermal conditions.

The first paper to investigate the existence of multiple steady-states within a Solid Oxide Fuel Cell for non-isothermal conditions was [47], using a small lumped-parameter model that considers just the necessary dynamics that are responsible for the existence of multiple steady-states. It also considers a 1D model, where up to five steady-states may exist (under a potentiostatic operation). It is the first paper to show that a multiplicity region

can be represented for any parameter by a hysteresis loop for a region of values of the bifurcation parameter. With a small lumped-parameter model, there is the potential to do some more mathematical analysis to clarify the stability of the steady-state branches, and determine the nature of the turning points. This has been done to an extent in [48], but this is for a 1D model, so it does not directly clarify the results produced in [47]. Also, the focus in this thesis is on producing a more detailed SOFC model.

Also, since very few equations are considered, the accuracy of the size and location of the multiplicity region may be questionable. The remaining work on steady-state multiplicity within SOFCs has been done mainly by Bavarian and Soroush in three papers [49, 50, 52]. The other two papers [50] and [52] are focused towards different types of SOFCs, but on the whole, their lumped-parameter models are much more detailed than [45] and [47], with more dynamics considered. Also, unlike [47], more work has been done to investigate the effect of different inlet parameters on SOFC performance (same with [45]), although some of those inlet parameters are clumped together. There is also a glimpse into how cell parameters change from one steady-state solution to another during ignition [49] and extinction [52] after load changes. However, it has not been fully clarified in [49], [50] and [52] that the SOFC actually operates along a different steady-state branch by showing that it does not go back to its original steady-state value before ignition/extinction. Also, their models are not detailed enough. Except for [52], the heat-transfer coefficient was not only assumed constant, but also to have the same value for both the anode and the cathode (that despite air velocity being much higher than fuel velocity). Also, velocity is still assumed to be constant.

What will be done in this thesis is that a more detailed mathematical model of a Solid Oxide Fuel Cell will be provided. One where convective effects on the cell are fully taken into account by defining the heat-transfer coefficient in terms of two non-dimensional parameters. One where gas flow velocities are not assumed to be constant. The concentration

polarisation term will also be redefined such that it properly describes voltage loss due to mass transfer resistances. There will be more of an insight into certain non-dimensional parameters to see which gas flow dynamics are more dominant, and how they affect SOFC performance. There will be a more detailed parametric analysis of the effects of different inlet parameters on SOFC performance (rather than two parameters clumped together). More importantly, it will be shown via transient calculations, that the SOFC has more than one operating regime by investigating the transient behaviour of the SOFC during ignition and extinction.

As for the dynamic behaviour of a SOFC, most of the work mentioned above investigates the behaviour of a SOFC after a change in the current density after a certain amount of time. The main observation is that an increase in current density causes an (almost) instant drop in cell voltage due to the slow response of cell temperature after the change. The same effect is noticed after a change in the external load resistance. In this thesis, the external load resistance component will be expressed in terms of the tanh function. This is not only to simulate the step-change in R_{load} after a certain amount of time (where there is a smooth change in R_{load}), but to also investigate the evolution of different SOFC parameters with time. The transient results from chapter 7 will be compared with equivalent transient results that consider an external load resistance component.

Chapter 3

SOFC Model

3.1 Introduction

In this chapter, the mathematical model of the SOFC considered in this thesis will be presented. The SOFC is a planar, electrolyte-supported SOFC (see figure 3.1). The SOFC is modelled using a lumped-parameter (zero-dimensional) model. The model presented in this chapter is based on the model by Bavarian and Soroush (2012) [49], with a few modifications and clarifications.

In this model, the following dynamics are considered:

- Consumption/production rates of Hydrogen, Oxygen and Water in the electrochemical reactions, and voltage losses due to activation, Ohmic and concentration overpotentials (section 3.2);
- Temperature of the PEN structure, which encompasses the two electrodes and the solid electrolyte in-between in figure 3.1 (including heat production and heat loss within the cell). The derivation of the heat-transfer coefficients (new from [49]) is also covered in this section (section 3.3);
- Mass transfer and diffusion within the electrodes, in an area within the electrode known as the electrode diffusion layer (located between the external electrode surface

and the reaction zone/TPB in figure 3.1). Derivation of the molar flux terms (which was not covered in [49]) is covered as well as the diffusion coefficients (section 3.4);

- Mass, momentum and energy transfer of the two gas flows within the two gas channels. In the model given in [49], only mass and energy conservation were considered with velocity assumed to be constant (section 3.5).

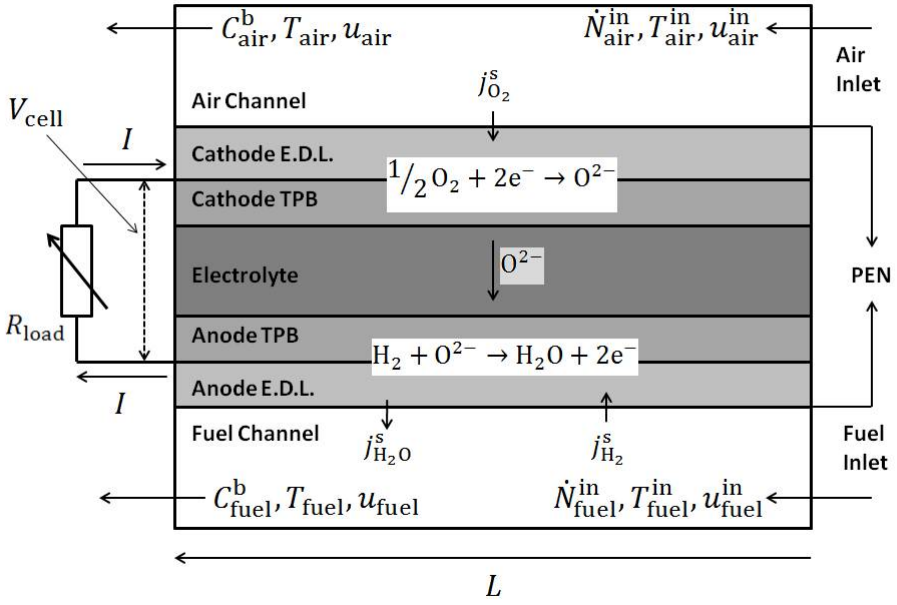

Figure 3.1: A general schematic of the planar SOFC system, including the external circuit. The SOFC has length L, with the fuel and air entering the SOFC from the R.H.S. The inlet parameters considered for both gas flows are the inlet molar flow rate $\dot{N}_j^{\text{in}}$ (plus the inlet mole fractions y^{in} of the individual gaseous species), the inlet temperature T_j^{in}, and the inlet velocity u_j^{in} ($j = \text{fuel, air}$). The outlet parameters include the bulk gas flow concentration C_j^{b} (plus the mole fractions y of each individual gaseous species), the temperature T_j, and the velocity u_j. Hydrogen and Oxygen travel from their respective gas channels to their respective TPBs via the Electrode Diffusion Layer (E.D.L.), with j^{s} representing the molar flux per unit area into the cell surface. The two electrochemical reactions are assumed to take place on the surface of the TPB. Oxygen ions O^{2-} travel from the Cathode TPB via the electrolyte to take part in the Oxidation reaction on the Anode TPB. Water produced from the Oxidation reaction leaves the SOFC with molar flux $j^{\text{s}}_{H_2O}$. The external circuit of the SOFC on the L.H.S. draws a current I from the SOFC as the electrons pass through it. The current passes through an external load resistance component, represented by a rheostat. The potential difference between the Anode and the Cathode is represented by the cell voltage V_{cell}. The PEN section encloses both electrodes (the E.D.L. and the TPB) and the electrolyte.

The equations related to each section will be derived in detail, including any changes from the equations derived in [49]. This is followed by a run down of how both the steady-state and dynamic model will be solved, what cases are considered and how certain profiles will be derived (section 3.6). Performance parameters such as fuel utilisation, voltage efficiency and electrical efficiency are covered in Appendix C. The Péclet number for heat and mass transfer is covered in Appendix D. The consolidated list of all the equations for the steady-state and dynamic SOFC models is given in Appendix F.
Before the model is derived, the following assumptions are made:

- Temperature distribution along the two electrodes and the electrolyte is assumed to be uniform;
- Each subsystem (*i.e.* gas channels, electrodes) within the SOFC is locally homogeneous;
- Radiation and conduction of heat within the cell is assumed to be negligible;
- All gases are assumed to be ideal.
- The gases experience no friction within the walls of the channel, and viscosity effects are neglected (except when deriving an expression for the heat-transfer coefficient);

3.2 Electrochemical Model

The main reactions which take place within the cell are the two half-cell reactions

$$H_2 + O^{2-} \rightarrow H_2O + 2e^- \tag{3.1}$$

and

$$\frac{1}{2}O_2 + 2e^- \rightarrow O^{2-} \tag{3.2}$$

leading to the overall cell reaction

$$H_2 + \frac{1}{2}O_2 \rightarrow H_2O. \tag{3.3}$$

Since the fuel flow only consists of Hydrogen, the consumption rates of Hydrogen and Oxygen and the production rate of Water in the electrochemical reactions can be described in terms of the cell current I using *Faraday's law* (if the current is known [18, p 306])

$$R_{H_2} = \frac{I}{2F}, \quad R_{O_2} = \frac{I}{4F}, \quad R_{H_2O} = \frac{I}{2F}, \tag{3.4}$$

where the *Faraday constant* $F = 96485$ C/mol.

3.2.1 Reversible Cell Voltage

The reversible cell potential E in a Solid Oxide Fuel Cell can be described using a combination of the 1st and 2nd laws of thermodynamics [18][pp 56-60], leading to the following expression

$$E = \frac{-\Delta^r G}{n^{el} F} \tag{3.5}$$

where $n^{el}(= 2)$ is the number of electrons transferred in the electrochemical reactions, and $\Delta^r G$ is the Gibbs free energy of the reaction. $\Delta^r G$ can be described in terms of the reaction enthalpy $\Delta^r H$ and the reaction entropy $\Delta^r S$, and is a function of the cell temperature T_{cell} and pressure p,

$$\Delta^r G(T_{\text{cell}}, p) = \Delta^r H(T_{\text{cell}}, p) - T_{\text{cell}} \Delta^r S(T_{\text{cell}}, p).$$

As all gases are assumed to be ideal, the reaction enthalpy is just a function of temperature, so

$$\Delta^r G(T_{\text{cell}}, p) = \Delta^r H(T_{\text{cell}}) - T_{\text{cell}} \Delta^r S(T_{\text{cell}}, p).$$

The reaction entropy can be defined in terms of the reaction entropy at constant pressure $\Delta^r S_p(T_{\text{cell}})$ and the logarithm of the partial pressure of any chemical species taking part in the electrochemical reaction:

$$\Delta^r S(T_{\text{cell}}, p) = \Delta^r S_p(T_{\text{cell}}) - R\log(K)$$

where

$$K = \Pi_j \left(\frac{p_j}{p_0}\right)^{\nu_j^{\text{S}}} \quad (j = \text{H}_2, \text{H}_2\text{O}, \text{O}_2)$$

is the equilibrium constant, p_0 is the standard atmospheric pressure (= 1 atm), and ν_j^{S} is the Stoichiometric coefficient of the reactants and products in reaction (3.3) ($\nu_{\text{H}_2}^{\text{S}} = -1,\ \nu_{\text{O}_2}^{\text{S}} = -1/2,\ \nu_{\text{H}_2\text{O}}^{\text{S}} = 1$). With this, the reversible cell potential can be described by the Nernst potential E

$$E = \frac{-\Delta^r G_p(T_{\text{cell}})}{2F} - \frac{RT_{\text{cell}}}{2F}\log(K), \tag{3.6}$$

where $\Delta^r G_p(T_{\text{cell}})$ represents the total free energy change at constant pressure, and is defined in terms of the reaction enthalpy and the reaction entropy at constant pressure

$$\Delta^r G_p(T_{\text{cell}}) = \Delta^r H(T_{\text{cell}}) - T_{\text{cell}}\Delta^r S_p(T_{\text{cell}}). \tag{3.7}$$

The first term on the R.H.S. of equation (3.6) is the standard electrode potential term (defined as E_0), which is a function of T_{cell}. The partial pressures of Hydrogen, Water and Oxygen are defined within the bulk gas flow in the two gas channels, similar to the definition of the reversible cell voltage given in [49]. Taking all this into account,

$$E = E_0(T_{\text{cell}}) - \frac{RT_{\text{cell}}}{2F}\log\left(\frac{p_{\text{H}_2\text{O}}^{\text{b}}}{p_{\text{H}_2}^{\text{b}}}\left(\frac{p_0}{p_{\text{O}_2}^{\text{b}}}\right)^{1/2}\right). \tag{3.8}$$

The enthalpy H and entropy S of Hydrogen, Oxygen and Water at constant pressure can be defined in terms of its specific heat capacity [7, p 2-2]:

$$H_i = H_i|_{T=298.15} + \int_{298.15}^{T} C_{\mathrm{p},i}(t)\mathrm{d}t,$$

$$S_i = S_i|_{T=298.15} + \int_{298.15}^{T} \frac{C_{\mathrm{p},i}(t)}{t}\mathrm{d}t,$$

where $i = \mathrm{H_2},\ \mathrm{O_2},\ \mathrm{H_2O}$. $H_i|_{T=298.15}$ and $S_i|_{T=298.15}$ represent the enthalpy and entropy of chemical species i at standard temperature $T = 298.15$ K. The reaction enthalpy $\Delta^r H(T_{\mathrm{cell}})$ and reaction entropy $\Delta^r S_p(T_{\mathrm{cell}})$ at constant pressure from equation (3.7) can be defined as a difference between the enthalpy/entropy at the inlet and the enthalpy/entropy at the outlet:

$$\Delta^r H(T_{\mathrm{cell}}) = \sum_{i\in\{\mathrm{H_2,H_2O,O_2}\}} \nu_i^{\mathrm{S}} H_i|_{T_{\mathrm{cell}}^{\mathrm{out}}} - \sum_{i\in\{\mathrm{H_2,H_2O,O_2}\}} \nu_i^{\mathrm{S}} H_i|_{T_{\mathrm{cell}}^{\mathrm{in}}},$$

$$\Delta^r S(T_{\mathrm{cell}}) = \sum_{i\in\{\mathrm{H_2,H_2O,O_2}\}} \nu_i^{\mathrm{S}} S_i|_{T_{\mathrm{cell}}^{\mathrm{out}}} - \sum_{i\in\{\mathrm{H_2,H_2O,O_2}\}} \nu_i^{\mathrm{S}} S_i|_{T_{\mathrm{cell}}^{\mathrm{in}}}.$$

Since there is no given value for T_{cell} at the inlet (there is only an insulating boundary condition at the inlet where no heat escapes), an approximation for E_0 is taken from a paper from Campanari and Iora [58], where their approximation for E_0 is based on the formulae from an earlier edition of the Fuel Cell Handbook [70]. So for this problem, $E_0 = 1.273\ \mathrm{V} - \left(2.7645 \times 10^{-4}\ \frac{\mathrm{V}}{\mathrm{K}}\right) T_{\mathrm{cell}}$.

Therefore, the final expression for the reversible voltage E is

$$E = 1.273\ \mathrm{V} - \left(2.7645 \times 10^{-4}\ \frac{\mathrm{V}}{\mathrm{K}}\right) T_{\mathrm{cell}} - \frac{RT_{\mathrm{cell}}}{2F} \log\left(\frac{p_{\mathrm{H_2O}}^{\mathrm{b}}}{p_{\mathrm{H_2}}^{\mathrm{b}}} \left(\frac{p_0}{p_{\mathrm{O_2}}^{\mathrm{b}}}\right)^{1/2}\right). \tag{3.9}$$

3.2.2 Actual Cell Voltage

In reality, the actual cell voltage is not reversible and is lower than the idealised voltage given by the Nernst potential due to any cracks and fissures in the electrolyte which cause electrons to leak into the electrolyte, and mainly due to polarisations/overpotentials in the cell (see subsection 1.3.2 [pp 19-21]). These polarisations are:

- Activation Polarisation in the anode and cathode ($\eta_{\text{act}}^{\text{An}}, \eta_{\text{act}}^{\text{Cat}}$);
- Ohmic Polarisation (η_{Ohm});
- Concentration Polarisation (η_{conc}).

Not taking into account any cracks or fissures in the electrolyte, the actual cell voltage is given below

$$V_{\text{cell}} = E - \eta_{\text{act}}^{\text{An}} - \eta_{\text{act}}^{\text{Cat}} - \eta_{\text{Ohm}} - \eta_{\text{conc}}. \tag{3.10}$$

Activation Polarisation

This is the voltage drop associated with the complex steps associated with the activation of the electrochemical reactions (3.1) and (3.2). In qualitative terms [18], any activation polarisation effects is dependent on the material properties and micro-structure of the electrodes, the cell temperature, atmosphere and the current density. The activation polarisation term is defined implicitly using the **Butler-Volmer equation** [25, p 63]

$$i = i_0 \left\{ \exp\left(\theta_{\text{f}} \frac{F}{RT_{\text{cell}}} \eta_{\text{act}}\right) - \exp\left(-\theta_{\text{b}} \frac{F}{RT_{\text{cell}}} \eta_{\text{act}}\right) \right\} \tag{3.11}$$

where i is the current density, i_0 is the exchange current density, defined in terms of the chemical species in the electrode and the activation energy of the electrochemical reactions within the electrode, and θ_{f} and θ_{b} are transfer coefficients associated with the forward

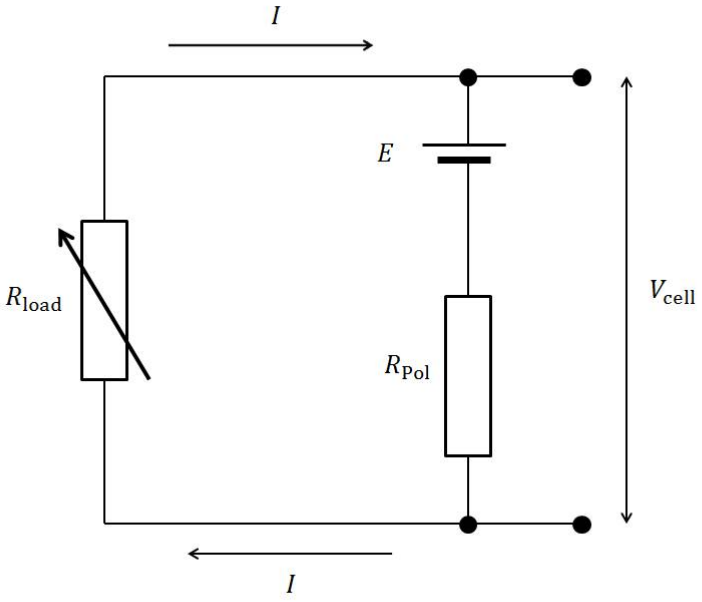

Figure 3.2: A schematic of the equivalent circuit of a SOFC operating under an external load. R_{Pol} represents the resistance in the cell due to activation, Ohmic and concentration polarisations. Since the transient behaviour of the cell under load changes is considered here as well, R_{load} can be represented by a rheostat.

and backward reactions of the electrochemical reaction within the electrode respectively. With the exception of a few special cases (*e.g.* $\theta_{\text{f}} = \theta_{\text{b}}$), η_{act} cannot be defined explicitly in terms of i.

If we assume that the reaction is a one-step, single electron transfer process, the transfer coefficients can be set equal to a common transfer reaction coefficient θ ($\theta_{\text{f}} = \theta,\ \theta_{\text{b}} = -(1-\theta)$) [25, p 63], and the Butler-Volmer equation becomes

$$i = i_0 \left\{ \exp\left(\theta \frac{F}{RT_{\text{cell}}} \eta_{\text{act}}\right) - \exp\left(-(1-\theta)\frac{F}{RT_{\text{cell}}}\eta_{\text{act}}\right)\right\}. \tag{3.12}$$

Also, if $\theta = 0.5$, equation (3.12) can be re-arranged such that we have an explicit expression for η_{act} in the form

$$\eta_{\text{act}} = 2\frac{RT_{\text{cell}}}{F} \sinh^{-1}\left(\frac{i}{i_0}\right). \tag{3.13}$$

For this model, θ_{f} and θ_{b} are not equal to unity, which means that both activation polarization terms are defined implicitly. The exchange current density represents the electrode reaction rate at equilibrium potential (when the forward and backward reaction rates are the same). This means that they can be described using Arrhenius law [25, p 64]:

$$i_0^{\mathrm{An}} = \gamma^{\mathrm{An}} \left(\frac{p_{\mathrm{H_2}}^{\mathrm{tpb}}}{p_0} \right) \left(\frac{p_{\mathrm{H_2O}}^{\mathrm{tpb}}}{p_0} \right) \exp\left(-\frac{E_{\mathrm{act,An}}}{RT_{\mathrm{cell}}} \right) \tag{3.14}$$

$$i_0^{\mathrm{Cat}} = \gamma^{\mathrm{Cat}} \left(\frac{p_{\mathrm{O_2}}^{\mathrm{tpb}}}{p_0} \right)^{0.25} \exp\left(-\frac{E_{\mathrm{act,Cat}}}{RT_{\mathrm{cell}}} \right) \tag{3.15}$$

The expressions for i_0^{An} is taken from Costamagna and Honegger [71], and the expression for i_0^{Cat} is taken from Achenbach [59]. The derivation of these expressions is based on experimental data on electrode materials for both electrodes at certain temperatures, and the influence of partial pressures on the overpotential. These expressions of i_0^{An} and i_0^{Cat} are quite common in SOFC mathematical modelling literature.

With these definitions of i_0^{An} and i_0^{Cat}, the activation polarization equations for the Anode and Cathode are

$$\begin{aligned} \frac{I}{LW} = {} & \gamma^{\mathrm{An}} \left(\frac{p_{\mathrm{H_2}}^{\mathrm{tpb}}}{p_0} \right) \left(\frac{p_{\mathrm{H_2O}}^{\mathrm{tpb}}}{p_0} \right) \exp\left(-\frac{E_{\mathrm{act,An}}}{RT_{\mathrm{cell}}} \right) \cdot \\ & \left\{ \exp\left(\theta_{\mathrm{f}}^{\mathrm{An}} \frac{F}{RT_{\mathrm{cell}}} \eta_{\mathrm{act}}^{\mathrm{An}} \right) - \exp\left(-\theta_{\mathrm{b}}^{\mathrm{An}} \frac{F}{RT_{\mathrm{cell}}} \eta_{\mathrm{act}}^{\mathrm{An}} \right) \right\}, \end{aligned} \tag{3.16}$$

$$\begin{aligned} \frac{I}{LW} = {} & \gamma^{\mathrm{Cat}} \left(\frac{p_{\mathrm{O_2}}^{\mathrm{tpb}}}{p_0} \right)^{0.25} \exp\left(-\frac{E_{\mathrm{act,Cat}}}{RT_{\mathrm{cell}}} \right) \cdot \\ & \left\{ \exp\left(\theta_{\mathrm{f}}^{\mathrm{Cat}} \frac{F}{RT_{\mathrm{cell}}} \eta_{\mathrm{act}}^{\mathrm{Cat}} \right) - \exp\left(-\theta_{\mathrm{b}}^{\mathrm{Cat}} \frac{F}{RT_{\mathrm{cell}}} \eta_{\mathrm{act}}^{\mathrm{Cat}} \right) \right\}, \end{aligned} \tag{3.17}$$

where $I/(LW)$ is equal to the *current density* i, γ^{An} and γ^{Cat} are pre-exponential factors for the reactions that take place in the anode and cathode respectively, L is the cell length, W is the cell width, and $E_{\mathrm{act,An}}$ and $E_{\mathrm{act,Cat}}$ are the activation energy terms for the

electrochemical reactions that take place in the anode and cathode respectively. Values of γ^{An}, γ^{Cat}, L, W, $E_{\mathrm{act,An}}$ and $E_{\mathrm{act,Cat}}$ plus other geometric and various values/parameters mentioned in this chapter can be found in Appendix A.

Ohmic Polarisation

This is the voltage drop due to a combination of electrical resistances in the electrodes, ionic resistivity in the electrolyte, and charge-transfer resistances and capacitance processes in the reaction zones. When looking at the resistivity of the electrodes and the electrolyte, the focus is on the *Area Specific Resistivity* of these cell components, and is described in terms of the specific resistivity of the anode (ρ^{An}), electrolyte (ρ^{Ele}), and cathode (ρ^{Cat}) ($\Omega\mathrm{m}^{-1}$) along with the current density,

$$\eta_{\mathrm{ohm}} = \rho^{\mathrm{An}} d_{\mathrm{An}} i + \rho^{\mathrm{Ele}} d_{\mathrm{Ele}} i + \rho^{\mathrm{Cat}} d_{\mathrm{Cat}} i, \tag{3.18}$$

where d_{An}, d_{Ele}, d_{Cat} represent the thickness of the anode, electrolyte and cathode respectively in the PEN structure. Ohmic resistivity is dominated by ionic resistivity in the electrolyte (which plays a big part in the existence of multiple steady-states in a solid oxide fuel cell [47]), and the specific resistivity of the electrolyte is exponential in T_{cell}^{-1} [47]

$$\rho^{\mathrm{Ele}} = \frac{1}{\beta_i} \exp\left(\frac{\beta_{ii}}{T_{\mathrm{cell}}}\right) \tag{3.19}$$

with $\beta_i = 3.34 \times 10^4\ \Omega^{-1}\mathrm{m}^{-1}$ and $\beta_{ii} = 1.03 \times 10^4$ K [71]. Therefore equation (3.18) is only expressed in terms of the specific resistivity of the electrolyte, while the specific resistivity of the anode and cathode are neglected (they are only expressed as constants in [71]). The material of the electrolyte in which the expression of ρ^{Ele} is based on in [71] is yttria-stabilised zirconia (YSZ) (the anode is made from Ni/YSZ, and the cathode from strontium-doped lanthanum magnetite).

Concentration Polarisation

This is the drop in voltage associated due to the physical resistance of gaseous species through the electrodes at a given current density. Concentration polarisation is affected by certain parameters, including binary diffusion within the electrodes, the micro-structure of the electrodes, the partial pressures of the chemical species within the two electrodes and current density. The concentration polarization differs in both electrodes, and are both described in terms of the limiting current density of the electrode [18, pp 233-237]. The concentration overpotential in the anode is

$$\eta_{\text{conc}}^{\text{An}} = \frac{RT_{\text{cell}}}{2F}\left[\log\left(1 + \frac{p_{\text{H}_2}^{\text{tpb}}}{p_{\text{H}_2\text{O}}^{\text{tpb}}}\frac{i}{i_{l,\text{An}}}\right) - \log\left(1 - \frac{i}{i_{l,\text{An}}}\right)\right] \tag{3.20}$$

where $i_{l,\text{An}}$ is the anode-limiting current density [18, p 234]. This is defined as

$$i_{l,\text{An}} = \frac{2Fp_{\text{H}_2}^{\text{tpb}}D_{\text{eff,An}}}{RT_{\text{cell}}\Delta_{\text{An}}}, \tag{3.21}$$

where $p_{\text{H}_2}^{\text{tpb}}$ is the partial pressure of Hydrogen in the TPB, $D_{\text{eff,An}}$ is the effective diffusion coefficient of the anode, and Δ_{An} is the thickness of the electrode diffusion layer in the anode [18, p 234]. The effective diffusion coefficient of the anode is defined as

$$D_{\text{eff,An}} = \frac{\varepsilon_{\text{An}}}{\tau_{\text{An}}}D_{\text{H}_2,\text{H}_2\text{O}}$$

where $D_{\text{H}_2,\text{H}_2\text{O}}$ represents the binary diffusion coefficient of Hydrogen within Water, ε_{An} represents the porosity of the anode, and τ_{An} represents the tortuosity of the anode. Similarly for the cathode,

$$\eta_{\text{conc}}^{\text{Cat}} = -\frac{RT_{\text{cell}}}{4F}\log\left(1 - \frac{i}{i_{l,\text{Cat}}}\right) \tag{3.22}$$

where $i_{l,\mathrm{Cat}}$ is the cathode-limiting current density [18, p 236]. This is defined as

$$i_{l,\mathrm{Cat}} = \frac{4F p_{\mathrm{O_2}}^{\mathrm{tpb}} D_{\mathrm{eff,Cat}}}{\left(1 - \frac{p_{\mathrm{O_2}}^{\mathrm{tpb}}}{p_0}\right) RT_{\mathrm{cell}} \Delta_{\mathrm{Cat}}}, \tag{3.23}$$

where $p_{\mathrm{O_2}}^{\mathrm{tpb}}$ is the Oxygen TPB partial pressure, $D_{\mathrm{eff,Cat}}$ is the effective diffusion coefficient in the cathode, and Δ_{Cat} is the thickness of the electrode diffusion layer within the cathode [18, p 236]. The effective diffusion coefficient of the cathode is defined as

$$D_{\mathrm{eff,Cat}} = \frac{\varepsilon_{\mathrm{Cat}}}{\tau_{\mathrm{Cat}}} D_{\mathrm{O_2,N_2}}$$

where $D_{\mathrm{O_2,N_2}}$ is the binary diffusion coefficient of Oxygen within Nitrogen, $\varepsilon_{\mathrm{Cat}}$ represents the porosity of the cathode, and τ_{Cat} is the tortuosity of the cathode. More information regarding the derivation of the diffusion coefficients can be found in subsection 3.4.2.

Both concentration polarisation terms are defined such that if $i \to i_{l,\mathrm{An}}$ or $i \to i_{l,\mathrm{Cat}}$, $\eta_{\mathrm{conc}} \to \infty$. Concentration polarisation has more of an effect on cell voltage at higher values of current density (see figure 1.9), especially the closer i approaches to either $i_{l,\mathrm{An}}$ or $i_{l,\mathrm{Cat}}$.

Combining all these terms together, the concentration overpotential is

$$\eta_{\mathrm{conc}} = \frac{RT_{\mathrm{cell}}}{2F}\left[\log\left(1 + \frac{p_{\mathrm{H_2}}^{\mathrm{tpb}}}{p_{\mathrm{H_2O}}^{\mathrm{tpb}}}\frac{i}{i_{l,\mathrm{An}}}\right) - \log\left(1 - \frac{i}{i_{l,\mathrm{An}}}\right)\right] - \frac{RT_{\mathrm{cell}}}{4F}\log\left(1 - \frac{i}{i_{l,\mathrm{Cat}}}\right). \tag{3.24}$$

3.3 Temperature of the PEN structure

In this section, we consider the temperature of the PEN structure, as well as the heat production and heat removal within the cell. The temperature of the cell is affected by the net enthalpy fluxes into the cell, and the electrical energy that is exported into the external load, and convective heat transfer in both the fuel and air flows either side of the

cell. The energy conservation equation for the solid cell component is written in the form

$$(d_{\mathrm{An}} + d_{\mathrm{Ele}} + d_{\mathrm{Cat}})(\rho_{\mathrm{cell}} C_{\mathrm{p,cell}}) \frac{\mathrm{d}T_{\mathrm{cell}}}{\mathrm{d}t} = \Delta H_{\mathrm{R}} - E_e - q_{\mathrm{conv,an}} - q_{\mathrm{conv,cat}}, \tag{3.25}$$

where ΔH_{R} represents the net enthalpy flux from the reactions into the cell, E_e represents the electrical energy flux, $q_{\mathrm{conv,an}}$ and $q_{\mathrm{conv,cat}}$ represent the heat lost from the cell due to forced convection on the anode and cathode side of the cell walls respectively (all per unit area), ρ_{cell} is the density of the cell, and $C_{\mathrm{p,cell}}$ is the specific heat capacity of the cell.

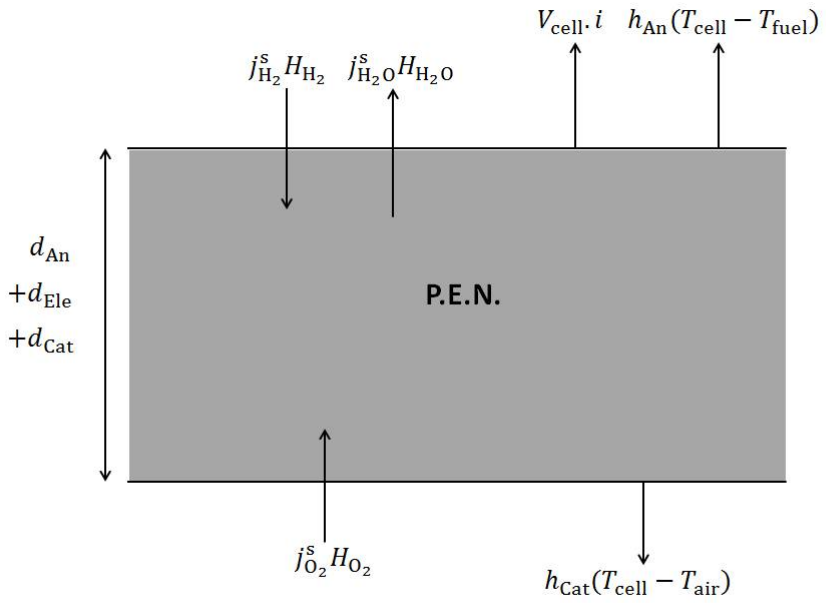

Figure 3.3: A schematic of the solid cell component. Temperature distribution is assumed to be uniform across both electrodes and the electrolyte, hence the thickness of the solid cell component is given as a sum of the thickness of each individual component d_j (j =An, Cat, Ele). The temperature of the cell is affected by enthalpy fluxes into/out of the cell, electrical energy exported into the external circuit, and forced convection on the walls either side of the cell.

3.3.1 Net Enthalpy Flux

The enthalpy flux term ΔH_{R} is defined as follows

$$\Delta H_{\mathrm{R}} = j^{\mathrm{s}}_{\mathrm{H_2}} H_{\mathrm{H_2}} + j^{\mathrm{s}}_{\mathrm{O_2}} H_{\mathrm{O_2}} - j^{\mathrm{s}}_{\mathrm{H_2O}} H_{\mathrm{H_2O}},$$

where j^{s}_i ($i = \mathrm{H_2},\ \mathrm{O_2},\ \mathrm{H_2O}$) represents the molar flux per unit area of Hydrogen, Oxygen and Water passing through the cell surface into the cell (definitions given in section 3.4), and H_i represents the enthalpy of Hydrogen, Oxygen and Water.

The enthalpies of Hydrogen, Oxygen and Water are defined in terms of an integral of the molar specific heat capacity of the substance between temperature T and the standard temperature 298.15 K [7, p 2-2],

$$H_i = H_i|_{T=298.15} + \int_{298.15}^{T} C_{\mathrm{p},i}(t)\mathrm{d}t \quad (i = \mathrm{H_2}, \mathrm{O_2}, \mathrm{H_2O}) \tag{3.26}$$

where $H_i|_{T=298.15}$ represents the enthalpy at standard temperature, and $C_{\mathrm{p},i}$ represents the molar specific heat capacity of the substance. Once the integral is evaluated, a first-order polynomial fit is applied to each enthalpy with respect to temperature:

$$H_i = a_i + b_i T_j \quad (i = \mathrm{H_2}, \mathrm{O_2},\ j = \text{fuel, air})$$
$$H_{\mathrm{H_2O}} = a_{\mathrm{H_2O}} + b_{\mathrm{H_2O}} T_{\mathrm{cell}}$$

This was done using the *polyfit* command in MATLAB where each enthalpy term was evaluated between 900-2000 K. The reason for such a large temperature range is that since Water is produced from the electrochemical reactions located inside the cell, the enthalpy for Water is a function of the cell temperature T_{cell} rather than a function of the fluid temperature. As it will be seen in chapters 4-7, operating temperatures at

least as high as 2000 K will be dealt with after ignition takes place. The enthalpies of Hydrogen, Oxygen, air (and Water in the advection term of the fuel energy conservation equation) are functions of fluid temperature (fuel for Hydrogen, air for Oxygen and air). The polynomial approximations, as well as relative errors of these approximations, can be found in Appendix E.

3.3.2 Electrical Energy

The electrical energy exported from the cell to the external circuit is defined in terms of the surface power density of the SOFC

$$E_e = V_{\text{cell}} \cdot i. \tag{3.27}$$

For a SOFC operating under a constant external load, the cell voltage and cell current are coupled by Ohm's law

$$V_{\text{cell}} = I R_{\text{load}} \tag{3.28}$$

where R_{load} represents the external load resistance.

3.3.3 Convection

The convection terms in the cell energy conservation equation are associated with the energy exchange between a surface (*i.e.* the walls of the cell) and a adjacent fluid (*i.e* the fuel and air flows either side of the cell). The convection terms for the anode and the cathode are given in the form [72, p 208]

$$q_{\text{conv},j} = h_k(T_{\text{cell}} - T_j) \quad (j = \text{fuel}, \text{air}) \quad (k = \text{An}, \text{Cat}) \tag{3.29}$$

where h_k is the heat-transfer coefficient applied to the outer wall of electrode k, and T_j is the temperature of the fluid outside the cell wall. The heat-transfer coefficient can be

described by the dimensionless *Nusselt number*, which is given as

$$Nu = \frac{hL}{k} \tag{3.30}$$

where the length of the SOFC L is the length scale, and k represents the thermal conductivity of the fluid. The Nusselt number measures the ratio of convective heat transfer (represented by hL) to conductive heat transfer. Equation (3.30) can be re-arranged in terms of the heat-transfer coefficient.

To obtain an explicit expression for both heat-transfer coefficients, an alternative approximation is needed for the Nusselt number which takes into account the fluid properties of both gas flows. The convection inside the cell channels is forced convection upon the cell walls. So the approximation used for the Nusselt number in both the fuel and air flows is based on an expression of Nu for an external flow parallel to a plane surface in the laminar range ($Re < 2 \times 10^5$)[72, p 311]

$$Nu = 0.664 Pr^{1/3} Re^{1/2} \quad (Pr \geqslant 0.6) \tag{3.31}$$

where Pr is the *Prandtl number* of the fluid flow, and Re is the *Reynolds number* of the fluid flow. The Prandtl number Pr, which measures the ratio of the viscous diffusion rate with the thermal diffusion rate, is

$$Pr = \frac{(C_\mathrm{p}/M)\mu}{k} \tag{3.32}$$

where C_p is the molar specific heat capacity (with units $\mathrm{J/(mol \cdot K)}$), M is the molar mass of the fluid flow (with units kg/mol), μ is the dynamic viscosity (with units $\mathrm{Pa \cdot s}$), and the thermal conductivity of the fluid k (which has units W/(mK)). The Reynolds

number of the fluid flow is given as

$$Re = \frac{C^{\mathrm{b}} M u L}{\mu} \tag{3.33}$$

where C^{b} is the molar concentration of the bulk gas flow in the gas channel and u is the fluid velocity. With these expressions of the Nusselt number, Prandtl number, and the Reynolds number, the heat-transfer coefficients of the fuel and air flow are

$$h_{\mathrm{An}} = 0.664 \frac{k_{\mathrm{fuel}}}{L} \left(\left(\sum_{i=\mathrm{H_2,H_2O}} \frac{y_i C_{\mathrm{p},i}}{M_i} \right) \frac{\mu_{\mathrm{fuel}}}{k_{\mathrm{fuel}}} \right)^{1/3} \left(\frac{C^{\mathrm{b}}_{\mathrm{fuel}} M_{\mathrm{fuel}} u_{\mathrm{fuel}} L}{\mu_{\mathrm{fuel}}} \right)^{1/2}, \tag{3.34}$$

$$h_{\mathrm{Cat}} = 0.664 \frac{k_{\mathrm{air}}}{L} \left(\frac{(C_{\mathrm{p,air}}/M_{\mathrm{air}})\mu_{\mathrm{air}}}{k_{\mathrm{air}}} \right)^{1/3} \left(\frac{C^{\mathrm{b}}_{\mathrm{air}} M_{\mathrm{air}} u_{\mathrm{air}} L}{\mu_{\mathrm{air}}} \right)^{1/2}, \tag{3.35}$$

where y_i ($i = \mathrm{H_2},\ \mathrm{H_2O}$) represents the mole fraction of a substance within a gas flow. This expression of the heat-transfer coefficient was used in [52]. The expression of $C_{\mathrm{p,fuel}}$ is given by the summation term in (3.34). Similarly, μ_{fuel}, k_{fuel} and $C^{\mathrm{b}}_{\mathrm{fuel}}$ can be expressed as follows,

$$\mu_{\mathrm{fuel}} = \sum_{i=\mathrm{H_2,H_2O}} y_i \mu_i, \quad k_{\mathrm{fuel}} = \sum_{i=\mathrm{H_2,H_2O}} y_i k_i, \quad C^{\mathrm{b}}_{\mathrm{fuel}} = \sum_{i=\mathrm{H_2,H_2O}} y_i C^{\mathrm{b}}_i.$$

The derivations of C_{p}, μ and k for each of the individual substances (plus air), and the polynomial approximations applied to them can be found in Appendix E.

3.3.4 Cell Temperature Equation and Heat Production/Removal within the SOFC

The final energy conservation equation of the cell is given below

$$(d_{\mathrm{An}} + d_{\mathrm{Ele}} + d_{\mathrm{Cat}})(\rho_{\mathrm{cell}} C_{\mathrm{p,cell}}) \frac{\mathrm{d}T_{\mathrm{cell}}}{\mathrm{d}t} = \Delta H_{\mathrm{R}} - V_{\mathrm{cell}} i - h_{\mathrm{An}}(T_{\mathrm{cell}} - T_{\mathrm{fuel}}) - h_{\mathrm{Cat}}(T_{\mathrm{cell}} - T_{\mathrm{air}}). \tag{3.36}$$

The energy equation can be re-written in terms of the heat production in the cell Q_{P} and the amount of heat removed from the cell Q_{R}. The main source of heat production from the cell comes from the electrochemical reactions, and is described by the first two terms on the RHS of (3.36), whereas heat removal is due to forced convection on either side of the cell wall and is described by the final two terms on the RHS of (3.36). Therefore Q_{P} and Q_{R} are defined as follows:

$$Q_{\mathrm{P}} = (\Delta H_{\mathrm{R}} - V_{\mathrm{cell}} i) LW; \tag{3.37}$$

$$Q_{\mathrm{R}} = [h_{\mathrm{An}}(T_{\mathrm{cell}} - T_{\mathrm{fuel}}) - h_{\mathrm{Cat}}(T_{\mathrm{cell}} - T_{\mathrm{air}})] LW. \tag{3.38}$$

From [45] and [46], the number of steady-state solutions in a fuel cell can be determined by the number of intersections between the two curves as T_{cell} varies. As it will be shown in subsection 4.2.2, the amount of heat removed from the cell by convection is linear in T_{cell}, while the amount of heat produced rises exponentially until concentration polarisation effects take shape, in which the rate of change of Q_{P} with respect to T_{cell} reaches a peak, then drops with rising T_{cell} until Q_{P} is zero.

3.4 Mass Transfer and Diffusion within the Electrodes

Within the electrodes, there is a layer between the cell surface and the TPB known as the *electrode diffusion layer* (see figure 3.4), where Hydrogen and Oxygen travel to the TPB

to take part in the electrochemical reactions, and Water produced from electrochemical reaction (3.1) travels out of the electrode. Unlike the gas channels, mass transport within the electrodes is mainly due to diffusion. Also, when modelling mass transfer within the electrodes, especially the ease in which Hydrogen and Oxygen molecules travel through the diffusion layer into the TPB to take part in the electrochemical reactions, the porosity and tortuosity of both electrodes need to be taken into account.

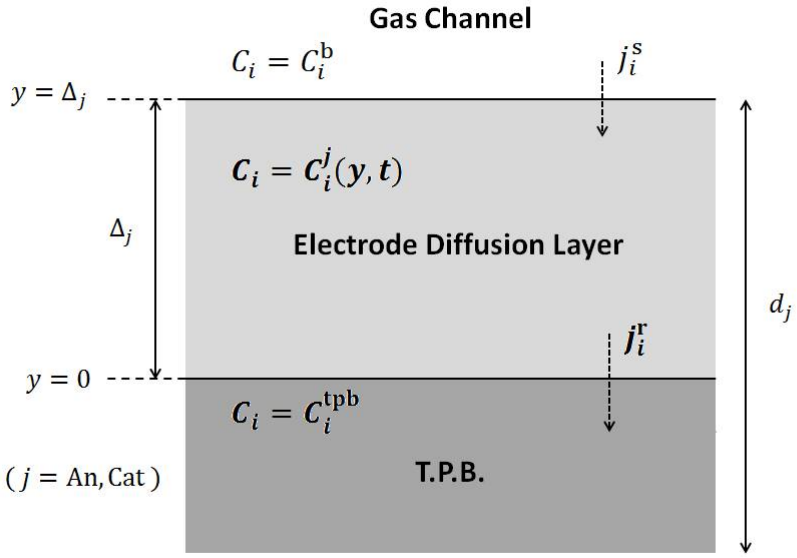

Figure 3.4: A schematic of the electrode diffusion layer. It is located in the electrode (with thickness d_j) between the external cell surface and the TPB. The thickness of the layer is given by Δ_j. The concentration C_i ($i = \mathrm{H_2},\ \mathrm{H_2O},\ \mathrm{O_2}$) is defined for each of the three regions. j_i^{s} represents the molar flux per unit area of i into the cell surface, and j_i^{r} the same, but from the electrode diffusion layer to the TPB. Mass transfer within the electrode can be described using the diffusion equation, with two boundary conditions located at $y = 0$ (TPB), and $y = \Delta_j$ (cell surface).

In this section, the equations modelling mass transfer within the electrode will be covered, including the derivation of mass conservation equations for Hydrogen, Oxygen and Water within the TPB. These equations are based on the steady-state solution of the diffusion equation within the electrode diffusion layer. This is followed by a description of diffusion

within the electrodes, where both binary diffusion and Knudsen diffusion are taken into account.

3.4.1 Mass Conservation in the TPB

Mass transport within the electrode diffusion layer can be described using the **Diffusion Equation**

$$\frac{\partial C_i^j}{\partial t} = D_{\text{eff},i}\frac{\partial^2 C_i^j}{\partial y^2} \quad (i = \text{H}_2, \text{H}_2\text{O}, \text{O}_2) \quad (j = \text{An}, \text{Cat}), \tag{3.39}$$

where C_i^j represents the concentration of Hydrogen, Water and Oxygen within the Anode-side/Cathode-side electrode diffusion layer, and $D_{\text{eff},i}$ is the effective diffusion coefficient of Hydrogen, Water and Oxygen. The boundary conditions are located on the cell surface, and the location of the TPB. The boundary condition on the TPB ($y = 0$) can be described using **Fick's Law for bi-molecular diffusion**

$$j_i^{\text{r}} = -D_{\text{eff},i}\frac{\partial C_i^j}{\partial y}(0, t) \tag{3.40}$$

where j_i^{r} represents the molar flux per unit area of chemical species i entering the diffusion layer from the reaction zone. Similarly, the molar flux per unit area through the surface of the cell j_i^{s} can be defined as

$$j_i^{\text{s}} = D_{\text{eff},i}\frac{\partial C_i^j}{\partial y}(\Delta_j, t). \tag{3.41}$$

The boundary condition for C_i^j at the cell surface ($y = \Delta_j$ ($j = \text{An},\ \text{Cat}$) where Δ_j represents the thickness of the diffusion layer) and at the surface of the TPB ($y = 0$) are

$$C_i^j(\Delta_j, t) = C_i^{\text{b}}, \quad C_i^j(0, t) = C_i^{\text{tpb}} \tag{3.42}$$

where C_i^{b} represents the concentration of chemical species i within the bulk gas flow in the gas channel, and C_i^{tpb} represents the concentration of i at the surface of the TPB region. The initial condition is given as $C_i^j(y,0) = C_i^0(y)$. Based on previous works such as [73], and results shown in chapter 7, the diffusive time scales for diffusion within the electrodes are very small (at most of order 10^{-3} s). So diffusion within the electrode diffusion layer is assumed to be at steady-state, meaning that the time derivative in equation (3.39) is neglected. So all that is needed is a solution to the steady-state diffusion equation

$$\frac{\mathrm{d}^2 C_i^j}{\mathrm{d}y^2} = 0 \tag{3.43}$$

along with the boundary conditions given in (3.42). Solving (3.43) along with the boundary conditions gives us

$$C_i^j(y) = C_i^{\mathrm{tpb}} + \frac{y}{\Delta_j}[C_i^{\mathrm{b}} - C_i^{\mathrm{tpb}}]. \tag{3.44}$$

At the surface of the TPB, using the boundary condition given in equation (3.42) for $y = 0$, j_i^{r} in equation (3.40) becomes

$$j_i^{\mathrm{r}} = \frac{D_{\mathrm{eff},i}}{\Delta_j}[C_i^{\mathrm{tpb}} - C_i^{\mathrm{b}}]. \tag{3.45}$$

At the surface of the cell, j_i^{s} in equation (3.41) for Hydrogen and Oxygen is defined as

$$j_i^{\mathrm{s}} = -j_i^{\mathrm{r}} = \frac{D_{\mathrm{eff},i}}{\Delta_j}[C_i^{\mathrm{b}} - C_i^{\mathrm{tpb}}], \tag{3.46}$$

since Hydrogen and Oxygen enter the cell surface, while for Water, it is defined as

$$j_i^{\mathrm{s}} = j_i^{\mathrm{r}} = \frac{D_{\mathrm{eff},i}}{\Delta_j}[C_i^{\mathrm{tpb}} - C_i^{\mathrm{b}}], \tag{3.47}$$

since Water leaves the cell surface. The term $D_{\text{eff},i}/\Delta_j$ within equations (3.45)-(3.47) is the mass-transfer resistance term over the layer thickness Δ_j of the electrode diffusion layer. This takes into the account of the effects of the electrode porosity and tortuosity on the mass transfer of each individual gaseous species within that layer.

As all gases inside the fuel cell are assumed to be ideal, $C_i^{\text{tpb}} = p_i^{\text{tpb}}/(RT_{\text{cell}})$. Considering C_i^j at the surface of the TPB region, the mass conservation equations of Hydrogen, Water and Oxygen over the whole electrode diffusion layer region can be described in terms of the molar flux entering/leaving the cell surface, and the amount produced/consumed within the TPB due to the electrochemical reactions (defined in equation (3.4)). The three conservation equations are

$$\frac{LW\Delta_{\text{An}}}{R}\frac{\mathrm{d}}{\mathrm{d}t}\left(\frac{p_{\text{H}_2}^{\text{tpb}}}{T_{\text{cell}}}\right) = j_{\text{H}_2}^{\text{s}}LW - R_{\text{H}_2} \quad \left(R_{\text{H}_2} = \frac{I}{2F}\right); \tag{3.48}$$

$$\frac{LW\Delta_{\text{An}}}{R}\frac{\mathrm{d}}{\mathrm{d}t}\left(\frac{p_{\text{H}_2\text{O}}^{\text{tpb}}}{T_{\text{cell}}}\right) = -j_{\text{H}_2\text{O}}^{\text{s}}LW + R_{\text{H}_2\text{O}} \quad \left(R_{\text{H}_2\text{O}} = \frac{I}{2F}\right); \tag{3.49}$$

$$\frac{LW\Delta_{\text{Cat}}}{R}\frac{\mathrm{d}}{\mathrm{d}t}\left(\frac{p_{\text{O}_2}^{\text{tpb}}}{T_{\text{cell}}}\right) = j_{\text{O}_2}^{\text{s}}LW - R_{\text{O}_2} \quad \left(R_{\text{O}_2} = \frac{I}{4F}\right). \tag{3.50}$$

The reason why these conservation equations are considered over the whole electrode diffusion layer region is that C_i^{tpb} over time is affected by mass transfer resistances within the electrode diffusion layer (which are incorporated within j_i^{s}) as the individual gaseous species diffuse from/to the cell surface to/from the TPB (as well as the reaction rate R_i). The electrochemical reactions are assumed to take place on the boundary between the electrode diffusion layer and the TPB ($y = 0$), so the reaction rate terms R_i represent the source/sink term in those equations.

3.4.2 Diffusion

Effective Diffusion Coefficients

The effective diffusion coefficient of Hydrogen, Oxygen and Water is defined in terms of the porosity ε of the electrode, the tortuosity τ of the electrode, and the diffusion coefficient D_i:

$$D_{\text{eff},i} = \frac{\varepsilon_j}{\tau_j} D_i \quad (i = \text{H}_2, \text{H}_2\text{O}, \text{O}_2) \quad (j = \text{An}, \text{Cat}) \tag{3.51}$$

The Diffusion coefficient D_i takes account of the diffusion of chemical species i within another fluid m (binary diffusion) and Knudsen diffusion (where the pore diameter is smaller than the mean free path of the molecules), and is written in terms of the binary diffusion coefficient of chemical species i diffusing within chemical species m $D_{i,m}$, and the Knudsen diffusion coefficient D_{K_i} [72, p 421]

$$\frac{1}{D_i} = \frac{1}{D_{i,m}} + \frac{1}{D_{K_i}}. \tag{3.52}$$

Here, we assume that the mean free path of the molecules within the electrode is larger than the pore diameter, such that the molecules collide frequently with the pore walls. The effective diffusion coefficients of Hydrogen, Water and Oxygen are

$$D_{\text{eff},\text{H}_2} = \frac{\varepsilon_{\text{An}}}{\tau_{\text{An}}} \left(\frac{D_{\text{H}_2,\text{H}_2\text{O}} D_{K_{\text{H}_2}}}{D_{\text{H}_2,\text{H}_2\text{O}} + D_{K_{\text{H}_2}}} \right); \tag{3.53}$$

$$D_{\text{eff},\text{H}_2\text{O}} = \frac{\varepsilon_{\text{An}}}{\tau_{\text{An}}} \left(\frac{D_{\text{H}_2,\text{H}_2\text{O}} D_{K_{\text{H}_2\text{O}}}}{D_{\text{H}_2,\text{H}_2\text{O}} + D_{K_{\text{H}_2\text{O}}}} \right); \tag{3.54}$$

$$D_{\text{eff},\text{O}_2} = \frac{\varepsilon_{\text{Cat}}}{\tau_{\text{Cat}}} \left(\frac{D_{\text{O}_2,\text{N}_2} D_{K_{\text{O}_2}}}{D_{\text{O}_2,\text{N}_2} + D_{K_{\text{O}_2}}} \right). \tag{3.55}$$

Binary Diffusion Coefficients

For the diffusion of one fluid within another fluid, the binary diffusion coefficient of fluid i within fluid m is defined using Fuller's correlation [66]

$$D_{i,m} = \frac{10^{-3} T^{1.75} \left(\frac{1}{M_i} + \frac{1}{M_m}\right)^{0.5}}{p \left[\Sigma \nu_i^{1/3} + \Sigma \nu_m^{1/3}\right]^2} \tag{3.56}$$

where T is the temperature in K, M_i and M_m represent the molar masses of i and m respectively with units g/mol, p is the pressure in atm, and the ν terms represent special diffusion parameters which are summed over atoms, groups and structural features of i and m. In this expression of $D_{i,m}$, these diffusion parameters have units of atomic volume (*i.e.* cm^3/mol) [66], hence they are referred to as atomic diffusion volumes. Data for ν is mainly available for simple molecules [72, p 410], including the gaseous species considered for this SOFC. The binary diffusion coefficient given in (3.56) was defined in [66] using non-linear least-squares analysis, and its units are cm^2/s. The constant 10^{-3} is an arbitrary constant chosen so that the diffusion volumes would correspond closely to the molecular volume values obtained by Le Bas [74]. Given the units of the other parameters in (3.56), the units of 10^{-3} are chosen so that the dimensions of $D_{i,m}$ are equal to cm^2/s. The units of this arbitrary constant are $(cm^4 \cdot \text{ atm})/(K^{1.75} \cdot mol^{7/6} \cdot s)$.

In this model, the units of the diffusion coefficient are m^2/s, so $D_{i,m}$ is multiplied by 10^{-4} (1 cm=10^{-2} m). The molar masses M_i of each individual gaseous species in this model have units kg/mol, so they are multiplied by 10^3 to ensure dimensional consistency (1 kg=10^3 g). Pressure p in this model has units Pa, so the pressure term is divided by p_0 which represents 1 atm of pressure (1 atm=1.013×10^5 Pa). Also, since diffusion is considered within the electrodes, T is given as T_{cell} (as the temperature is assumed to be uniformally distributed across the whole cell component).

Taking this all into account, the two binary diffusion coefficients $D_{\mathrm{H_2,H_2O}}$ and $D_{\mathrm{O_2,N_2}}$ are

$$D_{\mathrm{H_2,H_2O}} = \frac{\left(10^{-3}\frac{\mathrm{cm^4\cdot atm}}{\mathrm{K^{1.75}\cdot mol^{7/6}\cdot s}}\right)(T_{\mathrm{cell}})^{1.75}\left(\frac{1}{M_{\mathrm{H_2}}\times(10^3\ \mathrm{g})}+\frac{1}{M_{\mathrm{H_2O}}\times(10^3\ \mathrm{g})}\right)^{0.5}}{[(p^{\mathrm{tpb}}_{\mathrm{H_2}}+p^{\mathrm{tpb}}_{\mathrm{H_2O}})/p_0]\left[\Sigma\nu^{1/3}_{\mathrm{H_2}}+\Sigma\nu^{1/3}_{\mathrm{H_2O}}\right]^2}\times(10^{-4}\ \mathrm{m^2}); \tag{3.57}$$

$$D_{\mathrm{O_2,N_2}} = \frac{\left(10^{-3}\frac{\mathrm{cm^4\cdot atm}}{\mathrm{K^{1.75}\cdot mol^{7/6}\cdot s}}\right)(T_{\mathrm{cell}})^{1.75}\left(\frac{1}{M_{\mathrm{O_2}}\times(10^3\ \mathrm{g})}+\frac{1}{M_{\mathrm{N_2}}\times(10^3\ \mathrm{g})}\right)^{0.5}}{[(p^{\mathrm{tpb}}_{\mathrm{O_2}}+p^{\mathrm{b}}_{\mathrm{N_2}})/p_0]\left[\Sigma\nu^{1/3}_{\mathrm{O_2}}+\Sigma\nu^{1/3}_{\mathrm{N_2}}\right]^2}\times(10^{-4}\ \mathrm{m^2}), \tag{3.58}$$

where the partial pressure of Nitrogen in the bulk air flow is considered since Nitrogen does not take place in the electrochemical reactions.

Knudsen Diffusion Coefficients

Knudsen diffusion occurs when the mean free path of the molecules is larger than the pore diameter, which means that the molecules collide frequently with the pore walls within the electrode. The Knudsen diffusion coefficient is described in terms of the pore mean radius in the electrodes and T_{cell}, and is defined using the expression obtained by Chan et al. [75]

$$D_{K_i} = \left(97\frac{\mathrm{m\cdot g^{1/2}}}{\mathrm{s(K\cdot mol)^{1/2}}}\right)\delta_j\sqrt{\frac{T_{\mathrm{cell}}}{M_i\times(10^3\ \mathrm{g})}} \tag{3.59}$$

where δ_j is the pore mean radius of the electrode (given in m), and molar mass M_i has units kg/mol. The Knudsen diffusion coefficients of Hydrogen, Water and Oxygen are

$$D_{K_{\mathrm{H_2}}} = \left(97\frac{\mathrm{m\cdot g^{1/2}}}{\mathrm{s(K\cdot mol)^{1/2}}}\right)\delta_{\mathrm{An}}\sqrt{\frac{T_{\mathrm{cell}}}{M_{\mathrm{H_2}}\times(10^3\ \mathrm{g})}}; \tag{3.60}$$

$$D_{K_{\mathrm{H_2O}}} = \left(97\frac{\mathrm{m\cdot g^{1/2}}}{\mathrm{s(K\cdot mol)^{1/2}}}\right)\delta_{\mathrm{An}}\sqrt{\frac{T_{\mathrm{cell}}}{M_{\mathrm{H_2O}}\times(10^3\ \mathrm{g})}}; \tag{3.61}$$

$$D_{K_{\mathrm{O_2}}} = \left(97\frac{\mathrm{m\cdot g^{1/2}}}{\mathrm{s(K\cdot mol)^{1/2}}}\right)\delta_{\mathrm{Cat}}\sqrt{\frac{T_{\mathrm{cell}}}{M_{\mathrm{O_2}}\times(10^3\ \mathrm{g})}}. \tag{3.62}$$

3.5 Gas Flow Dynamics

This subsystem covers the dynamics of the gas flow in the gas channels. For this, we consider the mass conservation of the gas flow as a whole and its individual components, the energy conservation of both gas flows, and the momentum conservation of both gas flows. The inlet parameters of this SOFC are the inlet gas flow temperatures $T_{\text{fuel}}^{\text{in}}$ and $T_{\text{air}}^{\text{in}}$, the inlet gas flow velocities $u_{\text{fuel}}^{\text{in}}$ and $u_{\text{air}}^{\text{in}}$, the inlet molar flow rates of both gas flows $\dot{N}_{\text{fuel}}^{\text{in}}$ and $\dot{N}_{\text{air}}^{\text{in}}$, and the inlet mole fractions y_i^{in} of chemical species i (= H_2, H_2O, O_2, N_2). The values of these inlet parameters are given in Appendix B.

3.5.1 Mass Conservation

The mass conservation equation is of the form

$$LWh^j \frac{\mathrm{d}C_i^{\text{b}}}{\mathrm{d}t} = \dot{N}_i^{\text{in}} - \dot{N}_i^{\text{out}} + \dot{N}_i^{\text{gen}}. \tag{3.63}$$

Here C_i^{b} represents the molar concentration of chemical species i in the bulk gas flow, L the cell length, h^j is the height of gas channel j (=fuel, air), W is the cell width, $\dot{N}_i^{\text{in}}$ is the molar flow rate of chemical species i at the inlet, $\dot{N}_i^{\text{out}}$ is the molar flow rate of chemical species i at the outlet, and $\dot{N}_i^{\text{gen}}$ is the rate of change of the number of moles of chemical species i within the gas flow due to molar fluxes into/out of the cell surface.
C_i^{b} is written in the form $C_j^{\text{b}} \cdot y_i$ where C_j^{b} (j =fuel, air) represents the concentration of the bulk gas flow, and y_i is the mole fraction of chemical species i. The molar flow rate of chemical species i at the inlet is written in terms of the molar flow rate of gas flow j (=fuel, air) at the inlet $\dot{N}_j^{\text{in}}$

$$\dot{N}_i^{\text{in}} = \dot{N}_j^{\text{in}} y_i^{\text{in}} = u_j^{\text{in}} \cdot (C_j^{\text{b}})^{\text{in}} \cdot y_i^{\text{in}} \cdot Wh^j.$$

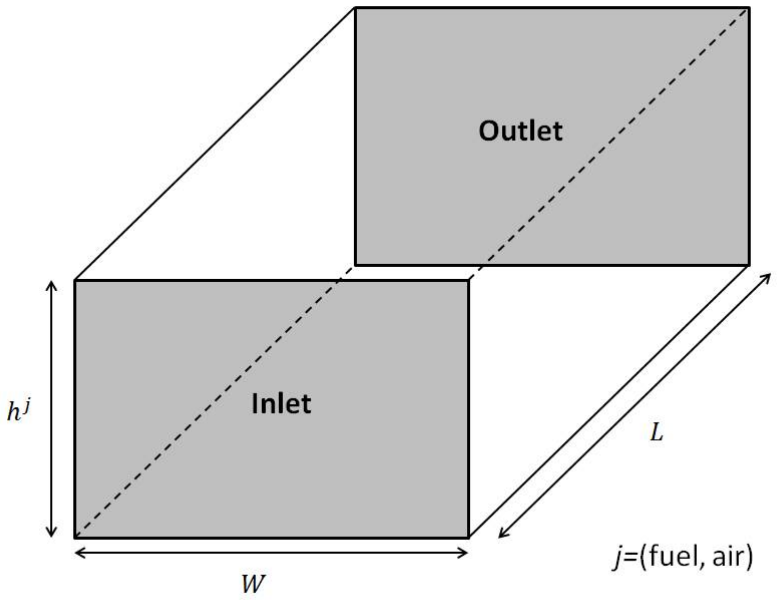

Figure 3.5: A schematic of a SOFC gas channel. L represents the length of the cell, W represents the cell width, and h^j $(j = \text{fuel, air})$ represents the height of the gas channel

The molar flow rate at the outlet is written in the form

$$\dot{N}_i^{\text{out}} = u_j \cdot C_j^{\text{b}} \cdot y_i \cdot W h^j,$$

where u_j is the velocity of gas flow j. The generation/removal term takes account of molar flux into/out of the whole outer electrode surface area either to take part in the electrochemical reactions, or to enter the bulk gas flow,

$$\dot{N}_i^{\text{gen}} = j_i^{\text{s}} \cdot LW.$$

The mass conservation equations for Hydrogen, Water and Oxygen are

$$LWh^{\text{fuel}}\frac{\mathrm{d}C^{\text{b}}_{\text{fuel}}y_{\text{H}_2}}{\mathrm{d}t} = \dot{N}^{\text{in}}_{\text{fuel}}y^{\text{in}}_{\text{H}_2} - u_{\text{fuel}}C^{\text{b}}_{\text{fuel}}y_{\text{H}_2}Wh^{\text{fuel}} - j^{\text{s}}_{\text{H}_2}LW; \tag{3.64}$$

$$LWh^{\text{fuel}}\frac{\mathrm{d}C^{\text{b}}_{\text{fuel}}y_{\text{H}_2\text{O}}}{\mathrm{d}t} = \dot{N}^{\text{in}}_{\text{fuel}}y^{\text{in}}_{\text{H}_2\text{O}} - u_{\text{fuel}}C^{\text{b}}_{\text{fuel}}y_{\text{H}_2\text{O}}Wh^{\text{fuel}} + j^{\text{s}}_{\text{H}_2\text{O}}LW; \tag{3.65}$$

$$LWh^{\text{air}}\frac{\mathrm{d}C^{\text{b}}_{\text{air}}y_{\text{O}_2}}{\mathrm{d}t} = \dot{N}^{\text{in}}_{\text{air}}y^{\text{in}}_{\text{O}_2} - u_{\text{air}}C_{\text{air}}y_{\text{O}_2}Wh^{\text{air}} - j^{\text{s}}_{\text{O}_2}LW. \tag{3.66}$$

The mass conservation equations for the fuel and air flow can be obtained by adding the two conservation equations for Hydrogen and Water on the fuel channel side, and Oxygen and Nitrogen on the air channel side (no Nitrogen is consumed/produced within the air channel). This is because the sum of the mole fractions of all the chemical species within a particular gas flow is equal to one.

The mass conservation equation of the fuel and air flow is of the same format as in equation (3.63), except that the final term represents the rate of change of the number of moles within the whole gas flow due to the net molar flux into the cell. The mass conservation equations for the fuel and air flow are

$$LWh^{\text{fuel}}\frac{\mathrm{d}C^{\text{b}}_{\text{fuel}}}{\mathrm{d}t} = \dot{N}^{\text{in}}_{\text{fuel}} - u_{\text{fuel}}C^{\text{b}}_{\text{fuel}}Wh^{\text{fuel}} + (j^{\text{s}}_{\text{H}_2\text{O}} - j^{\text{s}}_{\text{H}_2})LW \tag{3.67}$$

$$LWh^{\text{air}}\frac{\mathrm{d}C^{\text{b}}_{\text{air}}}{\mathrm{d}t} = \dot{N}^{\text{in}}_{\text{air}} - u_{\text{air}}C^{\text{b}}_{\text{air}}Wh^{\text{air}} - j^{\text{s}}_{\text{O}_2}LW. \tag{3.68}$$

3.5.2 Energy Conservation

Taking into account forced convection on the walls of the cell from the gas flow either side of the cell, and enthalpy fluxes moving into and out of the cell, the energy conservation

equation of the gas flow in either gas channel is

$$LWh^j \frac{\mathrm{d}(C_j^{\mathrm{b}} C_{\mathrm{p},j} T_j)}{\mathrm{d}t} = \dot{N_j}^{\mathrm{in}} H_j^{\mathrm{in}} - \dot{N_j}^{\mathrm{out}} H_j^{\mathrm{out}} + h_j(T_{\mathrm{cell}} - T_j)LW + \sum_i N_i^{\mathrm{b}} H_i LW \quad (j = \mathrm{fuel}, \mathrm{air}), \tag{3.69}$$

where H_j is the enthalpy of gas flow j. For the fuel flow, it is defined in terms of the enthalpy of Hydrogen and Water, and for the advection term, the enthalpy of Water is a function of T_{fuel} rather than T_{cell}

$$\begin{aligned} H_{\mathrm{fuel}} &= y_{\mathrm{H_2}} H_{\mathrm{H_2}} + y_{\mathrm{H_2O}} H_{\mathrm{H_2O}} \\ &= y_{\mathrm{H_2}}(a_{\mathrm{H_2}} + b_{\mathrm{H_2}} T_{\mathrm{fuel}}) + y_{\mathrm{H_2O}}(a_{\mathrm{H_2O}} + b_{\mathrm{H_2O}} T_{\mathrm{fuel}}). \end{aligned}$$

The inlet term in equation (3.69) stays as it is for both gas flows, while the outlet term $\dot{N_j}^{\mathrm{out}} H_j^{\mathrm{out}}$ is defined as

$$\dot{N_j}^{\mathrm{out}} H_j^{\mathrm{out}} = u_j \cdot C_j^{\mathrm{b}} \cdot H_j \cdot W \cdot h^j.$$

The final term in (3.69) takes account of the enthalpy fluxes of Hydrogen, Oxygen and Water either into or out of the cell. Since only oxygen takes part in the electrochemical reaction in the cathode-side TPB, the energy conservation equation for the air flow is

$$LWh^{\mathrm{air}} \frac{\mathrm{d}(C_{\mathrm{air}}^{\mathrm{b}} C_{\mathrm{p,air}} T_{\mathrm{air}})}{\mathrm{d}t} = \dot{N}_{\mathrm{air}}^{\mathrm{in}} H_{\mathrm{air}}^{\mathrm{in}} - u_{\mathrm{air}} C_{\mathrm{air}}^{\mathrm{b}} H_{\mathrm{air}} W h^{\mathrm{air}} + h_{\mathrm{Cat}}(T_{\mathrm{cell}} - T_{\mathrm{air}})LW + j_{\mathrm{O_2}}^{\mathrm{s}} H_{\mathrm{O_2}} LW. \tag{3.70}$$

The energy conservation equation for the fuel flow is

$$LWh^{\mathrm{fuel}} \frac{\mathrm{d}(C_{\mathrm{fuel}}^{\mathrm{b}} C_{\mathrm{p,fuel}} T_{\mathrm{fuel}})}{\mathrm{d}t} = \dot{N}_{\mathrm{fuel}}^{\mathrm{in}} H_{\mathrm{fuel}}^{\mathrm{in}} - u_{\mathrm{fuel}} C_{\mathrm{fuel}}^{\mathrm{b}} H_{\mathrm{fuel}} W h^{\mathrm{fuel}} + h_{\mathrm{An}}(T_{\mathrm{cell}} - T_{\mathrm{fuel}})LW + (j_{\mathrm{H_2O}}^{\mathrm{s}} H_{\mathrm{H_2O}} - j_{\mathrm{H_2}}^{\mathrm{s}} H_{\mathrm{H_2}})LW. \tag{3.71}$$

3.5.3 Momentum Conservation

Unlike the model in [49], momentum conservation for both gas flows is considered in this model. Friction on the gas walls is neglected, and so are viscosity effects since the Péclet number $Pe \gg 1$ for mass transfer in both gas flows. Hence the general momentum conservation equation is described in terms of the pressure gradient and mass fluxes into/out of the cell surface:

$$LWh^j \frac{\mathrm{d}(C_j^{\mathrm{b}} M_j u_j)}{\mathrm{d}t} = \dot{N}_j^{\mathrm{in}} u_j^{\mathrm{in}} M_j - C_j^{\mathrm{b}} M_j u_j^2 W h^j + \frac{\dot{N}_j^{\mathrm{in}} R T_j^{\mathrm{in}}}{u_j^{\mathrm{in}}} - P_j^{\mathrm{b}} W h^j + (\sum_i M_i j_i^{\mathrm{s}}) u_j LW. \tag{3.72}$$

The first two terms on the right-hand side of equation (3.72) represent the advection terms, the next two terms represent the pressure gradient (where the pressure of the bulk gas flow $P_j^{\mathrm{b}} = C_j^{\mathrm{b}} R T_j$ due to the ideal gas law assumption), and the final term represents the net mass flux of Hydrogen, Water and Oxygen into the cell surface.

Since there is a value for the molar mass of air, the momentum conservation equation for the air flow is

$$LWh^{\mathrm{air}} \frac{\mathrm{d}(C_{\mathrm{air}}^{\mathrm{b}} M_{\mathrm{air}} u_{\mathrm{air}})}{\mathrm{d}t} = \dot{N}_{\mathrm{air}}^{\mathrm{in}} u_{\mathrm{air}}^{\mathrm{in}} M_{\mathrm{air}} - C_{\mathrm{air}}^{\mathrm{b}} M_{\mathrm{air}} u_{\mathrm{air}}^2 W h^{\mathrm{air}} + \frac{\dot{N}_{\mathrm{air}}^{\mathrm{in}} R T_{\mathrm{air}}^{\mathrm{in}}}{u_{\mathrm{air}}^{\mathrm{in}}} - C_{\mathrm{air}}^{\mathrm{b}} R T_{\mathrm{air}}^{\mathrm{b}} W h^{\mathrm{air}} + M_{\mathrm{O_2}} j_{\mathrm{O_2}}^{\mathrm{s}} u_{\mathrm{air}} LW. \tag{3.73}$$

As for the fuel flow, the molar mass of the fuel flow is described in terms of the molar mass of Hydrogen and Water:

$$M_{\mathrm{fuel}} = y_{\mathrm{H_2}} M_{\mathrm{H_2}} + y_{\mathrm{H_2O}} M_{\mathrm{H_2O}}.$$

Therefore, the momentum conservation equation for the fuel flow is

$$LWh^{\text{fuel}}\frac{\mathrm{d}}{\mathrm{d}t}\left(\left(\sum_{i\in \mathrm{H_2,H_2O}} y_i M_i\right) C^{\text{b}}_{\text{fuel}} u_{\text{fuel}}\right) = \left(\sum_{i\in \mathrm{H_2,H_2O}} y_i M_i\right)\left[\dot{N}^{\text{in}}_{\text{fuel}} u^{\text{in}}_{\text{fuel}} - C^{\text{b}}_{\text{fuel}} u^2_{\text{fuel}} W h^{\text{fuel}}\right] + \frac{\dot{N}^{\text{in}}_{\text{fuel}} R T^{\text{in}}_{\text{fuel}}}{u^{\text{in}}_{\text{fuel}}} - C^{\text{b}}_{\text{fuel}} R T_{\text{fuel}} W h^{\text{fuel}} + [M_{\mathrm{H_2O}} j^{\text{s}}_{\mathrm{H_2O}} - M_{\mathrm{H_2}} j^{\text{s}}_{\mathrm{H_2}}] u_{\text{fuel}} LW. \quad (3.74)$$

3.6 Solution Method

Overall, the model is a differential and algebraic equation system (DAE) consisting of twelve first-order ordinary differential equations (ODEs), and three non-linear, implicit algebraic equations. This DAE system is of the form

$$\dot{\mathbf{x}} = \mathbf{f}(\mathbf{x}, t),$$

where three elements of $\dot{\mathbf{x}}$ are equal to zero. In steady-state form, this becomes a system of fifthteen algebraic equations of the form

$$\mathbf{f}(\mathbf{x}) = 0.$$

The steady-state model is solved for three different modes of operation

1. Constant External Load (constant parameter-R_{load});
2. Potentiostatic Operation (constant parameter-V_{cell});
3. Galvanostatic Operation (constant parameter-I).

For the first mode of operation, V_{cell} and I are coupled using **Ohm's Law** ($V_{\text{cell}} = I \cdot R_{\text{load}}$). The equations for the steady-state model for each of the three modes of operation and the

dynamic model are presented in Appendix F. For this section, there will be a run-down into how the steady-state and dynamic models are solved.

3.6.1 Steady-State Model

For each of the three modes of operation, the constant parameter is treated as the bifurcation parameter (x_B), and these equations are solved in MATLAB using the built-in solver *fsolve* for different values of x_B. *fsolve* is useful for solving systems of non-linear equations, and is based on trust-region methods (its default setting is the Trust-Region-Dogleg method). Just like Newton's method, an initial guess vector is required to find the roots of the non-linear system of equations.

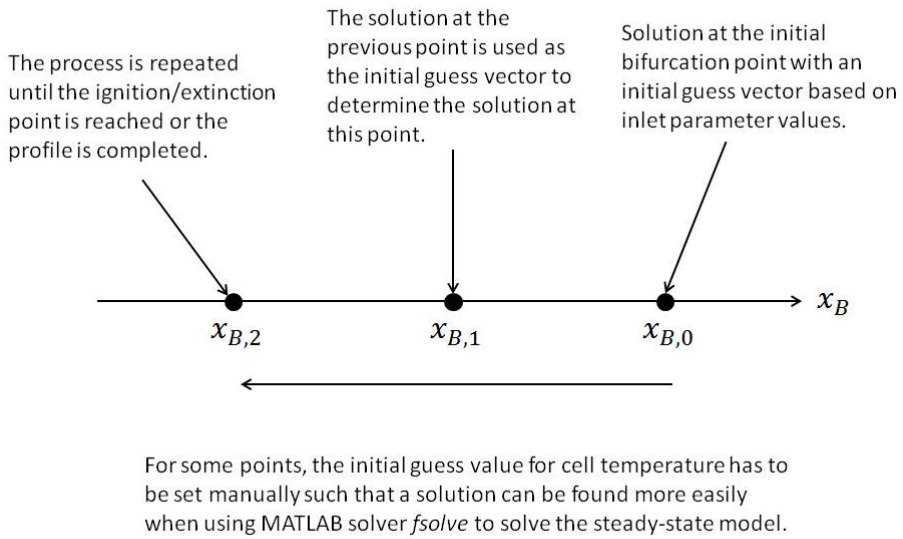

Figure 3.6: A diagram showing the process of how the steady-state solutions of the steady-state model are obtained for each bifurcation point $x_{B,i}$. The MATLAB solver *fsolve* is used to solve the steady-state model at each bifurcation point.

In the cases of a constant external load and the potentiostatic mode of operation, x_B is initially chosen so that the cell current is as close to zero as possible (so that complete profiles can be obtained for rising current density). The initial guess vector used to enable

fsolve to find a solution to the non-linear system of equations is set up based on values of the inlet parameters (see Appendix B). The solution at that point is stable.

When using *fsolve* to solve the system of non-linear equations (or any built-in solver in MATLAB), you can set up an "options" vector, which enables you to modify the solver properties to suit the problem you are working with. In this case, the "options" vector is set up as follows:

```
options=optimoptions('fsolve','Display','iter')
```

The first entry in the bracket refers to the solver that is being modified. The second entry is the "Display" option, where you can set up the amount of information you want the solver to show on screen. The third entry is the chosen "Display" option *iter*, where information about the value of $||\mathbf{f}(\mathbf{x})||_2^2$ at each iteration is provided (as well as the norm at each step), with a final statement as to whether the equation is solved, whether the solver stops prematurely, or whether no solution can be found. If a solution is found, $||\mathbf{f}(\mathbf{x})||_2^2$ is of the order between order 10^{-20} and order 10^{-25}. The ignition point and extinction point is found if the solver says that the equation is solved, but the order of $||\mathbf{f}(\mathbf{x})||_2^2$ is as high as 10^{-7} (usually in the region between 10^{-7} and 10^{-12}).

As shown on figure 3.6, the solution for the next chosen value of the bifurcation parameter along the stable steady-state branch can be obtained by using the previous solution at the previous bifurcation parameter value as the initial guess vector. This process is repeated until the the value of the bifurcation parameter (in this case, either R_{load} or V_{cell}) reaches zero (*i.e.* there are no multiple steady-states), or until the ignition point is located.

However, for most of the points along the initial steady-state branch, and for almost all the points along the unstable steady-state branch and the second steady-state branch, *fsolve* will struggle to find a solution first time out. If the function vector fails to converge to zero within a certain number of iterations, it comes up with the message

```
Solver Stops Prematurely
```

along with the updated solution vector (which do not represent the roots to the steady-state model). To rectify this, there are two ways to do this:

- Set the updated solution vector as the initial guess vector and run *fsolve* again to help it converge to a solution. Repeat the process until this happens;
- Before running *fsolve*, manually set up the initial guess value for T_{cell} (usually higher than the predicted solution for T_{cell}) so that *fsolve* can solve the steady-state model first time.

The latter option is preferable since it is much quicker, and easier to obtain a full set of solutions for both cases, especially for bifurcation points close to ignition and extinction point.

Once the ignition point is located, the first solution along the unstable steady-state branch (where x_B is increased slightly) is obtained by setting the initial guess for T_{cell} higher than the value of T_{cell} at the ignition point. The rest of the initial guesses correspond to the solution on the ignition point. Once a solution is obtained which does not equal the equivalent solution for the same point on the lower stable steady-state branch, the same procedure is followed but for increasing values of x_B, until the extinction point is located. The same process is used to obtain the first solution along the upper stable steady-state branch (see figure 3.7). Once that is done, repeat the same process to obtain the remaining solutions along the upper stable steady-state branch.

The only automatic process in this method is using *fsolve* to solve the system of steady-state equations at a particular point. Otherwise, the rest of the process, including choosing your next bifurcation point to solve your system of equations on, and locating the ignition and extinction points has to be done manually.

As for the Galvanostatic operation, the first solution is obtained at $I = 0$. All the other solutions are obtained for rising I until $V_{\text{cell}} = 0$. The process used to obtain a full set of

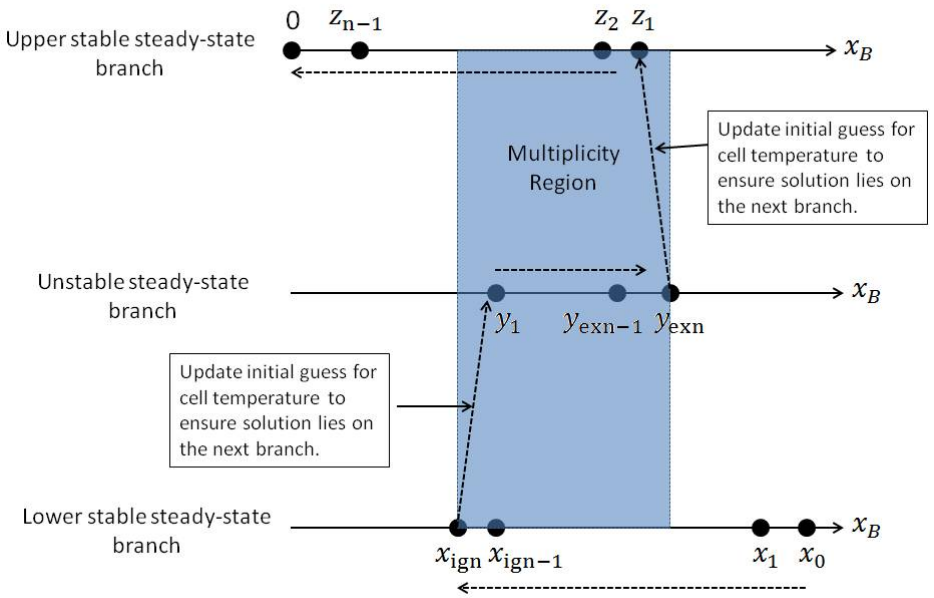

Figure 3.7: A diagram showing the range of values of the bifurcation parameter x_B across all three steady-state branches in which a steady-state solution is obtained, using the process shown in figure 3.6. The dashed arrows represent the direction across all three branches (plus the transition between branches) in which a full set of solutions are obtained. The blue box highlights the region of values of x_B where up to three steady-state solutions exist. When transitioning from one branch to another, the initial guess of T_{cell} is modified such that the solution for T_{cell} is higher than the equivalent solution on the lower branch.

solutions is the same as for the other two cases, only except that T_{cell} does not have to be modified manually. Also, as will be seen later on, there are no multiple steady-states for a SOFC operating under a constant cell current.

For all three cases, at least one value of T_{cell} exists for any value of x_B. This means that the heat production and heat removal curves for a certain fixed value of x_B can be obtained by setting T_{cell} as the bifurcation parameter, removing the cell temperature equation, and solving the remaining steady-state equations for increasing values of T_{cell} (starting from an initial value equal or close to the inlet gas flow temperatures). There are two additional equations in the model: one describing heat production within the cell (Q_{P}-equation (3.37)), and the other describing heat loss within the cell (Q_{R}-equation (3.38)).

The process for solving these equations is the same as the process for the other cases, only except that no multiple solutions exist for any value of T_{cell}.

3.6.2 Dynamic Model

The dynamic model consists of three non-linear, implicit algebraic equations and twelve first-order ODEs, making it a DAE system of index 1. In MATLAB, there are two Initial Value Problem (IVP) solvers that can deal with a DAE system of index 1:

- *ode15s*: This solver is useful for a stiff system of ODEs or DAEs. It is a variable order, multi-step solver based on Numerical Differential Formulas (NDFs). This solver is primarily used if the default IVP solver *ode45* (based on the 4-th order Runge-Kutta method) fails to produce a solution;
- *ode23t*: This solver is useful for solving a moderately stiff system of ODEs or DAEs. This solver uses the Trapezoidal rule to solve the IVP.

For this problem, *ode15s* is used to solve the DAE system since the system is highly coupled.

Using *ode15s* to solve the dynamic model, we can observe the transient behaviour of a SOFC operating under a constant external load subject to load changes after a certain amount of time. The initial conditions (ICs) for the IVP are based on the steady-state solution of the steady-state model for a particular point of R_{load} at which the fuel cell is turned on.

In this thesis, instead of considering a step-change in R_{load} at 100 seconds, R_{load} is expressed a smooth function of time. This is to avoid numerical difficulties associated with a step-change in R_{load}. It is defined in terms of the tanh function

$$R_{\text{load}}(t) = R_{\text{load}}^{(0)} + \frac{1}{2}\left[R_{\text{load}}^{(1)} - R_{\text{load}}^{(0)}\right]\left\{1 + \tanh\left(\frac{(t - t_{\text{s}})}{\omega}\right)\right\} \tag{3.75}$$

where $R_{\text{load}}^{(0)}$ is the initial value of R_{load} at $t = 0$, $R_{\text{load}}^{(1)}$ is the final value of R_{load}, t_{s} is the transition mid-point time (taken to be 100 seconds), and ω is a constant (defined in terms of seconds) that determines how quickly R_{load} changes from $R_{\text{load}}^{(0)}$ to $R_{\text{load}}^{(1)}$. With this expression of R_{load}, the dynamic model is solved over one time interval for all the cases considered in chapter 7 (including ignition and extinction). Over this interval, *ode15s* solves the dynamic model at multiple time-steps. The size of these time-steps vary depending on whether there is any significant transient activity in a certain time region. The higher the level in transient activity, the smaller the step-size is to ensure that a solution is obtained.

When using a built-in IVP solver to solve a system of ODEs or DAEs, there are certain properties you can modify to suit the IVP that you are trying to solve. In this case, the only property that needs to be modified is the length of the maximum time-step. This is to prevent any large time-steps occurring during periods where the profile is still in transition from one steady-state solution to another, resulting in a less than smooth profile. There are other properties associated with *ode15s* that can be modified, including *Relative Error Tolerance* and *Absolute Error Tolerance*. The *Relative Error Tolerance* is a measure of the error relative to the size of each component in the solution vector, with a default setting of 1×10^{-3} (or 0.1% accuracy). The *Absolute Error Tolerance* is the threshold below which the value of the i-th solution component is unimportant, and determines the accuracy when the solution reaches zero. Its default setting is 1×10^{-6}, and can be set as one individual value that applies to all the components of the solution vector, or as a vector with individual values for each component. Since R_{load} is expressed as a smooth function of time rather than an instant step-function, the relative and absolute tolerance values are left at its default setting.

To ensure that the parameters tend towards the new expected steady-state solution after the step-change, you can calculate the absolute error/difference of the transient solution

with the predicted steady-state solution at the value of R_{load} after the change in value of R_{load} (and on the right steady-state branch). If $\mathbf{x}_{\text{Dy}}(t)$ represents the solution of the dynamic model for increasing time after the step-change, and $\mathbf{x}_{\text{SS}}$ represents the predicted steady-state solution for the chosen value of R_{load} after the step-change, the relative error/difference can be calculated as follows:

$$E_{\text{Abs}} = ||\mathbf{x}_{\text{Dy}}(t) - \mathbf{x}_{\text{SS}}||_2.$$

In this thesis, the main aim is not only to observe the transient behaviour of the SOFC during ignition and extinction as well as for load changes along the lower stable steady-state branch, but to show explicitly that once the SOFC operates at a new steady-state branch, it remains on that branch after changing R_{load} back to its original value before the initial step change.

3.7 Summary

In this chapter, a lumped-parameter (electrolyte supported) SOFC model of a planar configuration was presented. This model builds upon the model presented by Bavarian and Soroush [49] in two key areas:

1. The heat-transfer coefficient is no longer assumed to be constant and of the same value in both gas channels. It is defined such that convective effects are fully taken into account;

2. Gas flow velocity is no longer assumed to be constant, adding another couple of equations into the system.

The model presented in this chapter takes into account the electrochemical model (*i.e.* reaction rates, cell voltage), temperature of the solid PEN structure, mass transfer and diffusion within the electrodes, and mass, momentum and energy transfer within the two

gas channels.

The SOFC is fuelled solely by Hydrogen, so there are only two electrochemical reactions to take account of in the cell. The reaction rates within the cell can be defined using Faraday's law. The derivation of the reversible cell voltage comes from a combination of the 1st and 2nd law of thermodynamics, and can be defined using the Nernst potential. The actual cell voltage produced by the cell is affected by activation, Ohmic and concentration polarisations in this model.

Activation polarisation is the voltage drop due to the delay in the activation of the electrochemical reactions due to the complex reaction steps associated with both reactions. It is defined using the Butler-Volmer equation, and unless the forward and backward reaction rates are equal to 0.5, the equations corresponding to activation polarisation within the anode and cathode are implicitly defined. Ohmic polarisation is the voltage drop due to a combination of electrical and ionic resistances in the electrodes and the electrolyte. It is defined in terms of the specific resistivity of the cell components. In this model, Ohmic resistivity is dominated by ionic resistivity in the electrolyte, and plays a key role in the existence of multiple steady-states within a SOFC. Concentration polarisation is the voltage drop due to the physical resistance of gaseous species within the electrodes at a given current density. Unlike the derivation in [49], it is defined in terms of limiting current densities within both electrodes. Concentration polarisation affects cell performance at high current densities.

For this model, the solid cell component consists of both electrodes and the electrolyte, which is also referred to as the PEN structure. The temperature of the solid cell component is affected by net enthalpy flux into the cell, electrical energy exported from the cell to the external circuit, and forced convection either side of the cell wall. Enthalpy flux is defined as the product of the molar flux per unit area of a gaseous species into the cell surface and the gas enthalpy, which is approximated using a first-order polynomial ap-

proximation with respect to temperature. In the case of Water, the enthalpy is a function of T_{cell} rather than T_{fuel} since Water is produced within the cell. The electrical energy is defined by the power density produced by the cell. The heat-transfer coefficients are approximated by using an averaged approximation of the Nusselt number throughout the length of the cell for an external flow parallel to a plane surface. This is defined in terms of two other dimensionless parameters: the Prandtl number, and the Reynolds number. As it will be seen in the next chapter, the heat-transfer coefficient values are very different for both gas channels.

The cell temperature equation can be expressed as a difference between the amount of heat produced in the cell (net enthalpy flux, electrical energy) and the amount of heat removed by the cell (forced convection). As shown in [45, 46, 47, 49], for any value of the bifurcation parameter, the number of intersections for rising T_{cell} can be determined by the number of intersections of both curves.

Mass transfer and diffusion within a electrode take place in a layer within the electrode between the cell surface and the TPB known as the electrode diffusion layer. Mass conservation equations of Hydrogen, Oxygen and Water at the TPB are considered, where the molar flux terms into the cell surface are obtained by solving the steady-state diffusion equation within the electrode diffusion layer. The diffusion time scales of the three gaseous species are very small (of order 10^{-4}), so diffusion within the cell is assumed to be quasi-steady-state. There are two Boundary Conditions (BCs): a Dirichlet BC on the cell surface, and a Neumann BC at the TPB defined using Fick's law for bi-molecular diffusion.

When considering diffusion within the cell, effective diffusivity is assumed (where porosity and tortuosity are taken into account), and it is defined in terms of binary and Knudsen diffusion (unlike the diffusion coefficients in the concentration polarisation term which is just defined in terms of binary diffusion). Binary diffusion is defined using Fuller's

correlation where the diffusional volumes of gaseous species are considered, and Knudsen diffusion is defined via an expression from Chan et al. [75] which takes the mean pore radius of the electrode into account.

In the two gas channels, mass, energy and momentum transfer are considered. For mass transfer, there are conservation equations for both gas flows as a whole, and for individual gaseous species (namely Hydrogen and Oxygen). Net gain/loss in the gas channel is due to molar fluxes into/out of the cell. For energy transfer, the temperature of the gas flow is affected by forced convection on the cell wall and net enthalpy fluxes into the cell. For momentum transfer, the gas flow velocity is affected by the pressure gradient and net momentum fluxes into the cell. No viscosity or surface tension/stresses are assumed.

Additional performance parameters such as fuel utilisation, and voltage and electrical efficiency are also considered in this thesis, and are covered in Appendix A. Also covered in the Appendix is the Péclet number for heat and mass transfer (Appendix D). For the next chapter, a few different non-dimensional parameters are covered to see what gas flow dynamics are more dominant, and how they affect cell performance.

The steady-state model for each of the three modes of operation, plus the dynamic model of a SOFC operating under a constant external load are presented in this chapter. The steady-state model can be solved using the built-in MATLAB solver *fsolve*, but the whole steady-state profile, including location of any ignition and extinction points, have to be determined manually. The dynamic model can be solved using the built-in IVP solver *ode15s*, which is the only one suitable for solving a stiff DAE system of index 1. The results produced from this model will be presented in the next four chapters.

Chapter 4

Constant External Load: Base Case

4.1 Introduction

The steady-state behaviour of a SOFC operating under a constant external load for a given set of inlet parameter values (Appendix B) is investigated in this chapter. This chapter starts off by investigating the change in T_{cell} for decreasing values of R_{load}, plus a look into the region where three steady-state solutions exist. This is followed by a look into heat production and heat removal within the cell (for varying T_{cell}) for five different values of R_{load}. Since $\dot{T}_{\text{cell}}$ in equation (3.36) is defined in terms of the difference between heat production and heat removal within the SOFC, the expected value of $\dot{T}_{\text{cell}}$ for varying values of T_{cell} at time $t = 0$ s can also be calculated. By calculating $\dot{T}_{\text{cell}}$ at $t = 0$ s for varying values of T_{cell}, not only can we check the number of steady-state solutions of T_{cell} for each of the five different values of R_{load}, but also its expected stability.

The profile for T_{cell} will be compared with equivalent profiles from [47] and [49], highlighting the main differences between the different models, plus the effect of the heat-transfer coefficients on the heat-removal curve Q_{R}.

In this chapter, the effects of multiple steady-state behaviour on other cell performance parameters including V_{cell}, P_{cell}, polarisations, voltage efficiency and electrical efficiency will also be investigated. This is followed by a look into how important gas flow parameters (concentration, temperature and velocity) are affected by steady-state multiplicity. The final section in this chapter covers the non-dimensional parameters mentioned in the previous chapter to determine which gas flow properties are more dominant in each gas channel.

4.2 Operating Cell Temperature

In this section, the steady-state behaviour of the SOFC is looked into where the inlet parameters are based on the values in Appendix B. We will look at the change in T_{cell} for decreasing values of R_{load}, including the region where up to three steady-state solutions exist. The profile for T_{cell} is backed up with profiles of the heat production and heat removal curves for rising T_{cell} at five different values of R_{load}. The number of steady-state solutions at these five different values of R_{load} can be determined by looking at the number of intersections between the two curves. The stability of the steady-state solutions of T_{cell} will also be looked into for each of the five different values of R_{load}.

4.2.1 Cell Temperature vs Load Resistance

Figures 4.2.1 and 4.2.2 show the profile of T_{cell} for decreasing values of R_{load}. The first steady-state solution is obtained for $R_{\text{load}} = 1000\ \Omega$, so that full profiles of cell parameters such as V_{cell} and P_{cell} for rising current density can be obtained (in the region where i is very close to zero). There is no multiple steady-state behaviour for very high values of R_{load}.

Looking at figure 4.2.1, when the SOFC operates along the lower, un-ignited steady-state branch, T_{cell} rises very gradually initially for decreasing R_{load}. It only rises very sharply

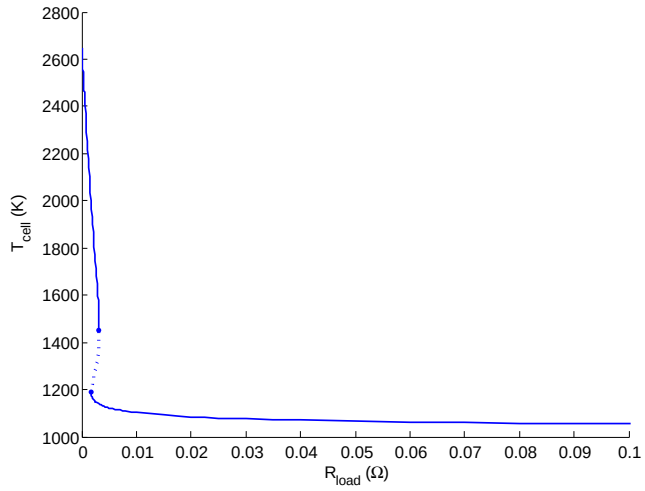

Figure 4.2.1: Cell Temperature profile for decreasing values of R_{load}. The operating cell temperature only rises sharply when R_{load} tends towards zero. The dashed curve represents the assumed unstable steady-state branch.

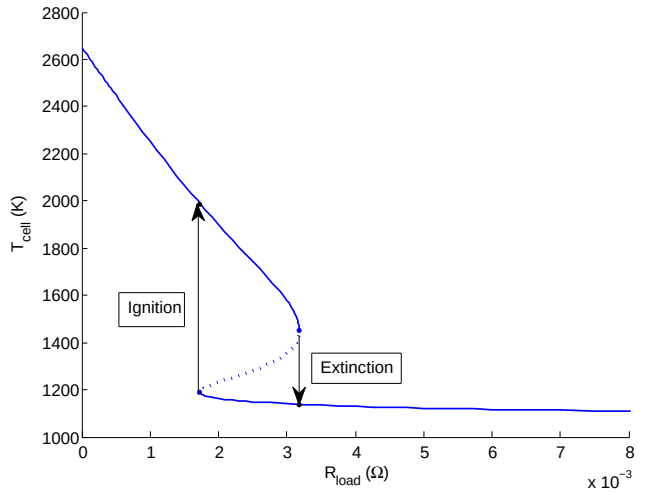

Figure 4.2.2: Zoom-in of the profile in figure 4.2.1, showing the location of the ignition and extinction states. The stable steady-state branches are represented by the thick blue curves, while the middle steady-state branch is represented by the dashed blue curve.

when R_{load} approaches very close to zero, where the multiplicity region exists (as shown by the dashed curve).

The multiplicity region is highlighted in figure 4.2.2, where the ignition and extinction states are also highlighted. For a SOFC operating along the lower, un-ignited steady-state branch, electrolyte conductivity increases along with rising T_{cell} (as R_{load} approaches the ignition point). This rise in T_{cell} causes a rise in current density, which in turn intensifies the electrochemical reaction rates, producing more heat at a localised spot within the cell. Since the temperature of the whole cell component is affected by the formation of "hot spots" within the cell, the hot spot is assumed to cover the whole cell component.

The ignition state is located at $R_{\text{load}} = 0.001732375\ \Omega$, where T_{cell} rises from around 1190 K to almost 1990 K: a rise of almost 800 K! 1990 K is too high an operating temperature for the components of the SOFC to operate on. The extinction point is located at $R_{\text{load}} = 0.00318746\ \Omega$, where T_{cell} drops from around 1450 K to just below 1140 K: a drop of just over 300 K. The multiplicity region is located for $R_{\text{load}} \in [0.001732375, 0.00318746]$, where three steady-state solutions exist. As can be seen in figure 4.2.2, if R_{load} is allowed to drop all the way down to zero, the SOFC will operate in excess of 2600 K.

In terms of making sure that the SOFC operates at a sensible operating temperature, it would be best if the SOFC operates along the lower, un-ignited steady-state branch only. There is also a significant region of the middle steady-state branch in which the SOFC can initially operate on where T_{cell} is not too high. However, as it will be seen in chapter 7, the middle steady-state branch is unstable, which means that the wrong change in value of R_{load} may lead to the SOFC operating along the ignited steady-state branch.

4.2.2 Heat Production and Removal

Since there is at least one value of T_{cell} associated with any value of R_{load}, the steady-state model in subsection F.1 can be simplified by making T_{cell} a constant parameter.

That means removing equation (F.4) from the steady-state model (while all the other equations remain the same), and setting T_{cell} as a constant parameter everywhere else. By choosing a fixed value of R_{load}, the system of steady-state equations can be solved for increasing values of T_{cell}, using the method described in subsection 3.6.1 (without any multiple solutions). In this model, there are two additional equations: one describing heat production in the cell (Q_{P}), and one describing heat removal in the cell (Q_{R}). The equations for Q_{P} and Q_{R} are given by equations (3.37) and (3.38) respectively.

This means that you can obtain a variety of different heat production and heat removal profiles with increasing T_{cell} for any fixed value of R_{load}. Also, since the cell temperature equation (3.36) is defined in terms of the difference between Q_{P} and Q_{R}, we can also obtain a variety of profiles of the expected value of $\dot{T}_{\text{cell}}$ at $t = 0$ s for varying T_{cell} for any fixed value of R_{load}. Profiles for heat production, heat removal and $\dot{T}_{\text{cell}}$ for varying T_{cell} are obtained for five different values of R_{load}: two where only one steady-state solution exists (one on the lower branch, the other on the upper branch), one where there are three steady-state solutions, one at the extinction point, and one at the ignition point. Not only will we clarify the number of solutions at each point of R_{load} by looking at the number of intersections between Q_{P} and Q_{R}, but we will also clarify the stability of the steady-state solutions of T_{cell} at each of the three steady-state branches.

Heat Production/Removal Profiles at $R_{\text{load}} = 0.005\ \Omega$

Figure 4.2.3 shows the relationship between the heat production curve Q_{P} and the heat removal curve Q_{R} for varying values of T_{cell}. The heat production term is defined in terms of the net enthalpy flux into the cell and the amount of electrical energy exported from the cell to the external circuit. The heat removal term is defined in terms of forced convection on the walls either side of the cell.

In figure 4.2.3, it can be seen that there is only one point of intersection between the two curves at a low value of T_{cell}. This intersection corresponds to the steady-state solution

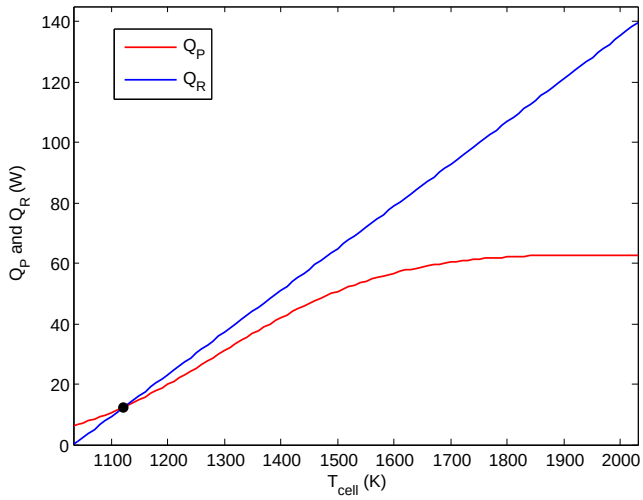

Figure 4.2.3: Profiles of the heat production curve Q_{P} and the heat removal curve Q_{R} for rising T_{cell} ($R_{\mathrm{load}} = 0.005\ \Omega$). The intersection point represents the steady-state solution of T_{cell}.

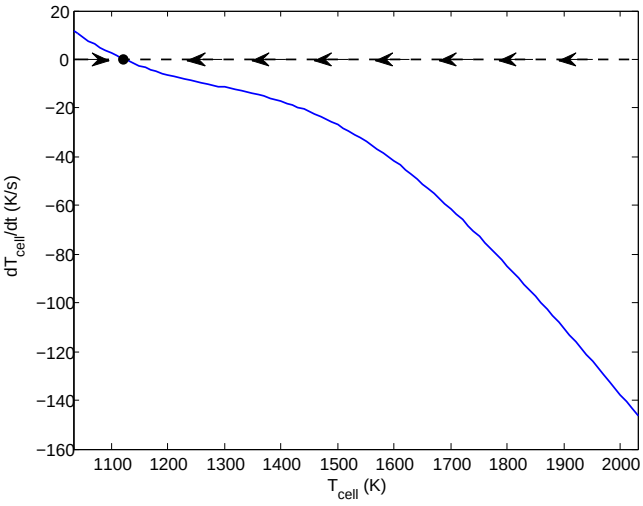

Figure 4.2.4: The profile of $\dot{T}_{\mathrm{cell}}$ for rising T_{cell} ($R_{\mathrm{load}} = 0.005\ \Omega$). This graph shows that the steady-state solution of T_{cell} at $R_{\mathrm{load}} = 0.005\ \Omega$ is stable.

of T_{cell} at $R_{\text{load}} = 0.005\ \Omega$ in figure 4.2.2, where $T_{\text{cell}} = 1122.389184145690$ K. So it is very likely that the point of intersection of the two curves is located at the steady-state solution of T_{cell} for $R_{\text{load}} = 0.005\ \Omega$.

Even though the heat-transfer coefficients are no longer assumed to be constant, the amount of heat removed by convection still appears to rise linearly with rising T_{cell}, starting from around zero when T_{cell} is equal to the inlet gas flow temperatures given in Appendix B. The heat production curve initially rises non-linearly with rising temperature due to the amount of heat produced from the electrochemical reactions. But the rise starts to level off near the end of the graph as mass transfer resistances within the electrode diffusion layer start to take a hold within the SOFC (especially with less Hydrogen being available for consumption at these temperatures). Eventually, Q_{P} will reach zero for a high enough value of T_{cell}.

If figure 4.2.3 validates the location of the steady-state solution of T_{cell} at $R_{\text{load}} = 0.005\ \Omega$, then figure 4.2.4 gives an insight into the stability of the steady-state solution of T_{cell}. At the same value of T_{cell} where Q_{P} and Q_{R} intersect, $\dot{T}_{\text{cell}} = 0$. For values of T_{cell} below 1122.389184145690 K, $\dot{T}_{\text{cell}} > 0$ at $t = 0$. This means that if the SOFC was switched on where the initial condition of T_{cell} is below 1122.389184145690 K, then T_{cell} would rise upwards towards that steady-state value. Similarly, if the initial condition of T_{cell} is above 1122.389184145690 K, then $\dot{T}_{\text{cell}} < 0$ at $t = 0$, which would mean that T_{cell} would drop towards that steady-state value when the SOFC is switched on. Since $\dot{T}_{\text{cell}} > 0$ for $T_{\text{cell}} < 1122.389184145690$ K, and $\dot{T}_{\text{cell}} < 0$ for $T_{\text{cell}} > 1122.389184145690$ K, the steady-state solution of T_{cell} at $R_{\text{load}} = 0.005\ \Omega$ is expected to be stable. This applies to any steady-state solution of T_{cell} along the un-ignited steady-state branch.

Heat Production/Removal profiles at $R_{\text{load}} = 0.00318746\ \Omega$

Figures 4.2.5 and 4.2.6 represent the profiles of Q_{P}, Q_{R} and $\dot{T}_{\text{cell}}$ respectively for R_{load} equal to the extinction point. Looking at figure 4.2.5, two things are evident. The first

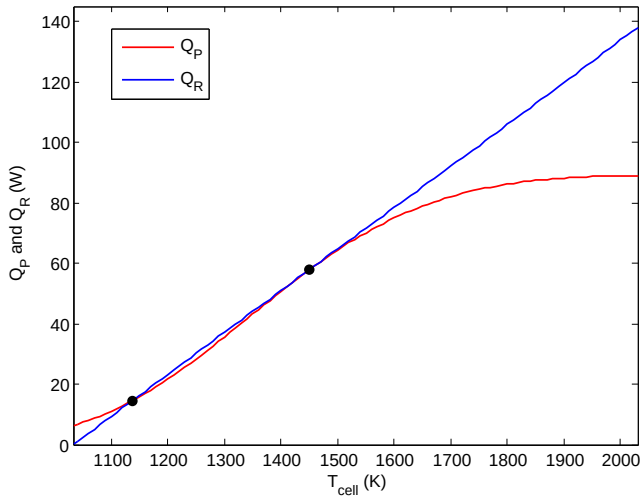

Figure 4.2.5: Profiles of the heat production curve Q_{P} and the heat removal curve Q_{R} for rising T_{cell} ($R_{\mathrm{load}} = 0.00318746\ \Omega$). At the extinction point, there are only two steady-state solutions.

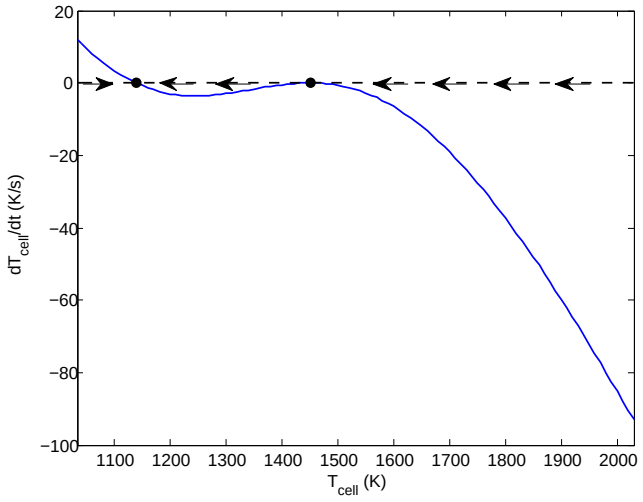

Figure 4.2.6: The profile of $\dot{T}_{\mathrm{cell}}$ for rising T_{cell} ($R_{\mathrm{load}} = 0.00318746\ \Omega$). The stability of the solution of T_{cell} at the extinction point requires more work.

thing being that the amount of heat removed by convection has dropped slightly, as shown on the right-hand side of figure 4.2.5 where Q_{R} is just less than 140 W (compared to figure 4.2.3 where Q_{R} is around 140 W). Secondly, there is a rise in the amount of heat produced in the cell for rising T_{cell}. This can be attributed to the lower value of R_{load} for this case. A drop in R_{load} causes an increase in electrochemical activity, which in turn increases the amount of heat produced in the cell. This means that there are two points in figure 4.2.5 at which both heat curves touch.

The first point in which Q_{P} and Q_{R} touch is located at the steady-state solution of T_{cell} on the lower, un-ignited steady-state branch. The value of T_{cell} at that point is around 1138.0996 K. The second point where Q_{P} and Q_{R} touch is located at the steady-state solution of T_{cell} at the extinction point (which represents one of the two turning points in figure 4.2.2). Q_{P} does not exceed Q_{R} after the second point of contact. T_{cell} at the extinction point is equal to 1450.6279 K.

It is quite difficult in figure 4.2.5 to determine the location of the second point of contact between Q_{P} and Q_{R}. This is shown more clearly in figure 4.2.6, where it clearly shows both points in which $\dot{T}_{\mathrm{cell}}$ is equal to zero. This suggests that the lower steady-state solution of T_{cell} is stable, just like the steady-state solution of T_{cell} in figure 4.2.3. However, the stability of the steady-state solution of T_{cell} at the extinction point is much more difficult to determine. If T_{cell} is below 1450.6279 K (but above 1138.0996 K), then $\dot{T}_{\mathrm{cell}}$ will be less than zero at time $t = 0$ s. This means that when the SOFC is switched on, you would expect T_{cell} to move down towards the steady-state solution of T_{cell} on the un-ignited branch. Also, $\dot{T}_{\mathrm{cell}}$ at $t = 0$ s is less than zero for values of T_{cell} above 1450.6279 K. But when the SOFC is switched on, it is not guaranteed that T_{cell} will tend towards that value as $t \to \infty$.

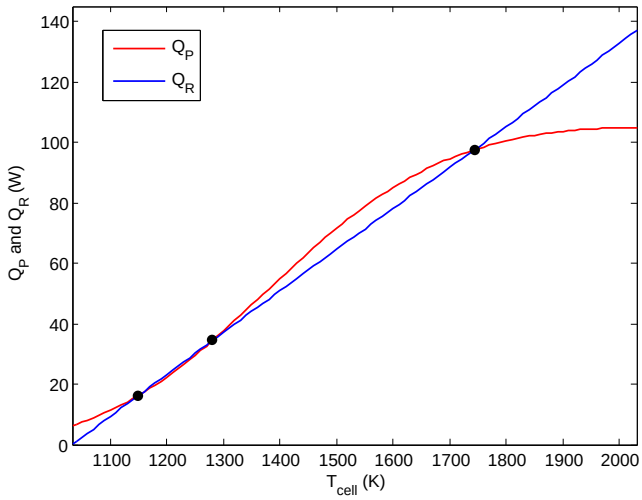

Figure 4.2.7: Profiles of the heat production curve Q_{P} and the heat removal curve Q_{R} for rising T_{cell} ($R_{\mathrm{load}} = 0.0025\ \Omega$). There are three possible steady-state solutions for T_{cell}.

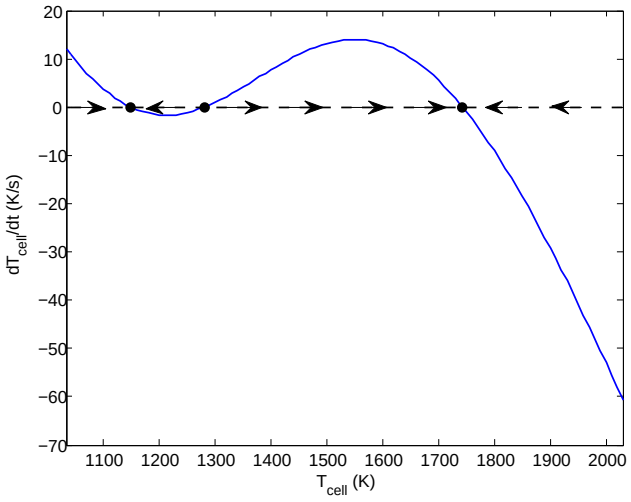

Figure 4.2.8: The profile of $\dot{T}_{\mathrm{cell}}$ for rising T_{cell} ($R_{\mathrm{load}} = 0.0025\ \Omega$). Two of the steady-state solutions are stable, while the one in the middle is unstable.

Heat Production/Removal profiles at $R_{\mathbf{load}} = 0.0025\ \Omega$

At this value of R_{load}, three steady-state solutions exist. The three values of T_{cell} where Q_{P} and Q_{R} intersect in figure 4.2.7 represent the three possible steady-state solutions of T_{cell}. While the amount of heat removed by convection decreases slightly in comparison to Q_{R} in figure 4.2.5, the amount of heat produced now starts to exceed 100 W for rising T_{cell}. This is due to a further increase in electrochemical activity as a result of the drop in R_{load}. The value of T_{cell} along the lower, un-ignited steady-state branch is equal to 1148.7991 K. The value of T_{cell} on the middle steady-state branch is equal to 1280.8338 K. The value of T_{cell} along the upper, ignited steady-state branch is equal to 1743.2807 K.

This is clarified further in figure 4.2.8, which suggests that the two extreme steady-state solutions of T_{cell} are stable. But this is not the case for the steady-state solution of T_{cell} in the middle. For values of T_{cell} between 1148.7991 K and 1280.8338 K, $\dot{T}_{\text{cell}} < 0$ at $t = 0$ s, which means that T_{cell} is expected to move away from the steady-state solution on the middle branch towards the steady-state solution of T_{cell} on the un-ignited branch when the SOFC is switched on. Similarly, $\dot{T}_{\text{cell}} > 0$ at $t = 0$ s for values of T_{cell} between 1280.8338 K and 1743.2807 K, which means that T_{cell} is expected to move towards the steady-state solution of T_{cell} on the ignited branch when the SOFC is switched on. This suggests that the steady-state solution of T_{cell} on the middle branch is unstable.

Heat Production/Removal profiles at $R_{\mathbf{load}} = 0.001732375\ \Omega$

$R_{\text{load}} = 0.001732375\ \Omega$ represents the location of the ignition point. The steady-state solution of T_{cell} at that point is located at the first point of contact of Q_{P} and Q_{R} (figure 4.2.9). The rise in Q_{P} for lower values of T_{cell} (due to a further increase in electrochemical activity) combined with a further drop in Q_{R} leads to the situation where the two curves no longer cross each other at a low value of T_{cell}.

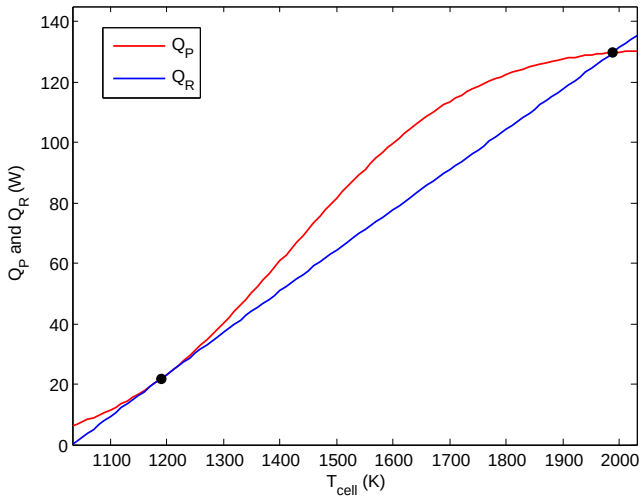

Figure 4.2.9: Profiles of the heat production curve Q_{P} and the heat removal curve Q_{R} for rising T_{cell} ($R_{\mathrm{load}} = 0.001732375\ \Omega$). The first point of contact is located at the ignition point.

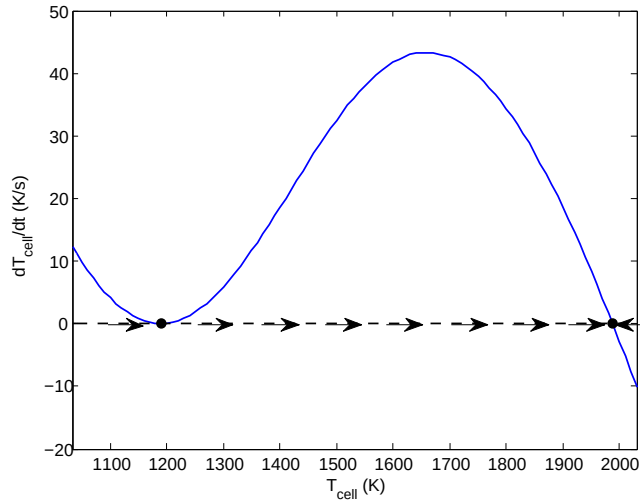

Figure 4.2.10: The profile of $\dot{T}_{\mathrm{cell}}$ for rising T_{cell} ($R_{\mathrm{load}} = 0.001732375\ \Omega$). The first steady-state solution of T_{cell} represents a turning point.

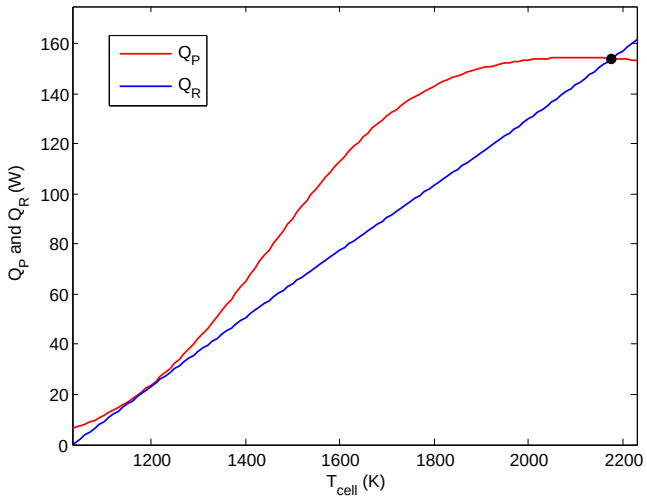

Figure 4.2.11: Profiles of the heat production curve Q_{P} and the heat removal curve Q_{R} for rising T_{cell} ($R_{\mathrm{load}} = 0.0012\ \Omega$). There is only one point of intersection at a very high value of T_{cell}.

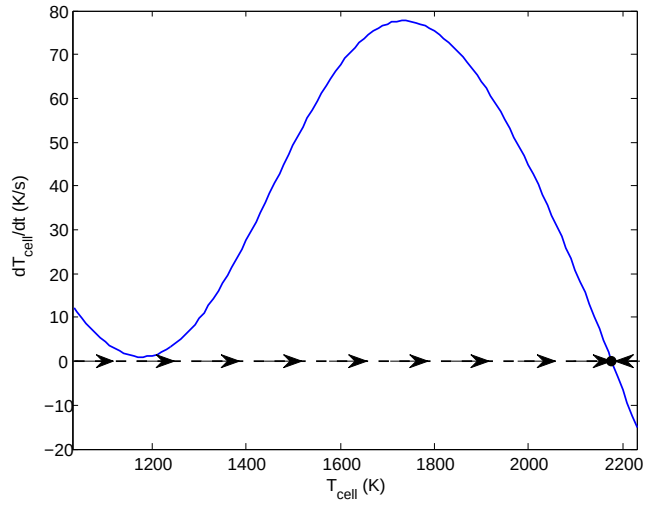

Figure 4.2.12: The profile of $\dot{T}_{\mathrm{cell}}$ for rising T_{cell} ($R_{\mathrm{load}} = 0.0012\ \Omega$). There is only one stable steady-state solution.

There are two steady-state solutions of T_{cell} at this point of R_{load}. The first steady-state solution (located at the ignition point) is equal to 1189.537 K. Since this is located at the ignition point, this represents a turning point, as seen by the direction of $\dot{T}_{\text{cell}}$ below and above that point (figure 4.2.10). For values of T_{cell} just above that point, the solution is expected to be unstable. However, for values of T_{cell} just below that point, it is not guaranteed that the solution is stable. More work is needed to determine the stability of that point.

The intersection occurs just before Q_{P} reaches its peak, which is around 130 W. The value of T_{cell} at that point of intersection is 1987.8753 K. Figure 4.2.10 suggests that this particular steady-state solution is stable. For values of R_{load} lower than this point, only one steady-state solution will exist where T_{cell} operates along the upper, ignited steady-state branch.

Heat Production/Removal profiles at $R_{\text{load}} = 0.0012\ \Omega$

At this point of R_{load}, there is only one point of intersection between the two curves in figure 4.2.11. This occurs just after Q_{P} reaches its peak (in excess of 150 W), where the steady-state solution of T_{cell} is equal to 2177.0578 K. On figure 4.2.11, it looks like the two curves are touching each other at a lower value of T_{cell}. But, as figure 4.2.12 testifies, there is a very small gap between the two curves, and $\dot{T}_{\text{cell}}$ does not equal zero in the region where the local minimum of $\dot{T}_{\text{cell}}$ is located. This suggests that the sole steady-state solution located on the upper, ignited steady-state branch is stable.

4.3 Comparison with previous works

Figures 4.3.1 and 4.3.2 show the equivalent T_{cell} profiles for decreasing values of R_{load}, including the multiplicity region.

The inlet parameters for both models in the production of these profiles are the same, except for the inlet gas flow temperatures. The inlet gas flow temperatures used for the

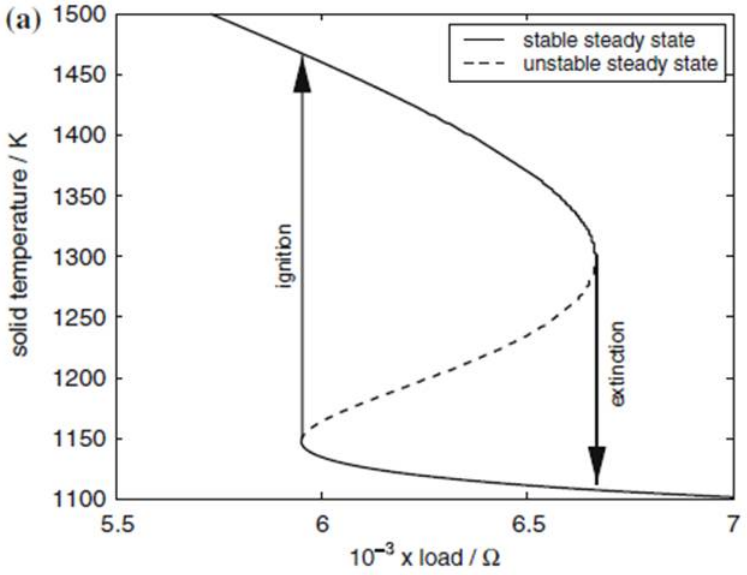

Figure 4.3.1: The cell temperature profile for decreasing values of R_{load} in [47]. The inlet gas flow temperatures in [47] are set at 980 K.

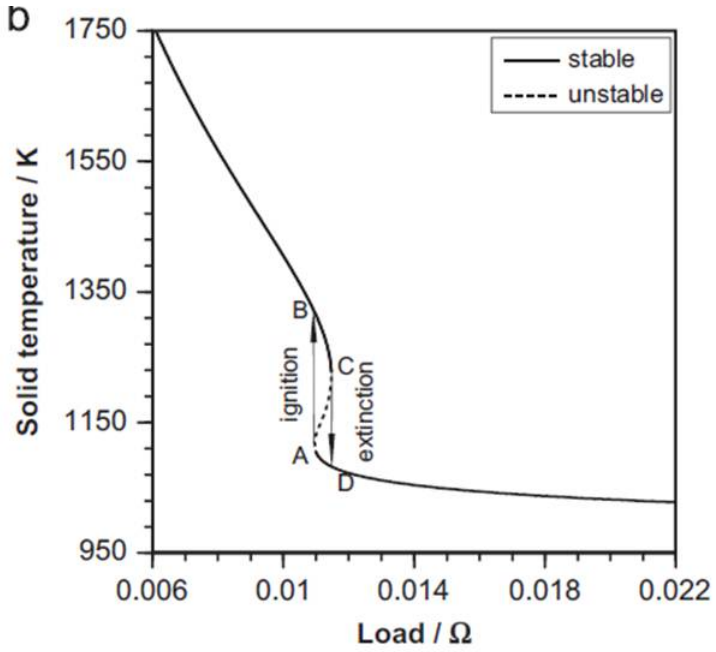

Figure 4.3.2: The cell temperature profile for decreasing values of R_{load} in [49]. The inlet gas flow temperatures in [49] are set at 950 K.

production of figure 4.3.1 in [47] is 980 K, while the inlet gas flow temperatures used for the production of figure 4.3.2 in [49] is 950 K. If the inlet gas flow temperatures were equal to 980 K in the model in [49], the operating cell temperature would just rise sharply as $R_{\text{load}} \to 0$, with no multiplicity region present in the profile.

Comparing the profile in figure 4.2.2 with the profiles from [47] and [49], the profile is more closer to the profile in [47] in terms of where the multiplicity region is located. One of the main reasons for this is due to the amount of heat removed by convection in all three models. In all three models, the definition of Q_{R} is the same. But there are differences in terms of which parameters in Q_{R} are kept constant in all three models.

In [47], the lumped-parameter model only consists of only four equations, modelling cell voltage, activation overpotentials in the Anode and the Cathode, and cell temperature. A lot of other parameters, including gas flow composition, temperature, velocity as well as the heat-transfer coefficients are assumed to be constant. The only variable that exists in Q_{R} is the solid cell temperature. The model in [49] is much more detailed than the model in [47], where the gas flow temperatures are assumed to be variables in Q_{R} as well. But the heat-transfer coefficients are still assumed to be constant (and of the same value) in [49].

Gas flow temperatures do rise with decreasing R_{load}, and according to [49], they rise linearly with rising cell temperature (where T_{cell} is constant along with R_{load}). This means that the amount of heat removed from the cell in the model from [49] is lower than the amount of heat removed from the cell in the model from [47]. The gap between the operating cell temperature and the gas flow temperatures does not grow as quickly for increasing cell temperature in [49] compared to [47].

Since the heat removal curve in [47] is steeper, R_{load} has to be dropped to enable the cell to operate at a higher operating temperature. The consequence of this is that the multiplicity region is located towards lower values of R_{load}. The multiplicity region is

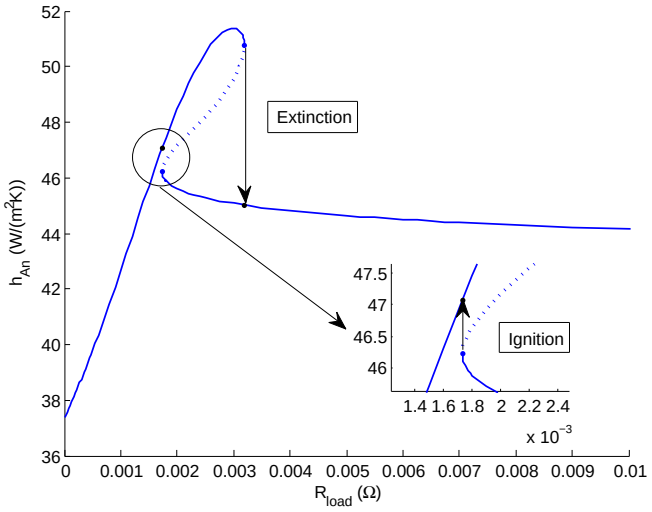

Figure 4.3.3: Profile of the Anode-side heat-transfer coefficient h_{An} for decreasing values in R_{load}, with the ignition state zoomed-in on the bottom L.H.S. of the graph.

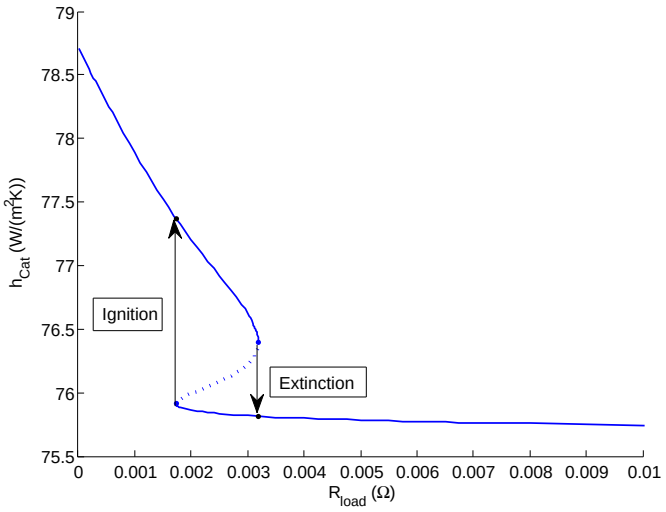

Figure 4.3.4: Profile of the Cathode-side heat-transfer coefficient h_{Cat} for decreasing values in R_{load}.

expected to be larger because the amount of heat produced from the cell at values of R_{load} as low as 6×10^{-3} Ω is going to be larger than the amount of heat produced from the cell if R_{load} is equal to values around 0.012 Ω. Plus the change in temperature after ignition is also expected to be larger since the rise in Q_{P} for low values of T_{cell} has to be much sharper to avoid contact with a steeper Q_{R} curve, with the sole point of intersection occurring at a higher value of T_{cell}.

The same thing can be said about the location of the multiplicity region in figure 4.2.2. In this model, all the parameters in Q_{R} are not constant, including the heat-transfer coefficients. The heat-transfer coefficients are defined in terms of the averaged Nusselt number over the length of the cell (for forced convection of an external flow over a parallel plate). The length scales in the heat-transfer coefficient and the gas flow Reynolds number are defined in terms of the cell length L. With this, the values of the heat-transfer coefficient are larger than 25 W/(m$^2 \cdot$ K) as shown in figures 4.3.3 and 4.3.4. h_{An} can reach as high as over 50 W/(m$^2 \cdot$ K) along the ignited steady-state branch, while h_{Cat} is in the range between 75–80 W/(m$^2 \cdot$ K). The large values of h_{An} and h_{Cat} is mainly due to the Reynolds number of both gas flows (see section 4.7).

Due to the larger values of h_{An} and h_{Cat} compared to [49] and [47], the amount of heat removed by convection in this model is larger than the amount of heat removed in the models from [47] and [49]. Looking at figures 4.3.5 and 4.3.6, where the inlet parameters are the same, and the value of R_{load} is the same, Q_{R} is much steeper in this model compared to the one in [49]. For cell temperature values up to 1480 K, the heat removal curve in figure 4.3.5 barely reaches over 30 W. However, in figure 4.3.6, the amount of heat removed from the cell already reaches close to 70 W. The amount of heat produced by the cell is about the same in both profiles.

For inlet parameter values set equal to the inlet parameter values in [47] and [49], where the inlet gas flow temperatures are equal to 980 K, T_{cell} in this model does not rise

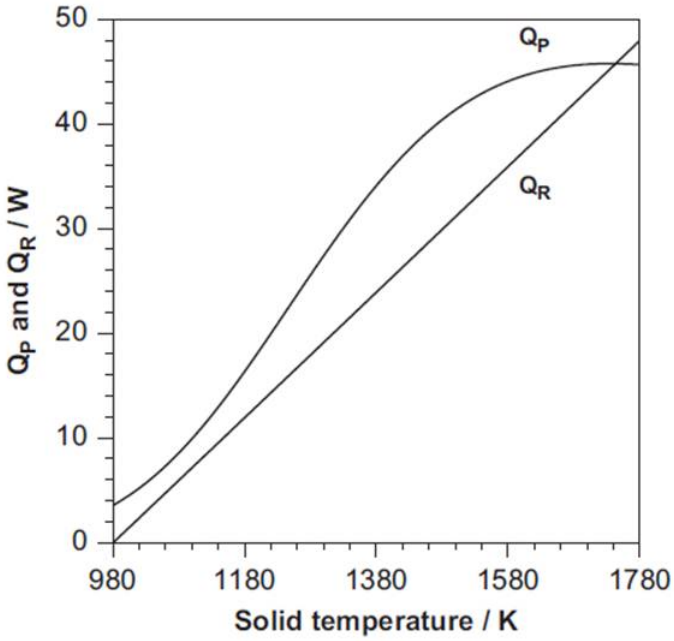

Figure 4.3.5: The heat production and heat removal curves for a SOFC in the model from [49]. The inlet gas temperatures are equal to 980 K, and $R_{\text{load}} = 0.0065\ \Omega$.

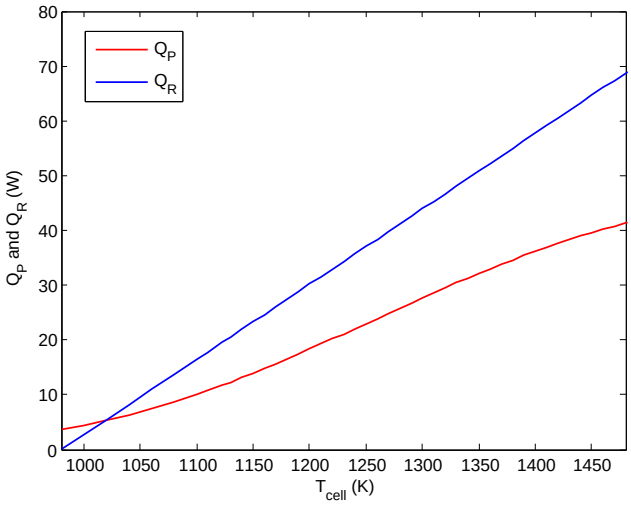

Figure 4.3.6: The equivalent heat production/removal profile from this model to the one in figure 4.3.5. The heat removal curve is a lot steeper.

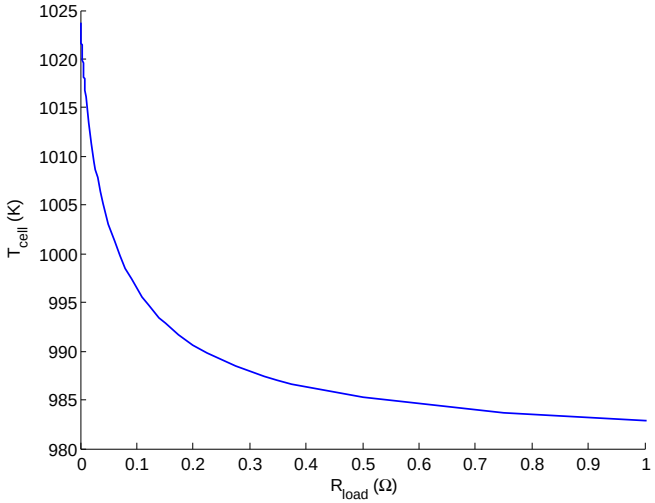

Figure 4.3.7: Profile of T_{cell} for decreasing R_{load}, where the inlet parameters are the same as the ones in [47] and [41].

that sharply at all for positive values of R_{load}. Even when R_{load} is equal to zero, T_{cell} barely reaches 1025 K, which is only an increase of about 45 K from the inlet gas flow temperatures (figure 4.3.7).

Increasing the inlet gas flow temperatures in this model from the values set in [47] and [49] has the consequence of moving the multiplicity region (including the ignition and extinction points) towards positive values of R_{load}. Removing it altogether would require a further increase in the inlet gas flow temperatures. Other inlet parameters can also be modified to remove the multiplicity region (see the next chapter).

4.4 Cell Voltage and Polarisations

Figures 4.4.1 and 4.4.2 represent the profiles for V_{cell} and the cell polarisations with increasing current density. The polarisations within the cell cover the area between the actual cell voltage V_{cell}, and the open circuit voltage E in figure 4.4.1. E drops with in-

creasing i due to increasing T_{cell}, and mass transfer limitations at high values of i. There is a very sharp drop in V_{cell} for low current density values due to a combination of activation and Ohmic polarisation effects (see figure 4.4.2). Activation polarisation effects are more dominant at very low values of i, where both activation polarisation terms rise very sharply for very low values of i. Ohmic Polarisation effects are stronger for slightly higher values of i, as shown by the η_{Ohm} curve overtaking the $\eta_{\text{act}}^{\text{Cat}}$ curve before turning downwards.

However, as the cell approaches the ignition state for decreasing values of R_{load}, V_{cell} starts to rise slightly as specific Ohmic resistivity starts to drop with increasing T_{cell} (which in turn intensifies the reaction rates, causing the SOFC to ignite). At the ignition point, the current density i is equal to 1.0989 A/cm^2, and V_{cell} is equal to 0.03046 V. After ignition, V_{cell} rises up to 0.2401 V and operates at a value of 8.6622 A/cm^2 for i. The extinction point is located at $i = 3.4092$ A/cm^2, where $V_{\text{cell}} = 0.1739$ V. After extinction, $V_{\text{cell}} = 0.03762$ V at $i = 0.7376$ A/cm^2.

Moving past the assumed unstable steady-state branch in the middle, V_{cell} increases for rising values of i, as more and more Hydrogen is converted to Water within the SOFC. Eventually for large enough values of i, V_{cell} will move towards zero due to the continuous decrease in the open circuit voltage E with increasing i. E falls more sharply as V_{cell} tends towards zero (see figure 4.4.1) due to concentration polarisation effects, which rises slightly for increasing i (see figure 4.4.2) as V_{cell} tends towards zero. The Anode activation polarisation term $\eta_{\text{act}}^{\text{An}}$ is still quite large when $V_{\text{cell}} = 0$ V, which means that there is still a bit of a delay in the activation of the oxidation reaction (3.1) at high current density values.

After ignition, $\eta_{\text{act}}^{\text{An}}$ drops from 0.3795 V to 0.2623 V, $\eta_{\text{act}}^{\text{Cat}}$ drops from 0.2341 V to 0.0217 V, η_{Ohm} drops from 0.3412 V to 0.0831 V, and η_{conc} rises from 0.0009374 V to 0.005607 V. $\eta_{\text{act}}^{\text{Cat}}$ drops down gradually towards zero for increasing values of i, due to a quicker

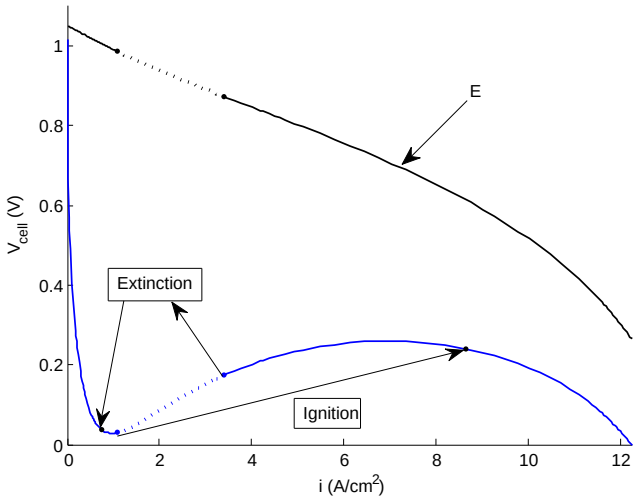

Figure 4.4.1: The V-I profile for a SOFC operating under a constant external load, along with the ignition and extinction states, and the open circuit voltage E.

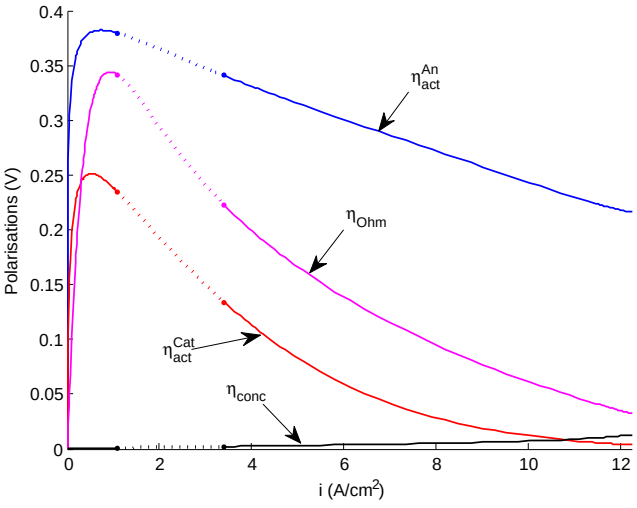

Figure 4.4.2: The polarisation curves of a SOFC operating under a constant external load.

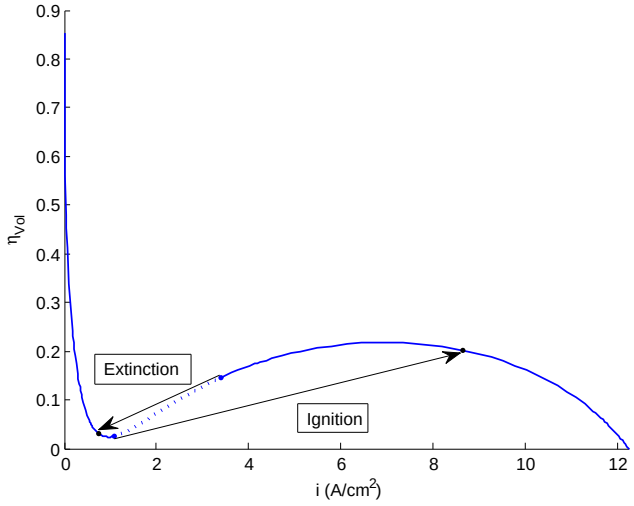

Figure 4.4.3: The profile of voltage efficiency η_{Vol} with rising current density.

activation of the reduction reaction (3.2). Ohmic polarisation also gradually drops down towards zero due to the rise in electrolyte conductivity with increasing T_{cell} (as a consequence of the increased electrochemical activity along the ignited steady-state branch). The Anode activation polarisation curve is higher than the Cathode activation polarisation curve since the oxidation reaction in the Anode is dependent on the presence of Oxygen ions from the reduction reaction.

Figure 4.4.3 represents the voltage efficiency profile (its definition is given in Appendix C). During the ignition phase, η_{Vol} jumps up from 2.558 % to 20.167 %, while in the extinction phase, η_{Vol} drops from 14.604 % to 3.1596 %. The profile for η_{Vol} is the same as V_{cell}, only except V_{cell} is divided by the ideal open circuit voltage (which is the open circuit voltage at standard conditions).

4.5 Power Density and Electrical Efficiency

In this section, the power density P_{cell} of the SOFC, and the electrical efficiency η_{el} of the SOFC for varying values of i are considered (η_{el} is defined in Appendix C). Figures 4.5.1 and 4.5.2 represent the profiles of P_{cell} and η_{el} respectively. At the bottom left-hand corner of figure 4.5.1, there is a small rise in the power density P_{cell} along the lower, un-ignited steady-state branch with increasing i. This is followed by a small drop due to mass transfer limitations as R_{load} moves closer to the ignition point.

But, just before R_{load} reaches the ignition point, the increase in electrolyte conductivity, and the increase in electrochemical activity causes V_{cell} to rise along with increasing i. This in turn causes P_{cell} to rise more sharply. After ignition, P_{cell} jumps from 0.0335 W/cm^2 to 2.0798 W/cm^2, which is close to the maximum obtainable power density (according to figure 4.5.1). The intensification of the reaction kinetics, and the increase in V_{cell} with increasing i causes P_{cell} to increase up towards a new peak, only going back down towards zero as mass transfer limitations take effect. During the extinction phase, P_{cell} drops from 0.5928 W/cm^2 down to 0.0277 W/cm^2.

The profile for electrical efficiency η_{el} in figure 4.5.2 is of the same shape as the power density profile in figure 4.5.1. It is defined in terms of the ideal thermodynamic efficiency of the cell, the voltage efficiency, and fuel utilisation (see Appendix C for the definition of these parameters). So the equation is very similar to the equation for P_{cell}. During ignition, η_{el} jumps up from 0.1585 % to 9.8497 %, which is close to the peak electrical efficiency of the cell. During extinction, η_{el} drops from 2.8074 % to 0.1314 %.

Electrical efficiency is low along the un-ignited steady-state branch since not enough fuel is consumed within the SOFC when it operates on that branch. It is only after ignition in which there is a notable rise in electrical efficiency as more fuel is utilised within the cell (thanks to higher electrochemical activity). In the next chapter, the effects of changing

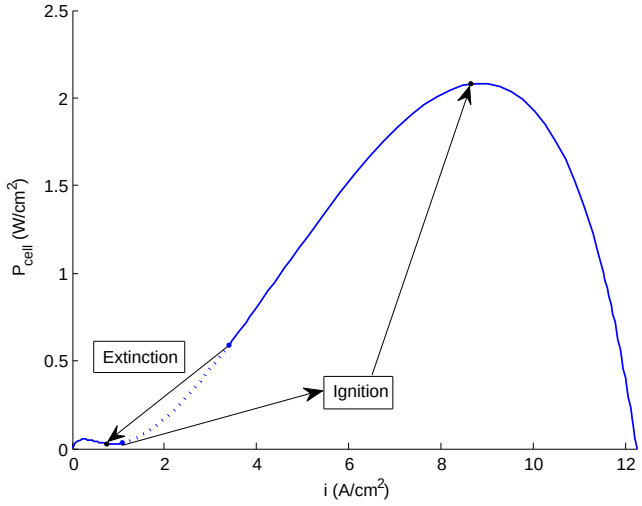

Figure 4.5.1: The P-I profile for a SOFC operating under a constant external load, along with the ignition and extinction states.

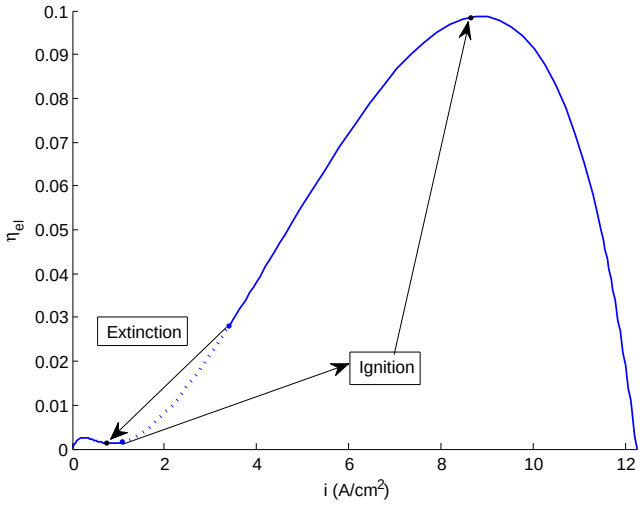

Figure 4.5.2: The electrical efficiency profile of a SOFC operating under a constant external load.

the inlet gas flow velocities and molar flow rates on power density and fuel utilisation (and subsequently, electrical efficiency) will be covered.

4.6 Gas Flow Properties

4.6.1 Gas Flow Concentration

Figures 4.6.1 and 4.6.2 represent the profiles of the bulk fuel flow concentration $C^{\mathrm{b}}_{\mathrm{fuel}}$ in the fuel channel and the bulk air flow concentration $C^{\mathrm{b}}_{\mathrm{air}}$ in the air channel for decreasing values of R_{load}. Even though both profiles have a quite similar shape, there is a larger decrease in fuel levels in the fuel cell compared to air levels as R_{load} is dropped (especially after ignition). This is mainly due to the larger consumption rates associated with the oxidation reaction (3.1) in the Anode compared to the reduction reaction (3.2) in the Cathode. Also, the Water produced from reaction (3.1) does not fully replace the Hydrogen that is consumed within the cell (mass transfer resistances within the Anode may also have a small effect).

After ignition, $C^{\mathrm{b}}_{\mathrm{fuel}}$ drops from 11.0187 mol/m^3 to 7.3243 mol/m^3 , while $C^{\mathrm{b}}_{\mathrm{air}}$ drops from 11.874 mol/m^3 to 11.1304 mol/m^3. Even though the drop in $C^{\mathrm{b}}_{\mathrm{air}}$ is not as great, there is more of a sharper drop as R_{load} approaches zero, since the Oxygen in the air flow is not replaced by anything. After extinction, $C^{\mathrm{b}}_{\mathrm{fuel}}$ rises from 9.4943 mol/m^3 to 11.3533 mol/m^3, while $C^{\mathrm{b}}_{\mathrm{air}}$ rises from 11.623 mol/m^3 to 11.9244 mol/m^3.

4.6.2 Mole Fractions

Figures 4.6.3-4.6.5 show the mole fraction profiles of Hydrogen, Water and Oxygen respectively, while figure 4.6.6 shows the profile of I for decreasing values of R_{load}. As shown in figure 4.6.1, even though any Hydrogen consumed in the reaction is replaced by Water, there is still an overall drop in $C^{\mathrm{b}}_{\mathrm{fuel}}$ after ignition. During ignition, $y_{\mathrm{H_2}}$ goes down from 0.8345 to 0.3833. This means that the overall concentration of Hydrogen in the bulk gas

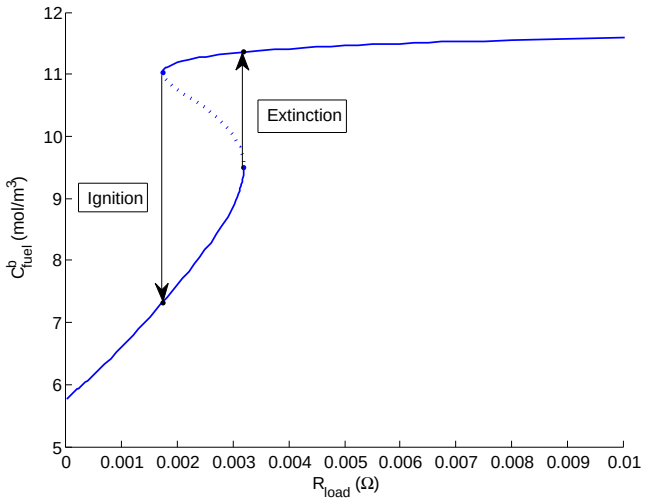

Figure 4.6.1: The profile for $C^{\mathrm{b}}_{\mathrm{fuel}}$ for decreasing values of R_{load}, including the ignition and extinction states.

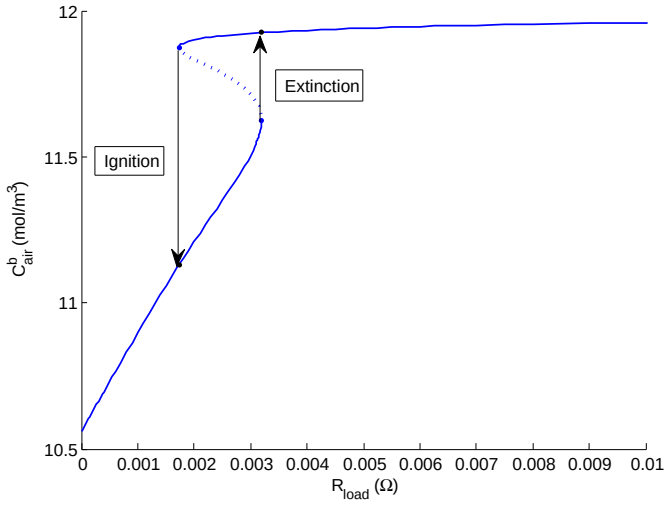

Figure 4.6.2: The profile for $C^{\mathrm{b}}_{\mathrm{air}}$ for decreasing values of R_{load}, including the ignition and extinction states.

flow drops from 9.1945 mol/m^3 to 2.8074 mol/m^3. The mole fraction of Water increases from 0.1655 to 0.6167 after ignition, but the concentration of Water in the bulk gas flow only rises from 1.8241 mol/m^3 to 4.5169 mol/m^3 after ignition.

As for Oxygen, its mole fraction drops from 0.199 to 0.1924 after ignition, which is a very small drop. This means that the concentration of Oxygen in the bulk gas flow only drops from 2.3634 mol/m^3 to 2.1411 mol/m^3 during the ignition phase. During the extinction phase, the mole fraction of Hydrogen rises from 0.6966 to 0.856 (the concentration of Hydrogen goes up from 6.6141 mol/m^3 to 9.7184 mol/m^3); the mole fraction of Water drops from 0.3034 to 0.144 (the concentration of Water drops from 2.8803 mol/m^3 to 1.6349 mol/m^3); and the mole fraction of Oxygen goes up from 0.197 to 0.1994 (the concentration of Oxygen goes up from 2.2899 mol/m^3 to 2.3772 mol/m^3).

Since the consumption rates of Hydrogen and Oxygen and the production rate of Water are defined in terms of the cell current I, it is no surprise to find that the shape of the profiles in figures 4.6.3-4.6.5 are very similar to the shape of the Cell current profile in figure 4.6.6. During ignition, I rises from 17.5823 A to 138.595 A, while during extinction, I drops from 54.5487 A to 11.8017 A.

Since fuel utilisation U_f is defined in terms of the consumption rate of Hydrogen (see Appendix C), U_f rises from 6.555 % to 51.671 % during ignition, and drops from 20.337 % to 4.3999 % during extinction. The amount of current that can be drawn from the cell before R_load reaches zero mainly depends on the amount of Hydrogen available in the fuel channel for consumption. This can be done by modifying $u^\mathrm{in}_\mathrm{fuel}$ and $\dot{N}^\mathrm{in}_\mathrm{fuel}$. The effects of both of these parameters on SOFC performance is shown on the next chapter.

4.6.3 Gas Flow Temperatures

Figures 4.6.7 and 4.6.8 show the profiles of T_fuel and T_air respectively for decreasing values of R_load. In terms of shape, the profiles of the gas flow temperatures are similar to the

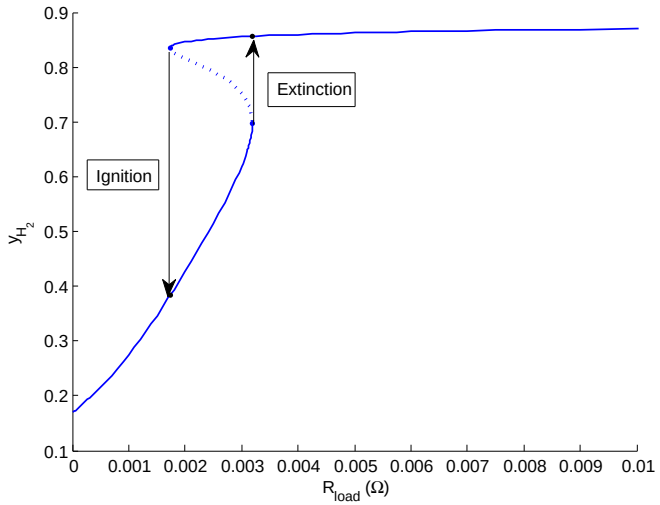

Figure 4.6.3: The profile for $y_{\mathrm{H_2}}$ for decreasing values of R_{load}, including the ignition and extinction states.

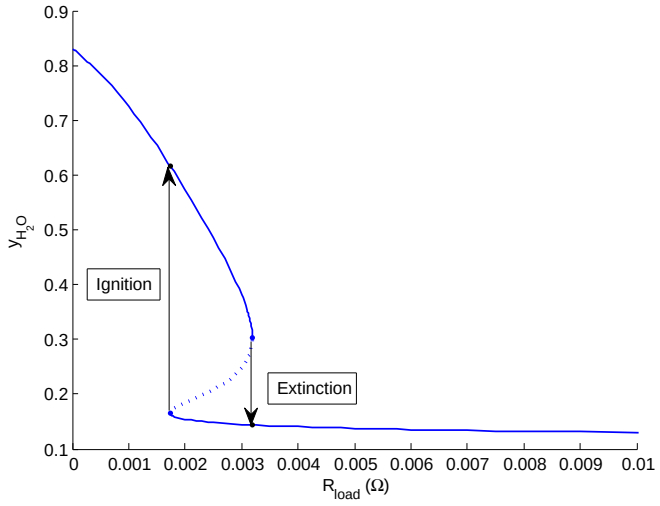

Figure 4.6.4: The profile for $y_{\mathrm{H_2O}}$ for decreasing values of R_{load}, including the ignition and extinction states.

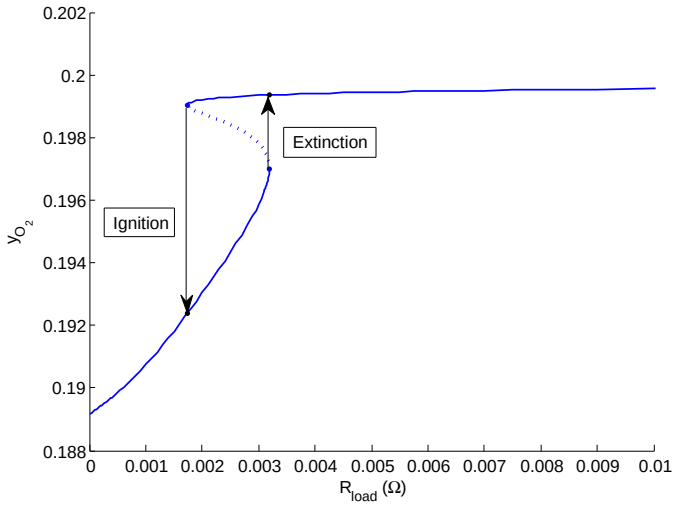

Figure 4.6.5: The profile for y_{O_2} for decreasing values of R_{load}, including the ignition and extinction states.

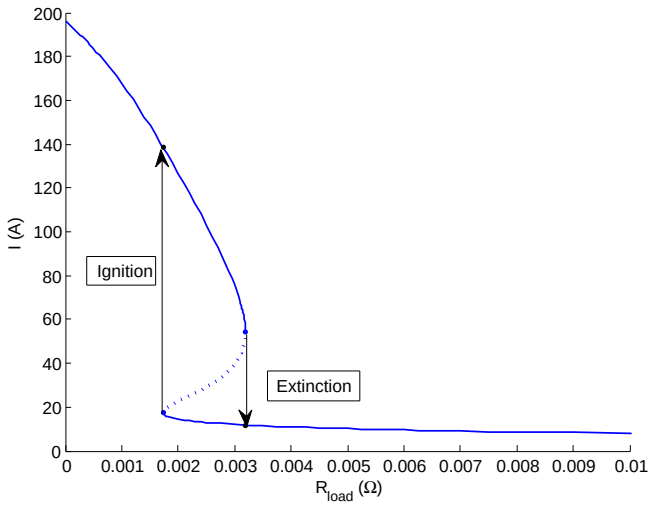

Figure 4.6.6: The profile for Cell current I for decreasing values of R_{load}, including the ignition and extinction states.

profile of T_{cell} in figure 4.2.2, only except that they do not go up at the same rate. Gas flow temperatures are affected by the net enthalpy flux into the cell, and the amount of heat transferred from the cell into the gas flow due to forced convection upon the cell walls.

T_{fuel} rises a lot further than T_{air} (especially along the ignited steady-state branch). Both gas flow temperatures rise due to convective effects (especially in the air flow, where the gas flow velocity is much higher). But in the fuel flow, more heat is transferred from the cell to the fuel flow via the enthalpy flux of Water from the cell to the bulk gas flow. The enthalpy of Water in the enthalpy flux term is a function of T_{cell} since it is produced within the cell. In the air flow, there is nothing from the reduction reaction to replace any of the Oxygen consumed within that reaction.

During the ignition phase, T_{fuel} rises from 1131.185 K to 1701.757 K (a rise of about 570 K), while T_{air} rises from 1046.1698 K to 1114.654 K (a rise of almost 70 K only). During the extinction phase, T_{fuel} drops from 1312.799 K to 1097.847 K (a drop of over 300 K), while T_{air} drops from 1068.321 K to 1041.832 K (a drop of nearly 30 K). Due to the huge difference between the two gas flow velocities (and the larger difference between T_{cell} and T_{air} compared to T_{cell} and T_{fuel}), it will be shown in the next chapter that modifying $T_{\text{air}}^{\text{in}}$ has more of an impact on cell performance compared to modifying $T_{\text{fuel}}^{\text{in}}$.

4.6.4 Gas Flow Velocities

Figures 4.6.9 and 4.6.10 show the profiles of u_{fuel} and u_{air} respectively for decreasing values of R_{load}. Unlike the models in [47] and [49], gas flow velocities are no longer assumed to be constant, so we can now observe how gas flow velocities are affected by steady-state multiplicity.

At a first glance, along the lower, un-ignited steady-state branch, there is hardly any change in the gas flow velocities at all. There is only a small rise in both gas flow

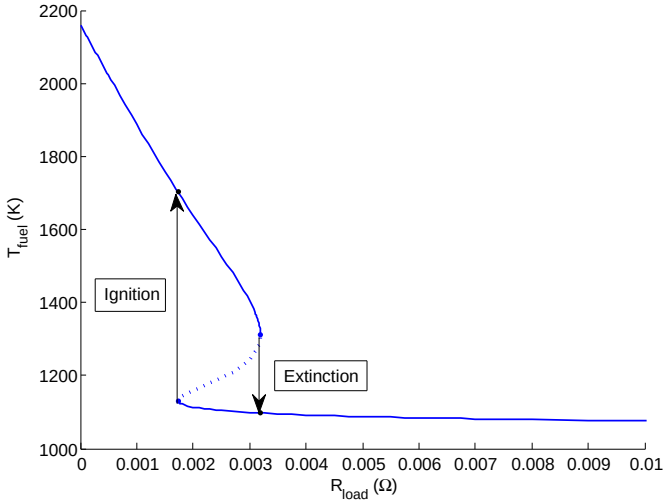

Figure 4.6.7: The profile for T_{fuel} for decreasing values of R_{load}, including the ignition and extinction states.

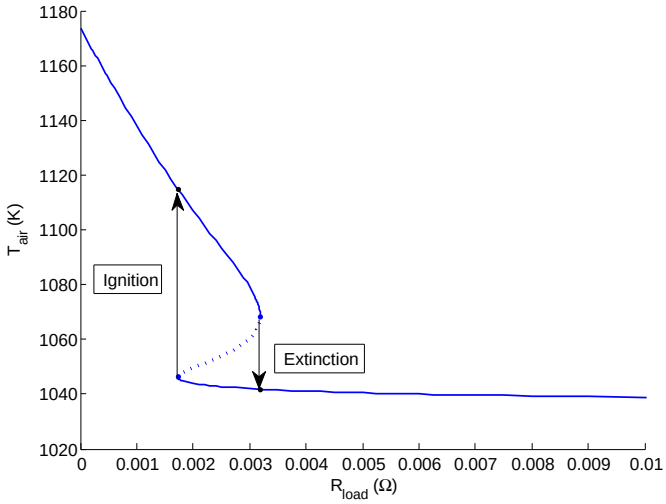

Figure 4.6.8: The profile for T_{air} for decreasing values of R_{load}, including the ignition and extinction states.

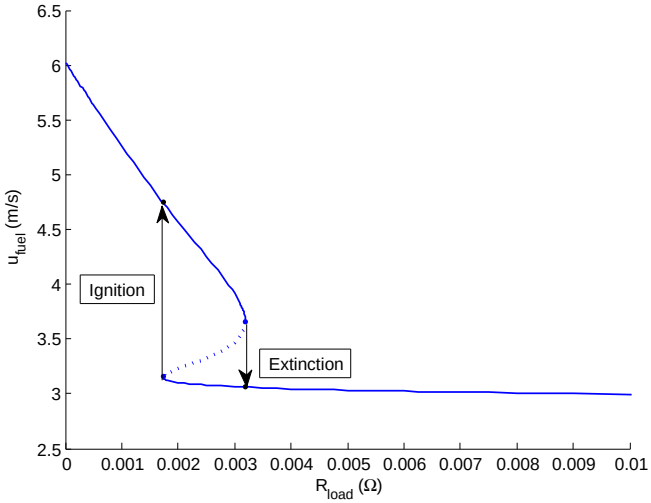

Figure 4.6.9: The profile for u_{fuel} for decreasing values of R_{load}, including the ignition and extinction states.

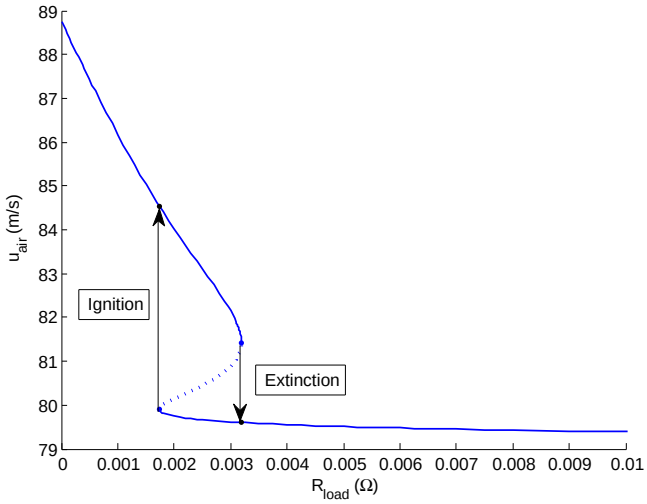

Figure 4.6.10: The profile for u_{air} for decreasing values of R_{load}, including the ignition and extinction states.

velocities as R_{load} moves closer to the ignition point. However, there is a more significant rise in both gas flow velocities after ignition. Since the concentration of both gas flows drop after ignition, there is an increase in the pressure drop across both gas channels, leading both gas flow velocities to increase after ignition. The pressure drop after ignition is larger for the air flow than it is for the fuel flow.

During the ignition phase, u_{fuel} rises from 3.1537 m/s to 4.7445 m/s, while u_{air} increases from 79.9111 m/s to 84.54495 m/s. During the extinction phase, u_{fuel} drops from 3.6601 m/s to 3.0608 m/s, while u_{air} drops from 81.4306 m/s to 79.6045 m/s. In the next chapter, the effects of changing both inlet gas flow velocities on SOFC performance will be covered. Changing the inlet gas flow velocities affects the amount of fuel/air entering the fuel/air channels.

4.7 Non-dimensional Parameters

The main reason as to why the multiplicity region is shifted towards even lower values of the external load resistance R_{load} compared to [49] and [47] is due to the increase in the amount of heat removed from the SOFC by convection. This was done by defining the heat-transfer coefficient in terms of the Nusselt number. The Nusselt number in both heat-transfer coefficients was based on an averaged approximation over the length of the gas channels, and written in terms of two other dimensionless parameters: the Prandtl number, and the Reynolds number (see equations (3.31)–(3.33)). The Prandtl number is a measure of the viscous diffusion rate over the thermal diffusion rate, while the Reynolds number is a measure of inertia over viscosity. Both of these numbers will be investigated in this section for both gas flows.

The Péclet number for heat and mass transfer within both gas channels will also be investigated in this section. The definition of those numbers is given in Appendix D. These results will help back up the other profiles shown in this section, and also give an

indication as to why certain terms like conduction and diffusion across the length of the cell are neglected.

4.7.1 Reynolds Numbers

The Reynolds number profiles for the fuel and air flow are given in figures 4.7.1 and 4.7.2. The critical Reynolds number in which the flow remains laminar is 2×10^5 [72, p 311], and as shown on both profiles, both gas flows are laminar (although the air side Reynolds number is of order 10^4). The fuel side Reynolds number on the other hand is of order 10^2, going up almost as high as 480. Both figures show that both flows are inertia driven (more so for the air flow since air velocity is much larger than fuel velocity).

The shape of the Reynolds number curve in figure 4.7.2 closely resembles the profile for $C^{\mathrm{b}}_{\mathrm{air}}$ in figure 4.6.2, so the air flow Reynolds number is mainly dominated by the amount of air inside the air channel. The air flow velocity u_{air} does not change that much in relation to its initial value. However, the shape of the fuel flow Reynolds number curve in figure 4.7.1 is mainly dominated by the fuel flow velocity u_{fuel}, which increases to over twice its initial value over the ignited steady-state branch. The effect of the decrease in $C^{\mathrm{b}}_{\mathrm{fuel}}$ only occurs along the ignited steady-state branch when R_{load} approaches zero.

During the ignition phase, Re_{fuel} rises from 308.105 to 473.116, while Re_{air} drops from 2.4549×10^4 to 2.3439×10^4. During the extinction phase, Re_{fuel} drops from 383.784 to 293.934, while Re_{air} rises from 2.4184×10^4 to 2.4619×10^4.

4.7.2 Prandtl Numbers

Figures 4.7.3 and 4.7.4 show the Prandtl number profiles of the fuel and air flow respectively. The Nusselt number approximation given in equation (3.31) is valid for values of the Prandtl number that are at least equal to 0.6. In figures 4.7.3 and 4.7.4, both Prandtl number values are around values between two and four. For the air flow, there is hardly a change in the Prandtl number, as it remains in a region between 2.32 and 2.36. The

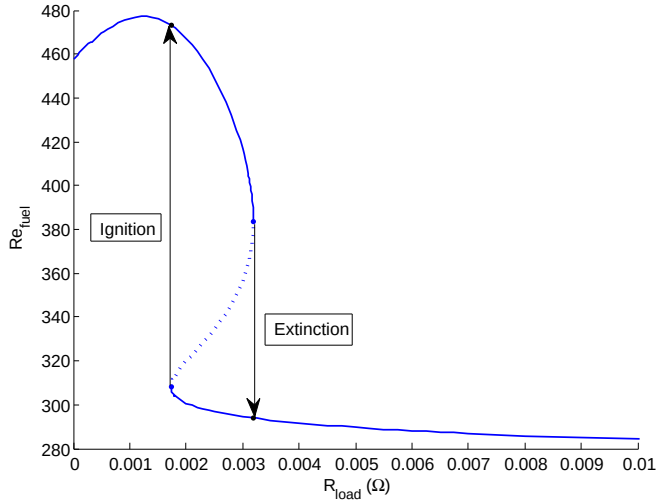

Figure 4.7.1: The profile for the fuel flow Reynolds number for decreasing values of R_{load}, including the ignition and extinction states.

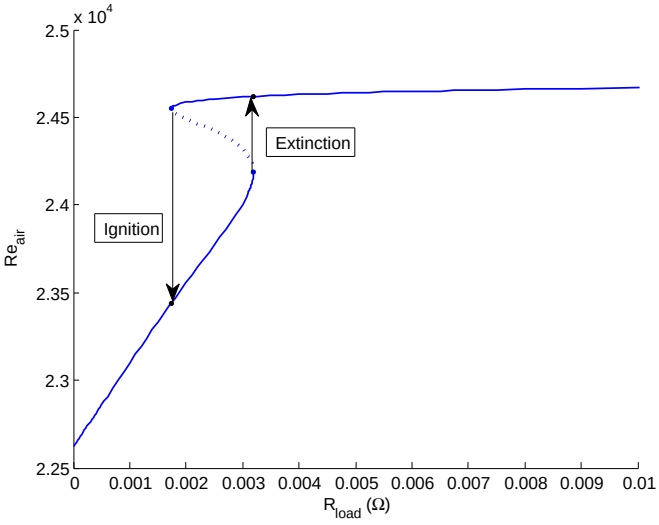

Figure 4.7.2: The profile for the air flow Reynolds number for decreasing values of R_{load}, including the ignition and extinction states.

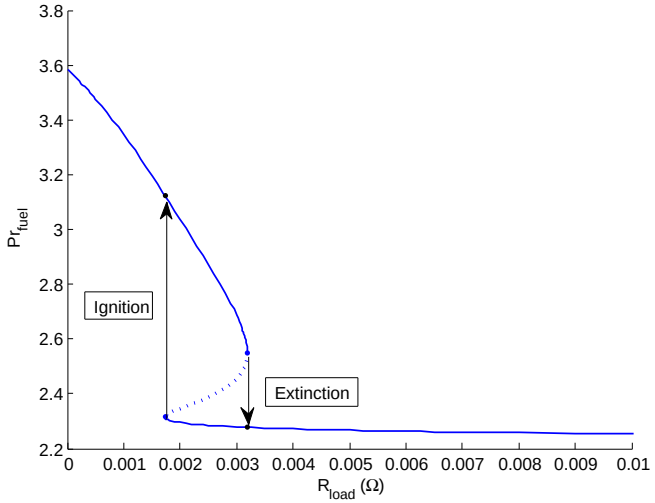

Figure 4.7.3: The profile for the fuel flow Prandtl number for decreasing values of R_{load}, including the ignition and extinction states.

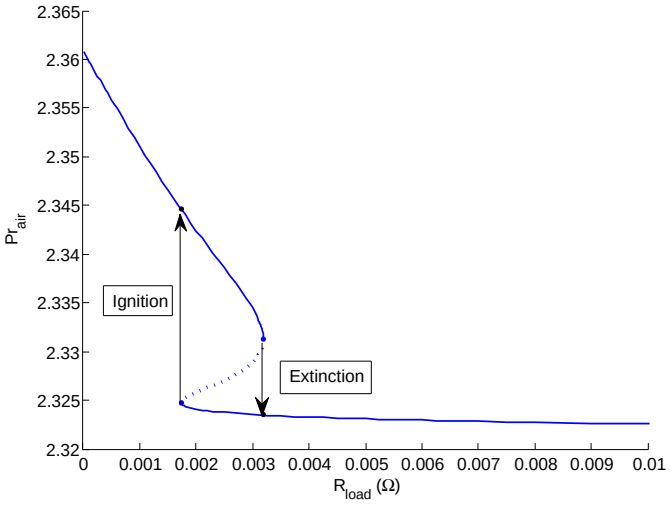

Figure 4.7.4: The profile for the air flow Prandtl number for decreasing values of R_{load}, including the ignition and extinction states.

fuel flow Prandtl number increases a bit more after ignition, going up to just over 3.1. Both figures show that there is not too much of a difference between viscous and thermal diffusivity across the length of both gas flow channels. But viscous diffusivity is slightly more dominant than thermal diffusivity.

During the ignition phase, Pr_{fuel} rises from 2.3146 to 3.1222, while Pr_{air} rises from 2.3248 to 2.3446. During the extinction phase, Pr_{fuel} drops from 2.5504 to 2.2775, while Pr_{air} drops from 2.3313 to 2.3235. The profiles for both Prandtl numbers can be backed up by looking into the Péclet numbers for both mass and heat transfer inside both gas channels. Since the heat-transfer coefficient is defined in terms of the Reynolds number and the Prandtl number (see equations (3.34) and (3.35)), the high values of the heat-transfer coefficients shown in figures 4.3.3 and 4.3.4 can be attributed mainly to the high values of the Reynolds number for both gas flows. The shape of the Reynolds number profiles may not be exactly the same as the shape of the heat-transfer coefficient profiles, but it is the main indicator as to how much heat is removed from the SOFC due to convection.

4.7.3 Péclet Numbers

Heat Transfer in both gas channels

Figures 4.7.5 and 4.7.6 show the profiles of the Péclet numbers for heat transfer inside the fuel and air flow. The Péclet number is defined as the ratio of the conduction time scale over the convection time scale (Appendix D.2). Alternatively, it can be described as the product of the Reynolds number (over the length of the channel) and the Prandtl number. As it can be seen in both profiles, the Péclet number is much larger than one for both profiles. This means that heat transfer of both gas flows across both gas channels (especially air) is mainly dominated by convection.

During the ignition phase, $Pe_{\text{H,fuel}}$ jumps up from 380.049 to 667.1499, while $Pe_{\text{H,air}}$ drops down from 5.7071×10^4 to 5.4954×10^4. During the extinction phase, $Pe_{\text{H,fuel}}$ drops down

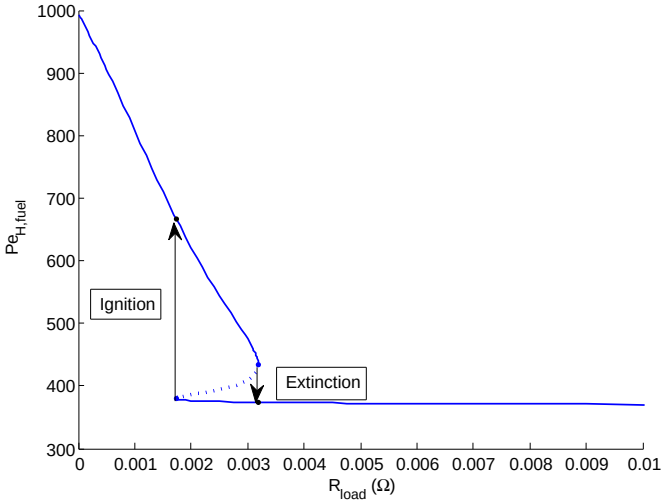

Figure 4.7.5: The profile for the fuel flow heat transfer Péclet number for decreasing values of R_{load}, including the ignition and extinction states.

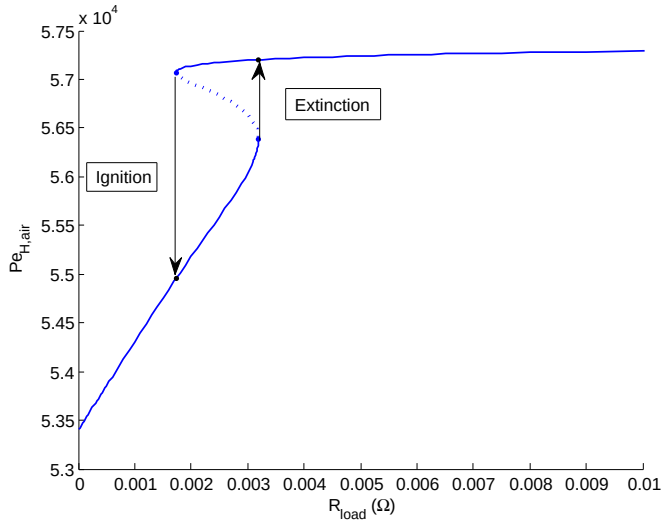

Figure 4.7.6: The profile for the air flow heat transfer Péclet number for decreasing values of R_{load}, including the ignition and extinction states.

from 433.569 to 374.024, while $Pe_{\mathrm{H,air}}$ jumps up from 5.6381×10^4 to 5.7202×10^4. Since the values of the heat transfer Péclet numbers for both gas flows are so large, there is no conduction term within energy conservation equations (3.70) and (3.71) since conduction plays a very small part in the transfer of heat across the gas channel.

Mass Transfer in both gas channels

Figures 4.7.7 and 4.7.8 represent the profiles of the mass transfer Péclet numbers for the fuel and air flow respectively, where advection and diffusion are considered across the length of the cell. It is defined as the diffusion time-scale over the advection time-scale (Appendix D.1). Just like the Péclet numbers for heat transfer across the length of the cell, it is clear that advection across the length of the cell is more dominant than diffusion across the length of the cell (especially in the air channel).

During the ignition phase, $Pe_{\mathrm{ML,fuel}}$ drops down from 137.007 to 95.207, while $Pe_{\mathrm{ML,air}}$ drops down from 1.4245×10^4 to 6.6116×10^3. During the extinction phase, $Pe_{\mathrm{ML,fuel}}$ jumps up from 118.7596 to 141.501, while $Pe_{\mathrm{ML,air}}$ jumps up from 1.0556×10^4 to 1.5231×10^4. Since the advection time scale for the mass transfer Péclet number is the same as the convection time scale for the heat transfer Péclet number, it becomes clear that heat transfer via conduction across the length of the channel takes longer than mass trasnfer via diffusion. This is because the values of the mass transfer Péclet number is not as big as the heat transfer Péclet number. This in turn leads to the Prandtl number profiles given in figures 4.7.3 and 4.7.4.

The non-dimensional form of the equations given in this model are not considered in this thesis. But if the equations were to be non-dimensionalised (especially the mass conservation equations), the length scales for advection and diffusion within the gas channels would be different. This is because diffusion within the gas channels is considered over the height of the gas channels rather than the length. This is why we consider the mass transfer Péclet number for both gas flows with different length scales for the two different

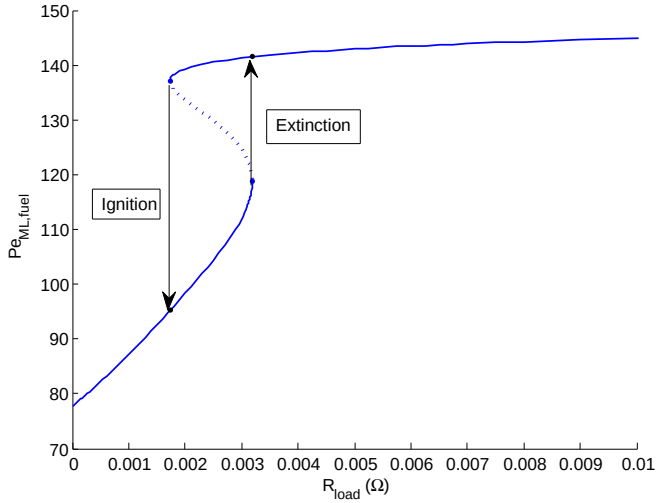

Figure 4.7.7: The profile for the fuel flow mass transfer Péclet number for decreasing values of R_{load}, including the ignition and extinction states.

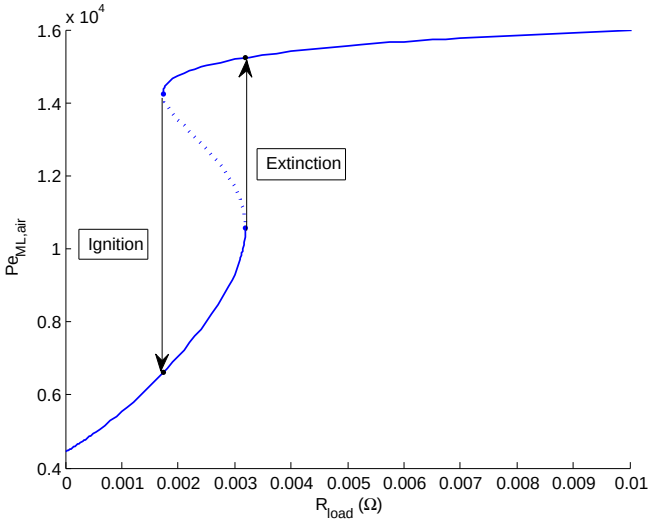

Figure 4.7.8: The profile for the air flow mass transfer Péclet number for decreasing values of R_{load}, including the ignition and extinction states.

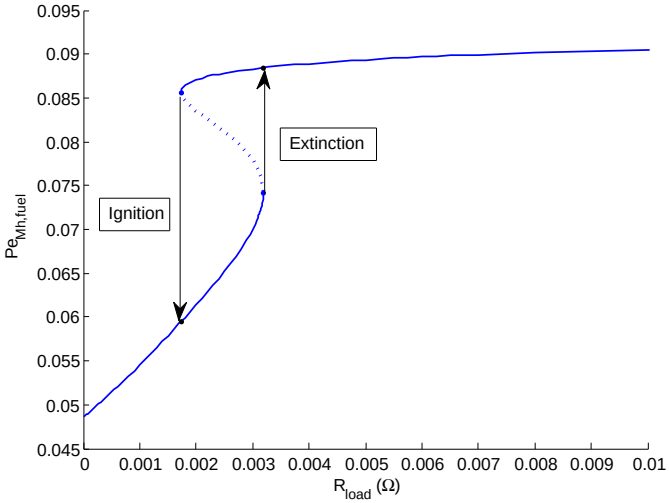

Figure 4.7.9: The profile for the fuel flow mass transfer Péclet number for decreasing values of R_{load}, with different length scales for advection and diffusion.

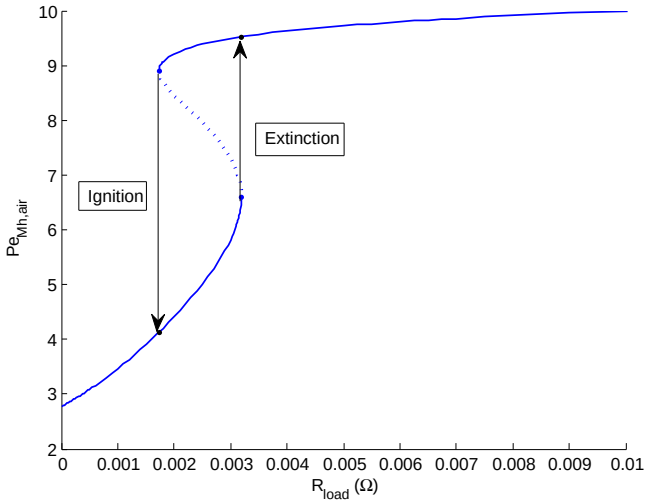

Figure 4.7.10: The profile for the air flow mass transfer Péclet number for decreasing values of R_{load}, with different length scales for advection and diffusion.

time scales (Appendix D.1).

The profiles of these particular mass transfer Péclet numbers are shown in figures 4.7.9 and 4.7.10. Given the conditions in Appendix D (section D.1), it is clear that diffusion across the height of the channel has a much stronger effect than advection across the length of the channel. The Péclet numbers would need to exceed 1600 for advective effects across the length of the channel to become more dominant. In terms of the time-scales, the diffusion time-scale across the height of the fuel channel is shorter than the advection time-scale across the length of the fuel channel. As for the air channel, there is not much of a difference between the two time-scales. More information about the different time-scales can be found in section 7.2.

During the ignition phase, $Pe_{\mathrm{Mh,fuel}}$ drops down from 0.08563 to 0.0595 while $Pe_{\mathrm{Mh,air}}$ drops down from 8.9033 to 4.1323. During the extinction phase, $Pe_{\mathrm{Mh,fuel}}$ jumps up from 0.07422 to 0.08844, while $Pe_{\mathrm{Mh,air}}$ jumps up from 6.5974 to 9.5197.

4.8 Summary

In this chapter, the steady-state results for a SOFC operating under a constant external load were investigated, where the inlet parameter values were based on the values given in Appendix B. Compared to previous results, the multiplicity region is shifted towards lower values of R_{load} (even with higher inlet gas flow temperatures). This is due to an increase in the amount of heat removed by convection, where the heat-transfer coefficients are no longer assumed to be constant. They are defined in terms of an averaged approximation of the Nusselt number over the length of the cell. With this approximation, the heat-transfer coefficient values are now much larger than the previously assumed value of 25 $\mathrm{W}/(\mathrm{m}^2 \cdot \mathrm{K})$.

Profiles of heat production, heat removal and $\dot{T}_{\mathrm{cell}}$ for rising T_{cell} were observed for five different values of R_{load}. For those five different values of R_{load}, the number of steady-

state solutions can be found by looking at the number of intersections of Q_{P} and Q_{R}, and the expected stability of those steady-state solutions on each of the three steady-state branches can be found by looking at the profiles of $\dot{T}_{\mathrm{cell}}$ for varying T_{cell}. The lower un-ignited steady-state branch and the upper ignited steady-state branch seem to be stable, while the steady-state branch in-between is assumed to be unstable. More work is needed to determine the stability of the ignition and extinction points however.

Cell voltage initially drops for low current density values along the un-ignited steady-state branch due to activation and Ohmic polarisation effects. However, just before the ignition point, V_{cell} starts to rise as electrolyte conductivity starts to rise with rising T_{cell} (as shown by the drop in η_{Ohm}). After the ignition, the SOFC operates close to the maximum voltage obtainable along the ignited steady-state branch (hence close to the maximum voltage efficiency value obtainable on that branch). V_{cell} eventually drops down to zero for increasing i due to mass transfer limitations at high i (when R_{load} approaches zero). Cathode activation polarisation and Ohmic polarisation gradually tend towards zero as i increases, but there is still a noticeable drop in V_{cell} due to activation polarisation effects in the Anode.

Along the un-ignited steady-state branch, there is a small peak that exists in the power density curve. After ignition, power density P_{cell} reaches an even higher peak, as more current is drawn from the cell, and V_{cell} increases along with increased cell conductivity. This peak corresponds to the peak in electrical efficiency (which is just below 10 % at an operating temperature of just below 2000 K), where a rise in I results in a rise in the amount of fuel utilised within the cell along with rising voltage efficiency.

In the gas channels, there is a noticeable drop in the concentration of both gas flows after ignition. The drop in fuel concentration is greater than air concentration due to the higher consumption rates, and the lack of Water coming out of the cell to replace the Hydrogen that is consumed within the cell. Over half the amount of fuel is utilised after ignition.

Air concentration and Oxygen levels do not decrease greatly after ignition. The drop in gas concentration leads to a larger pressure loss within both gas channels, causing both gas flow velocities to increase after ignition. Fuel Temperature increases much more than air temperature along with rising T_{cell} due to the enthalpy flux of Water from the cell to the fuel flow, transferring extra heat from the cell to the fuel flow.

Looking at the non-dimensional parameters, the Reynolds numbers for both gas flows are big (especially in the air flow). Inertia dominates over viscosity for both gas flows (especially the air flow, where the values are not too far away from the critical Reynolds number value). The shape of the air flow Reynolds number is mainly based on the air concentration profile, while the fuel flow Reynolds number profile is mostly based on the fuel velocity profile, except when R_{load} approaches zero along the ignited steady-state branch, where fuel concentration starts to dominate.

The Prandtl number for the fuel flow ranges between 2 to 4, while the Prandtl number for the air flow is in the region between 2.32 and 2.365. So for both gas flows, viscous diffusion effects are slightly more dominant than thermal diffusion effects. Since the values of the Prandtl numbers are both close to one, the heat-transfer coefficients are mainly dominated by the Reynolds number terms for both gas flows.

The profiles for both Prandtl numbers are backed up by the Péclet number profiles for mass transfer and heat transfer across the length of the cell. The Péclet numbers for mass transfer are lower than the Péclet numbers for heat transfer. This signals that the diffusion time-scales across the length of the channel are smaller than the conduction time-scales (see section 7.2). If diffusion is considered across the height of the channel instead of the channel length, it turns out that diffusion is much more prominent across the height of the gas channel compared to the length.

Chapter 5

Constant External Load: Multiplicity Regions

5.1 Introduction

In this chapter we investigate the effect of each of the inlet parameter (except for mole fractions) on the performance of a SOFC operating under a constant external load. The inlet parameters considered include the inlet gas flow temperatures, the inlet gas flow velocities, and the inlet gas molar flow rates. Each of the inlet parameters will be investigated individually. In existing literature, not enough work has been done to show the effect that each individual parameter has on SOFC performance, including the existence and size of any multiplicity regions.

This chapter starts off by investigating how SOFC performance and steady-state multiplicity is affected by changes in $T_{\text{fuel}}^{\text{in}}$ and $T_{\text{air}}^{\text{in}}$ separately, followed by changes in $u_{\text{fuel}}^{\text{in}}$ and $u_{\text{air}}^{\text{in}}$ separately, then by changes in $\dot{N}_{\text{fuel}}^{\text{in}}$ and $\dot{N}_{\text{air}}^{\text{in}}$ separately. For each of the six inlet parameters there will be a 3D graph showing how the profile of T_{cell} varies for each inlet parameter, backed up with a few heat production/heat removal curves at a certain value of R_{load}. There will be additional 3D graphs showing how V_{cell} and P_{cell} are affected by

changes in each of the inlet parameters (plus any additional profiles to back up these profiles for certain cases). There will also be a multiplicity region graph for each of the six inlet parameters, showing the region where up to three steady-states exist.

5.2 Inlet fuel temperature $T_{\mathbf{fuel}}^{\mathbf{in}}$

Figure 5.2.1 represents the different R_{load} vs T_{cell} profiles for varying values of $T_{\text{fuel}}^{\text{in}}$, while figure 5.2.2 represents the multiplicity region for varying values of $T_{\text{fuel}}^{\text{in}}$. Varying the value of $T_{\text{fuel}}^{\text{in}}$ has the effect of either increasing or decreasing the amount of heat removed by convection. Increasing the value of $T_{\text{fuel}}^{\text{in}}$ has the effect reducing the amount of heat removed by convection (since the gap between T_{cell} and T_{fuel} is smaller), causing T_{cell} to rise. Since the cell is operating at a higher temperature, R_{load} does not need to be set as low as before to enable the cell to operate at a particular steady-state temperature. A higher operating temperature results in a slightly easier and quicker activation of the electrochemical reactions. But since R_{load} is higher, less work is done by the SOFC to operate at a higher temperature, so less heat is dissipated from the cell. This has the eventual result in moving the multiplicity region towards higher values of R_{load}. Not only that, but the multiplicity region shrinks as well, as shown in figure 5.2.2. The point at which the multiplicity region ends is located at a value of $T_{\text{fuel}}^{\text{in}}$ just above 1123 K.

Figures 5.2.3 and 5.2.4 show the heat production and heat removal curves for two different values of $T_{\text{fuel}}^{\text{in}}$ (R_{load} is set at 0.0025 Ω). There is a gap of 100 K between the two different values of $T_{\text{fuel}}^{\text{in}}$ considered in both of these figures. The changes in Q_{P} and Q_{R} are not massive, but it is noticeable that there is a slight drop in Q_{R}, and a slight rise in Q_{P} in figure 5.2.4 compared to figure 5.2.3. Figure 5.2.3 is the same as 4.2.7, where there are three steady-state solutions. But in figure 5.2.4, there is only one steady-state solution of T_{cell} close to 1800 K. The rise in Q_{P} and the drop in Q_{R} is due to a reduction in the amount of heat produced in the cell being dissipated away from the cell due to convection.

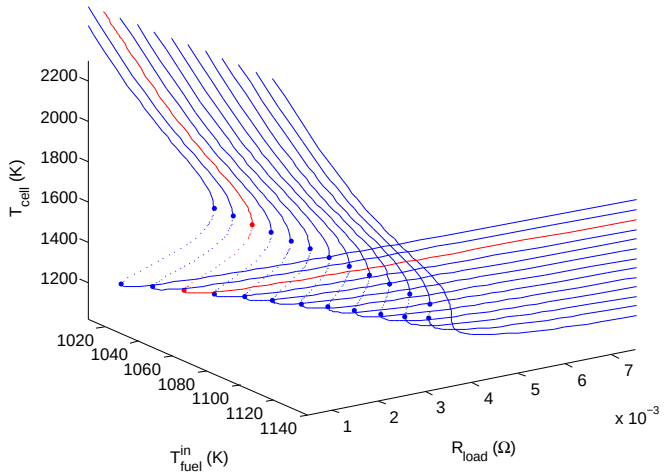

Figure 5.2.1: R_{load} vs T_{cell} for varying values of $T_{\text{fuel}}^{\text{in}}$. The red profile represents the original profile in chapter 4.

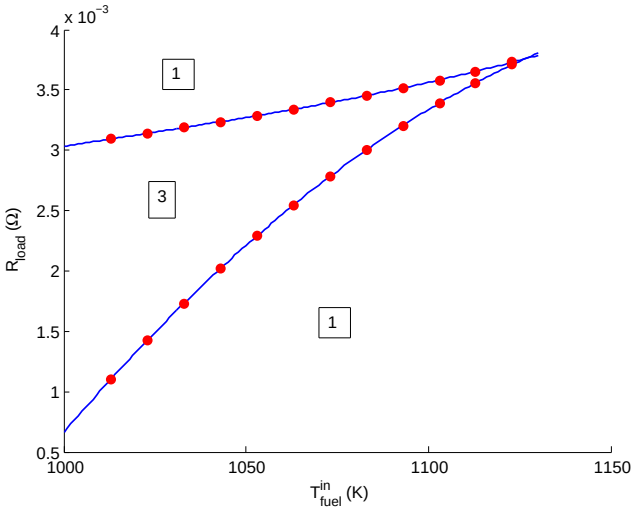

Figure 5.2.2: The multiplicity region for changes in $T_{\text{fuel}}^{\text{in}}$. The boxed numbers represent the number of steady-state solutions in a particular region. The red points represent the location of the ignition and extinction points.

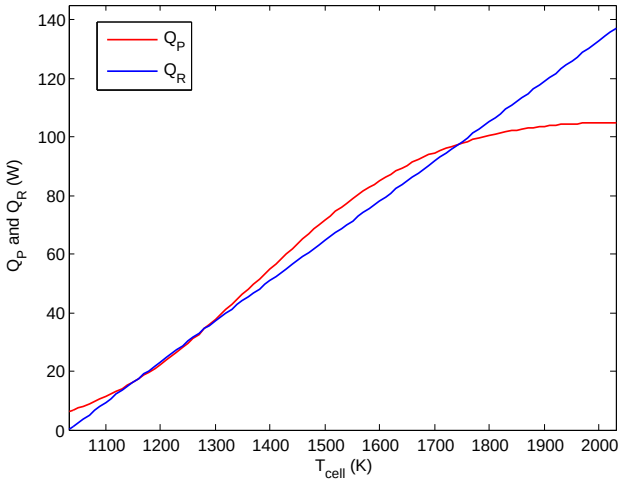

Figure 5.2.3: Heat Production (Red) and Heat Removal (Blue) Curves for rising T_{cell}, where $T_{\text{fuel}}^{\text{in}} = 1033$ K ($R_{\text{load}} = 0.0025\ \Omega$).

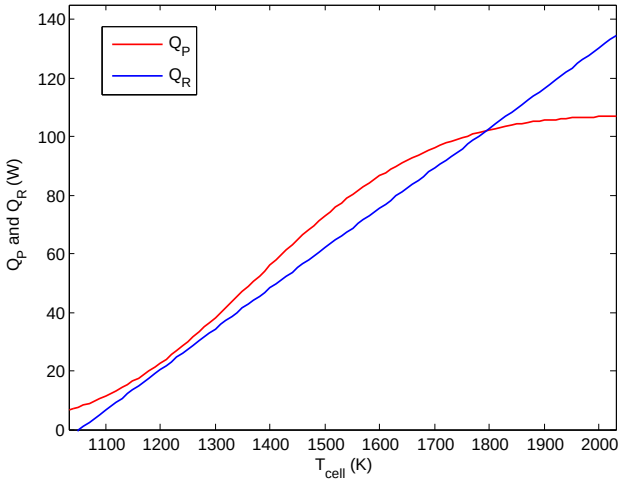

Figure 5.2.4: Heat Production (Red) and Heat Removal (Blue) Curves for rising T_{cell}, where $T_{\text{fuel}}^{\text{in}} = 1133$ K ($R_{\text{load}} = 0.0025\ \Omega$).

The multiplicity region graph in figure 5.2.2 is computed in MATLAB by applying a polynomial curve fit onto the set of ignition points and another one for the set of extinction points. The red points on the lower curve in figure 5.2.2 represent the location of the ignition points for various values of $T_{\text{fuel}}^{\text{in}}$, while the red points on the upper curve represent the location of the extinction points. The location of these ignition and extinction points were determined when computing the profiles for figures 5.2.1, 5.2.5 and 5.2.6. There is a set of twelve ignition and extinction points, located for inlet fuel temperatures between 1013 K and 1123 K, with a gap of 10 K between the location of each set of ignition/extinction points. Once the ignition and extinction points were located, the MATLAB function *polyfit* was used to determine a third-order polynomial approximation for the set of ignition points, and for the set of extinction points. Then by setting these polynomial approximations as anonymous functions in MATLAB, these approximations were evaluated for a range of points along the $T_{\text{fuel}}^{\text{in}}$ axis (including the location of the ignition and extinction points), leading to the profile in figure 5.2.2. This is the method used to produce all the multiplicity region graphs in this thesis. Since all the located ignition and extinction points lie on the two curves, these polynomial approximations are a very good fit for the set of ignition and extinction points given.

Figures 5.2.5 and 5.2.6 represent the different V-I and P-I profiles for varying values of $T_{\text{fuel}}^{\text{in}}$. At an initial glance, it looks like not much as changed to the profiles of V_{cell} and P_{cell} as $T_{\text{fuel}}^{\text{in}}$ is increased (besides the size of the unstable steady-state branch). But on closer inspection, it becomes noticeable that V_{cell} rises very gradually with rising $T_{\text{fuel}}^{\text{in}}$ (especially around the local minimum close to the ignition point), as well as P_{cell}.

The main reason for this is that the higher operating temperatures associated with the increase in $T_{\text{fuel}}^{\text{in}}$ leads to a quicker activation of the electrochemical reactions (reducing activation polarisation), as well as increasing electrolyte conductivity (reducing Ohmic polarisation). Since activation and Ohmic polarisation drop with increasing $T_{\text{fuel}}^{\text{in}}$, then

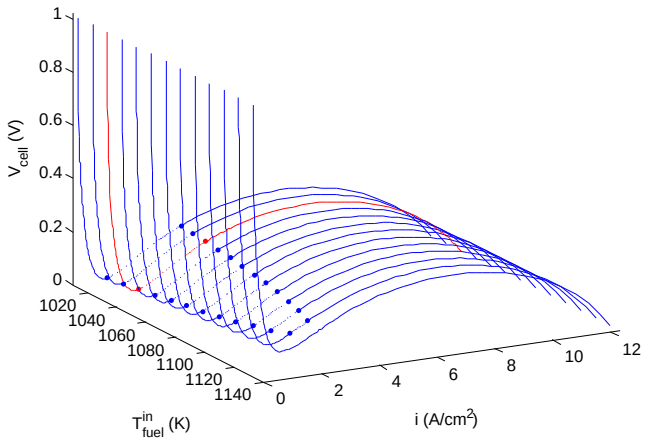

Figure 5.2.5: i vs V_{cell} for varying values of $T_{\text{fuel}}^{\text{in}}$. The red profile represents the original profile in chapter 4.

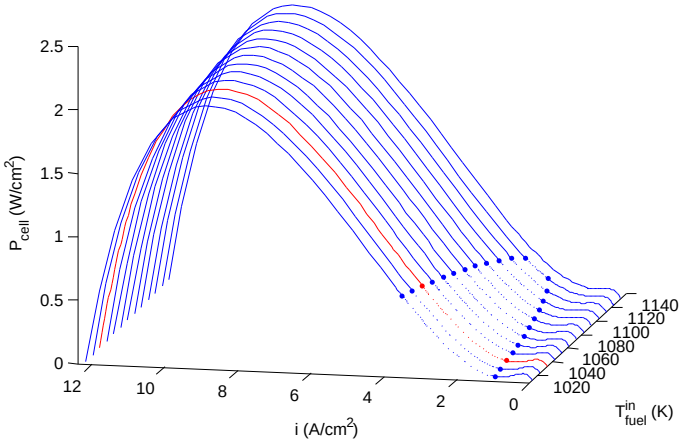

Figure 5.2.6: i vs P_{cell} for varying values of $T_{\text{fuel}}^{\text{in}}$. The red profile represents the original profile in chapter 4.

V_{cell} rises gradually as a consequence of this. The rise in T_{cell} also results in a rise in the amount of current drawn from the cell, which aligned with the increase in V_{cell}, leads to a rise in P_{cell}.

Since i increases along with increasing T_{cell}, fuel utilisation levels also go up slightly. This, along with rising voltage efficiency, results in a slight increase in electrical efficiency as well. At the extreme end of the graph in 5.2.6 where $T_{\text{fuel}}^{\text{in}} = 1133$ K, electrical efficiency at its peak rises above 10% when the SOFC operates at peak power density. Even though the operating temperature at the power density peak is too high, it does signal that increasing the inlet fuel temperature does lead to a slightly more efficient cell. However, as it will be seen later on in the chapter, modifying some of the other inlet parameters, especially in the fuel flow side, has a more deeper impact on SOFC performance.

5.3 Inlet air temperature $T_{\text{air}}^{\text{in}}$

Figure 5.3.1 represents the R_{load} vs T_{cell} profiles for different values of $T_{\text{air}}^{\text{in}}$. Just like figure 5.2.1, the multiplicity region disappears when $T_{\text{air}}^{\text{in}}$ is increased. However, the SOFC is more sensitive to changes in $T_{\text{air}}^{\text{in}}$ compared to changes in $T_{\text{fuel}}^{\text{in}}$.

Increasing $T_{\text{air}}^{\text{in}}$ has the same effect on the cell as increasing $T_{\text{fuel}}^{\text{in}}$. But, the air flow heat-transfer coefficient is much larger than the one for the fuel flow. Reducing the difference between T_{cell} and T_{air} results in much less heat being removed from the cell if $T_{\text{air}}^{\text{in}}$ is increased instead of $T_{\text{fuel}}^{\text{in}}$. There is a much sharper shift of the multiplicity region towards higher values of R_{load}, and when $T_{\text{air}}^{\text{in}}$ is set at 1063 K, the multiplicity region has already disappeared. This is over 60 K less than the value of $T_{\text{fuel}}^{\text{in}}$.

On the multiplicity region graph in figure 5.3.2, there is no steady-state multiplicity once $T_{\text{air}}^{\text{in}}$ is around 1060 K. Just like the multiplicity region in figure 5.2.2, a third-order polynomial approximation was fitted to the ignition points and the extinction points. There is a set of eight ignition and extinction points for values of $T_{\text{air}}^{\text{in}}$ ranging between 1023 K and

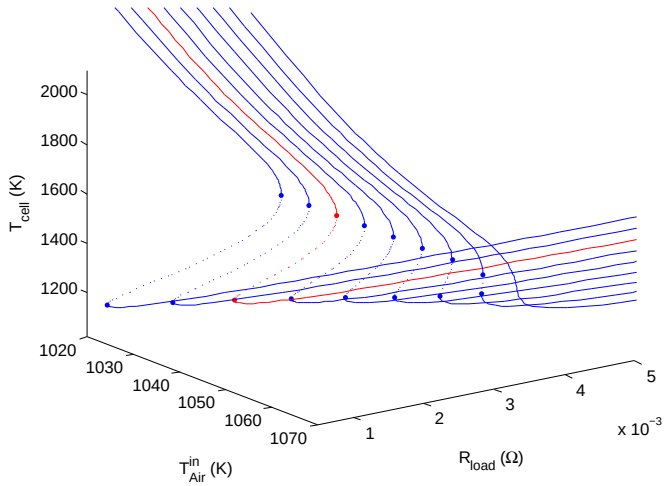

Figure 5.3.1: R_{load} vs T_{cell} for varying values of $T_{\text{air}}^{\text{in}}$. The red profile represents the original profile in chapter 4.

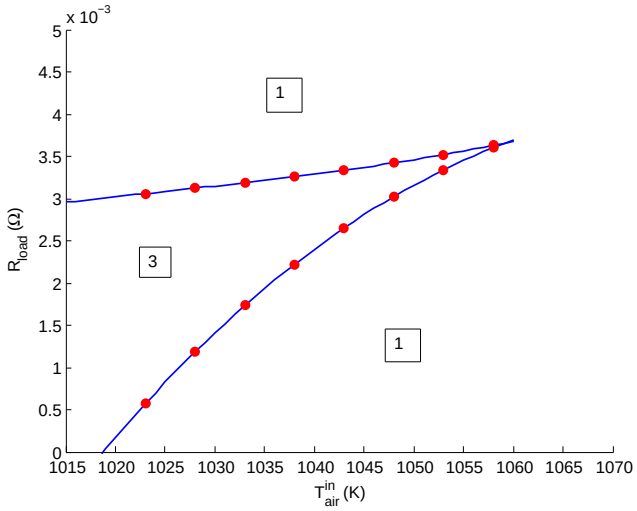

Figure 5.3.2: The multiplicity region for changes in $T_{\text{air}}^{\text{in}}$. The boxed numbers represent the number of steady-state solutions in a particular region. The red points represent the location of the ignition and extinction points.

1058 K, with a gap of 5 K between the location of each pair of ignition/extinction points. What is also noticeable in figure 5.3.2 is that if $T_{\text{air}}^{\text{in}}$ is set below 1020 K, the ignition point is no longer located for positive values of R_{load}, meaning that there are three possible steady-state solutions located at $R_{\text{load}} = 0\ \Omega$.

Figure 5.3.3 represents the V-I profiles for different values of $T_{\text{air}}^{\text{in}}$. Just like the profile in 5.2.5, V_{cell} rises when $T_{\text{air}}^{\text{in}}$ is set at a larger value. This can be seen a lot more clearly in figure 5.3.3. The reasons for this are the same as for the case when $T_{\text{fuel}}^{\text{in}}$ is set at a higher value. The only main difference being that $T_{\text{air}}^{\text{in}}$ does not need to be modified as much as $T_{\text{fuel}}^{\text{in}}$ to affect SOFC performance.

Figure 5.3.4 represents the P-I profiles for different values of $T_{\text{air}}^{\text{in}}$. Just like the profile in 5.2.6, the peak power density achieved by the SOFC rises as $T_{\text{air}}^{\text{in}}$ is increased. However, just like the P-I profiles in 5.2.6, there is not a huge rise in power density, especially along the lower, un-ignited steady-state branch. This also means that there is not a huge rise in the electrical efficiency of the SOFC either.

To summarise the effects of the inlet gas temperatures on SOFC performance, increasing the gas flow temperatures has the effect reducing the amount of heat lost by convection. Increasing either inlet parameter reduces the gap between T_{cell} and the gas flow temperature, reducing the impact of the heat transfer coefficient. This means that less heat is given off from the electrochemical reactions to be carried away by the two gas flows either side of the cell, and more heat is conserved within the cell. The rise in T_{cell} results in a quicker and easier activation of the electrochemical reactions, since R_{load} does not need to be set at a lower value to enable the SOFC to operate at the same steady-state temperature.

The shift in values of T_{cell} towards higher values of R_{load} means that the multiplicity region is shifted towards higher values of R_{load}. The size of the multiplicity region also shrinks if either $T_{\text{fuel}}^{\text{in}}$ or $T_{\text{air}}^{\text{in}}$ is raised. Eventually, if either $T_{\text{fuel}}^{\text{in}}$ or $T_{\text{air}}^{\text{in}}$ is set high enough, the

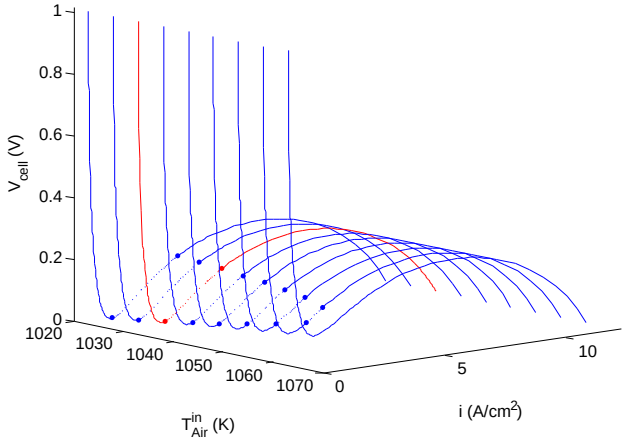

Figure 5.3.3: i vs V_{cell} for varying values of $T_{\text{air}}^{\text{in}}$. The red profile represents the original profile in chapter 4.

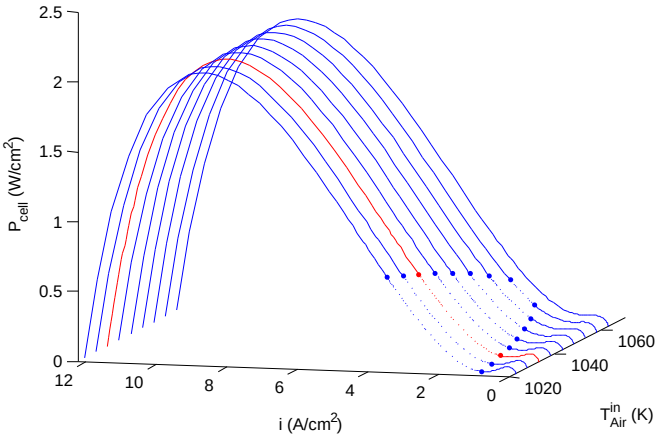

Figure 5.3.4: i vs P_{cell} for varying values of $T_{\text{air}}^{\text{in}}$. The red profile represents the original profile in chapter 4.

multiplicity region disappears altogether, and there is a more gradual rise in T_{cell} with decreasing R_{load}. Since a higher operating temperature enables a quicker activation of the electrochemical reactions as well as an increase in electrolyte conductivity, V_{cell} also rises gradually for higher inlet gas temperature values (especially along the lower stable steady-state branch). Since V_{cell} rises with increasing inlet gas flow temperatures, so does P_{cell}. However, there is not a significant rise in the amount of power produced by the SOFC. Changing one of the other four inlet parameters may have a more significant effect on the amount of power produced. The same thing can be said for electrical efficiency, where both voltage efficiency and fuel utilisation increase slightly, resulting in electrical efficiency values of around 10%.

Compared to the 3D graph of T_{cell} in [49], where they consider the change of both inlet gas flow temperatures simultaneously, the shape of the profiles are very similar in how they change when the inlet gas flow temperatures are increased. The shape of the multiplicity region curves given in this section are similar to the one given in [49]. The 3D graph in [49] does not highlight the effect that $T_{\text{fuel}}^{\text{in}}$ and $T_{\text{air}}^{\text{in}}$ has on SOFC performance separately. However, if both inlet gas flow temperatures are increased simultaneously, it is very likely that the multiplicity region is likely to be even smaller than the ones shown in figures 5.2.2 and 5.3.2. Since the multiplicity region graphs in [47] and [49] are set for different values of the heat transfer coefficient, a direct comparison between the size of the multiplicity region graphs in this thesis with the ones from those two papers cannot be made.

5.4 Inlet fuel velocity $u_{\text{fuel}}^{\text{in}}$

Figure 5.4.1 represents the R_{load} vs T_{cell} profiles for varying values of $u_{\text{fuel}}^{\text{in}}$. Even though the values of $u_{\text{fuel}}^{\text{in}}$ are much smaller than the value of $u_{\text{air}}^{\text{in}}$, modifying $u_{\text{fuel}}^{\text{in}}$ has a drastic effect on SOFC performance. Decreasing $u_{\text{fuel}}^{\text{in}}$ shifts the multiplicity region towards higher values of R_{load}, where the multiplicity region gets smaller. Eventually when $u_{\text{fuel}}^{\text{in}}$ is

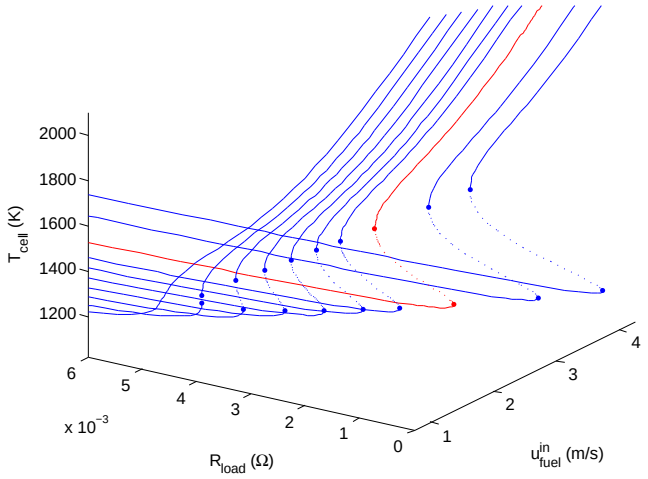

Figure 5.4.1: R_{load} vs T_{cell} for varying values of $u_{\text{fuel}}^{\text{in}}$. The red profile represents the original profile in chapter 4.

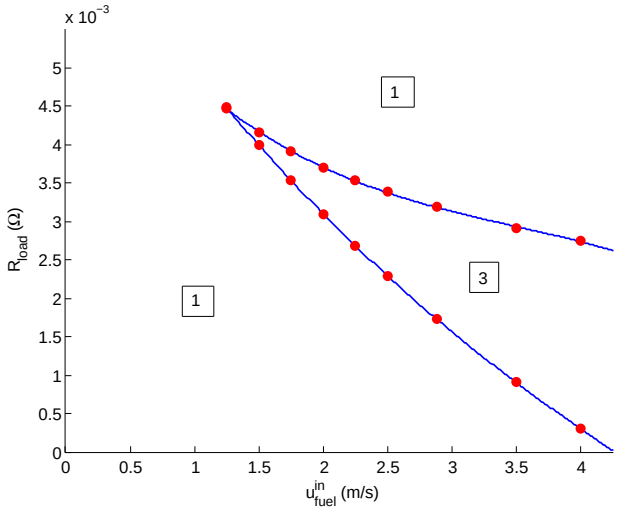

Figure 5.4.2: The multiplicity region for changes in $u_{\text{fuel}}^{\text{in}}$. The boxed numbers represent the number of steady-state solutions in a particular region. The red points represent the location of the ignition and extinction points.

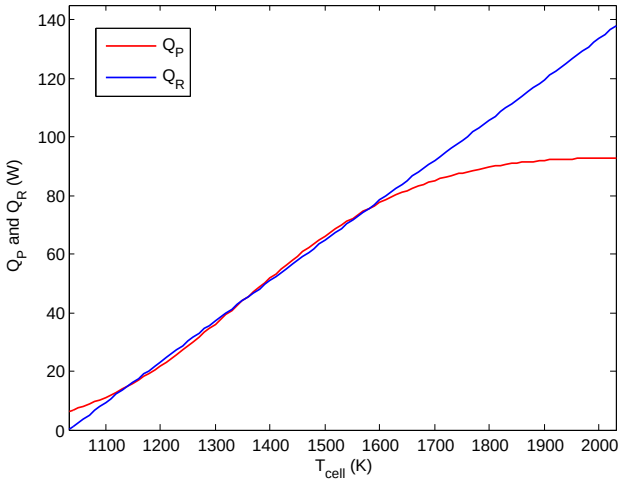

Figure 5.4.3: Heat Production (Red) and Heat Removal (Blue) Curves for rising T_{cell}, where $u_{\text{fuel}}^{\text{in}} = 2.88$ m/s ($R_{\text{load}} = 0.003\ \Omega$).

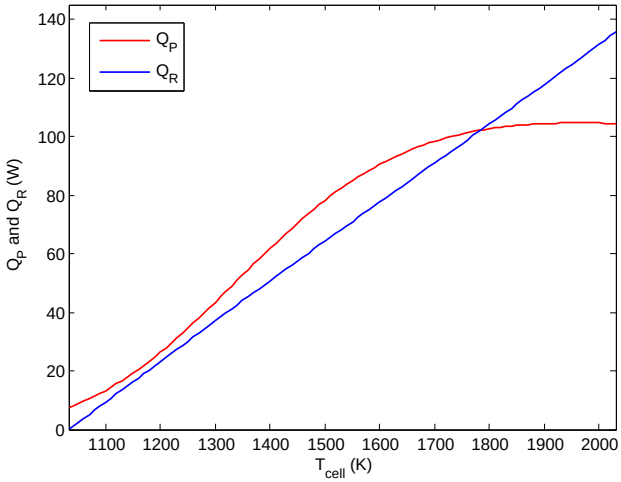

Figure 5.4.4: Heat Production (Red) and Heat Removal (Blue) Curves for rising T_{cell}, where $u_{\text{fuel}}^{\text{in}} = 1$ m/s ($R_{\text{load}} = 0.003\ \Omega$).

less than 1.25 m/s, the multiplicity region disappears altogether. Unlike the multiplicity regions in figures 5.2.2 and 5.3.2, the location of the ignition and extinction points when the multiplicity region shown in figure 5.4.2 is on the verge of disappearing is close to 0.0045 Ω.

There are two main reasons as to why decreasing $u_{\text{fuel}}^{\text{in}}$ reduces and removes the multiplicity region. Firstly, lowering $u_{\text{fuel}}^{\text{in}}$ lowers the amount of heat removed from the cell by convection in the fuel flow side. This is noticeable in figures 5.4.3 and 5.4.4 where lowering $u_{\text{fuel}}^{\text{in}}$ lowers the heat removal curve Q_{R} (albeit not by much). The second reason as to why decreasing $u_{\text{fuel}}^{\text{in}}$ removes the multiplicity region is because of its effect on fuel concentration levels in the fuel channel.

The only inlet parameter that is being modified in this section is $u_{\text{fuel}}^{\text{in}}$. The inlet molar flow rate of the fuel flow $\dot{N}_{\text{fuel}}^{\text{in}}$ is kept fixed at 1.39×10^{-3} mol/s. Lowering $u_{\text{fuel}}^{\text{in}}$ results in a higher concentration of fuel in the fuel channel. Since the inlet mole fraction of Hydrogen is kept fixed at 0.9, there is more Hydrogen available for consumption within the SOFC. A rise in fuel concentration levels (including Hydrogen concentration levels) within the fuel channel means that more Hydrogen can be consumed within the SOFC. The increase in electrochemical activity as a result of this leads to a rise in the amount of heat produced within the cell. Figures 5.4.3 and 5.4.4 show a big difference in the amount of heat produced within the cell, with Q_{P} remaining below 100 W in figure 5.4.3 for $u_{\text{fuel}}^{\text{in}} = 2.88$ m/s, and Q_{P} exceeding 100 W in figure 5.4.4 for $u_{\text{fuel}}^{\text{in}} = 1$ m/s.

This increase in the amount of heat produced shifts the steady-state values of T_{cell} towards higher values of R_{load}. The rise in T_{cell} also leads to a rise in the amount of current flowing through the external circuit, increasing the reaction rates. Since $\dot{N}_{\text{fuel}}^{\text{in}}$ is fixed at the same value given in Appendix B, the increase in I results in more fuel being utilised within the SOFC. The fuel utilisation profile is shown in figure 5.4.5, where fuel utilisation within the SOFC can be as high as just over 80% at peak current density when $u_{\text{fuel}}^{\text{in}}$ is set at 1

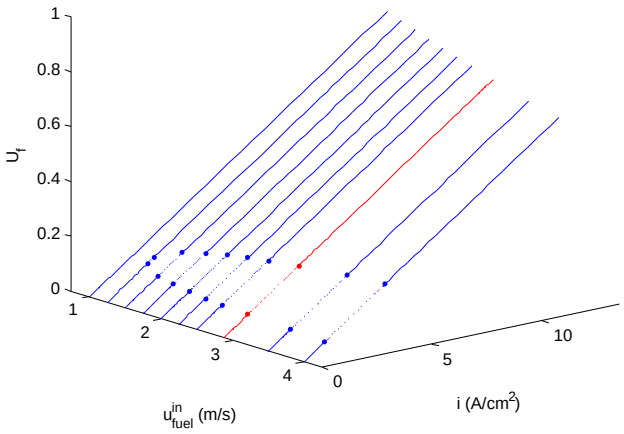

Figure 5.4.5: i vs U_{F} for varying values of $u^{\mathrm{in}}_{\mathrm{fuel}}$. The red profile represents the base case profile in chapter 4.

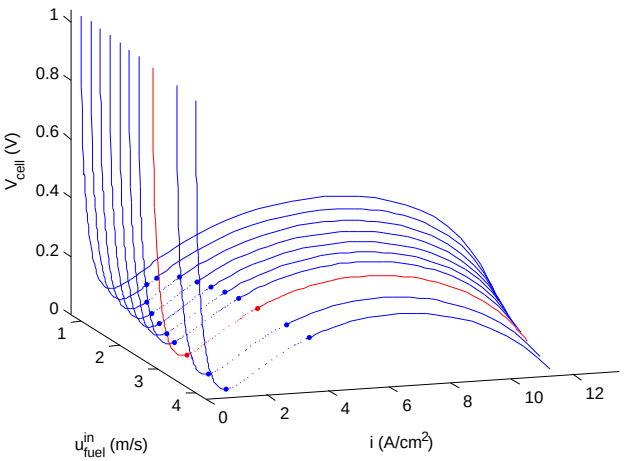

Figure 5.4.6: i vs V_{cell} for varying values of $u^{\mathrm{in}}_{\mathrm{fuel}}$. The red profile represents the original profile in chapter 4.

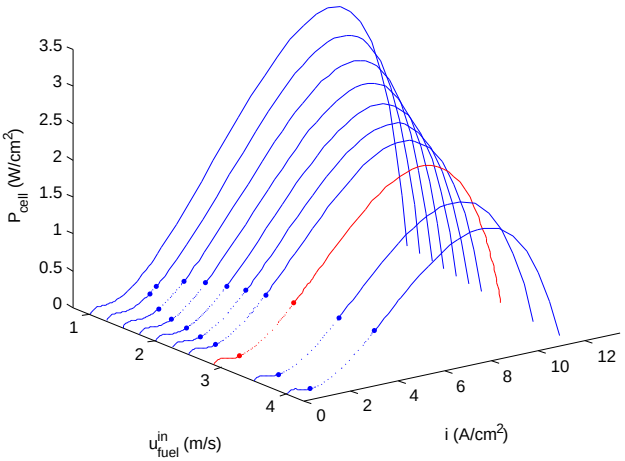

Figure 5.4.7: i vs P_{cell} for varying values of $u^{\text{in}}_{\text{fuel}}$. The red profile represents the original profile in chapter 4.

m/s.

In figure 5.4.6, V_{cell} not only goes up as $u^{\text{in}}_{\text{fuel}}$ goes down, but also covers a larger current density region before V_{cell} reaches zero. The the rise in V_{cell} is linked with the drop in activation and Ohmic polarisation associated with higher operating temperatures for the same values of R_{load}. The rise in both i and V_{cell} results in a more drastic rise in P_{cell} (as shown in figure 5.4.7), with P_{cell} rising as high as almost 3.5 W/cm^2 when $u^{\text{in}}_{\text{fuel}}$ is equal to 1 m/s. The rise in fuel utilisation associated with the drop in $u^{\text{in}}_{\text{fuel}}$ means that electrical efficiency also goes up, reaching a peak of around 16% when $u^{\text{in}}_{\text{fuel}} = 1$ m/s.

The only main downside of this peak is that the operating temperature at this peak will be much higher than before. But overall, the efficiency and performance of the cell does improve when $u^{\text{in}}_{\text{fuel}}$ is lowered, as long as $\dot{N}^{\text{in}}_{\text{fuel}}$ is kept fixed. The effect of changing $\dot{N}^{\text{in}}_{\text{fuel}}$ on SOFC performance will be investigated later on in this chapter. As for the multiplicity region in figure 5.4.2, nine pairs of ignition/extinction points were determined in the

derivation of this multiplicity region. The ignition/extinction points were determined for values of $u_{\text{fuel}}^{\text{in}}$ equal to 1.25 m/s, 1.5 m/s, 1.75 m/s, 2 m/s, 2.25 m/s, 2.5 m/s, 2.88 m/s (original value), 3.5 m/s and 4 m/s. A third order polynomial approximation was fitted onto the set of ignition and the set of extinction points.

5.5 Inlet air velocity $u_{\text{air}}^{\text{in}}$

Figure 5.5.1 represents the R_{load} vs T_{cell} profiles for varying values of $u_{\text{air}}^{\text{in}}$. Compared to the profile in figure 5.4.1, the effect of lowering $u_{\text{air}}^{\text{in}}$ on SOFC performance is very similar to the effect of lowering $u_{\text{fuel}}^{\text{in}}$ on cell performance, only except the range of values of $u_{\text{air}}^{\text{in}}$ considered here is much broader.

Just like with $u_{\text{fuel}}^{\text{in}}$, lowering $u_{\text{air}}^{\text{in}}$ lowers the amount of heat removed by convection, and also increases air (and Oxygen) levels within the air channel, which means that more Oxygen is available for consumption. The inlet molar flow rate of the air flow is kept fixed. As $\dot{N}_{\text{air}}^{\text{in}}$ is larger than $\dot{N}_{\text{fuel}}^{\text{in}}$ (it is set at 3.8 mol/s), $u_{\text{air}}^{\text{in}}$ has to be lowered a lot more to ensure that more air is present in the air channel at the same level as the increase in fuel concentration levels in the fuel channel due to a drop in $u_{\text{fuel}}^{\text{in}}$. A drop in $u_{\text{air}}^{\text{in}}$ increases the amount of air (and Oxygen) in the air channel, which means that more Oxygen is available for consumption within the reduction reaction (3.2) in the Cathode. The increase in Oxygen available for consumption leads to an increase in electrochemical activity, increasing T_{cell}, and increasing cell current I along with it. Since the consumption rate of Oxygen is lower than the consumption rate of Hydrogen, much more Oxygen is needed to enable the cell to operate at a higher operating temperature compared to before. But otherwise, the effects of lowering $u_{\text{air}}^{\text{in}}$ on SOFC performance is the same as lowering $u_{\text{fuel}}^{\text{in}}$, only except it has to be reduced by much more.

Figure 5.5.2 represents the multiplicity region of the SOFC for varying values of $u_{\text{air}}^{\text{in}}$. The multiplicity region disappears only when $u_{\text{air}}^{\text{in}}$ is as low as 10 m/s. The region in

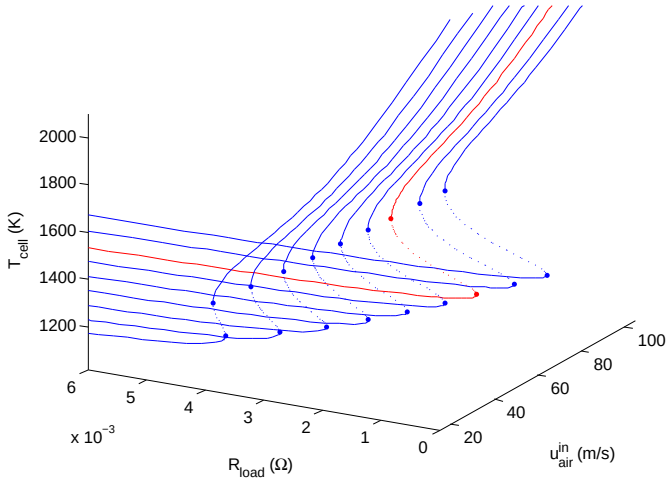

Figure 5.5.1: R_{load} vs T_{cell} for varying values of $u_{\text{air}}^{\text{in}}$. The red profile represents the original profile in chapter 4.

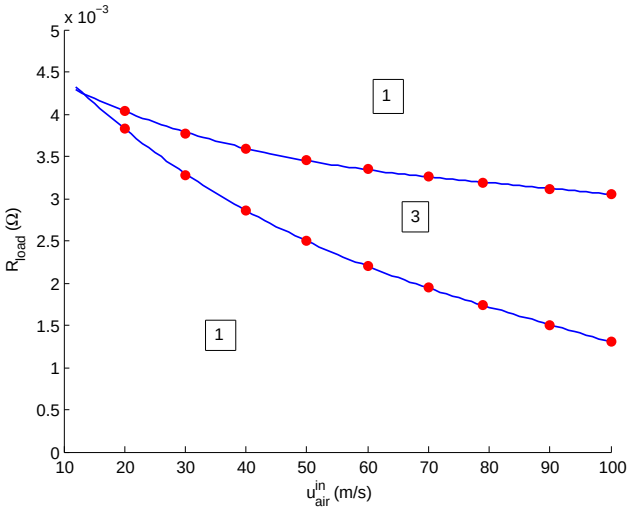

Figure 5.5.2: The multiplicity region for changes in $u_{\text{air}}^{\text{in}}$. The boxed numbers represent the number of steady-state solutions in a particular region. The red points represent the location of the ignition and extinction points.

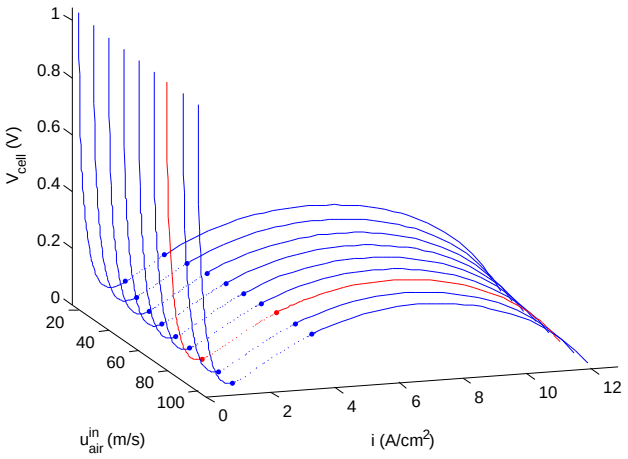

Figure 5.5.3: i vs V_{cell} for varying values of $u_{\text{air}}^{\text{in}}$. The red profile represents the original profile in chapter 4.

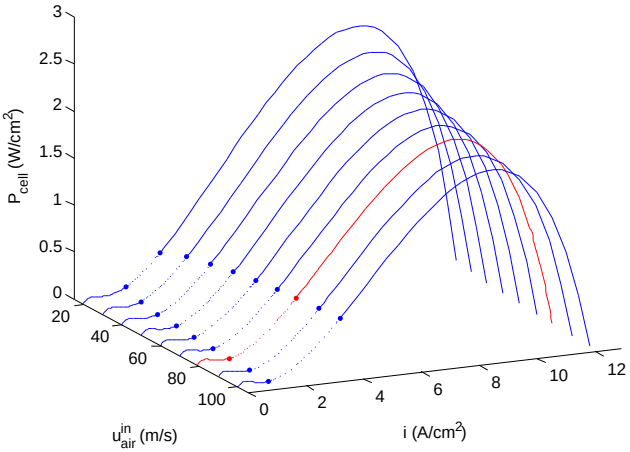

Figure 5.5.4: i vs P_{cell} for varying values of $u_{\text{air}}^{\text{in}}$. The red profile represents the original profile in chapter 4.

figure 5.5.2 is thinner than the multiplicity region in figure 5.4.2, which means that the SOFC is less sensitive to changes in $u_{\text{air}}^{\text{in}}$ compared to changes in $u_{\text{fuel}}^{\text{in}}$. In the derivation of the multiplicity region in figure 5.5.2, nine pairs of ignition/extinction points were considered for values of $u_{\text{air}}^{\text{in}}$ equal to 20 m/s, 30 m/s, 40 m/s, 50 m/s, 60 m/s, 70 m/s, 78.98 m/s (original value), 90 m/s and 100 m/s. A third-order polynomial approximation was applied to the set of ignition points and extinction points.

Figures 5.5.3 and 5.5.4 show the V-I profiles and P-I profiles respectively for different values of $u_{\text{air}}^{\text{in}}$. Just like the equivalent profiles in section 5.4, there is a rise in both V_{cell} and P_{cell} over a larger region of current density values. The extent in which V_{cell} and P_{cell} is not as high for changes in $u_{\text{air}}^{\text{in}}$ compared to changes in $u_{\text{fuel}}^{\text{in}}$. But the effects are more or less the same.

Overall, modifying the inlet gas flow velocities affects SOFC performance (as well as the existence and shift of the multiplicity region) more than by modifying the inlet gas flow temperatures. This is because there is a link between the inlet gas flow velocity and the inlet molar flow rate, where, if the inlet molar flow rate is kept fixed, decreasing the inlet gas flow velocity results in a higher concentration of fuel/air within their respective channels, at a lower velocity. Since the inlet mole fractions of Hydrogen and Oxygen are also kept fixed, a rise in fuel/air levels means that there is more Hydrogen/Oxygen available to be consumed within the SOFC. The increase in electrochemical activity results in a rise in the amount of heat produced in the cell. The shift in the heat production curve (aligned with a slight drop in the heat removal curve) shifts the cell temperature values towards higher values of R_{load} (more so compared to increasing the inlet gas flow temperatures). The bigger rise in T_{cell} associated with lowering the inlet gas flow velocities results in a bigger rise in I (resulting in a new peak for current density i). A rise in I results in a rise in the consumption rate of Hydrogen and Oxygen. Since the inlet fuel molar flow rate is kept fixed, this means that more fuel is utilised within the cell. The rise

in T_{cell} results in a rise in V_{cell} due to a drop in activation and Ohmic polarisation. The rise in V_{cell} and i results in a rise in P_{cell} towards a new peak. Since both fuel utilisation and voltage efficiency rise with lowering $u^{\text{in}}_{\text{fuel}}$ and $u^{\text{in}}_{\text{air}}$, there is also a rise in electrical efficiency towards a new peak (with efficiency values exceeding 16% for a drop in $u^{\text{in}}_{\text{fuel}}$). Overall, dropping the inlet gas velocity (especially the fuel velocity) results in a more efficient cell. This was not shown clearly enough in [49] where they only consider one increase and one decrease in both inlet gas flow velocities.

5.6 Inlet Fuel Molar Flow rate $\dot{N}^{\text{in}}_{\text{fuel}}$

Figure 5.6.1 represents the R_{load} vs T_{cell} profiles for varying values of $\dot{N}^{\text{in}}_{\text{fuel}}$. The behaviour of T_{cell} varies much more for changes in $\dot{N}^{\text{in}}_{\text{fuel}}$ compared to the other inlet parameters considered so far. As it turns out, neither in increasing $\dot{N}^{\text{in}}_{\text{fuel}}$ nor decreasing $\dot{N}^{\text{in}}_{\text{fuel}}$ has much of an impact in terms of removing the multiplicity region altogether, as shown in figure 5.6.2. In figure 5.6.1, it looks like that increasing and decreasing $\dot{N}^{\text{in}}_{\text{fuel}}$ actually increases the multiplicity region towards lower values of R_{load} (more sharply if $\dot{N}^{\text{in}}_{\text{fuel}}$ is lowered).

As mentioned before in this chapter, there is a link between the inlet molar flow rate and the inlet gas velocity. Decreasing the inlet gas velocity increases the concentration of fuel/air within their respective gas channels (at a lower flow velocity) if the inlet molar flow rate is kept fixed. In this case however, the inlet gas flow velocity is kept fixed. This means that modifying the inlet molar flow rate changes the concentration of fuel/air entering the cell, only this time it enters the cell at the same inlet gas flow velocity. Decreasing $\dot{N}^{\text{in}}_{\text{fuel}}$ reduces the concentration of fuel (and Hydrogen) entering the fuel channel, meaning that there is less Hydrogen available for consumption within the fuel cell. Since the inlet fuel velocity is fixed, reducing $\dot{N}^{\text{in}}_{\text{fuel}}$ also lowers the amount of heat removed from the cell due to convection, since there is a lower concentration of fuel entering the fuel channel. As it

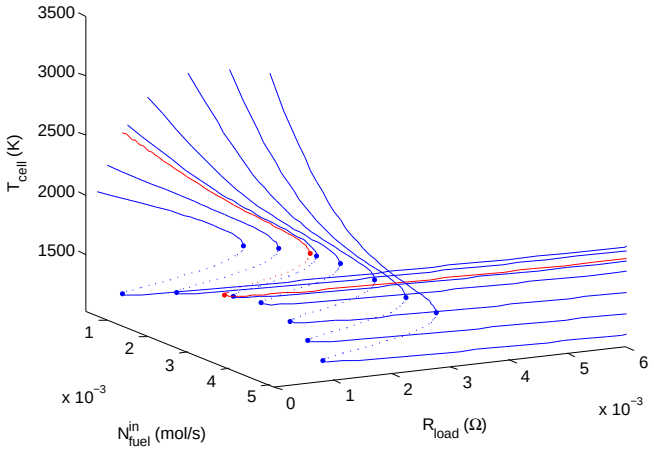

Figure 5.6.1: R_{load} vs T_{cell} for varying values of $\dot{N}^{\text{in}}_{\text{fuel}}$. The red profile represents the original profile in chapter 4.

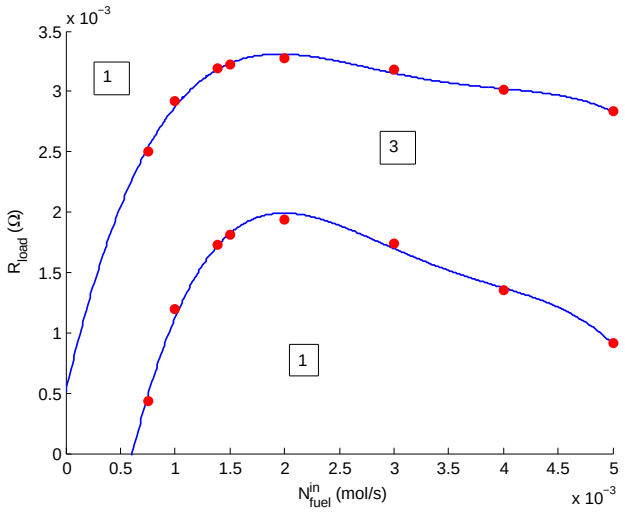

Figure 5.6.2: The multiplicity region for changes in $\dot{N}^{\text{in}}_{\text{fuel}}$. The boxed numbers represent the number of steady-state solutions in a particular region. The red points represent the location of the ignition and extinction points.

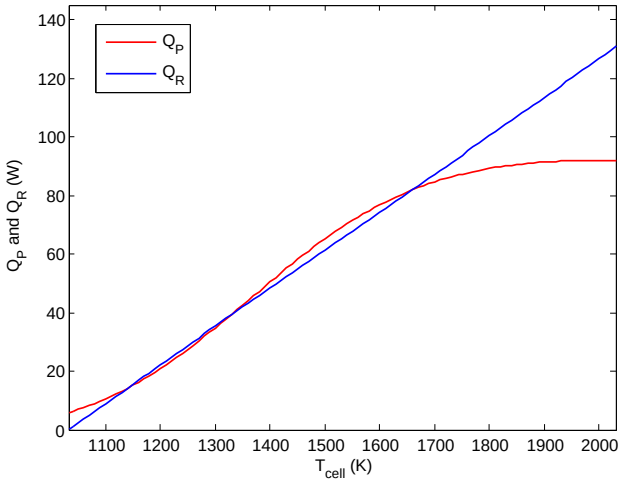

Figure 5.6.3: Heat Production (Red) and Heat Removal (Blue) Curves for rising T_{cell}, where $\dot{N}^{\text{in}}_{\text{fuel}} = 1 \times 10^{-3}$ mol/s ($R_{\text{load}} = 0.0025\ \Omega$).

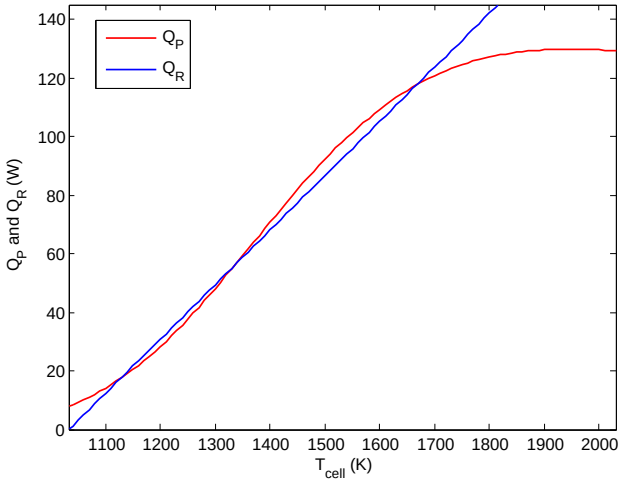

Figure 5.6.4: Heat Production (Red) and Heat Removal (Blue) Curves for rising T_{cell}, where $\dot{N}^{\text{in}}_{\text{fuel}} = 5 \times 10^{-3}$ mol/s ($R_{\text{load}} = 0.0025\ \Omega$).

turns out, modifying $\dot{N}_{\text{fuel}}^{\text{in}}$ has a much bigger impact on the amount of heat removed by convection compared to modifying the inlet gas velocities and temperatures.

Looking at figure 5.6.3, compared to the equivalent profile for the base case in figure 4.2.7, reducing $\dot{N}_{\text{fuel}}^{\text{in}}$ does impact both the amount of heat produced within the cell (whose peak is lower than 100 W) and the amount of heat removed by convection (as shown by a less steeper Q_{R} curve). The effect of $\dot{N}_{\text{fuel}}^{\text{in}}$ on Q_{R} is even more noticeable when $\dot{N}_{\text{fuel}}^{\text{in}}$ is increased. Increasing $\dot{N}_{\text{fuel}}^{\text{in}}$ increases the concentration of fuel entering the fuel cell, at the same velocity as before. The consequence of this is that this greatly increases the amount of heat removed by convection as shown in figure 5.6.4.

The curve for Q_{R} is much steeper than before. As a result of this, the values of T_{cell} along the lower, un-ignited steady-state branch are shifted towards lower values of R_{load}. This means that R_{load} has to be reduced to a lower value to encourage greater electrochemical activity. But the consequence of this is that not only is the ignition point located at a lower value of R_{load}, but the change in T_{cell} after ignition will be a lot larger if the SOFC ignites (as figure 5.6.1 shows).

Since there is a lot more Hydrogen within the cell, there is the potential for the cell to operate at much higher operating temperatures, with a higher current density peak, higher cell voltage, and much higher power density curves as more and more Hydrogen is consumed within the fuel cell. This only occurs when the cell operates along the upper, ignited steady-state branch, where the higher operating temperatures encourage greater electrochemical activity within the cell. This corresponds with the rise in the heat production curve in 5.6.4.

Operating temperatures increase a lot more along the ignited steady-state branch as $\dot{N}_{\text{fuel}}^{\text{in}}$ is increased. The larger rise in T_{cell} along the ignited branch results in a larger rise in I, resulting in much larger consumption rates. And the mixture of rising T_{cell} and rising I results in larger values of V_{cell} and P_{cell} for a much wider range of values of the current

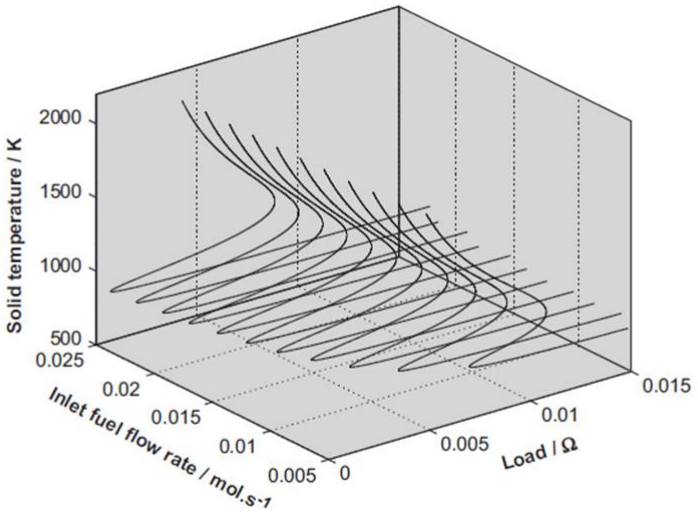

Figure 5.6.5: The equivalent 3D profile of T_{cell} for changes in the inlet fuel molar flow rate in [49].

density. But this only occurs along the ignited steady-state branch, where the amount of heat produced in the SOFC can overcome the amount of heat removed by convection.

Comparing figure 5.6.1 to the equivalent profile in [49] (see figure 5.6.5), the profiles are very different. The reason as to why the multiplicity region here varies a lot more in this model compared to [49] is because the amount of heat produced in the SOFC in this model is more sensitive to changes in $\dot{N}_{\text{fuel}}^{\text{in}}$ than it is in [49]. The model in [49] does not fully take into effect the change in amount of heat produced in the SOFC when $\dot{N}_{\text{fuel}}^{\text{in}}$ is modified. The change in the profile of T_{cell} is mainly due to the change in the amount of heat removed by convection more than a change to both the amount of heat produced and heat removed from the SOFC in [49]. Plus, they only consider temperature values up to just above 2000 K, so any sharp rises in T_{cell} along the ignited steady-state branch due to more Hydrogen being available for consumption is not shown.

The effect of a rise in $\dot{N}_{\text{fuel}}^{\text{in}}$ on V_{cell} and P_{cell} is shown in figures 5.6.6 and 5.6.7. The amount in which both of these parameters rise along the assumed unstable and ignited steady-state branches, and the increase in the range of current density values is much, much

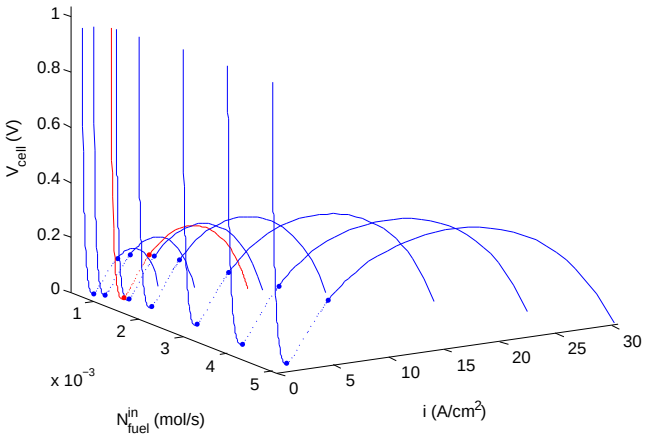

Figure 5.6.6: i vs V_{cell} for varying values of $\dot{N}^{\text{in}}_{\text{fuel}}$. The red profile represents the original profile in chapter 4.

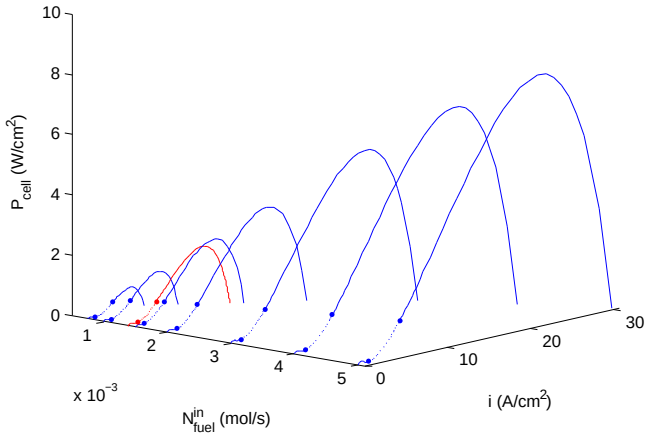

Figure 5.6.7: i vs P_{cell} for varying values of $\dot{N}^{\text{in}}_{\text{fuel}}$. The red profile represents the original profile in chapter 4.

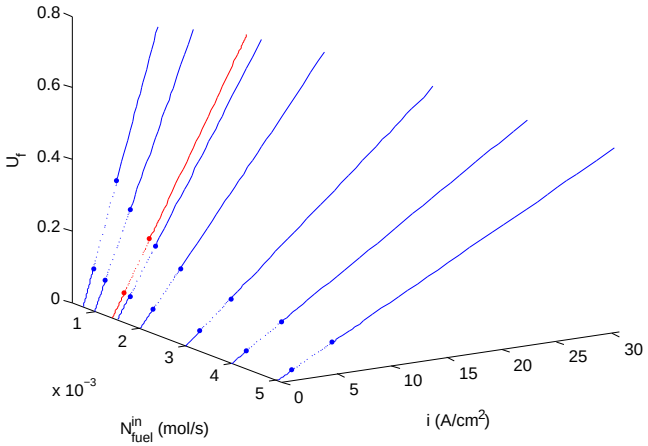

Figure 5.6.8: i vs U_{F} for varying values of $\dot{N}^{\mathrm{in}}_{\mathrm{fuel}}$. The red profile represents the profile for the base case in chapter 4.

greater than the equivalent curves for all the other previous sections. For $\dot{N}^{\mathrm{in}}_{\mathrm{fuel}} = 5 \times 10^{-3}$ mol/s, the peak current density value is slightly higher then 30 A/cm^2. Across these values, V_{cell} exceeds 0.4 V along the ignited steady-state branch, and P_{cell} has a peak that exceeds 8 W/cm^2.

However, raising $\dot{N}^{\mathrm{in}}_{\mathrm{fuel}}$ actually lowers the percentage of fuel utilised within the SOFC (as shown in figure 5.6.8) since there is a lot more Hydrogen that needs to be consumed. Despite the large rise in T_{cell} and I, there is still plenty of Hydrogen which is left unused. The reason why parameters such as T_{cell} and I increase greatly is because of the increased supply of Hydrogen within the SOFC. But that does not equate to higher fuel utilisation levels. To increase fuel utilisation, $u^{\mathrm{in}}_{\mathrm{fuel}}$ would have to be decreased as well to ensure that more Hydrogen is consumed within the SOFC at lower temperatures. As a consequence of lower fuel utilisation, electrical efficiency does not rise as much as P_{cell} when $\dot{N}^{\mathrm{in}}_{\mathrm{fuel}}$ is raised. In fact, it only goes up to a peak of around 11%, which is not as high as the peak

achieved when $u^{\text{in}}_{\text{fuel}}$ is set equal to 1 m/s.

Since the multiplicity region does not disappear for a rise or drop in $\dot{N}^{\text{in}}_{\text{fuel}}$, the multiplicity region in figure 5.6.2 looks very different to the other multiplicity regions considered. There are eight pairs of ignition/extinction points considered for values of $\dot{N}^{\text{in}}_{\text{fuel}}$ equal to 0.75×10^{-3} mol/s, 1×10^{-3} mol/s, 1.39×10^{-3} mol/s (original value), 1.5×10^{-3} mol/s, 2×10^{-3} mol/s, 3×10^{-3} mol/s, 4×10^{-3} mol/s, and 5×10^{-3} mol/s. Due to how the ignition and extinction points are spread out, a fourth order polynomial approximation was fitted to the set of ignition points and the set of extinction points. The fit is not as good as the other fits in this section, but the points are still very close to the curves.

5.7 Inlet Air Molar Flow Rate $\dot{N}^{\text{in}}_{\text{air}}$

Figure 5.7.1 represents the R_{load} vs T_{cell} profiles for varying values of $\dot{N}^{\text{in}}_{\text{air}}$. Compared to the profile in figure 5.6.1, the behaviour of the cell for changes in $\dot{N}^{\text{in}}_{\text{air}}$ is a bit more predictable. Lowering $\dot{N}^{\text{in}}_{\text{air}}$ lowers the amount of air entering the cell, and since the inlet air velocity is set at 78.98 m/s, it lowers the amount of heat removed by convection. The amount of heat produced does not change greatly since Oxygen levels in the Air flow do not drop down by a huge amount. This is partly due to the lower consumption rate of Oxygen in the SOFC compared to the consumption rate of Hydrogen. But it is mainly due to how big the inlet air velocity is (which remains fixed), which means that only a certain amount of Oxygen can be consumed within the fuel cell with the air flow travelling as fast as it is. As shown in the multiplicity region graph in figure 5.7.2, reducing $\dot{N}^{\text{in}}_{\text{air}}$ shifts the multiplicity region towards higher values of R_{load}. The multiplicity region disappears for $\dot{N}^{\text{in}}_{\text{air}}$ less than 2.5×10^{-2} mol/s.

If $\dot{N}^{\text{in}}_{\text{air}}$ is increased, then more air enters the cell at a velocity of 78.98 m/s at the inlet. This means that more heat is removed from the cell by convection on the air flow side. The amount of heat produced in the cell does not vary that much, so the size of the multiplicity

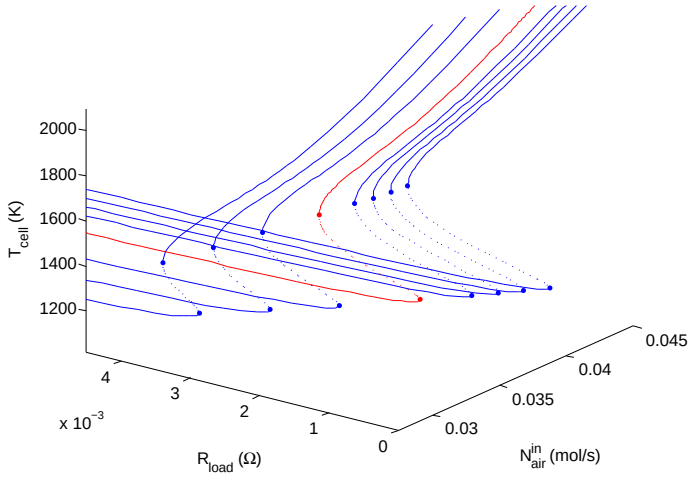

Figure 5.7.1: R_{load} vs T_{cell} for varying values of $\dot{N}_{\text{air}}^{\text{in}}$. The red profile represents the original profile in chapter 4.

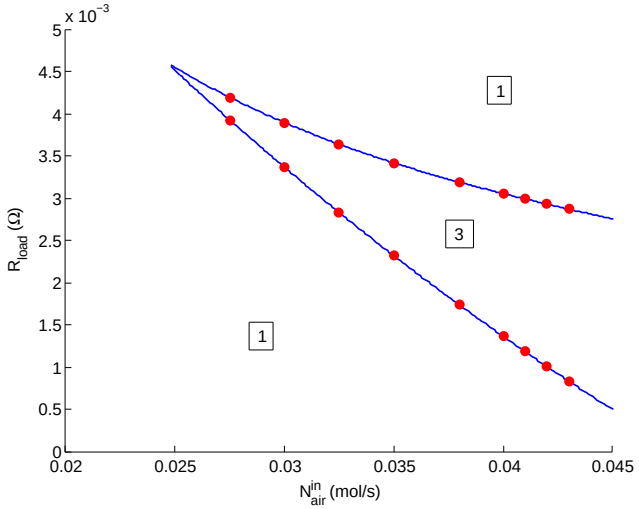

Figure 5.7.2: The multiplicity region for changes in $\dot{N}_{\text{air}}^{\text{in}}$. The boxed numbers represent the number of steady-state solutions in a particular region. The red points represent the location of the ignition and extinction points.

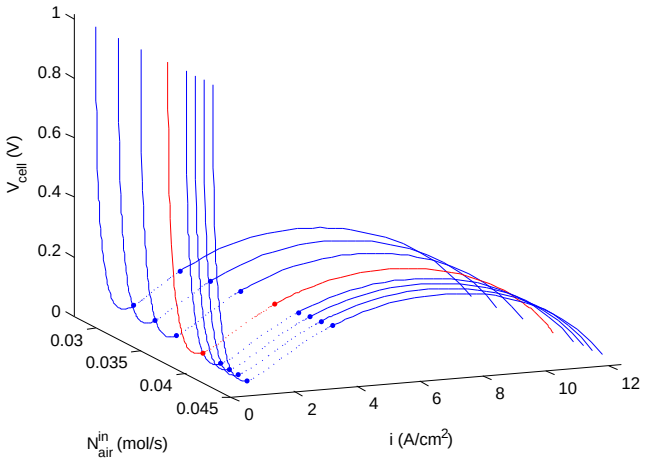

Figure 5.7.3: i vs V_{cell} for varying values of $\dot{N}_{\text{air}}^{\text{in}}$. The red profile represents the original profile in chapter 4.

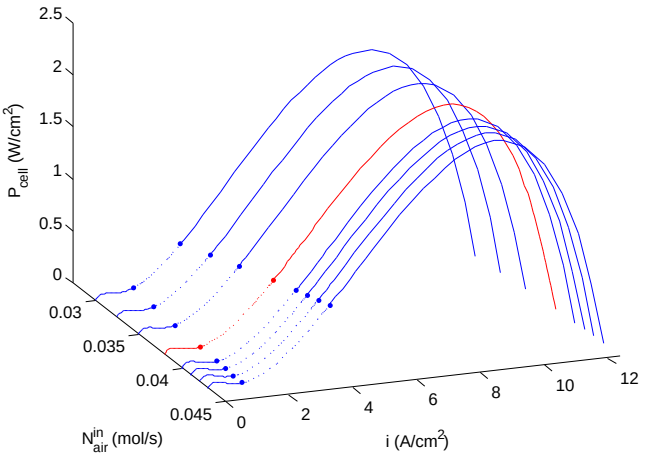

Figure 5.7.4: i vs P_{cell} for varying values of $\dot{N}_{\text{air}}^{\text{in}}$. The red profile represents the original profile in chapter 4.

region increases for higher values of $\dot{N}_{\text{air}}^{\text{in}}$. There were nine pairs of ignition/extinction points considered for values of $\dot{N}_{\text{air}}^{\text{in}}$ equal to 0.0275 mol/s, 0.03 mol/s, 0.0325 mol/s, 0.035 mol/s, 0.038 mol/s (original value), 0.04 mol/s, 0.041 mol/s, 0.042 mol/s, and 0.043 mol/s. A third-order polynomial approximation was fitted to the set of ignition points and the set of extinction points. The profile shown in figure 5.7.1 is more similar to the equivalent profile in [49] in terms of how the multiplicity region is affected for changes in $\dot{N}_{\text{air}}^{\text{in}}$. The only difference is that the SOFC considered here is more sensitive to changes in $\dot{N}_{\text{air}}^{\text{in}}$ compared to the SOFC in [49].

The V-I profiles and P-I profiles for varying values of $\dot{N}_{\text{air}}^{\text{in}}$ are shown in figures 5.7.3 and 5.7.4. There is not a huge change in V_{cell} and P_{cell} for different values of $\dot{N}_{\text{air}}^{\text{in}}$. The only main difference is that for higher values of $\dot{N}_{\text{air}}^{\text{in}}$, there is more Oxygen available for consumption within the SOFC, which results in a higher current density peak. However, this just results in a shift of the V_{cell} and P_{cell} profiles (along the ignited steady-state branch) towards higher values of i. There is not a huge change in the amount of fuel consumed, and how efficient the cell is. Changing $\dot{N}_{\text{air}}^{\text{in}}$ mainly affects the amount of heat removed by convection.

5.8 Summary

In this chapter, the effect of each individual inlet parameter related to the fuel and air flow on SOFC performance (and steady-state multiplicity) was investigated. The six inlet parameters considered were $T_{\text{fuel}}^{\text{in}}$, $T_{\text{air}}^{\text{in}}$, $u_{\text{fuel}}^{\text{in}}$, $u_{\text{air}}^{\text{in}}$, $\dot{N}_{\text{fuel}}^{\text{in}}$ and $\dot{N}_{\text{air}}^{\text{in}}$. Changing the inlet gas flow temperatures affects the heat of the solid cell component. Increasing either of the inlet gas flow temperatures lowers the amount of heat removed by convection (since the gap between T_{cell} and the gas flow temperature is lower), causing a rise in the operating cell temperature T_{cell}. A rise in T_{cell} results in a quicker and easier activation of the electrochemical reactions, increasing V_{cell}. This rise in V_{cell} causes the power density P_{cell}

to rise towards a new peak. Also, since the amount of fuel and air entering the cell is unchanged, as well as its velocity at the inlet, more fuel is utilised at these higher temperatures, which in turn increases the electrical efficiency of the cell.

Looking at the multiplicity regions in figures 5.2.2 and 5.3.2, increasing the inlet gas flow temperatures shifts the multiplicity region towards higher values of R_{load}, where it also shrinks. If the inlet gas flow temperature is set high enough, the multiplicity region disappears altogether, removing any threat of the formation of any localised hot spots. The SOFC is more sensitive to changes in $T_{\text{air}}^{\text{in}}$ than $T_{\text{fuel}}^{\text{in}}$ because of the larger value of the Cathode-side heat-transfer coefficient compared to the Anode-side heat-transfer coefficient. The reduction in the gap between T_{cell} and T_{air} associated with a rise in $T_{\text{air}}^{\text{in}}$ greatly reduces the impact of the Cathode-side heat-transfer coefficient. The rise in T_{cell} with rising $T_{\text{fuel}}^{\text{in}}$ and $T_{\text{air}}^{\text{in}}$ means that R_{load} can be set at higher values.

SOFC performance is influenced more by changes in the inlet gas flow velocities, and changes in the inlet molar flow rates (for the fuel flow at least). Changing the inlet gas flow velocities not only affects the amount of heat removed by convection, but it also affects the concentration levels of both gas flows in their respective gas channels. Reducing the inlet gas flow velocities increases the concentration of fuel/air in the fuel/air channel, since the inlet molar flow rates are kept fixed. Since there is more fuel/air in the fuel/air channel at a lower velocity, there is more Hydrogen/Oxygen available for consumption within the SOFC (since inlet mole fractions are also kept fixed). This increase in electrochemical activity not only results in a rise in T_{cell} (which in turn results in a rise in V_{cell} due to the reduction in activation and Ohmic polarisation), but also a rise in the cell current I due to the larger amount of Hydrogen/Oxygen available for consumption. This results in the current density i reaching towards a new peak. Power density also increases along with rising V_{cell} and i, and since more fuel is utilised within the cell, the electrical efficiency of the cell is larger as well.

For both multiplicity regions in figures 5.4.2 and 5.5.2, the multiplicity region is shifted towards larger values of R_{load} for a decrease in either $u_{\text{fuel}}^{\text{in}}$ or $u_{\text{air}}^{\text{in}}$. The SOFC is more sensitive to changes in $u_{\text{fuel}}^{\text{in}}$ than $u_{\text{air}}^{\text{in}}$, since $\dot{N}_{\text{fuel}}^{\text{in}}$ is also small as well. Plus, the consumption rate of Hydrogen is larger than Oxygen. A small change in $u_{\text{fuel}}^{\text{in}}$ results in a quite big change in the amount of Hydrogen available for consumption within the SOFC.

Changing $\dot{N}_{\text{fuel}}^{\text{in}}$ and $\dot{N}_{\text{air}}^{\text{in}}$ has a much bigger impact on the amount of heat removed by convection than changing the other four inlet parameters considered in this chapter. Changing $\dot{N}_{\text{fuel}}^{\text{in}}$ has a more drastic effect on SOFC performance than you get by changing $\dot{N}_{\text{air}}^{\text{in}}$, especially as there is no value of $\dot{N}_{\text{fuel}}^{\text{in}}$ in figure 5.6.2 in which the multiplicity region disappears. Since the inlet gas flow velocities are kept fixed, modifying $\dot{N}_{\text{fuel}}^{\text{in}}$ changes the concentration of fuel entering the fuel channel. But it enters the fuel channel at the same velocity. This has the effect of increasing the amount of heat removed by convection on the fuel flow side more drastically. Because of this, the multiplicity region increases in size, and shifts towards lower values of R_{load}. It is only for higher values of T_{cell} along the ignited steady-state branch in which there is a significant increase in electrochemical activity (due to the larger amount of Hydrogen available), resulting in T_{cell}, I, V_{cell} and P_{cell} reaching new, much larger peaks across the ignited steady-state branch. However, because of the larger amount of Hydrogen that enters the SOFC at the same inlet velocity, less of the fuel is utilised within the SOFC, which means that electrical efficiency is does not rise as much as P_{cell}.

Modifying $\dot{N}_{\text{air}}^{\text{in}}$ mainly affects the amount of heat removed by convection, lowering it when it is dropped. It does not affect the amount of heat produced in the cell due to the electrochemical reactions that much since the velocity of the air flow is still very high. Only by modifying $u_{\text{air}}^{\text{in}}$ can you affect the amount of heat produced in the cell due to increased electrochemical activity within the cell.

Taking all of this into account, the best way to improve cell performance is to not only

increase the concentration of fuel and air within their respective gas channels, but to also make sure that it enters the gas channels at a lower velocity. This is not only to ensure that more Hydrogen/Oxygen is available for consumption, but also to lower the amount of heat removed from the cell due to convection. Doing this for the fuel flow will ensure that more Hydrogen is consumed within the SOFC for higher values of R_{load}, which in turn increases the operating temperature; the amount of current drawn from the cell; the amount of fuel utilised within the cell; the voltage and power density; and the electrical efficiency. Decreasing the inlet gas flow velocities will reduce the multiplicity region and ensure a more efficiently operating cell. You can increase $\dot{N}^{\text{in}}_{\text{fuel}}$ to increase the amount of Hydrogen entering the fuel channel. But it would be best to couple that with a drop in $u^{\text{in}}_{\text{fuel}}$ to ensure that more fuel is utilised for lower operating temperatures, improving the efficiency of the cell. As for the air flow, SOFC performance can be maximised by increasing the inlet air temperature, and decreasing the inlet air velocity so that more Oxygen is consumed within the SOFC. Raising both inlet gas flow temperatures can also improve the performance of the cell, but not as much as decreasing the inlet gas flow velocities.

Chapter 6

Results: Potentiostatic and Galvanostatic Operations

6.1 Introduction

In this chapter, the steady-state performances of a SOFC under a potentiostatic (constant cell voltage) and a galvanostatic (constant cell current) operation are investigated. This chapter starts off by looking into the steady-state behaviour of the SOFC operating under a constant cell voltage with inlet parameter values based on the values in Appendix B. Heat production and heat removal at five different points of V_{cell} will also be looked into to see how heat production and heat removal varies for this mode of operation. Multiplicity regions for changes in the six inlet parameters covered in the previous chapter will also be investigated. This chapter finishes by looking at the steady-state behaviour of the SOFC operating under a constant cell current with the inlet parameters based on the values in Appendix B. Only one steady-state solution exists for that mode of operation

6.2 Potentiostatic Operation

In this section, the steady-state behaviour of the SOFC under a potentiostatic operation is investigated, where the inlet parameters are equal to the values given in Appendix B. The steady-state equations for this case are given in Appendix F.1. The heat production and heat removal curves for varying T_{cell} will be investigated for five different values of V_{cell}, showing the transition of both curves from one steady-state solution to three, then back to one as V_{cell} is lowered. This section ends by looking at the multiplicity regions of the SOFC under a potentiostatic operation for changes in each of the six inlet parameters considered in the previous chapter.

6.2.1 Base Case

Figure 6.2.1 shows the profile of T_{cell} for different values of V_{cell}. Looking at the figure, there is more than one steady-state solution for $V_{\text{cell}} \in [0.028517, 0.2595521]$. Compared to the equivalent profiles from [47] and [49] (with different values of the inlet gas flow temperatures), the multiplicity region is noticeably smaller than those two profiles, with the multiplicity region being of a size around 0.3 V in [47], and being as big as just over 0.35 V in [49] (where the inlet gas flow temperatures are equal to 950 K). Another thing that is noticeable is that the change in T_{cell} after ignition is not as big as the change in T_{cell} in [47] and [49], with T_{cell} going up from just over 1170 K to around 2590 K after ignition. The main reason for the difference in the size of the multiplicity region, and the lower value of T_{cell} after ignition compared to [47] and [49] is because of the amount of heat that is removed from the cell due to convection in this model (which is larger here than in [47] and [49]).

Despite this, the rise in T_{cell} for this mode of operation is more severe compared to the rise in T_{cell} after ignition for a Solid Oxide Fuel Cell operating under a constant external load. The values of T_{cell} along the ignited steady-state branch are higher for this mode of

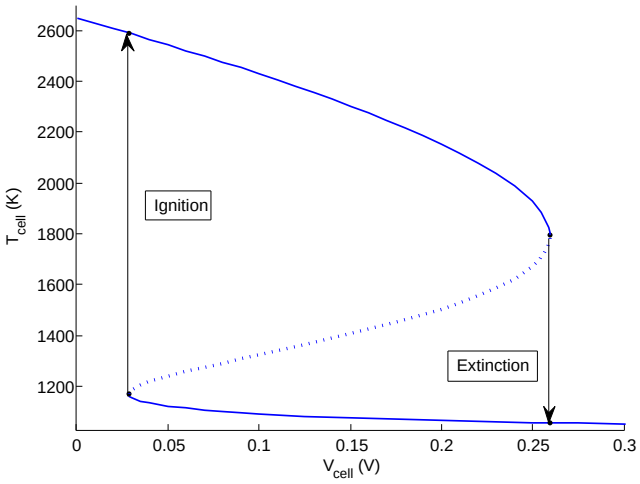

Figure 6.2.1: V_{cell} vs T_{cell} for a Solid Oxide Fuel Cell operating under a potentiostatic operation, with the inlet parameters based on the values in Appendix B.

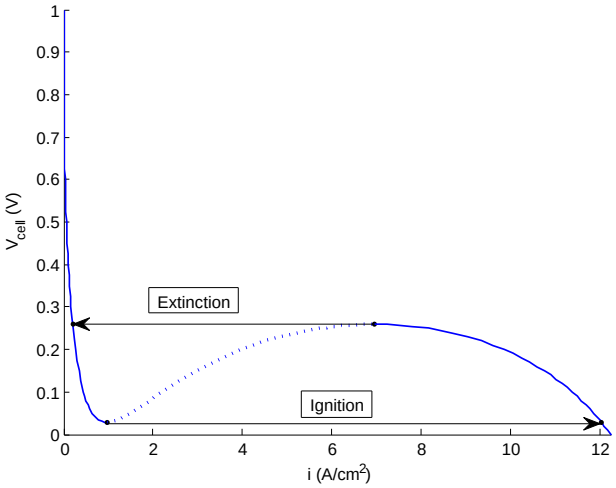

Figure 6.2.2: i vs V_{cell} for a Solid Oxide Fuel Cell operating under a potentiostatic operation, with the inlet parameters based on the values in Appendix B.

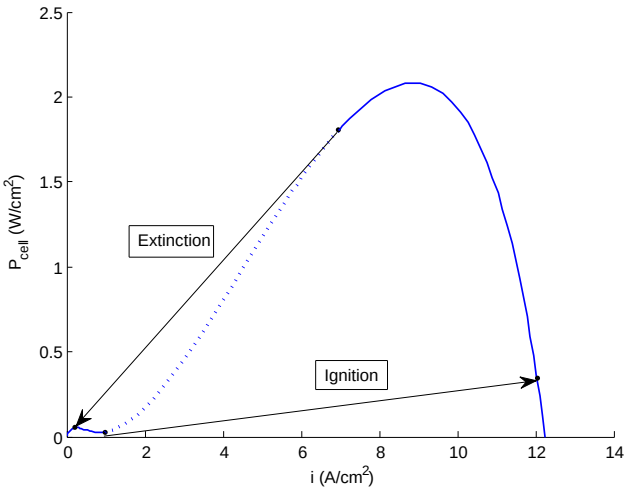

Figure 6.2.3: i vs V_{cell} for a Solid Oxide Fuel Cell operating under a potentiostatic operation, with the inlet parameters based on the values in Appendix B.

operation compared to the constant external load case. During the extinction phase, T_{cell} drops from around 1795 K to around 1057 K.

Figure 6.2.2 represents the V-I profile of a Solid Oxide Fuel Cell operating under a constant cell voltage. Since V_{cell} is the constant bifurcation parameter in this case, the value of V_{cell} does not change during ignition and extinction. Only the current density i changes during ignition and extinction in figure 6.2.2. During the ignition phase, i jumps up from 0.9681 A/cm^2 to 12.0421 A/cm^2, which is located near the end of the V-I profile. This results in a rise in fuel utilisation from around 5.775% to 71.8317%–a jump of over 65%! During extinction, i drops from 6.9541 A/cm^2 down to 0.2034 A/cm^2.

Figure 6.2.3 represents the Power Density profile P_{cell} for rising values of i. Compared to the power density profile in chapter 4, the peak of P_{cell} in figure 6.2.3 is not as high as the peak in figure 4.5.1, and the value of P_{cell} after ignition is not as high as the value of P_{cell} after ignition for the constant external load case. After ignition, P_{cell} only rises from

around 0.0276 W/cm^2 to around 0.3434 W/cm^2. After ignition, the SOFC is operating at a point along the ignited steady-state branch where i is very close to its limiting current density value (where mass transfer resistances take shape as V_{cell} approaches zero). This also affects the rise in electrical efficiency as well (since voltage efficiency is very close to zero), with electrical efficiency only going up to around 1.3% after ignition (despite a large rise in fuel utilisation). During the extinction phase, power density drops down from a much higher value of around 1.8049 W/cm^2 to around 0.0528 W/cm^2 (while electrical efficiency drops down from around 8.5% to around 0.25%).

6.2.2 Heat Production/Heat Removal profiles for rising T_{cell}

Figures 6.2.4-6.2.8 represent the profiles of the heat production (Q_{P}) and the heat removal (Q_{R}) curves with rising T_{cell} for five different fixed values of V_{cell}. Since the value of T_{cell} after ignition is larger its equivalent value for the constant external load case, a larger range of values for T_{cell} is considered. The steady-state model is the same as the steady-state model for a Solid Oxide Fuel Cell operating under a constant cell voltage, only except the equation for T_{cell} is removed since T_{cell} is constant, and the equations for Q_{P} (equation (3.37)) and Q_{R} (equation (3.38)) are incorporated into the model.

Running down each figure in this subsection, V_{cell} for each figure goes down in descending order. Comparing these profiles with the equivalent heat production/removal profiles in chapter 4, the main difference between the two modes of operation is the rise in the amount of heat produced with rising T_{cell}. The rise in Q_{P} for this mode of operation is quite sluggish for low values of T_{cell} compared to the constant external load mode of operation. However, for higher values of T_{cell}, there is a more prolonged rise in Q_{P} towards its peak value for this mode of operation.

When V_{cell} is dropped, the amount of heat produced within the SOFC can rise up to a peak exceeding 200 W, whereas the peak of the heat production curve in chapter 4 only

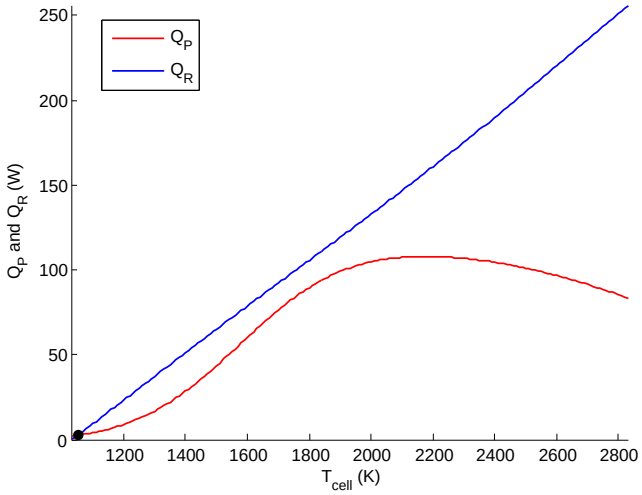

Figure 6.2.4: Profiles of the heat production curve Q_{P} and the heat removal curve Q_{R} for rising T_{cell} ($V_{\mathrm{cell}} = 0.3$ V).

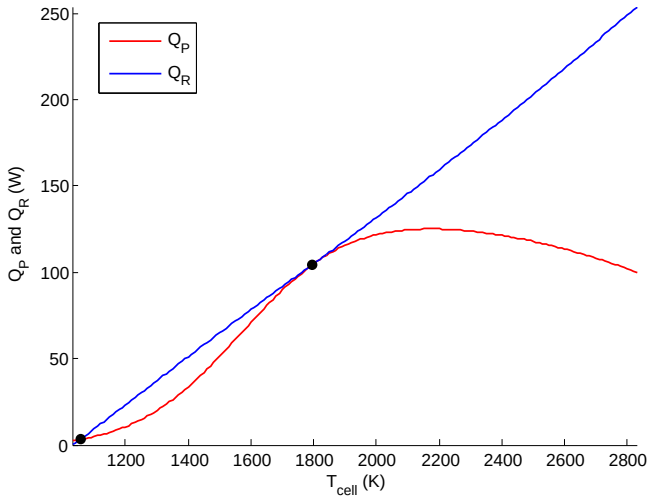

Figure 6.2.5: Profiles of the heat production curve Q_{P} and the heat removal curve Q_{R} for rising T_{cell} ($V_{\mathrm{cell}} = 0.2595521$ V).

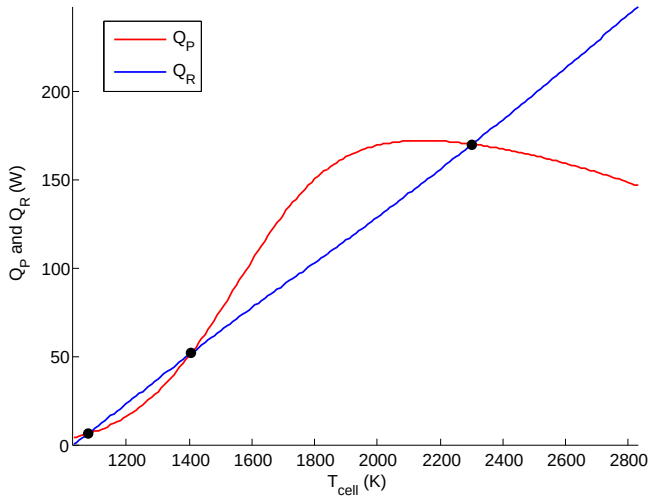

Figure 6.2.6: Profiles of the heat production curve Q_{P} and the heat removal curve Q_{R} for rising T_{cell} ($V_{\mathrm{cell}} = 0.15$ V).

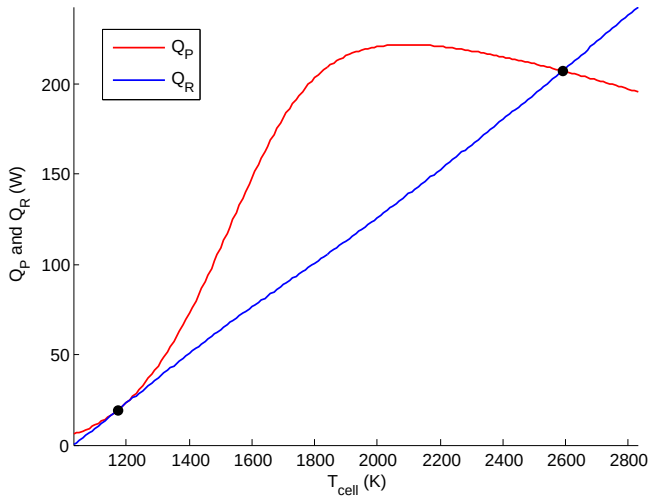

Figure 6.2.7: Profiles of the heat production curve Q_{P} and the heat removal curve Q_{R} for rising T_{cell} ($V_{\mathrm{cell}} = 0.028517$ V).

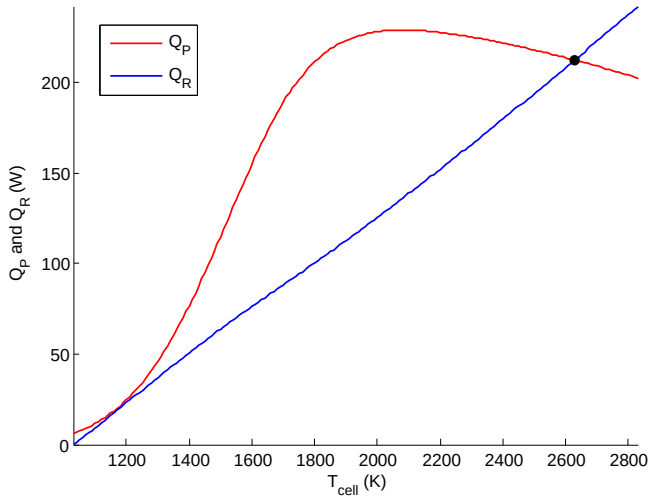

Figure 6.2.8: Profiles of the heat production curve Q_{P} and the heat removal curve Q_{R} for rising T_{cell}. The curves do not quite meet at $T_{\mathrm{cell}} \approx 1200$ K ($V_{\mathrm{cell}} = 0.01$ V).

just exceeds 150 W. The peak occurs around the same value of T_{cell} as it does for the case of a constant external load, only except the rise in Q_{P} is much sharper for a drop in V_{cell} than it is for a drop in R_{load} in chapter 4.

The amount of heat removed from the SOFC for this mode of operation is more or less the same as the amount of heat removed from the SOFC under a constant external load. Looking at the heat production curves in chapter 4, the shape of Q_{P} after it reaches its peak is not investigated since it already intersects with the Q_{R} curve for the final/only time. However, since the values of T_{cell} along the ignited steady-state branch within the multiplicity region for this case is larger than the values for the constant external load case, the shape of the Q_{P} curve after it reaches its peak can be seen (until it intersects with Q_{R}). Looking at figures 6.2.6-6.2.8, the heat production curve only drops slightly for increasing T_{cell}. This, along with the fact that Q_{P} reaches a higher peak means that as the value of V_{cell} decreases, means that Q_{P} intersects Q_{R} for the final/only time at higher

values of T_{cell} where T_{cell} is located on the ignited steady-state branch.

6.2.3 Multiplicity Regions

The method for determining the multiplicity regions for this mode of operation is the same as the method used in the previous chapter. Apply a polynomial fit to a set of ignition points and a set of extinction points for each case using *polyfit* in MATLAB. Then define these polynomial fits as anonymous functions in MATLAB, and evaluate those functions for a range of values of each inlet parameter. The multiplicity regions for each inlet parameter considered in the previous chapter is shown in figures 6.2.9-6.2.14.

Changes in inlet gas flow temperatures

Looking at the multiplicity regions for changes in the inlet gas temperatures (figures 6.2.9 and 6.2.10), it is apparent that for this mode of operation, they have to be increased a lot more to remove the multiplicity region altogether. In the case of $T_{\text{fuel}}^{\text{in}}$, they have to be increased a lot more for the multiplicity region to be removed, especially as there is still a sizeable multiplicity region for values of $T_{\text{fuel}}^{\text{in}}$ around 1400 K. As for $T_{\text{air}}^{\text{in}}$, the multiplicity region shrinks a lot faster when $T_{\text{air}}^{\text{in}}$ is raised. The effect of changing the inlet gas flow temperatures on T_{cell} has already been explained in sections 5.2 and 5.3. However, similar to the region in [49], it is more difficult to remove the multiplicity region altogether for rises in the inlet gas flow temperatures. Just like the previous chapter, the SOFC is more sensitive to changes in $T_{\text{air}}^{\text{in}}$ than $T_{\text{fuel}}^{\text{in}}$. To remove any trace of steady-state multiplicity from the SOFC, it would be best to increase both inlet temperatures simultaneously. For both sets of ignition and extinction points, a third-order polynomial approximation was fitted to both sets of points.

Changes in inlet gas flow velocities

The multiplicity regions for changes in inlet fuel and air flow velocities are given in figures 6.2.11 and 6.2.12 respectively. Unlike the equivalent multiplicity regions in the pre-

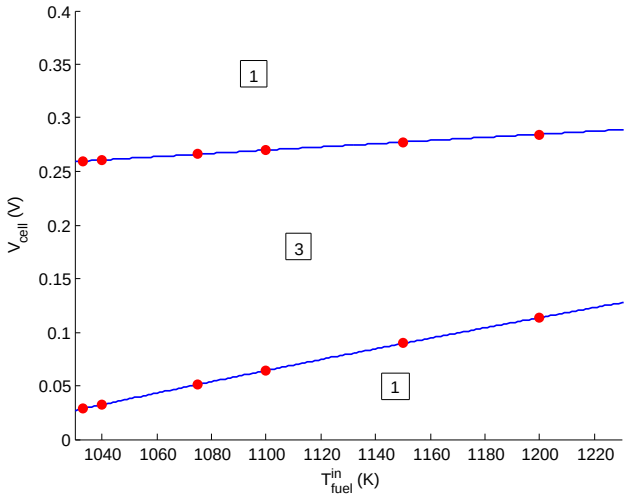

Figure 6.2.9: The multiplicity region for changes in $T_{\text{fuel}}^{\text{in}}$. The boxed numbers represent the number of steady-state solutions in a particular region. The red points represent the location of the ignition and extinction points.

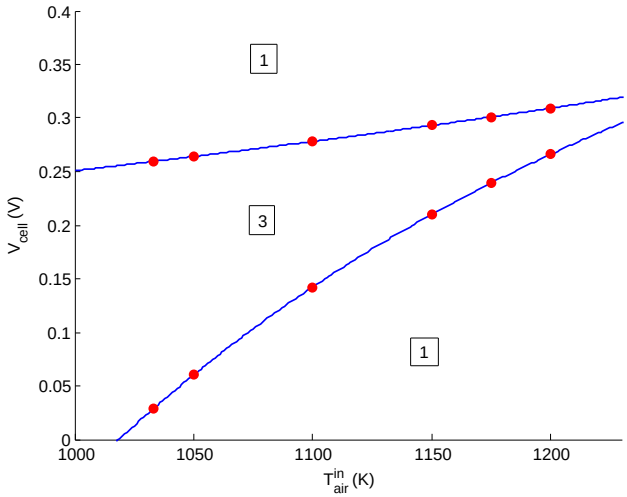

Figure 6.2.10: The multiplicity region for changes in $T_{\text{air}}^{\text{in}}$. The boxed numbers represent the number of steady-state solutions in a particular region. The red points represent the location of the ignition and extinction points.

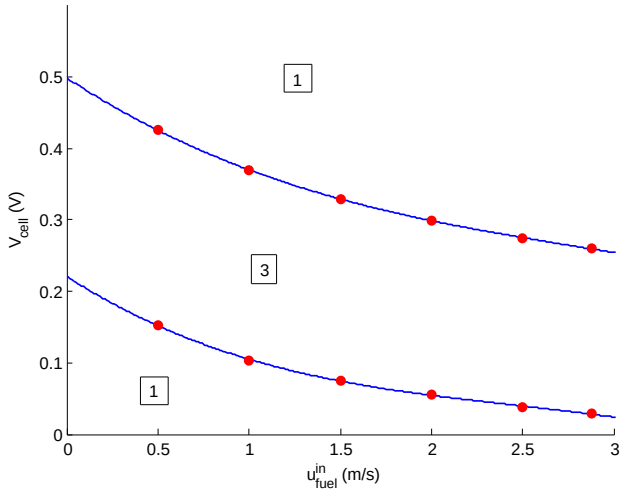

Figure 6.2.11: The multiplicity region for changes in $u_{\text{fuel}}^{\text{in}}$. The boxed numbers represent the number of steady-state solutions in a particular region. The red points represent the location of the ignition and extinction points.

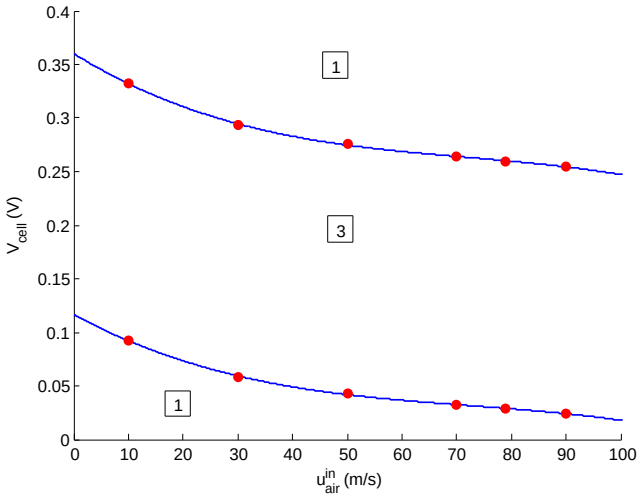

Figure 6.2.12: The multiplicity region for changes in $u_{\text{air}}^{\text{in}}$. The boxed numbers represent the number of steady-state solutions in a particular region. The red points represent the location of the ignition and extinction points.

vious chapter, the multiplicity region does not shrink for lower values of $u_{\text{fuel}}^{\text{in}}$ and $u_{\text{air}}^{\text{in}}$. Instead, the multiplicity region is just shifted towards higher values of V_{cell}. One possible reason for this is due to the sluggish dynamics of the SOFC along the un-ignited steady-state branch. As shown on the heat production/removal profiles in the previous subsection, the rise in Q_{P} for low values of T_{cell} is not as sharp for this mode of operation compared to the constant external load mode of operation (plus the peak is greater for this mode of operation). This means that even though the steady-state values of T_{cell} are shifted towards higher values of V_{cell} when either inlet gas flow velocity is decreased, the shift is bigger for values of T_{cell} along the upper part of the unstable steady-state branch, and the ignited steady-state branch compared to the un-ignited branch. This means that the multiplicity region does not disappear for lower values of $u_{\text{fuel}}^{\text{in}}$ or $u_{\text{air}}^{\text{in}}$. Instead, the best way to remove the multiplicity region would be to increase either of the gas flow velocities. But it would result in a less efficiently operating SOFC. For both sets of ignition and extinction points, a third-order polynomial approximation was fitted to both sets of points.

Changes in inlet molar flow rates

Figures 6.2.13 and 6.2.14 represent the multiplicity regions for changes in the fuel and air inlet molar flow rates. Just like the case of a constant external load, increasing $\dot{N}_{\text{fuel}}^{\text{in}}$ has the effect of removing more heat from the cell due to convection, because there is a larger amount of fuel entering the SOFC at the same inlet velocity. Plus, there is a sharp increase in the amount of heat produced for values of T_{cell} along the ignited steady-state branch due to more fuel being available for consumption. This results in the expansion of the multiplicity region shown in figure 6.2.13. Decreasing $\dot{N}_{\text{fuel}}^{\text{in}}$ does reduce the amount of heat removed by convection, but it also reduces the amount of produced within the SOFC due to a drop in the amount of fuel available for consumption (especially at higher values of T_{cell}. This means that it is likely that the multiplicity region does actually disappear

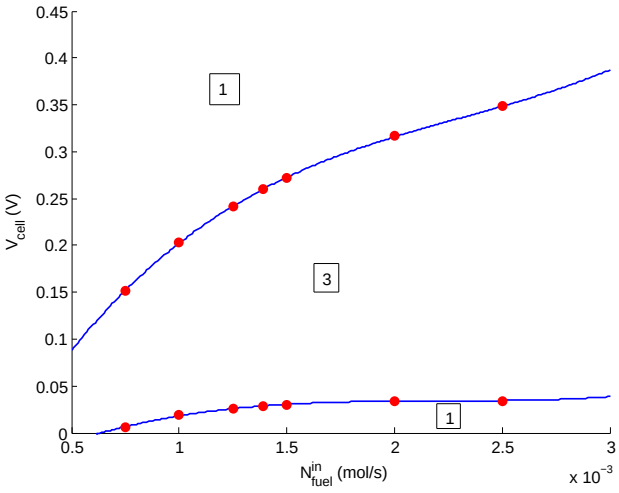

Figure 6.2.13: The multiplicity region for changes in $\dot{N}^{\text{in}}_{\text{fuel}}$. The boxed numbers represent the number of steady-state solutions in a particular region. The red points represent the location of the ignition and extinction points.

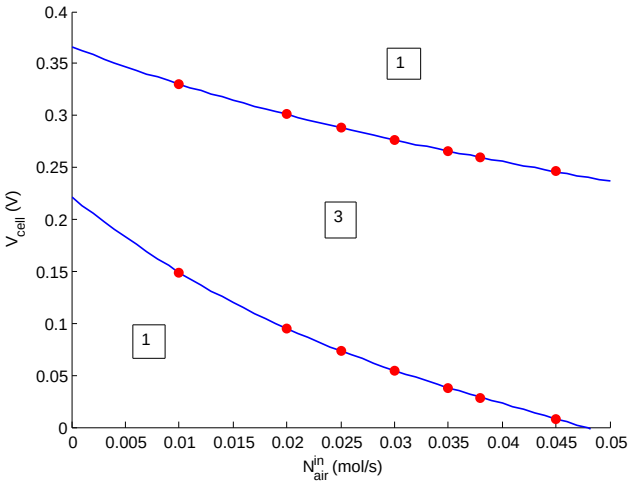

Figure 6.2.14: The multiplicity region for changes in $\dot{N}^{\text{in}}_{\text{air}}$. The boxed numbers represent the number of steady-state solutions in a particular region. The red points represent the location of the ignition and extinction points.

for non-negative values of V_{cell} for values of $\dot{N}^{\text{in}}_{\text{fuel}}$ below 0.5×10^{-3} mol/s.

As for the multiplicity region in 6.2.14, an increase in air does not result in a sharper increase in Q_{P} for higher values of T_{cell}. Instead, increasing $\dot{N}^{\text{in}}_{\text{air}}$ just mainly increases the amount of heat removed by convection, shifting the multiplicity region towards lower values of V_{cell}. Decreasing $\dot{N}^{\text{in}}_{\text{air}}$ shifts the multiplicity region towards higher values of V_{cell}, where it does shrink. But not enough for the multiplicity region to disappear before $\dot{N}^{\text{in}}_{\text{air}}$ reaches zero. For both sets of ignition and extinction points, a third-order polynomial approximation was fitted to both sets of points.

What is noticeable in those multiplicity regions is that for a Solid Oxide Fuel Cell operating under a constant cell voltage, it is more difficult to remove the multiplicity region by modifying any of the inlet parameters covered in the previous chapter (with the exception of $\dot{N}^{\text{in}}_{\text{fuel}}$). This is mainly because of the larger amount of heat produced within the SOFC for this mode of operation compared to the constant external load operation, plus the slower rise in Q_{P} for low values of T_{cell}.

6.3 Galvanostatic Operation

For a Solid Oxide Fuel Cell operating under a Galvanostatic operation, the cell current I is treated as the constant bifurcation parameter. Setting I as a constant parameter removes most of the non-linearity associated with the SOFC model. The equation for I in the other two modes of operation now becomes the equation for V_{cell}, and that equation is no longer implicit. Setting I as a constant parameter fixes the reaction rates as well, meaning that the amount of Hydrogen (and Oxygen) consumed within the SOFC can be directly controlled. As a result of this, as shown in figure 6.3.1, no multiple steady-state solutions exist for a Solid Oxide Fuel Cell operating under a constant cell current.

Looking at the profile for T_{cell} in figure 6.3.1, rising I just results in a rise in T_{cell}. This is because a rise in I results in a rise in the electrochemical reaction rates, which in turn

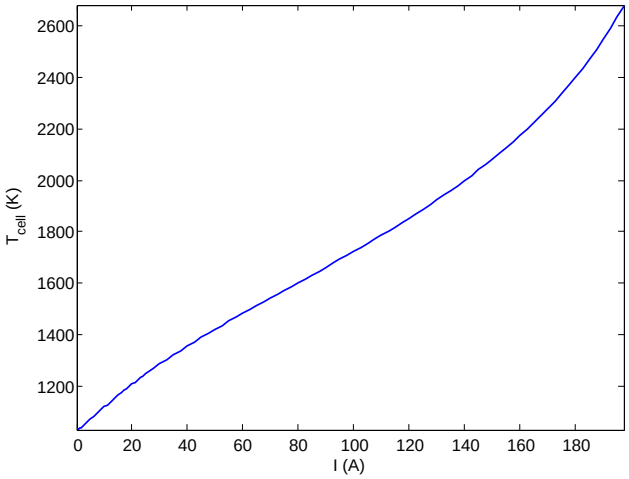

Figure 6.3.1: I vs T_{cell} for a Solid Oxide Fuel Cell operating under a galvanostatic operation, with the inlet parameters based on the values in Appendix B.

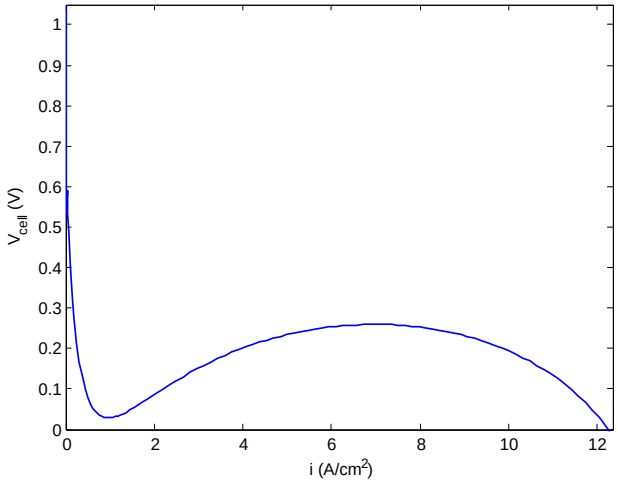

Figure 6.3.2: i vs V_{cell} for a Solid Oxide Fuel Cell operating under a galvanostatic operation, with the inlet parameters based on the values in Appendix B.

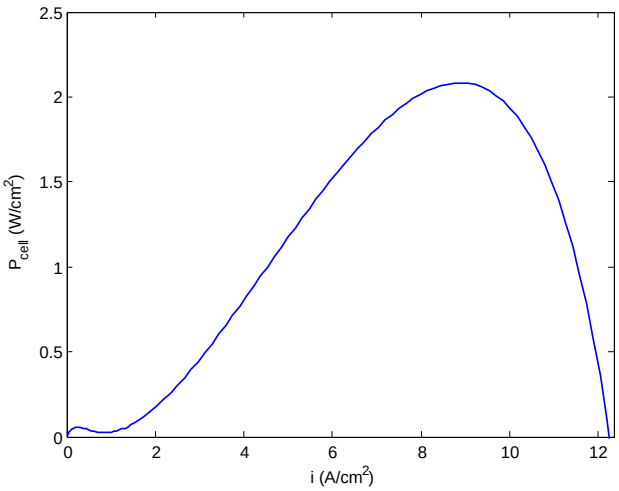

Figure 6.3.3: i vs V_{cell} for a Solid Oxide Fuel Cell operating under a galvanostatic operation, with the inlet parameters based on the values in Appendix B.

increases the operating temperature of the SOFC since more heat is produced. It rises slightly more sharply for values of I approaching the limiting current density.

The shape of the V-I and P-I profiles in figures 6.3.2 and 6.3.3 respectively are very similar to the equivalent profiles for the potentiostatic mode of operation, and the constant external load mode of operation. The only difference is that there is no location of any unstable steady-state branch. Since electrolyte conductivity is still defined in terms of T_{cell}, a rise in T_{cell} does result eventually in a rise in conductivity, leading V_{cell} to rise as the activation and Ohmic polarisations decrease with increasing T_{cell} for large enough values of i. But since I is controlled in this mode of operation, we do not get the intensification of the electrochemical reaction rates associated with the other two modes of operation. Therefore, there is no sudden jump in V_{cell} and P_{cell} due to the SOFC igniting.

6.4 Summary

In this chapter, the steady-state behaviour plus the existence of multiple steady-states for a Solid Oxide Fuel Cell operating under a potentiostatic operation, and a galvanostatic operation was investigated. For the potentiostatic case, up to three steady-state solutions were found. Compared to the constant external load case, a lot more heat is produced within the SOFC when V_{cell} is dropped compared to the amount of heat produced when R_{load} is dropped (but not for low values of T_{cell}). Hence a larger rise in T_{cell} after ignition compared to the constant external load case. This larger rise in T_{cell} also means a larger rise in i after ignition. But since this is located near the limiting current density value, the jump in P_{cell} after ignition is not as great for the potentiostatic case as it is for the constant external load case.

Since more heat is produced within the cell for the potentiostatic case (at high values of T_{cell}), it is more difficult to remove the multiplicity regions by changing the inlet parameter values. The inlet gas flow temperatures have to be increased a lot more (especially $T_{\text{fuel}}^{\text{in}}$) to remove the multiplicity region. Modifying the inlet gas flow velocities only shifts the multiplicity region towards higher or lower values of V_{cell} without significantly modifying the size of the region. Modifying $\dot{N}_{\text{air}}^{\text{in}}$ does not remove the multiplicity region either, but lowering $\dot{N}_{\text{fuel}}^{\text{in}}$ does remove the multiplicity region since less heat is produced from the cell due to less fuel entering the cell (as well as less heat being removed by convection). As for the galvanostatic case, setting I as a constant parameter fixes the reaction rates and removes most of the non-linearity in the model. This results in no multiple steady-state solutions since the reaction rates can be controlled directly. The shape of the V-I and P-I profiles are very similar to equivalent profiles for the other two modes of operation since a rise in T_{cell} does result in a rise in electrolyte conductivity. But since this does not affect the electrochemical reaction rates indirectly as well, there is not the intensification of the

electrochemical reaction rates that would occur for the other two cases (especially as they can be controlled in this case). Hence, no hot spots are formed.

Chapter 7

Transient behaviour of the SOFC

7.1 Introduction

In this chapter, the dynamic behaviour of the SOFC under load changes will be observed, where R_{load} is expressed as a smooth function of time. The inlet parameters are based on the values in Appendix B (equivalent to the base case in chapter 4).

This chapter starts off by reviewing the different time scales considered when looking at the transient behaviour of a Solid Oxide Fuel Cell, including the time-scales which are present in the model. After this, the transient behaviour of a Solid Oxide Fuel Cell for changes in R_{load} is considered. However, instead of considering a step-change in R_{load}, R_{load} is expressed in terms of the tanh function, so that it is now a smooth function of time.

R_{load} is defined by the following equation

$$R_{\text{load}}(t) = R_{\text{load}}^{(0)} + \frac{1}{2}\left[R_{\text{load}}^{(1)} - R_{\text{load}}^{(0)}\right]\left\{1 + \tanh\left(\frac{(t - t_{\text{s}})}{\omega}\right)\right\} \tag{7.1}$$

where $R_{\text{load}}^{(0)}$ is the initial value of R_{load} at $t = 0$, $R_{\text{load}}^{(1)}$ is the final value of R_{load}, t_{s} is the transition mid-point, and ω is a constant value (defined in terms of seconds) which affects how quickly R_{load} changes from $R_{\text{load}}^{(0)}$ to $R_{\text{load}}^{(1)}$. In this chapter, t_{s} is equal to 100 seconds.

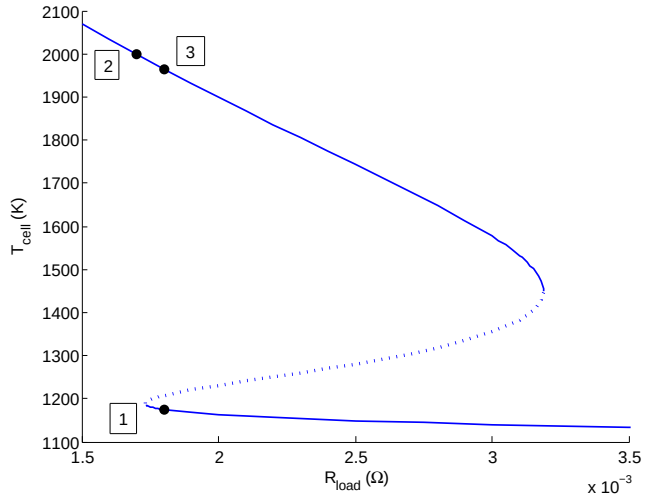

Figure 7.1.1: The steady-state profile of T_{cell} from figure 4.2.2, showing the expected change in T_{cell} during ignition, when R_{load} changes from 0.0018 Ω (point 1) to 0.0017 Ω (point 2). Point 3 shows the expected value of T_{cell} when R_{load} changes back to 0.0018 Ω.

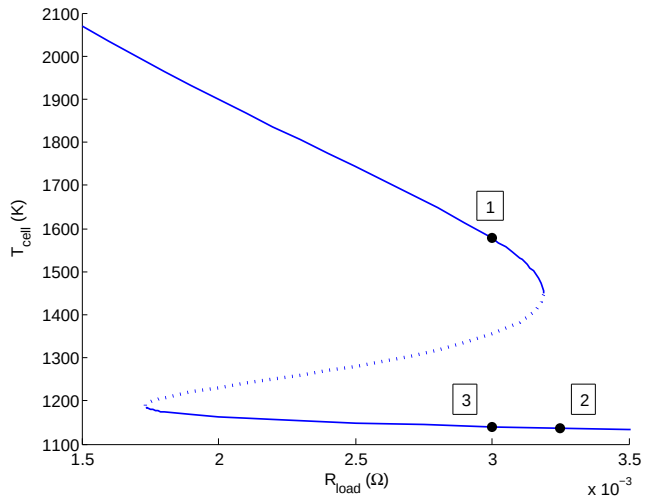

Figure 7.1.2: The steady-state profile of T_{cell} from figure 4.2.2, showing the expected change in T_{cell} during extinction, when R_{load} changes from 0.003 Ω (point 1) to 0.00325 Ω (point 2). Point 3 shows the expected value of T_{cell} when R_{load} changes back down to 0.003 Ω.

The reason why a smooth transition in R_{load} is considered here is to avoid any numerical difficulties associated with a step-change in R_{load}.

Firstly, the evolution of different SOFC parameters with time is investigated by looking at the change in R_{load} from 10 Ω to 5 Ω for six different values of ω. The values of ω considered are 10 s, 5 s, 2.5 s, 1 s, 0.5 s and 0.25 s. For each SOFC parameter, the development of the each transient profile as ω is lowered will be investigated. For all the other transient cases considered in this chapter, ω is taken as 0.25 seconds, in which R_{load} closely resembles a step-change from $R_{\text{load}}^{(0)}$ to $R_{\text{load}}^{(1)}$ around 100 seconds.

After investigating the evolution of the different SOFC parameters with time, the focus shifts towards the transient behaviour of the SOFC for that given expression of R_{load} where $\omega = 0.25$ seconds. The results obtained for the case where R_{load} changes from 10 Ω to 5 Ω will be compared with equivalent results from other papers (namely [49] and [67]).

After that, the transient behaviour of the SOFC is considered for three cases. The first case considered concerns the transient behaviour of the SOFC during the ignition phase. R_{load} initially operates at point 0.0018 Ω on the un-ignited steady-state branch (point 1 in figure 7.1.1). At around 100 seconds, R_{load} changes from 0.0018 Ω to 0.0017 Ω. Since there is only one steady-state solution at $R_{\text{load}} = 0.0017$ Ω, T_{cell} is expected to rise up to a new steady-state located at point 2 of figure 7.1.1, on the ignited steady-state branch. After that, there is another change in R_{load} from 0.0017 Ω (point 2) back to 0.0018 Ω. As it will be shown later on, T_{cell} only moves down towards another value on the ignited steady-state branch after that change (point 3), rather than going back towards its original value on point 1. This second change in R_{load} highlights that there is more than one operating region within a Solid Oxide Fuel Cell.

The same approach is take for the second case, where the transient behaviour of the SOFC during the extinction phase is considered. The first change considered is the change from $R_{\text{load}} = 0.003$ Ω to $R_{\text{load}} = 0.00325$ Ω around 100 seconds, where T_{cell} is expected to drop

from a value on the ignited branch (point 1 in figure 7.1.2), to a value on the un-ignited branch (point 2 in figure 7.1.2). After that, there is another change in R_{load} from 0.00325 Ω (point 2) to 0.003 Ω (point 3), where T_{cell} continues to operate along the un-ignited branch rather than go back towards the ignited branch.

The final case considered is the transient behaviour of the SOFC where it initially operates on the unstable steady-state branch. Starting from a steady-state solution on that branch for $R_{\text{load}} = 0.0025$, an increase and a decrease in R_{load} is considered to show that the SOFC veers away from that branch towards a new steady-state solution along either the ignited steady-state branch or the un-ignited steady-state branch.

7.2 Time scales

A comprehensive review of all the different time-scales in a Solid Oxide Fuel Cell and their expected magnitude can be found in the paper by Gemmen and Johnson [73]. The time-scales in a Solid Oxide Fuel Cell can range from the order of magnitude of 10^{-5} seconds to the order of magnitude of 10^{4} seconds. This is further summarised in another paper by Bhattacharyya and Rengaswamy [76], where they review different SOFC dynamic models. They say that the different time-scales in a Solid Oxide Fuel Cell can be split into three groups:

1. Time-scales in the order of milliseconds or less (10^{-5}–10^{-2}s). These include the time taken for the cell to charge (which can be as small as of order of 10^{-5} s [73]), mass diffusion within the electrode diffusion layer, and possibly stream-wise convection/advection across the length of the channels;

2. Time-scales in the order of seconds (10^{0}–10^{1} s). These include consumption of the cell reactants, stream-wise diffusion across the length of the channel and stream-wise conduction across the length of the channel. This time-scale range mainly covers gas flow dynamics (with the exception of convection).

3. Time-scales in the order of minutes or hours (10^2–10^4 or 10^5 s). These include the time taken for the cell to heat up, and stream-wise conduction across the length of the electrodes. This time-scale region covers the energy characteristics of the cell.

In this section, we consider the different time-scales that occur in the model, plus other time-scales for dynamics that have been neglected. Time-scales which are not considered in this section include the cell charging time-scale and stream-wise conduction within the two electrodes. Since the time taken for the cell to charge up is very small (of order 10^{-5} s), that time-scale can be ignored. As for the stream-wise conduction time-scales across the length of the electrode, the temperature is assumed to be uniformally distributed across all three cell components, so conduction within the anode and cathode is incorporated within the conduction of the whole cell component. Therefore, with regards to energy transfer in the cell, only the cell heating time-scale is considered in this section. The shorter time-scales are considered first, including mass diffusion within the electrode diffusion layer, mass diffusion across the height of the gas channels, and convection/advection across the length of the channels. The mid-range time-scales considered include the consumption of the reactants, mass diffusion across the length of the channels, and conduction across the length of the channels. The sole long-range time-scale considered is the cell heating-up time-scale.

7.2.1 Short-range time-scales

Mass Diffusion within the electrodes

Figures 7.2.1-7.2.3 represent the mass diffusion time-scales of the diffusion of Hydrogen, Water and Oxygen within the electrodes for decreasing values of R_{load}. The results are based on the base case model where the SOFC is operating under a constant external load with inlet parameters based on the values in Appendix B.

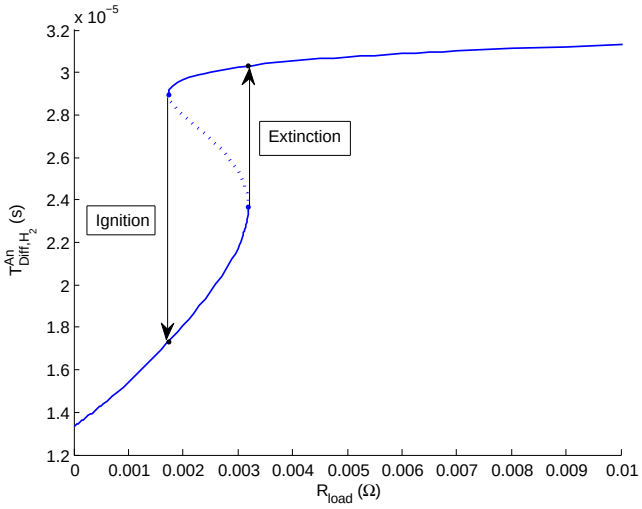

Figure 7.2.1: The profile of the diffusive time-scale for the diffusion of Hydrogen within the Anode for decreasing values of R_{load}.

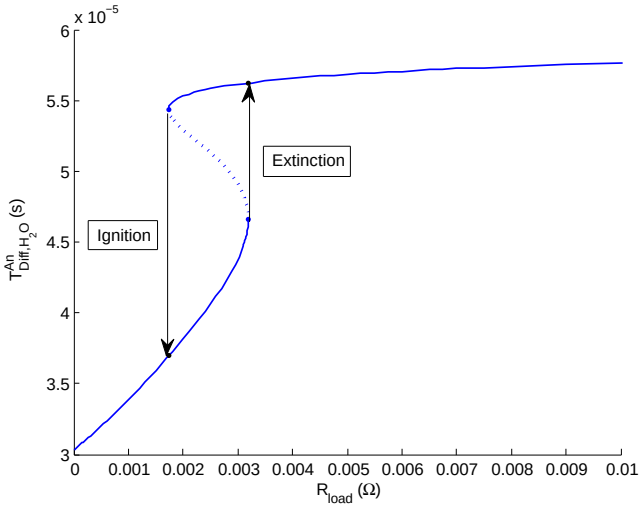

Figure 7.2.2: The profile of the diffusive time-scale for the diffusion of Water within the Anode for decreasing values of R_{load}.

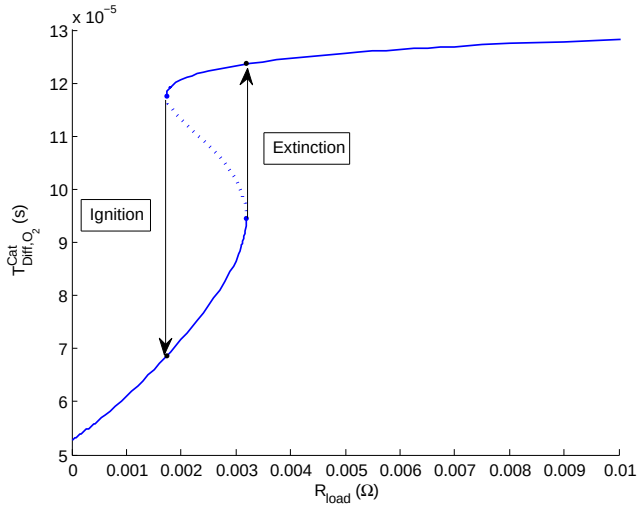

Figure 7.2.3: Zoom-in of the profile in figure 4.2.1, showing the location of the ignition and extinction states. The stable steady-state branches are represented by the thick blue curves, while the middle steady-state branch is represented by the dashed blue curve.

The characteristic time-scale representing mass diffusion within the electrodes is given by

$$T^{j}_{\mathrm{Diff},i} = \frac{\Delta_j^2}{D_{\mathrm{eff},i}} \quad (i = \mathrm{H_2},\ \mathrm{H_2O},\ \mathrm{O_2})\ (j = \mathrm{An},\ \mathrm{Cat}), \tag{7.2}$$

where Δ_j is the thickness of the electrode diffusion layer, and $D_{\mathrm{eff},i}$ is the effective diffusion coefficient. In [73], the time-scale for mass diffusion in the Cathode is of the order of 10^{-5} s, while the time-scale for mass diffusion in the Anode is of the order of 10^{-3} s. For this model however, the time-scales for the diffusion of Hydrogen, Water and Oxygen within the electrode diffusion layer is of the order of 10^{-5} s, especially along the ignited steady-state branch.

The time-scale for the diffusion of Oxygen within the Cathode diffusion layer is of the order of 10^{-4} s along the un-ignited steady-state branch. But, after ignition, the time-scales get smaller and smaller as more and more Hydrogen and Oxygen is consumed within the

SOFC at a higher operating temperature, and a higher conversion rate. The main reason as to why the time-scales in this model are smaller than the equivalent time-scales in [73] is because the thickness of the electrodes in [73] is thicker than the electrode diffusion layer thickness in this model. The electrode thickness in [73] is 1 mm, while the thickness of the electrode diffusion layer in this model is 0.05 mm (Appendix A). Also, the time-scales considered here cover the mass transfer of individual gas species within the electrodes via diffusion rather than the overall mass transfer in the whole electrode via diffusion. These time-scales are present in the model (in equations (3.48)–(3.50)).

Since the mass diffusion time-scales are very small, diffusion within the electrode is assumed to be at steady-state, which leads to the derivation of the molar flux into the cell surface per unit area equations in section 3.4. Also, the diffusion time-scale of Water is larger than the diffusion time-scale of Hydrogen. This means that it takes slightly longer for Water to diffuse from the cell to the gas flow. Hence Water is not travelling quickly enough to replace the Hydrogen that is consumed within the SOFC, which is partly responsible for the shape of the $C^{\mathrm{b}}_{\mathrm{fuel}}$ profile in figure 4.6.1.

Mass diffusion across the height of the gas channels

Figures 7.2.4 and 7.2.5 represent the mass diffusion time-scales for diffusion across the height of the fuel and air channels respectively. These diffusive scales are defined as follows:

$$T^{\mathrm{fuel}}_{\mathrm{Diff},h} = \frac{(h^{\mathrm{An}})^2}{D_{\mathrm{H_2,H_2O}}}, \quad T^{\mathrm{air}}_{\mathrm{Diff},h} = \frac{(h^{\mathrm{Cat}})^2}{D_{\mathrm{O_2,N_2}}}. \tag{7.3}$$

Diffusion coefficients within the gas flows are defined in terms of the binary diffusion coefficients instead of the effective diffusion coefficients. Since there is only one in each gas channel, we can just consider diffusion in both channels separately. These time-scales are present in the model (mainly in the gas flow conservation equations).

Since the height of the gas channels are larger than the thickness of the electrode diffusion

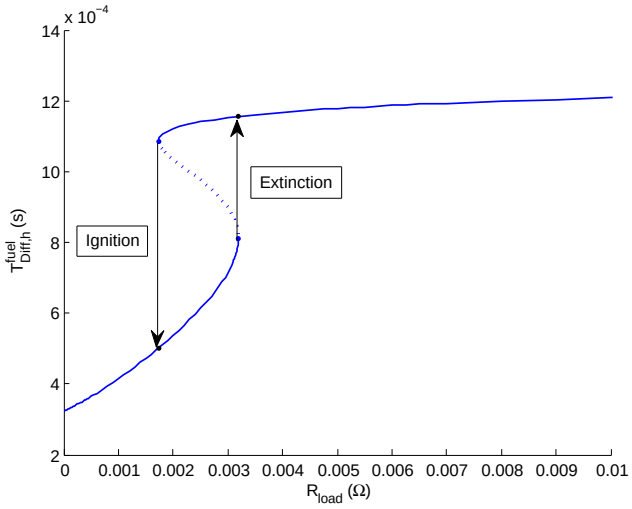

Figure 7.2.4: The profile of the diffusive time-scale for the mass diffusion across the height of the fuel channel for decreasing values of R_{load}.

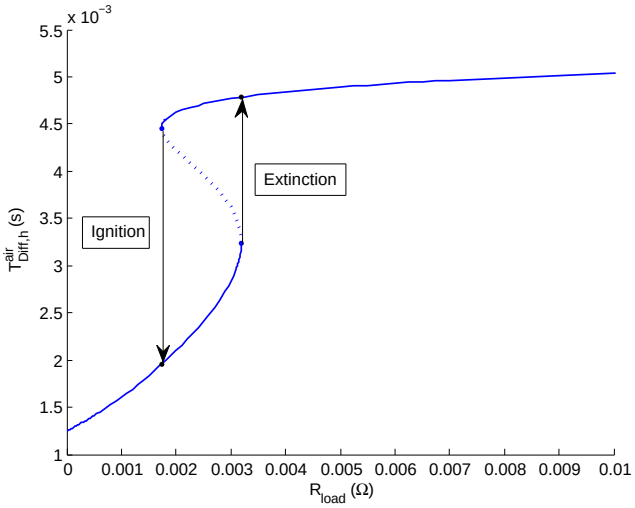

Figure 7.2.5: The profile of the diffusive time-scale for the mass diffusion across the height of the air channel for decreasing values of R_{load}.

layer (see Appendix A), it is no surprise that the time-scales for diffusion across the height of the gas channels is slightly bigger than for mass diffusion across the electrode. Despite this, the time-scales here are still very small, with both time-scales being of the order of 10^{-3} s. The time-scale for diffusion across the height of the fuel channel does drop down to the order of 10^{-4} s after ignition, but otherwise, remains of the order of 10^{-3} across the un-ignited steady-state branch.

For both diffusion within the electrodes and across the height of the gas channels, it is noticeable that diffusion of Oxygen across the height of the air channel and the Cathode takes a slightly longer than the diffusion of Hydrogen and Water across the fuel channel and the Anode. This could be down to the lower value of D_{O_2,N_2} in comparison to D_{H_2,H_2O}, which would suggest that the diffusion of Oxygen across the air channel and the Cathode is not as prominent as the diffusion of Hydrogen and Water in the fuel channel and Anode.

Convection/Advection across the length of the gas channels

Figures 7.2.6 and 7.2.7 represent the profiles for the convection/advection time-scales of fuel and air transfer respectively over the length of their respective gas channels. In [73], the convection time-scale is of order 10^{-1} s. In this model however, the time-scales are of the order 10^{-3}-10^{-2} s for the fuel flow, and of the order 10^{-4} s for the air flow. The convection/advection time-scale is defined as

$$T_{\text{Conv},j} = \frac{L}{u_j} \quad (j = \text{fuel},\ \text{air}) \tag{7.4}$$

Since the length scale L is the same for both channels, the convection/advection time-scales for fuel and air flow are very dependent on the gas flow velocities. Since the velocity of the air flow is much greater than the fuel flow, it is no surprise to find out that convection/advection across the length of the air channel is much quicker than it is across the length of the fuel channel.

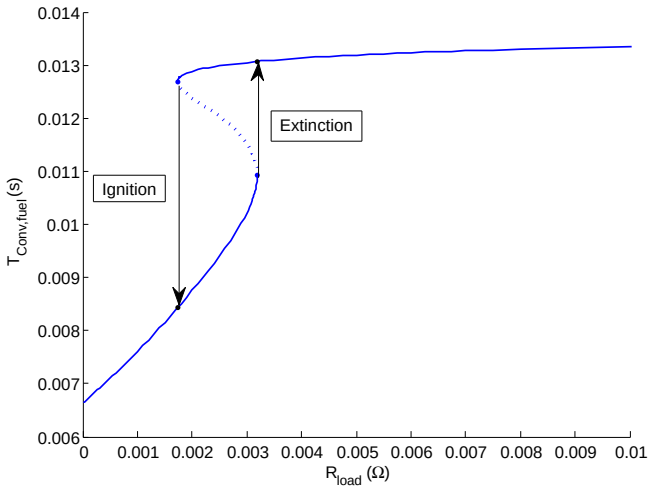

Figure 7.2.6: The profile of the convection/advection time-scale for fuel transfer across the length of the fuel channel for decreasing values of R_{load}.

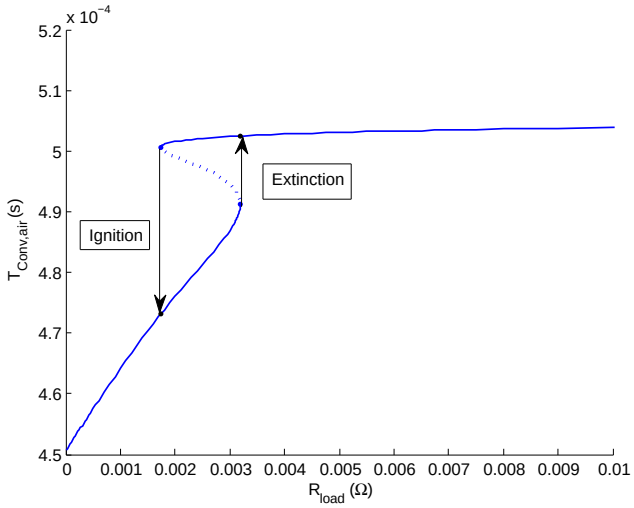

Figure 7.2.7: The profile of the convection/advection time-scale for air transfer across the length of the air channel for decreasing values of R_{load}.

In the fuel channel, the convection/advection time-scale is of the order of 10^{-2} s across the un-ignited steady-state branch, and falls down to being of the order of 10^{-3} s due to the increase in u_{fuel} after ignition (see figure 4.6.9). As for convection/advection in the air channel, the time taken hardly changes throughout all three steady-state branches. Along the un-ignited branch, it is very close to 5×10^{-4} s. After ignition, this drops close to 4.7×10^{-4} s, staying above 4.5×10^{4} s as R_{load} approaches zero.

These are the main short-range time-scales considered. Time-scales with regards to reaction kinetics and cell charging are not considered, since they are considered to be too small for practical applications, and double-layer capacitance effects are not considered for this SOFC model.

7.2.2 Mid-range time-scales

Cell Reactant Consumption

Figures 7.2.8 and 7.2.9 represent the time-scale profiles of the cell reactant consumption of Hydrogen and Oxygen respectively. The formula for this time-scale for the fuel and air flow is given by

$$T_{\text{Re,fuel}} = \frac{C^{\text{b}}_{\text{fuel}} h^{\text{An}}}{\frac{i}{2F}}, \quad T_{\text{Re,air}} = \frac{C^{\text{b}}_{\text{air}} h^{\text{Cat}}}{\frac{i}{4F}}. \tag{7.5}$$

In [73], the cell reactant time-scale is of the order of 10^{0} s. In this model, this is probably true with regards to the consumption of Oxygen into the cell. In general, the reactant consumption time-scales are usually of the order of 10^{-1} s along the un-ignited steady-state branch, dropping down to a magnitude of the order of 10^{-2} s after ignition. This signals the fact that after ignition, more fuel (and Oxygen) is consumed within the cell to participate in the electrochemical reactions at a much higher operating temperature.

As expected, the consumption rate of Oxygen into the SOFC takes slightly longer than the consumption rate of Hydrogen into the SOFC as the consumption rate of Hydrogen is twice the size of the consumption rate of Oxygen. After ignition, the magnitude of the

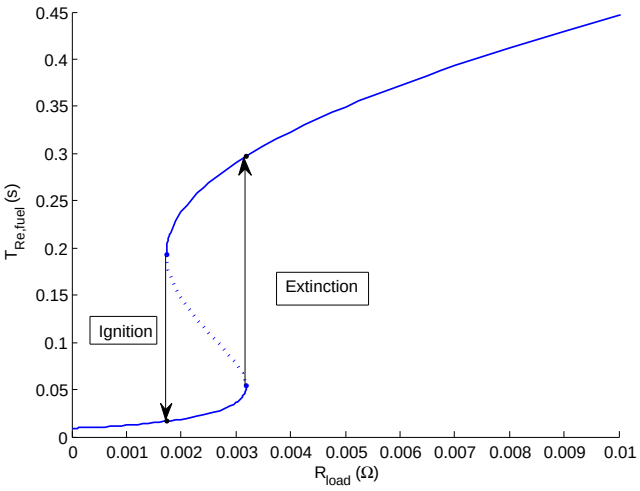

Figure 7.2.8: The profile of the cell reactant consumption time-scale for the consumption of Hydrogen for decreasing values of R_{load}.

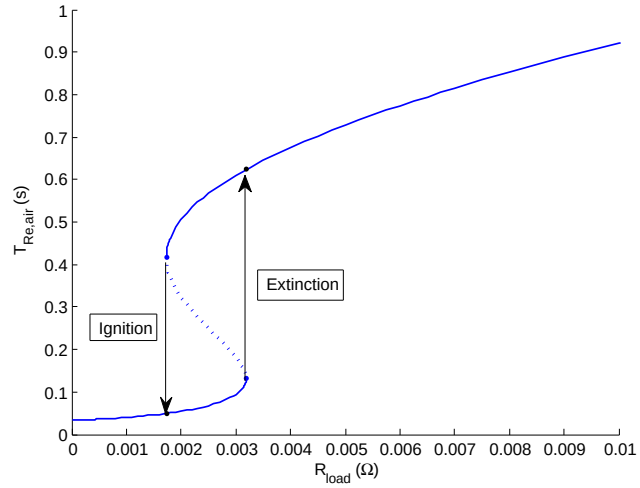

Figure 7.2.9: The profile of the cell reactant consumption time-scale for the consumption of Oxygen for decreasing values of R_{load}.

time-scale for the consumption rate of Hydrogen falls down to as low as the order of 10^{-3} s as R_{load} approaches zero, while the magnitude of the time-scale for the consumption rate of Oxygen falls down to the order of 10^{-2} s.

Diffusion across the length of the gas channels

Figures 7.2.10 and 7.2.11 represent the time-scale profiles for the diffusion of fuel and air across the length of their respective gas channels. The formulae for the diffusive time-scales across the length of the channels is

$$T^{\text{fuel}}_{\text{Diff},L} = \frac{L^2}{D_{\text{H}_2,\text{H}_2\text{O}}}, \quad T^{\text{air}}_{\text{Diff},L} = \frac{L^2}{D_{\text{O}_2,\text{N}_2}}. \tag{7.6}$$

For both the fuel and the air flow, the order of magnitude of the time-scales is mainly of the order of 10^0 s. In the air flow, convection/advection is dominant over the diffusion of air within the air channel, as shown by the Air flow Péclet number profile for mass transfer across the length of the cell in figure 4.7.8. The diffusion of air flow across the length of the air channel is close to nine seconds across the un-ignited steady-state branch. After ignition, this falls down to almost three seconds, and when R_{load} approaches zero, the time taken for air to diffuse across the air channel is around two seconds.

As for fuel flow, diffusion across the cell is a bit quicker, ranging between 1.75 seconds and around two seconds along the un-ignited steady-state branch. After ignition, this falls down to around 0.75 seconds, and dropping down to as low as 0.5 seconds as R_{load} approaches zero. In [73], the diffusive time-scales are assumed to be of order of magnitude 10^1 s. The reason why the time-scales presented here are of order of magnitude one less is that the length of the cell L is this model is shorter than the length of the cell considered in [73], where $L = 0.1$ m. This also explains why the convection time-scales are smaller in magnitude (plus the velocities of the gas flows may be higher).

However, diffusion is only considered across the height of the channels (not the length),

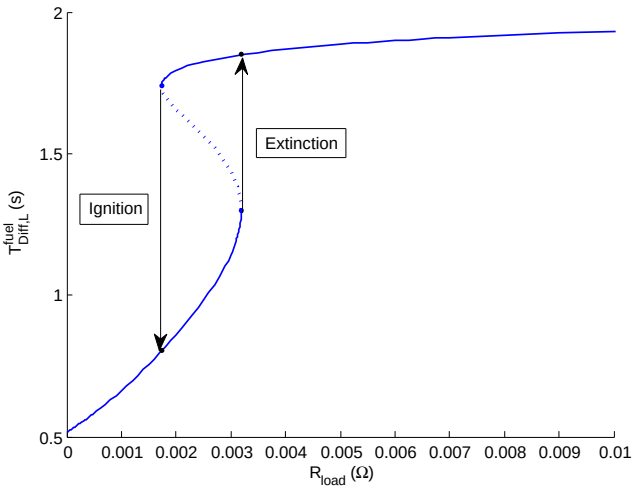

Figure 7.2.10: The profile of the diffusive time-scale for the diffusion of fuel across the length of the channel for decreasing values of R_{load}.

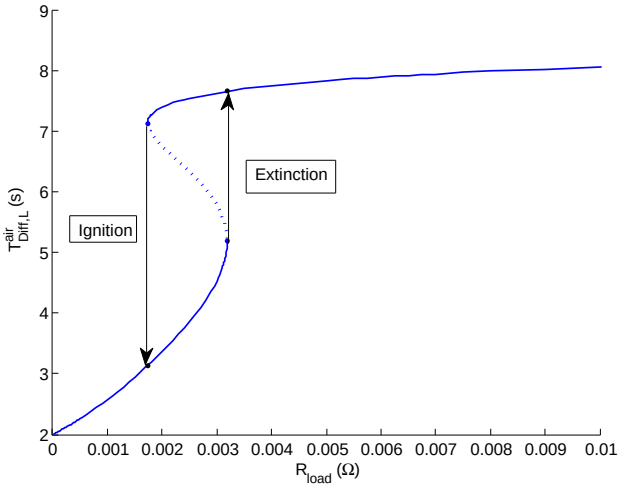

Figure 7.2.11: The profile of the diffusive time-scale for the diffusion of air across the length of the channel for decreasing values of R_{load}.

so these particular time-scales are not present in the transient calculations.

Conduction of the gas flows across the length of the channels

Figures 7.2.12 and 7.2.13 represent the conductive time-scale profiles for conduction of the fuel and air flows respectively in their respective gas channels. Compared to the diffusive time-scale profiles in figures 7.2.10 and 7.2.11, conduction of the fuel and air flows across the length of the cell takes longer overall. The conduction time-scale for the gas flow in the gas channel is given by

$$T_{\mathrm{Cond},j} = \frac{L^2}{\alpha_j} \quad (j = \mathrm{fuel}, \mathrm{air}) \tag{7.7}$$

where the thermal diffusivity term α_j is defined as

$$\alpha_j = \frac{k_j}{C_j^{\mathrm{b}} C_{\mathrm{p},j}}.$$

Looking at figures 7.2.12 and 7.2.13 across the un-ignited steady-state branch, the time taken for the conduction of the fuel and air flows in their respective gas channels hardly changes at all, with conduction across the air flow taking between 28 to around 29 seconds, and conduction across the fuel cell taking around 5 seconds. However, for conduction across the fuel channel, the time slightly drops across the assumed unstable steady-state branch, then rises again, crossing the un-ignited steady-state branch as thermal diffusivity goes down across the ignited steady-state branch. This could be due to the increased heat capacity of the fuel flow in comparison to the increase in thermal conductivity of the fuel flow. The order of the conduction time-scale for the fuel flow across the length of the fuel channel is of order of magnitude 10^0 s.

As for conduction in the air flow across the length of the air channel, the time-scale is of order of magnitude 10^1 s. Across the un-ignited steady-state branch, if falls down slowly

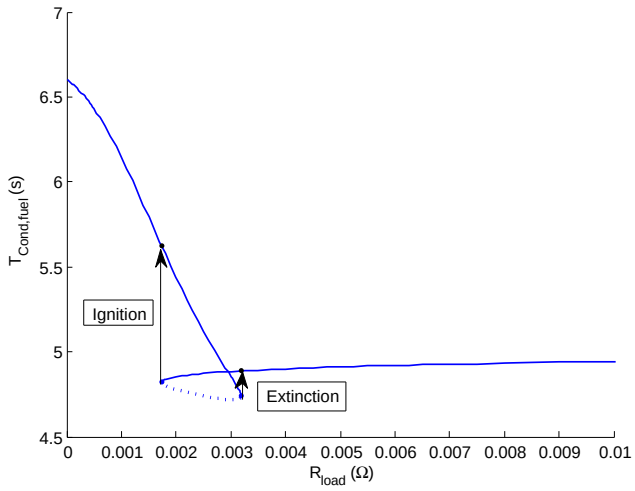

Figure 7.2.12: The profile of the Conductive time-scale for the conduction of the fuel flow across the length of the channel for decreasing values of R_{load}.

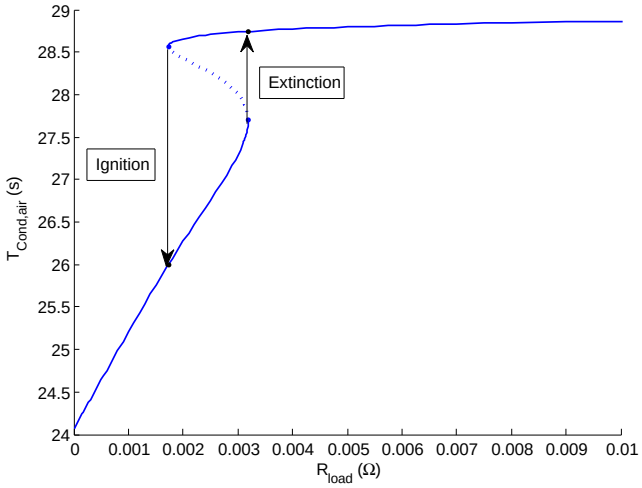

Figure 7.2.13: The profile of the Conductive time-scale for the conduction of the air flow across the length of the channel for decreasing values of R_{load}.

from around 29 seconds to around 28.5 seconds at the ignition point. After ignition, this falls down to around 26 seconds, and drops down to around 24 seconds as R_{load} approaches zero. Thermal diffusivity increases along the ignited steady-state branch. But, the profile in figure 7.2.13 shows that conduction across the air channel takes a bit more longer than conduction across the fuel channel, especially as T_{air} does not rise as much as T_{fuel} along the ignited steady-state branch. These time-scales compared to the diffusive time-scales across the length of the gas channels clarify the different Péclet number profiles for both heat and mass transfer across the length of the cell in subsection 4.7.3 in chapter 4. However, with exception of its appearance in the heat-transfer coefficients, conduction across the length of the gas channels is not considered in this model, so these time-scales are not present in the transient calculations.

7.2.3 Long-range time-scales

Since temperature across the different cell components are assumed to be uniform, the only long-range time scale considered is the cell heating/conduction time-scale across the length of the cell. This is defined to be

$$T_{\text{Cond,cell}} = \frac{L^2}{\alpha_{\text{cell}}} \tag{7.8}$$

where the thermal diffusivity of the cell is defined as

$$\alpha_{\text{cell}} = \frac{k_{\text{cell}}}{\rho_{\text{cell}} C_{\text{p,cell}}}$$

where k_{cell} is the thermal conductivity of the cell, ρ_{cell} is the density of the cell, and $C_{\text{p,cell}}$ is the specific heat capacity of the cell. Each of the three parameters are taken to be constant values. There are no separate values given for ρ_{cell} and $C_{\text{p,cell}}$ in [47] and [49], just one value for the product of the two parameters. The product of ρ_{cell} and $C_{\text{p,cell}}$ is

given as 1×10^6 J/(m$^3 \cdot$ K). However, the conductivity of the SOFC is not considered in this model, since it is considered to have a small impact on T_{cell}. This means that this particular time-scale is not present in the transient calculations. As an insight into how large this time-scale can be, $T_{\text{Cond}} = 2285.714$ seconds in [47], where $k_{\text{cell}} = 0.7$ W/(m^{2}K). The value of $\rho_{\text{cell}} \cdot C_{\text{p,cell}}$ is the same as in [49] and in this thesis. More work is needed to determine the relevant time-scales related to T_{cell}, but based on previous work on this topic, the time taken for the SOFC to reach a new steady-state is dependent on cell parameters like its density and heat capacity.

7.3 Evolution of SOFC parameters with time

In this section, the focus is on the evolution of SOFC parameters with time due to a change in R_{load}. Using the expression from equation (7.1), we consider the change in R_{load} from 10 Ω to 5 Ω where the transition mid-point is located at 100 seconds:

$$R_{\text{load}} = 10 - 2.5 \left\{ 1 + \tanh \left(\frac{t - 100}{\omega} \right) \right\}. \tag{7.9}$$

The transient behaviour of the SOFC is observed for six different expressions of R_{load} based on six different values of ω. The six values of ω considered are 10 s, 5 s, 2.5 s, 1 s, 0.5 s and 0.25 s.

Figure 7.3.1 shows how long R_{load} changes from 10 Ω to 5 Ω for six different values of ω. It clearly shows that when ω is lowered, the change in R_{load} is more focused around 100 seconds, and occurs a lot more quickly. For $\omega = 10$ seconds, the change in R_{load} takes around 60 seconds, starting at around 70 seconds, and finishing around 130 seconds. For $\omega = 0.25$ seconds, the change only takes around 1.5 seconds.

The effect of this on the transient profiles of all the SOFC parameters covered in this model will be investigated. Firstly, the electrical parameters such as cell current, cell

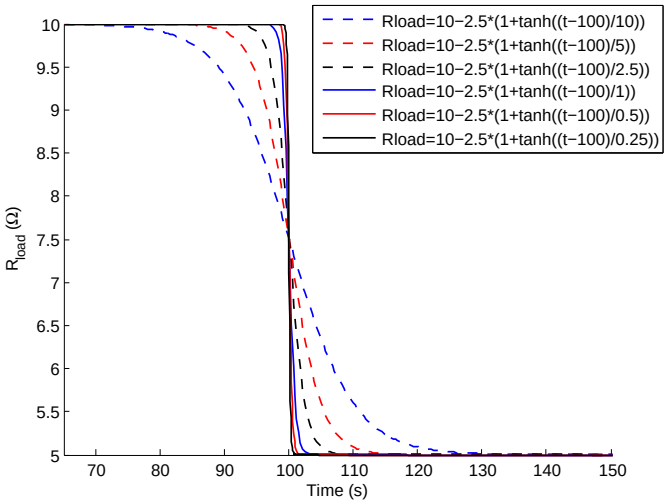

Figure 7.3.1: Six transient profiles of R_{load} based on six different values of ω. The lower ω is, the closer R_{load} resembles a step-function, changing from 10 Ω to 5 Ω around 100 seconds.

voltage and the polarisations will be covered first. The temperature of the solid cell structure is covered next, followed by the concentrations of Hydrogen, Oxygen and Water inside the reaction zones of both electrodes. Finally, the transient behaviour of the gas flow parameters will be covered.

7.3.1 Electrical parameters

Figures 7.3.2 and 7.3.3 represent the different transient profiles of I and V_{cell} respectively for the six different values of ω considered. The first thing to notice is that the transition of both I and V_{cell} from one steady-state solution to another takes roughly the same amount of time it takes R_{load} to change from 10 Ω to 5 Ω. The cell current I reacts to a change in value of R_{load}, going up as R_{load} drops. The different profiles of I intersect each other at around the same point at 100 seconds. After the quick change in I with decreasing R_{load} for low values of ω (=1 second or less), there is a much smaller, but gradual rise of I towards a new steady-state solution with rising T_{cell} (which is not shown

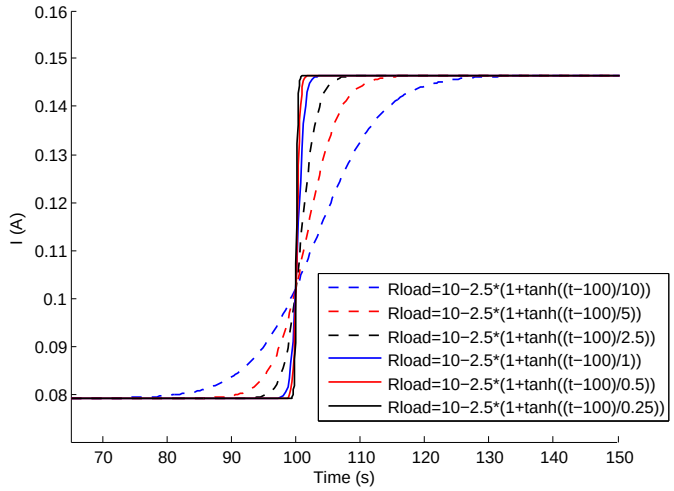

Figure 7.3.2: Six transient profiles of I based on six different values of ω. The transient behaviour of I is heavily influenced by the change in value of R_{load}.

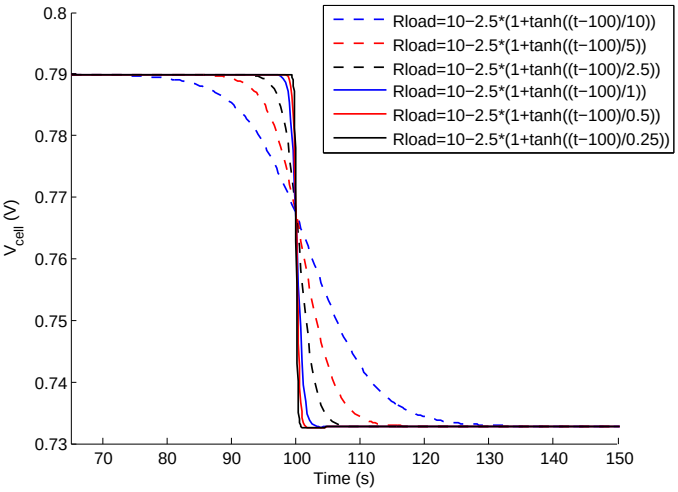

Figure 7.3.3: Six transient profiles of V_{cell} based on six different values of ω. The transient behaviour of V_{cell} is heavily influenced by the change in value of R_{load}.

clearly in figure 7.3.2). Despite this, the transient behaviour of I is very much affected by the change in value of R_{load}.

The same is also said for V_{cell}. Both V_{cell} and I are coupled by Ohm's law when the SOFC operates under a constant external load. For decreasing values of ω, we see that the transient behaviour of V_{cell} is also heavily influenced by a change in value of R_{load}. This is because V_{cell} and I are coupled by Ohm's law, which means that any change in value of R_{load} will also have an impact on V_{cell} as well as I. V_{cell} drops in this case due to the slow response of T_{cell} to react to the very quick dynamics that take place in the SOFC. It does rise gradually towards a new steady-state, but since the rise in T_{cell} is very small in this case (see figure 7.3.4), it is not clearly seen in that figure.

The transient behaviour of the different cell polarisations is also very influenced by changes in R_{load}. Since V_{cell} drops with decreasing R_{load}, all the cell polarisations rise along with decreasing R_{load}. Once $\omega = 0.25$ seconds, the rise in both activation polarisation terms, and the Ohmic polarisation term is followed by a slight, gradual drop towards a new steady-state solution (while η_{conc} rises slightly). What is noticeable is that for decreasing values of ω, the electrical based parameters evolve very quickly after a change in value of R_{load} (especially I), since I, V_{cell} and the polarisations are all coupled together, and I reacts to any change in value of R_{load}.

7.3.2 Solid Cell Temperature

Figure 7.3.4 represents the six different transient profiles of T_{cell}. Due to its large heat capacity, T_{cell} does not react as quickly to load changes compared to some of the other parameters (like I and V_{cell}). Even for values of ω equal to 5 s and 2.5 s, T_{cell} takes a little bit longer to reach a new steady-state value. However, what becomes apparent in this figure is that when $\omega = 1$ second, the long-term transient behaviour of T_{cell} for a change in R_{load} from 10 Ω to 5 Ω is set. The only difference between this profile of T_{cell} compared to

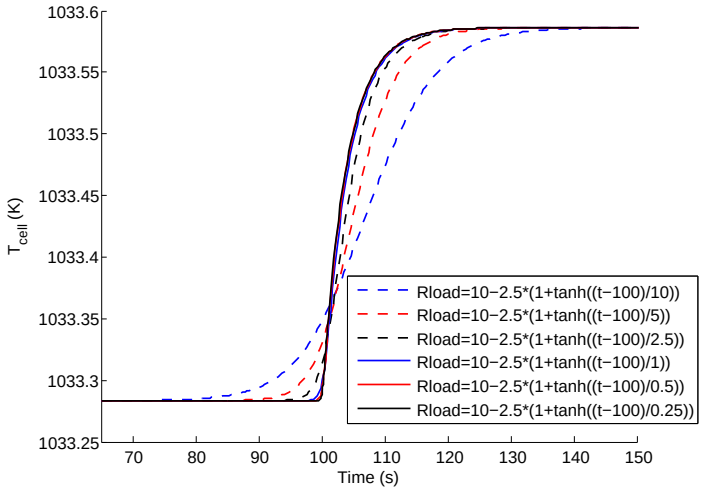

Figure 7.3.4: Six transient profiles of T_{cell} based on six different values of ω. The long-term transient behaviour of T_{cell} (and all the other cell parameters) is set when $\omega = 1$ second.

the other profiles of T_{cell} for lower values of ω is the profile around 100 seconds. Otherwise, there is hardly any difference at all between the three profiles associated with the three lowest values of ω.

At first inspection, the time taken for T_{cell} to reach close to a new steady-state value is just over 20 seconds (any other changes is very small at best). As it will be seen later on in subsection 7.3.6, the time taken for T_{cell} to reach a new steady-state when $\omega = 5$ seconds or lower occurs around 200 seconds (which for $\omega = 0.25$ seconds is around 100 seconds after the change in value of R_{load}). The reason for the gradual transition is related to the large heat capacity of the cell, where it takes time for the heat to spread across the whole cell.

7.3.3 Concentration in the TPB

Figures 7.3.5-7.3.7 represent the TPB concentrations of Hydrogen, Water and Oxygen respectively. As ω is lowered, the transient profile of each of the three parameters after

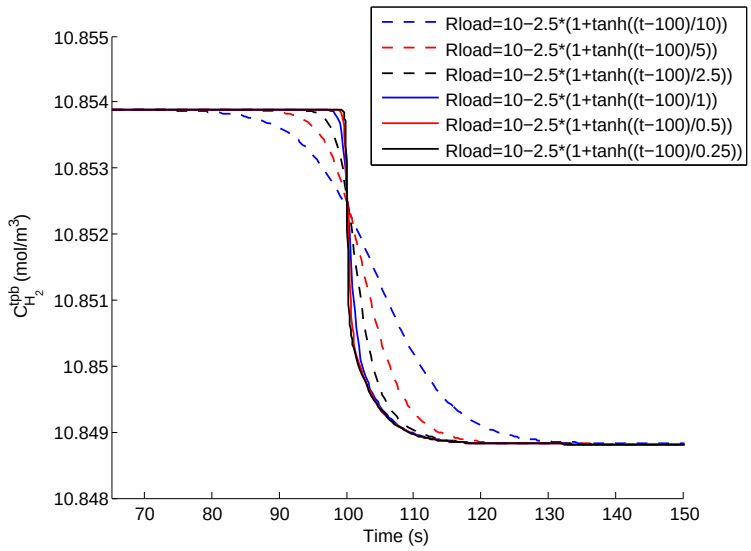

Figure 7.3.5: Six transient profiles of $C_{\mathrm{H_2}}^{\mathrm{tpb}}$ based on six different values of ω.

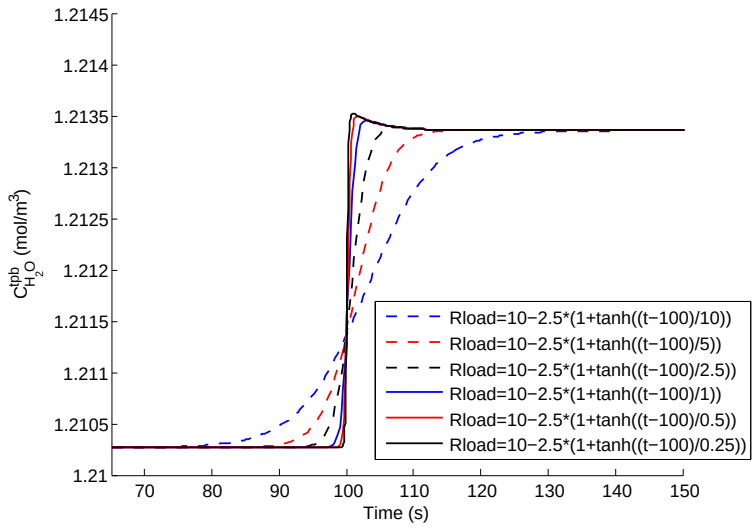

Figure 7.3.6: Six transient profiles of $C_{\mathrm{H_2O}}^{\mathrm{tpb}}$ based on six different values of ω.

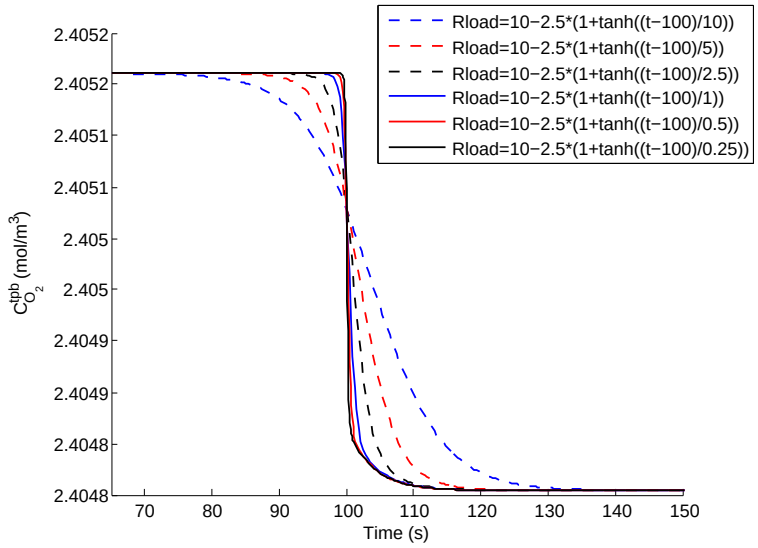

Figure 7.3.7: Six transient profiles of $C_{O_2}^{tpb}$ based on six different values of ω.

the change in value of R_{load} can be split up into two regions: one covering the change in these parameters within the time it takes R_{load} to change from 10 Ω to 5 Ω; the other covering the gradual transition of these parameters towards a new steady-state. As ω is lowered, the short-term transient profile of each of these parameters start to take shape. Since the concentration of Hydrogen, Oxygen and Water within the TPB is affected by the consumption/production rate (which is defined in terms of I), there is an initial drop in Hydrogen and Oxygen concentration levels, and an initial rise in Water concentration levels with decreasing R_{load}. All the quick dynamics, including mass diffusion within the electrodes, are incorporated within that time-frame.

After the time taken for R_{load} to go from 10 Ω to 5 Ω (for the cases where ω is equal to 1 second or lower), the long-term dynamics (influenced by the time taken for T_{cell} to reach a new steady-state) start to take effect on these profiles. In the case of Hydrogen and Oxygen (figure 7.3.7), the concentrations of both gaseous species gradually decrease towards a

new steady-state solution, as a little more Hydrogen and Oxygen is consumed within the electrochemical reactions. As for Water however, after the initial sharp increase, Water levels start to drop slightly towards a new steady-state, as the overall concentration of fuel in the TPB goes down with increasing time.

Looking at these profiles, it becomes clearer that with the expression of R_{load} given in equation (7.1), for low enough values of ω (=1 second and lower), the quicker dynamics within the SOFC has an effect on these profiles within the time-frame associated with the change in R_{load} from 10 Ω to 5 Ω. After R_{load} reaches very close to 5 Ω, any further transition towards a new steady-state is influenced by the time taken for T_{cell} to reach a new steady-state solution.

7.3.4 Fuel Flow Parameters

Figure 7.3.8 represents the different transient profiles of $C^{\text{b}}_{\text{fuel}}$ for six different values of ω. As ω is lowered, there is a small peak which forms around 100 seconds before $C^{\text{b}}_{\text{fuel}}$ gradually decreases towards a new steady-state value, as more fuel is consumed within the SOFC. The reason as to why a small peak forms around 100 seconds when ω is decreased is because there is a slightly higher amount of Water entering the fuel channel compared to the amount of Hydrogen leaving the fuel channel to enter the cell. Eventually, fuel concentration levels drop with increasing time as more Hydrogen is consumed within the SOFC.

As for the composition of the fuel flow, the change in value of the mole fractions of Hydrogen and Water mainly take place within the time it takes for R_{load} to change from 10 Ω to 5 Ω. Looking at figure 7.3.9, the multiple transient profiles of y_{H_2} is very similar in shape to the profile of V_{cell}. The mole fractions of Hydrogen, Oxygen and Water are mainly affected by consumption/production rates, which is defined by I. The cell current I rises in response to a drop in value of R_{load}, which in turn leads to a drop in y_{H_2}. Eventually,

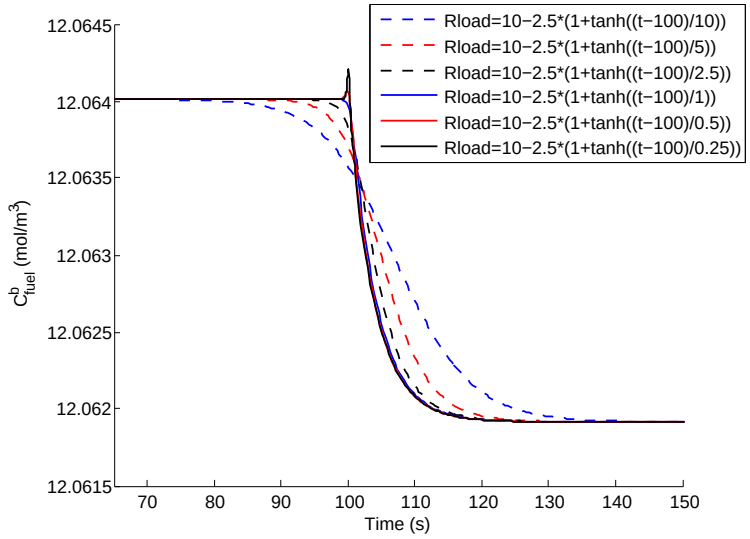

Figure 7.3.8: Six transient profiles of $C_{\text{fuel}}^{\text{b}}$ based on six different values of ω.

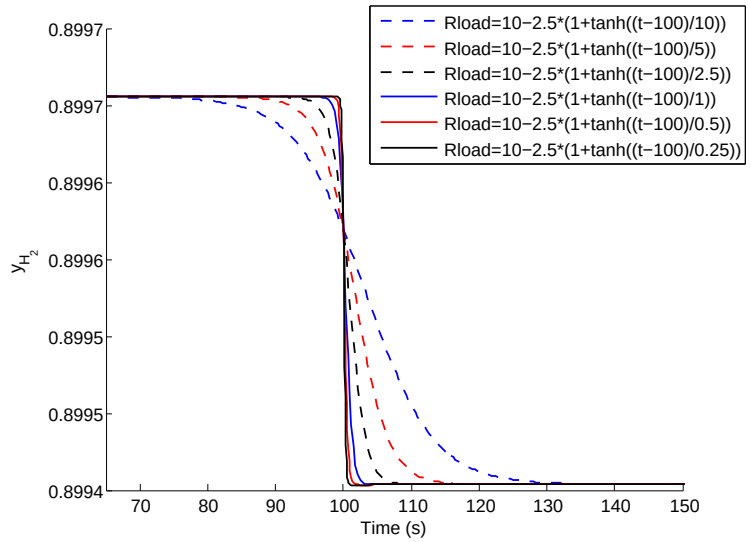

Figure 7.3.9: Six transient profiles of y_{H_2} based on six different values of ω.

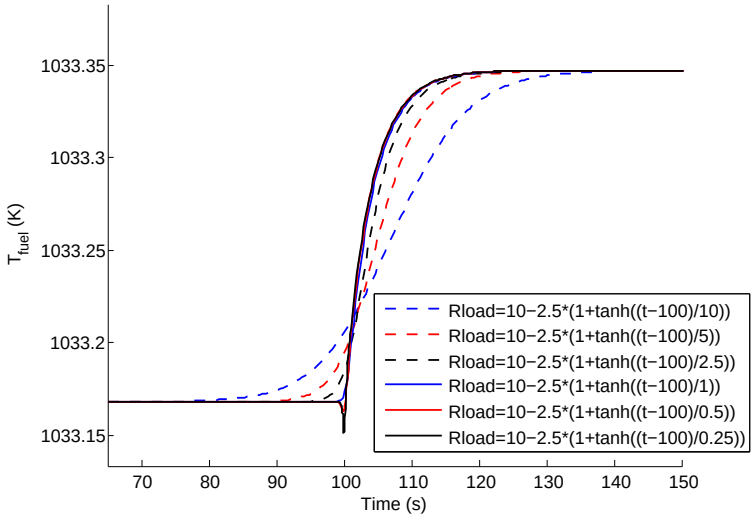

Figure 7.3.10: Six transient profiles of T_{fuel} based on six different values of ω.

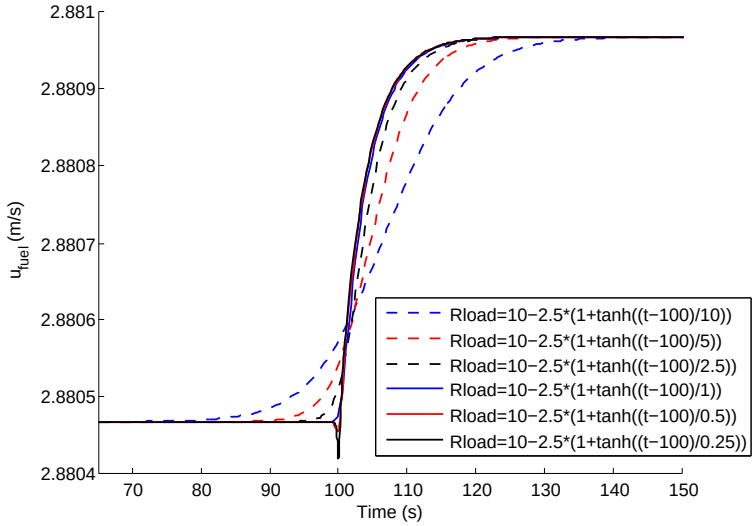

Figure 7.3.11: Six transient profiles of u_{fuel} based on six different values of ω.

y_{H_2} rises very slightly towards a new steady-state as Water levels in the fuel flow drop slightly.

The effect of having slightly more Water entering the SOFC compared to Hydrogen entering the SOFC for low values of ω is also shown in the multiple transient profiles of T_{fuel} (figure 7.3.10) and u_{fuel} (figure 7.3.11). For values of ω less than 1 second, a small drop starts to form in the profiles of both T_{fuel} and u_{fuel} around 100 seconds. In the case of u_{fuel}, this is caused by a slight increase in the bulk fuel flow pressure, caused by a slight increase in $C^{\text{in}}_{\text{fuel}}$. As for T_{fuel}, since there is a slight increase in $C^{\text{b}}_{\text{fuel}}$ around 100 seconds, the lack heat transfer from the cell to the fuel flow around that time causes T_{fuel} to drop slightly. A drop in fuel concentration (and hence fuel pressure) over time leads to an increase in both T_{fuel} and u_{fuel} up towards a new steady-state value.

7.3.5 Air Flow Parameters

Figure 7.3.12 represents the different transient profiles of $C^{\text{b}}_{\text{air}}$. Unlike $C^{\text{b}}_{\text{fuel}}$, there is no peak located around 100 seconds for low values of ω. There is just a simple drop from one steady-state value to another as Oxygen is consumed within the SOFC. Since none of the products from the reduction reaction (3.2) enters the air flow, the overall concentration of air drops as more Oxygen is consumed within the SOFC. The drop in Oxygen levels is reflected in figure 7.3.13, where the transient behaviour is very similar to I, V_{cell} and y_{H_2} in that the majority of the change in value occurs within the time-frame in which R_{load} changes from 10 Ω to 5 Ω.

Figure 7.3.14 represents the different transient profiles of T_{air}. Similar to T_{cell}, T_{air} rises gradually from one steady-state solution to another, as more heat is transferred from the cell to the air flow. The long-term steady-state profile is already set up once $\omega = 1$ second.

Figure 7.3.15 represents the different transient profiles of u_{air}. Unlike the other air flow parameters (and similar to u_{fuel}), for low enough values of ω, there is a slight drop in u_{air}

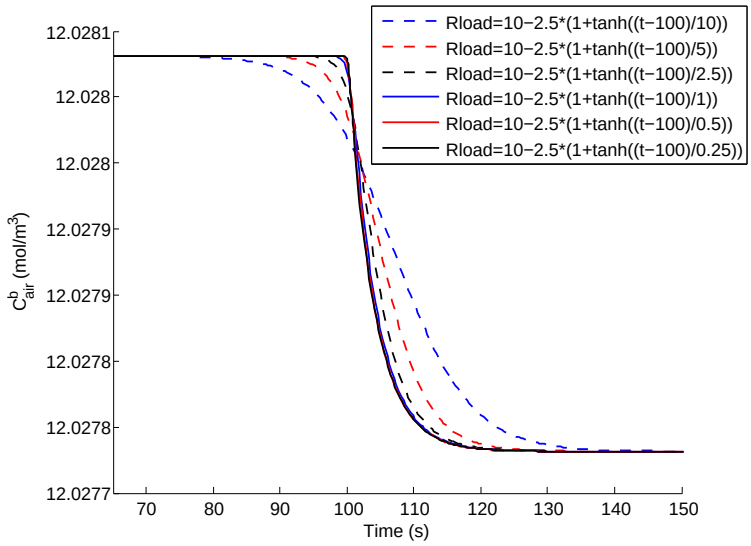

Figure 7.3.12: Six transient profiles of $C_{\text{air}}^{\text{b}}$ based on six different values of ω.

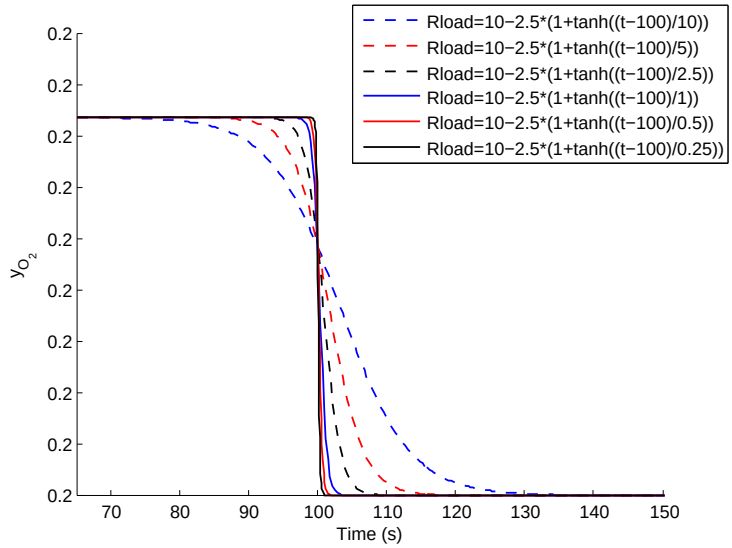

Figure 7.3.13: Six transient profiles of y_{O_2} based on six different values of ω.

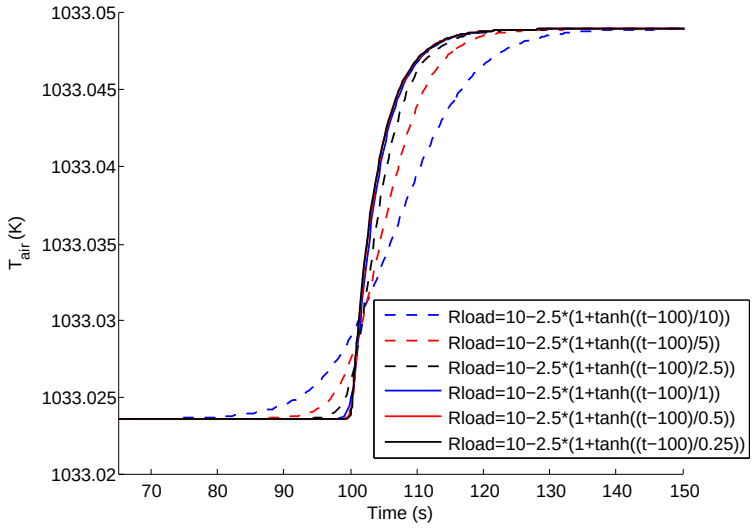

Figure 7.3.14: Six transient profiles of T_{air} based on six different values of ω.

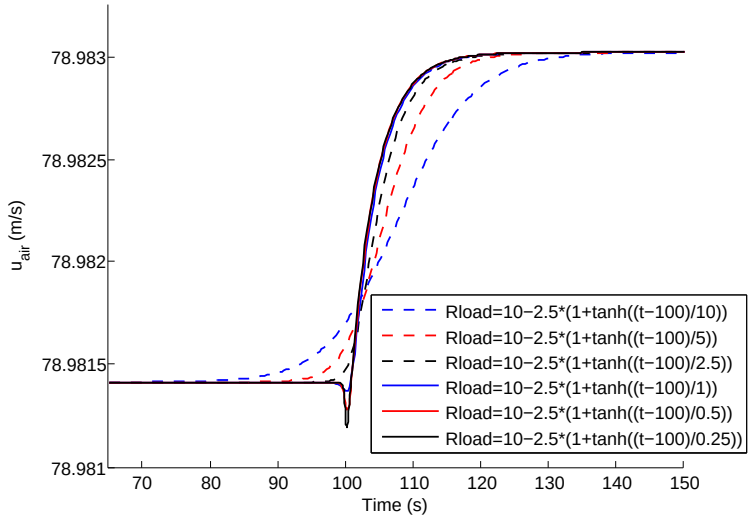

Figure 7.3.15: Six transient profiles of u_{air} based on six different values of ω.

around 100 seconds before it rises towards a new steady-state value. The reason for this is that for values of ω less than 1 second, bulk air flow pressure increases slightly around 100 seconds, forcing u_{air} to drop slightly. Eventually, due to decreasing air levels, u_{air} increases as the air pressure drops.

7.3.6 Time taken to reach a new steady-state

Since the thermal conductivity of the SOFC is not considered in this model, it is difficult to gauge exactly how long it takes T_{cell} (and the whole SOFC) to move towards a new steady-state solution. One way of looking at it is to look into the absolute difference of the solution vector from the dynamic model with the predicted steady-state solution vector at $R_{\text{load}} = 5\ \Omega$.

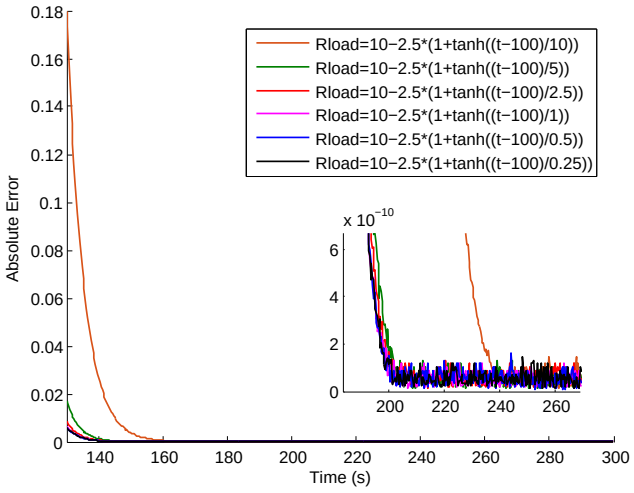

Figure 7.3.16: The profile showing the convergence of the six different solution vectors of the dynamic model towards the predicted steady-state solution at $R_{\text{load}} = 5\ \Omega$. The zoom-in part shows that five of the solution vectors stop converging around 200 seconds. The solution vector corresponding to $\omega = 10$ seconds in R_{load} stops around 240 seconds.

Figure 7.3.16 shows the convergence of the six different solution vectors of the dynamic model (corresponding to the six different values of ω in R_{load}) towards the predicted

steady-state solution vector at $R_{\text{load}} = 5\ \Omega$. The absolute difference between the solution vector of the dynamic model $\mathbf{x_T}(t)$ with the predicted steady-state solution $\mathbf{x_{SS}}$ is defined as

$$\Delta \mathbf{x}_{\text{AE}} = ||\mathbf{x_T}(t) - \mathbf{x_{SS}}||_2 \tag{7.10}$$

Using this equation, we see that with the exception of the solution vector corresponding to $\omega = 10$ seconds in R_{load}, the solution vectors stop converging around 200 seconds. This means that for the lowest value of ω, it takes around 100 seconds after the change in R_{load} is complete for the SOFC to fully settle down towards a new steady-state solution, even though the transient profiles in this section look like they have fully converged after around 20-30 seconds.

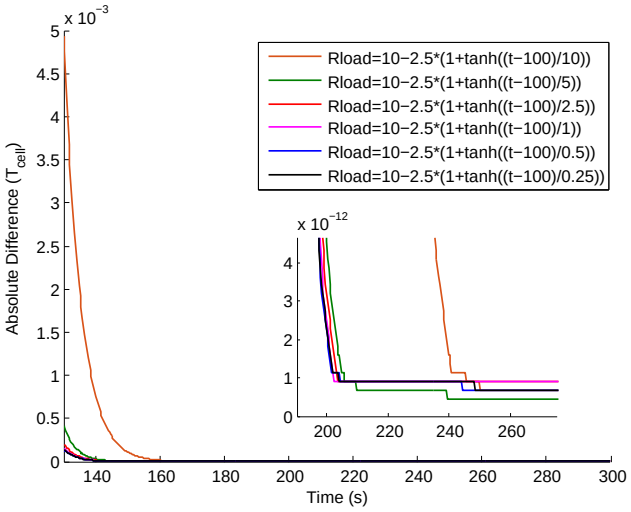

Figure 7.3.17: The profile showing the convergence of the six different profiles of T_{cell} towards its predicted steady-state solution at $R_{\text{load}} = 5\ \Omega$. The zoom-in part shows that five of the solution vectors stop converging around 200 seconds. The solution vector corresponding to $\omega = 10$ seconds in R_{load} stops around 240 seconds.

Figure 7.3.17 shows the convergence of the six different T_{cell} profiles towards the predicted steady-state solution of T_{cell} at $R_{\text{load}} = 5\ \Omega$. Compared with figure 7.10, there is really

not much difference between the time taken for each expression of T_{cell} to stop converging and for the different solution vectors of the transient model to stop converging. This is also more or less the same with every other SOFC parameter from the model. The amount of time taken for the SOFC to reach a new steady-state after a change in R_{load} depends on which part of the branch (un-ignited, ignited or unstable) the SOFC initially operates on. In this case, the SOFC initially operates in a region where there is very low electrochemical activity, and the change in T_{cell} is very small, which means that it does not take long for the SOFC to operate at a new steady-state. However, for starting values of R_{load} much closer to the multiplicity region, the change in T_{cell} after a change in R_{load} will be larger, leading to a longer transition from one steady-state solution to another.

7.4 Comparison with previous works

Figures 7.4.1–7.4.3 show the transient profiles of T_{cell}, I and V_{cell} respectively after a change in R_{load} from 10 Ω to 5 Ω around 100 seconds. This is for the case where $\omega = 0.25$ seconds, and for the rest of the transient profiles shown this chapter, ω will be set at this value. Even though R_{load} is not a step function which changes values exactly at 100 seconds, the transient profiles of these three parameters is not too dissimilar from other profiles in other papers where they consider a step-change in R_{load}. This includes the paper by Bavarian and Soroush [49], and the paper by Qi et al. [67].

There is plenty of work done where the transient behaviour of the SOFC is investigated for various load changes. But most of them do not consider an external load resistance component. Instead, load changes are represented by a step change in current density, or even cell voltage. The equivalent transient profiles of T_{cell}, I and V_{cell} from [49] are given in figure 7.4.4.

In terms of the shape of the profiles, they are very similar to the shape of the transient profiles in figures 7.4.1-7.4.3. The only main difference is the values of T_{cell}, I and V_{cell}

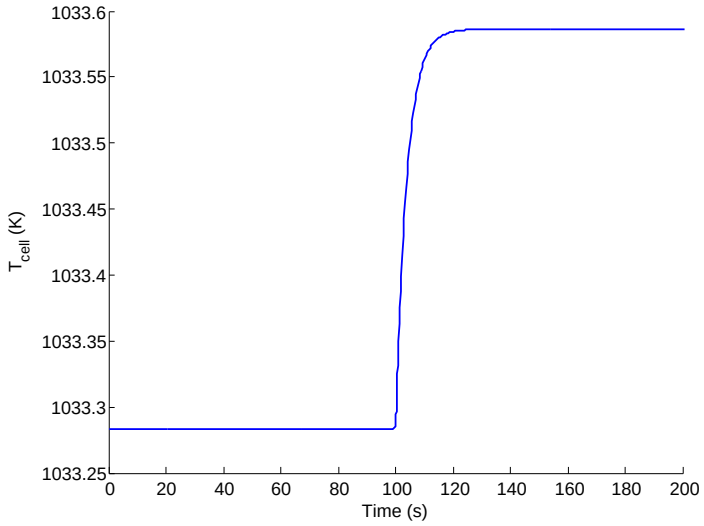

Figure 7.4.1: The transient profile of T_{cell} for a change in R_{load} from 10 Ω to 5 Ω.

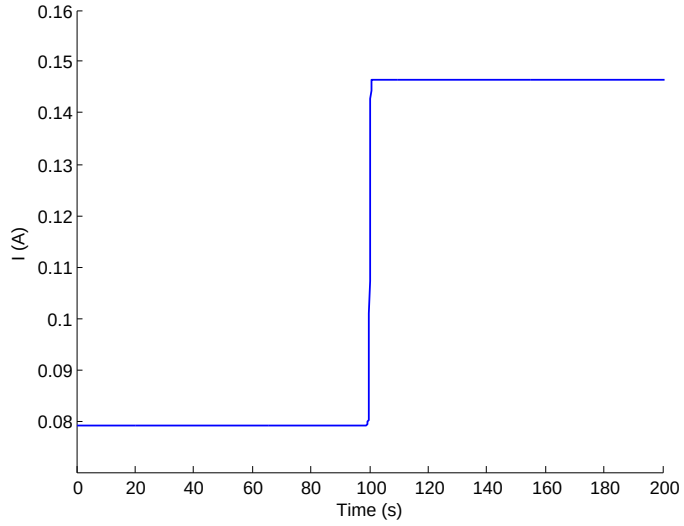

Figure 7.4.2: The transient profile of I for a change in R_{load} from 10 Ω to 5 Ω.

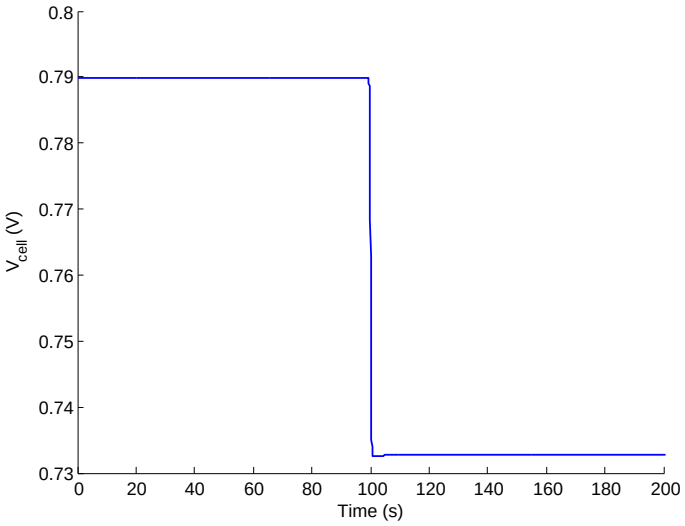

Figure 7.4.3: The transient profile of T_{cell} for a change in R_{load} from 10 Ω to 5 Ω.

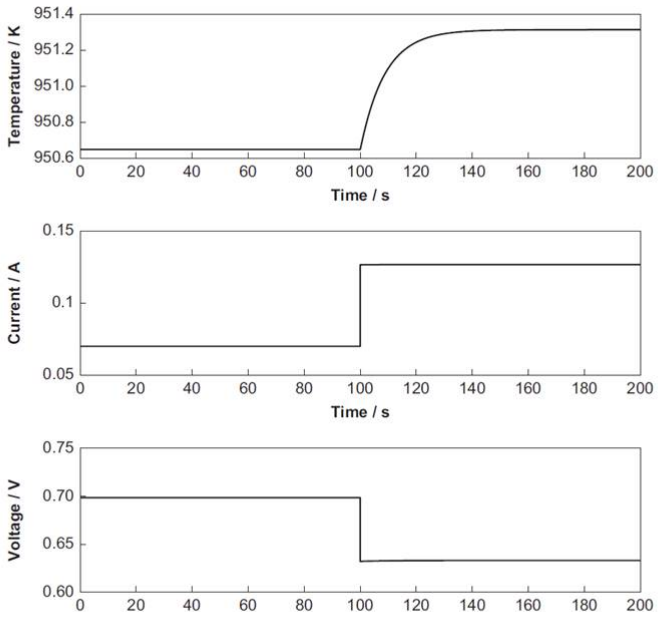

Figure 7.4.4: The transient profiles of T_{cell}, I and V_{cell} after R_{load} drops from 10 Ω to 5 Ω after 100 seconds by [49].

in [49] compared to this thesis which can be attributed to the modifications made to the model in [49], plus the change in value of the inlet gas flow temperatures. Since the change in T_{cell} in [49] is slightly larger than the change of T_{cell} here, it is probably not surprising that it seems to take a bit longer for T_{cell} to approach very closely towards a new steady-state value.

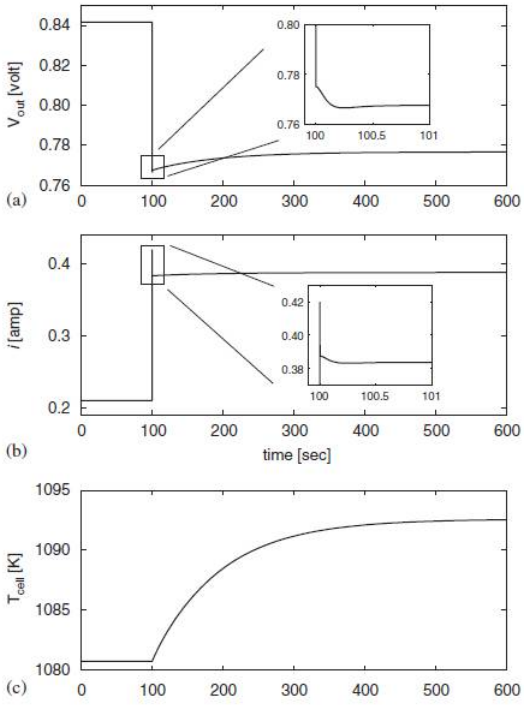

Figure 7.4.5: The transient profiles of T_{cell}, I and V_{cell} after R_{load} drops from 4 Ω to 2 Ω after 100 seconds by [69].

The equivalent transient profiles of T_{cell}, I and V_{cell} after a step-change in R_{load} by Qi et al. [67] is given in figure 7.4.5. Here, it takes longer for the cell parameters to reach a new steady-state. This is because the product of the cell heat capacity with the cell density in [67] is larger than the equivalent product of those two parameters in this thesis. The value of $C_{\text{p,cell}}$ given in [67] is 740 J/(kg · K), and if multiplied with the density of the

cell (which is equal to 4592 kg/m^3), their product is equal to 3398080 J/(m^3 · K)-just over three times larger than the equivalent product given in Appendix A. This suggests that the heat capacity of the cell in [67] may be larger than the heat capacity of the cell in this model. This, along with a larger rise in T_{cell} compared to the rise in T_{cell} in figure 7.4.1, would result in a longer transition from one steady-state value to another. The conductivity of the cell is not considered in [67].

There are some differences in the transient behaviour of I and V_{cell} in [67] compared to this thesis. In the model from [67], double-layer capacitance effects are considered, and that (along with diffusion effects in the electrodes) causes I to drop slightly after the sharp rise associated with the step-change in R_{load}. This also affects V_{cell} as well in that short time-period of about 0.2 seconds almost immediately after the step-change. But otherwise, the shape of the profile is very similar to the profile in figure 7.4.3.

Even though Methane is present in the fuel flow in [67], the shape of the transient profiles for Hydrogen, Oxygen and Water are very similar to the profiles shown in the previous section. The transient profiles of Hydrogen, Oxygen and Water in [67] were mainly affected by the change in the cell current I, affecting the consumption/production rates, and by the shift reaction (which occurs almost instantaneously) acting in the reverse direction to maintain equilibrium. Only a small amount of Methane was consumed by the shift reaction, meaning that there was not any long-term rise in Hydrogen levels.

7.5 Transient behaviour of the SOFC during ignition

In this section, the steady-state multiplicity of the SOFC is investigated more closely by looking at the transient behaviour of the SOFC during ignition. Firstly, the transient behaviour of the SOFC is investigated for a change in value of R_{load} around 100 seconds that causes the SOFC to ignite and operate along another steady-state branch. The initial value of R_{load} is chosen such that it is below the extinction point. To confirm that the

SOFC is operating along another steady-state branch, there will be another change in the value of R_{load} around 100 seconds where it goes back to its original value just above the ignition point. This is to show that the SOFC does not operate with the same parameter values as it did before the initial change in value of R_{load}.

7.5.1 Change in R_{load} from 0.0018 Ω to 0.0017 Ω

For this case, the SOFC initially operates on the lower, un-ignited steady-state branch located on the point $R_{\text{load}} = 0.0018\ \Omega$ (as shown in figure 7.5.1). The expression of R_{load} for this case is

$$R_{\text{load}} = 0.0018 - 0.00005 \left\{ 1 + \tanh\left(\frac{t - 100}{0.25} \right) \right\} \tag{7.11}$$

The transition of R_{load} for this case takes it beyond the location of the ignition point at $R_{\text{load}} = 0.001732375\ \Omega$. The expected transition in value of T_{cell} is shown on a zoom-in of the steady-state profile for T_{cell} in figure 4.2.2 (figure 7.5.1), where the operating temperature shifts from one steady-state branch to another. The initial conditions for this case are based on the predicted steady-state solutions for $R_{\text{load}} = 0.0018\ \Omega$ on the un-ignited steady-state branch. The change in T_{cell} after the step-change (along with close-ups of the profile just after the step-change, and during the first few hundred seconds) is shown in figure 7.5.2. At a first glimpse, it looks like T_{cell} has shifted towards its expected value after the step-change in figure 7.5.1.

Just after the change in R_{load}, T_{cell} rises gradually at first, as it reacts to more Hydrogen and Oxygen being consumed within the cell (caused by an instant rise in I). However, between 300 and 400 seconds, T_{cell} starts to rise more sharply rather than settle down, as the SOFC starts to ignite. After this particular change in value of R_{load}, the rise in electrolyte conductivity with rising T_{cell} causes the electrochemical reactions to intensify to an extent that a hot spot is formed (approaching 400 seconds). This causes T_{cell} to rise sharply at around 500 seconds towards a new steady-state solution at around 550

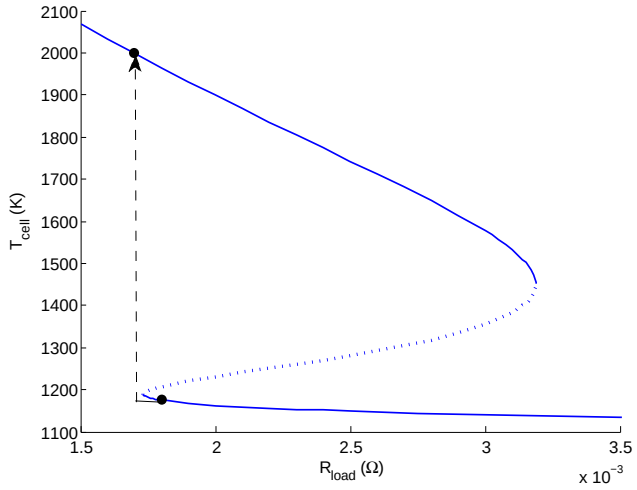

Figure 7.5.1: The steady-state profile of T_{cell} from the base case, showing the expected transition of T_{cell} from the point on $R_{\text{load}} = 0.0018\ \Omega$ of the un-ignited steady-state branch to the point on $R_{\text{load}} = 0.0017\ \Omega$ of the ignited steady-state branch.

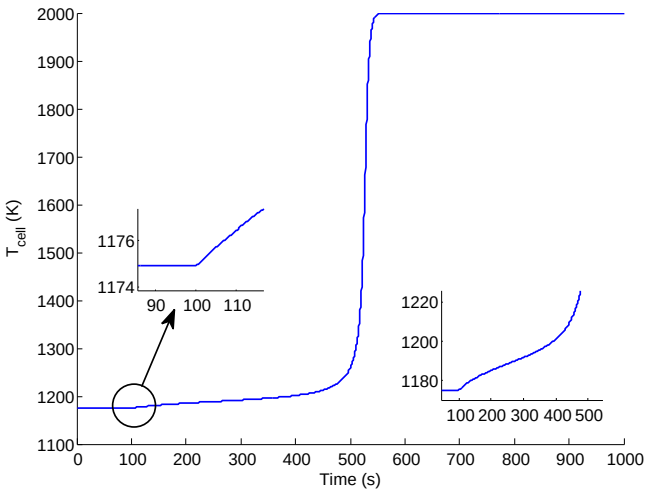

Figure 7.5.2: The transient profile for T_{cell} during the ignition phase after a change in R_{load} from $0.0018\ \Omega$ to $0.0017\ \Omega$ around 100 seconds. The profile just after 100 seconds, and during the first few hundred seconds are zoomed-in.

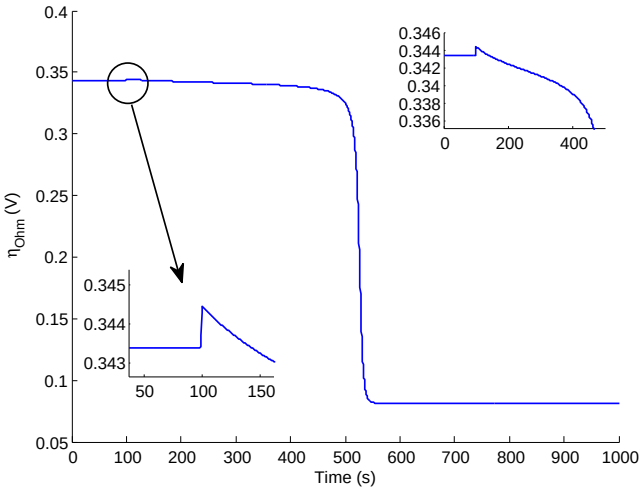

Figure 7.5.3: The transient profile for η_{Ohm} during the ignition phase after a change in R_{load} from 0.0018 Ω to 0.0017 Ω around 100 seconds. The profile just after 100 seconds, and during the first few hundred seconds are zoomed-in.

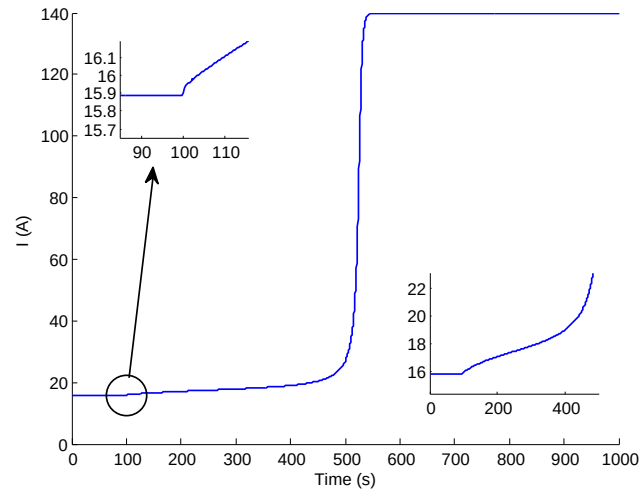

Figure 7.5.4: The transient profile for I during the ignition phase after a change in R_{load} from 0.0018 Ω to 0.0017 Ω around 100 seconds. The profile just after 100 seconds, and during the first few hundred seconds are zoomed-in.

seconds on the ignited branch. The absolute difference of T_{cell} with the predicted steady-state solution of T_{cell} is a low as the order of magnitude of 10^{-13} at 1000 seconds, so it definitely tends towards the predicted steady-state solution at $R_{\text{load}} = 0.0017\ \Omega$ shown in figure 7.5.1. It approaches very closely to the predicted steady-state solution close to 700 seconds.

Figure 7.5.3 shows the transient profile of η_{Ohm} during ignition, with close-ups of the profile just after the step-change, and during the first few hundred seconds. Since Ohmic resistivity is inversely proportional to conductivity, that means that a drop in Ohmic resistivity with rising T_{cell} eventually leads to the cell igniting (as reaction kinetics intensify), causing T_{cell} to rise sharply with a sharply decreasing η_{Ohm} profile. Just after the step-change, η_{Ohm} rises with rising I at first. After that, it decreases with rising T_{cell}, and starts to drop more sharply between 300 and 400 seconds as the hot spot starts to form. Eventually, it drops down towards a new steady-state solution along the ignited steady-state branch at around 550 seconds.

The transient profile for I during ignition is shown in figure 7.5.4. The cell current rises along with rising T_{cell} and rising electrolyte conductivity towards an ignited steady-state much higher than the previous steady-state solution. The sharp rise in I during the ignition phase leads to a sharp rise in the electrochemical reaction rates, causing a huge drop in Hydrogen levels (figure 7.5.6). Just after the change in value of R_{load}, there is an almost instant rise in I with decreasing R_{load}, which in turn causes an almost instant drop in V_{cell} in figure 7.5.5 (due to slow responding temperature dynamics). Eventually, both I and V_{cell} rise with increasing T_{cell}, rising more sharply after 400 seconds towards a new steady-state value at around 550 seconds.

Figures 7.5.6-7.5.8 represent the transient profiles of y_{H_2}, $y_{\text{H}_2\text{O}}$ and y_{O_2} during the ignition phase. Due to the large rise in I during the ignition phase, more and more Hydrogen is consumed within the cell, causing mole fraction levels of Hydrogen to drop from around

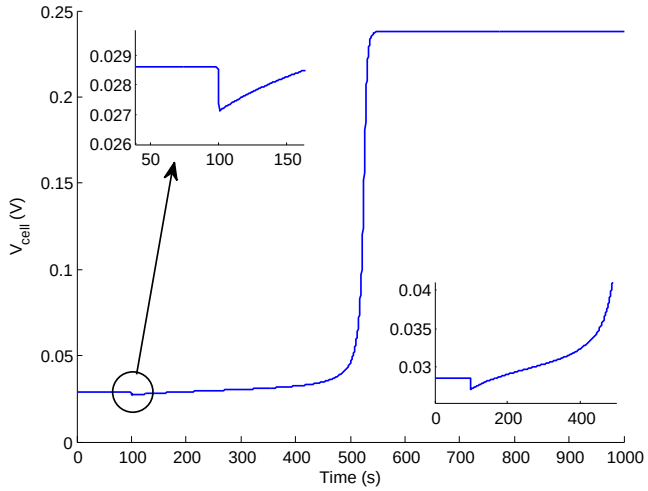

Figure 7.5.5: The transient profile for V_{cell} during the ignition phase after a change in R_{load} from 0.0018 Ω to 0.0017 Ω around 100 seconds. The profile just after 100 seconds, and during the first few hundred seconds are zoomed-in.

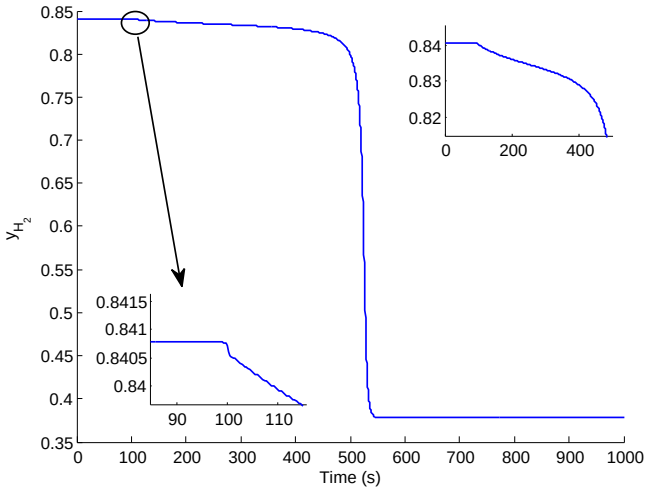

Figure 7.5.6: The transient profile for y_{H_2} during the ignition phase after a change in R_{load} from 0.0018 Ω to 0.0017 Ω around 100 seconds. The profile just after 100 seconds, and during the first few hundred seconds are zoomed-in.

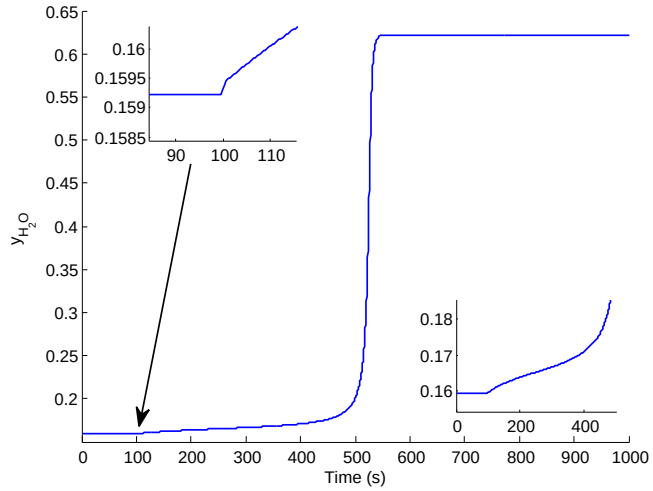

Figure 7.5.7: The transient profile for $y_{\mathrm{H_2O}}$ during the ignition phase after a change in R_{load} from 0.0018 Ω to 0.0017 Ω around 100 seconds. The profile just after 100 seconds, and during the first few hundred seconds are zoomed-in.

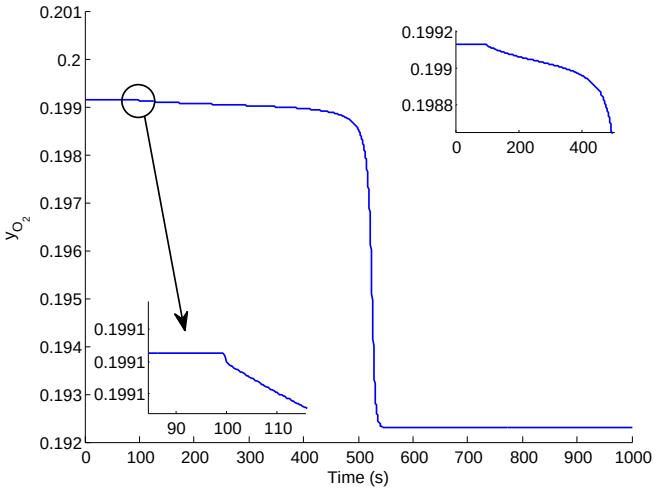

Figure 7.5.8: The transient profile for $y_{\mathrm{O_2}}$ during the ignition phase after a change in R_{load} from 0.0018 Ω to 0.0017 Ω around 100 seconds. The profile just after 100 seconds, and during the first few hundred seconds are zoomed-in.

0.841 before the step-change to around 0.37-0.38 after ignition. This means that mole fraction levels for Water rises from around 0.159 to around 0.62-0.63 after ignition. The amount of fuel utilised at $R_{\text{load}} = 0.0017\ \Omega$ rises up to around 52%. Oxygen levels also drop more significantly during ignition, falling down to as low as almost 0.192 after ignition.

Comparing the profiles from this subsection with the equivalent profiles in [49], even though the rise in T_{cell} is sharper here than the rise in T_{cell} in [49], it does not take much longer for the parameters to operate along a new, ignited steady-state here compared to the parameters in [49]. The formation of the hot spot seems to occur around the same time. However, it is not shown in [49], or any of their future papers that the SOFC still operates along that steady-state branch when R_{load} is changed back into its original value.

7.5.2 Change in R_{load} from 0.0017 Ω to 0.0018 Ω

Since the solution vector of the dynamic model at $t = 1000$ seconds is very close to the predicted steady-state solution vector at $R_{\text{load}} = 0.0017\ \Omega$, the initial conditions for this case are based on the predicted steady-state solution at $R_{\text{load}} = 0.0017\ \Omega$ (see Appendix H). For this case, R_{load} is expressed as follows

$$R_{\text{load}} = 0.0017 + 0.00005 \left\{ 1 + \tanh\left(\frac{t - 100}{0.25} \right) \right\} \tag{7.12}$$

Looking at figure 7.5.9, if R_{load} drops back down to its original value, then the operating temperature is expected to drop slightly, but not to the extent where it goes back to its original value located along the un-ignited steady-state branch.

This is confirmed in figure 7.5.10, where T_{cell} drops down by just over 40 K towards a new steady-state solution. This is located at a different steady-state branch compared to the value of T_{cell} located at the un-ignited steady-state branch for the same point of R_{load}. This shows us that if the SOFC ignites after a drop in R_{load}, the operating temperature

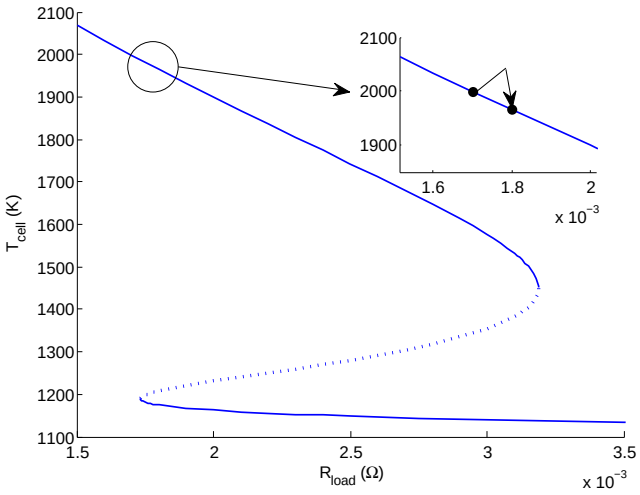

Figure 7.5.9: The steady-state profile of T_{cell} from the base case. Within the circle is the expected change in T_{cell} for a change in value of R_{load} from 0.0018 Ω to 0.0017 Ω.

does not go back to its original operating temperature before the drop in R_{load}. All the other parameters considered in the SOFC model are affected as well.

Looking at the time-scale profiles in section 7.2, we see that the quicker dynamics that occur in the SOFC including diffusion within the electrodes, reaction kinetics, convection within the gas channels, and even cell consumption rates occur more quickly, especially after ignition. However, with the expression of R_{load} given in equation (7.12), all these dynamics occur well within the period it takes for R_{load} to change from 0.0017 Ω to 0.0018 Ω (which is around 1.5 seconds). The drop in I and the rise in V_{cell} around 100 seconds occurs within the time period where R_{load} changes from 0.0017 Ω to 0.0018 Ω. However, since the drop in T_{cell} is more significant compared to the rise in T_{cell} in section 7.3, the quick changes in I and V_{cell} is followed by a gradual drop in both parameters towards a new steady-state value.

Even though R_{load} is increased, V_{cell} rises slightly after the rise in R_{load}. This is because

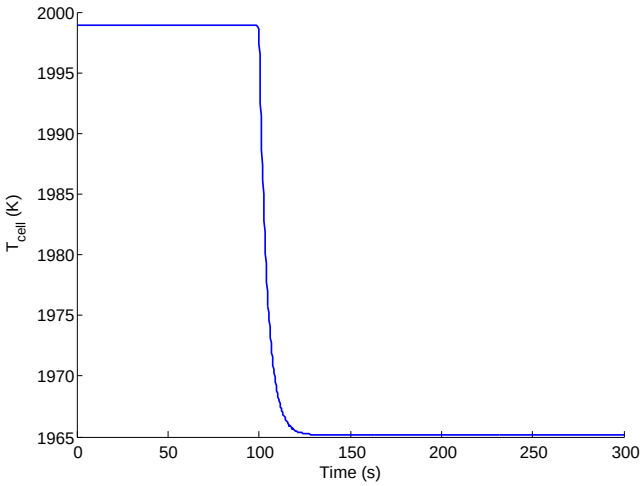

Figure 7.5.10: The transient profile of T_{cell} for a change in value of R_{load} from 0.0017 Ω to 0.0018 Ω around 100 seconds. The final value of T_{cell} is much higher than its initial value for the same value of R_{load}.

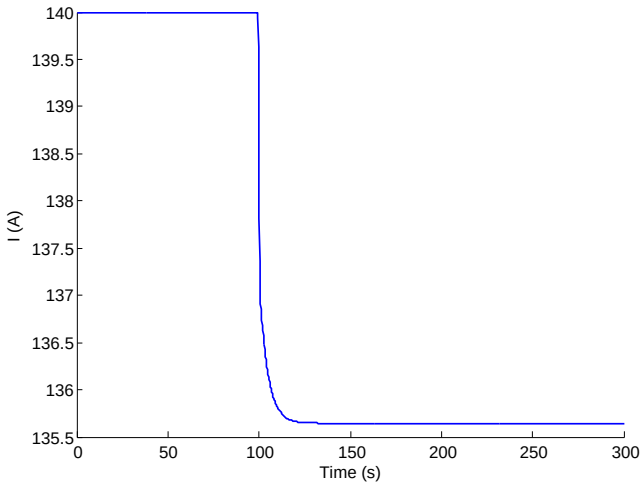

Figure 7.5.11: The transient profile of I for a change in value of R_{load} from 0.0017 Ω to 0.0018 Ω around 100 seconds. The final value of I is much higher than its initial value for the same value of R_{load}.

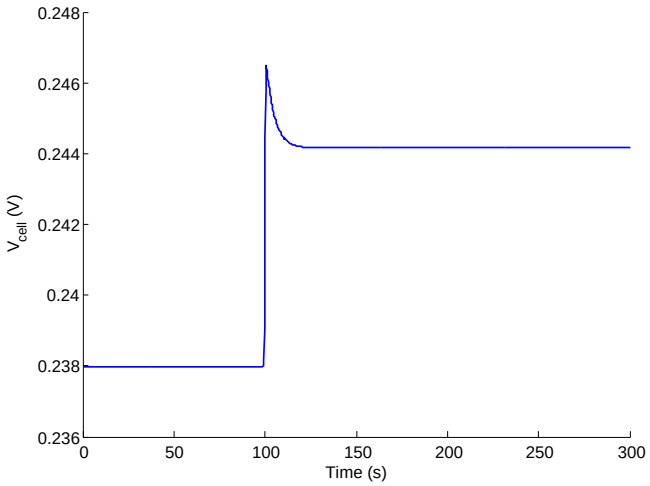

Figure 7.5.12: The transient profile of V_{cell} for a change in value of R_{load} from 0.0017 Ω to 0.0018 Ω around 100 seconds. The final value of V_{cell} is higher than its initial value for the same value of R_{load}.

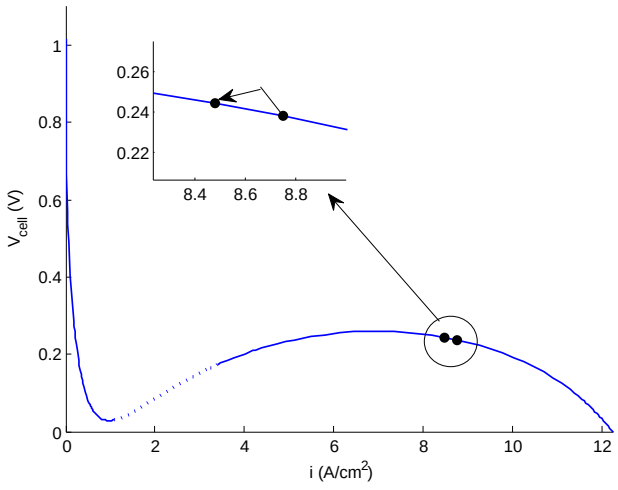

Figure 7.5.13: The V-I profile from the base case. Within the circle is the expected change in V_{cell} for a step-change in R_{load} from 0.0018 Ω to 0.0017 Ω, where V_{cell} rises.

if you locate the value of V_{cell} after the SOFC ignites in figure 4.4.1, it is located after V_{cell} reaches its peak along the ignited steady-state branch. Since a rise in R_{load} results in a drop in the current density i, a rise in R_{load} from 0.0017 Ω to 0.0018 Ω results in V_{cell} moving backwards along the ignited steady-state curve, past the value of V_{cell} after ignition, and finishing at a point along the ignited steady-state branch slightly higher than before. This is highlighted in figure 7.5.13.

Considering some of the other parameters, Ohmic Polarisation rises slightly with decreasing T_{cell}. There is a slight rise in Hydrogen and Oxygen (and fall in Water levels), as due to the drop in I, slightly less Hydrogen and Oxygen is consumed in the electrochemical reactions. The absolute difference of the solution vector to the dynamic model after the step-change with the expected steady-state solution vector at $R_{\text{load}} = 0.0018\ \Omega$ along the ignited steady-state branch at 300 seconds is of the order of 10^{-11}, and stops converging close to 240 seconds (almost 140 seconds after the change in value of R_{load}). Therefore, starting from a value of R_{load} less than the extinction point location of R_{load}, if R_{load} is dropped down to the extent that the SOFC ignites and operates at a much higher operating temperature along another steady-state branch, increasing it back to its original value will not bring down the operating temperature back to its original operating value.

7.6 Transient behaviour of the SOFC during extinction

In this section, the transient behaviour is investigated during the extinction phase. This is to show that for changes in value of R_{load} around the extinction point, once the SOFC drops down to the un-ignited steady-state branch, it stays there (as long as R_{load} is not dropped beyond the ignition point). The SOFC initially operates on the ignited-steady-state branch at $R_{\text{load}} = 0.003\ \Omega$, which is larger than the ignition point.

The transient behaviour of the SOFC is investigated initially for a change in value of

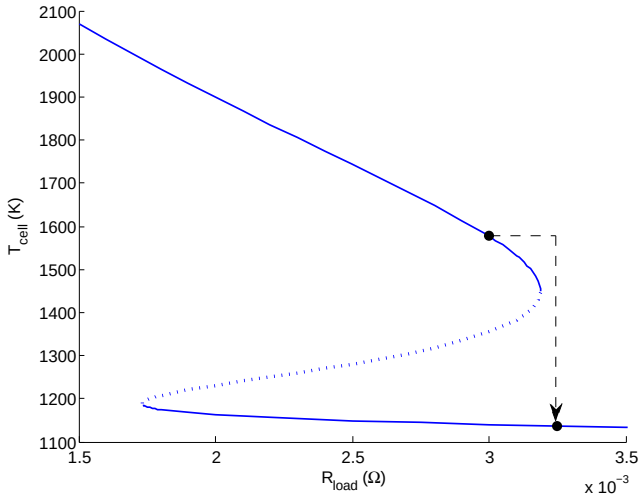

Figure 7.6.1: The steady-state profile of T_{cell} from the base case, showing the expected transition of T_{cell} after a change in value of R_{load} from 0.003 Ω to 0.00325 Ω.

R_{load} from 0.003 Ω to 0.00325 Ω around 100 seconds (which is beyond the location of the extinction point at 0.00318746 Ω), to investigate the behaviour of the SOFC during the extinction phase. After that, the transient behaviour of the cell is investigated for a change in value of R_{load} from 0.00325 Ω back down to $R_{\text{load}} = 0.003$ Ω (which is also larger than the ignition point) to show that the SOFC remains on the un-ignited steady-state branch, showing that there are two different stable steady-state branches.

7.6.1 Change in R_{load} from 0.003 Ω to 0.00325 Ω

For this particular case, R_{load} is expressed as follows:

$$R_{\text{load}} = 0.003 + 0.000125 \left\{ 1 + \tanh\left(\frac{t - 100}{0.25} \right) \right\}. \tag{7.13}$$

Figure 7.6.1 shows the expected transition of the operating temperature for a change in R_{load} from 0.003 Ω to 0.00325 Ω, where T_{cell} shifts from the ignited steady-state branch to

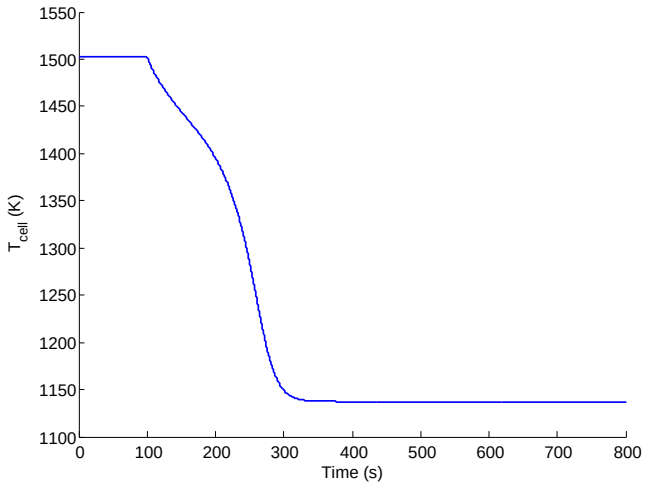

Figure 7.6.2: The transient profile of T_{cell} for a change in value of R_{load} from 0.003 Ω to 0.00325 Ω around 100 seconds, showing the behaviour of T_{cell} during the extinction phase.

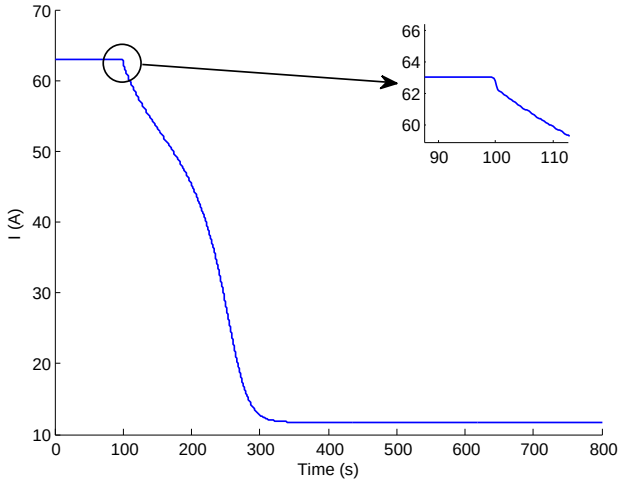

Figure 7.6.3: The transient profile of I for a change in value of R_{load} from 0.003 Ω to 0.00325 Ω around 100 seconds, showing the behaviour of I during the extinction phase.

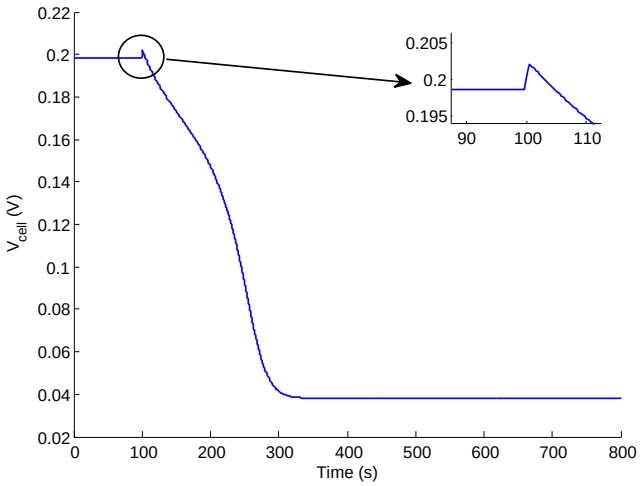

Figure 7.6.4: The transient profile of V_{cell} for a change in value of R_{load} from 0.003 Ω to 0.00325 Ω around 100 seconds, showing the behaviour of V_{cell} during the extinction phase.

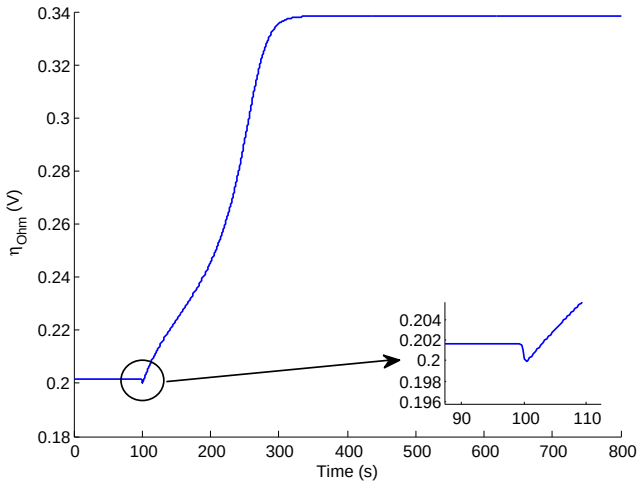

Figure 7.6.5: The transient profile of η_{Ohm} for a change in value of R_{load} from 0.003 Ω to 0.00325 Ω around 100 seconds, showing the behaviour of η_{Ohm} during the extinction phase.

the un-ignited steady-state branch. The initial conditions are set equal to the predicted steady-state solution located at $R_{\text{load}} = 0.003\ \Omega$ along the ignited steady-state branch.

Figure 7.6.2 represents the transient profile of T_{cell}. Looking at that profile, T_{cell} drops down towards a new steady-state solution on the un-ignited branch. The extinction phase seems to be quicker than the ignition phase, with the SOFC seemingly operating at a new-steady-state close to 400 seconds. In reality, T_{cell} takes a bit longer to operate at the new steady-state solution due to the large heat capacity (especially as the cell heating time-scale is so large). T_{cell} (and the solution vector of the dynamic model) stops converging towards its predicted steady-state solution around 700 seconds, where the absolute difference is of order 10^{-11}.

As expected, the transient profile of I in figure 7.6.3 shows a gradual drop in the cell current from one steady-state solution to another on another steady-state branch. Initially I drops down by a small amount during the period where R_{load} changes from 0.003 Ω to 0.00325 Ω, as shown by the close-up of the profile in figure 7.6.3. After that, I gradually drops down towards its predicted steady-state solution along the un-ignited steady-state branch, resulting in a quite large decrease in electrochemical activity.

The transient profiles for V_{cell} and η_{Ohm} are shown in figures 7.6.4 and 7.6.5 respectively. Looking at figure 7.6.5, the drop in T_{cell} from one operating branch to another is due to the drop in electrolyte conductivity with decreasing T_{cell}, which leads to a notable reduction in electrochemical activity to the extent that there is a sharp drop in the operating temperature. A drop in electrolyte conductivity is shown by the rise in η_{Ohm} after the change in value of R_{load}. As for V_{cell}, the location of V_{cell} after extinction on figure 4.4.1, is close to the minimum of the V_{cell} profile along the un-ignited steady-state branch. Therefore, after a quick initial rise with rising R_{load}, the change in V_{cell} during the extinction phase for values of R_{load} close to the extinction point is represented by a gradual drop with decreasing T_{cell}.

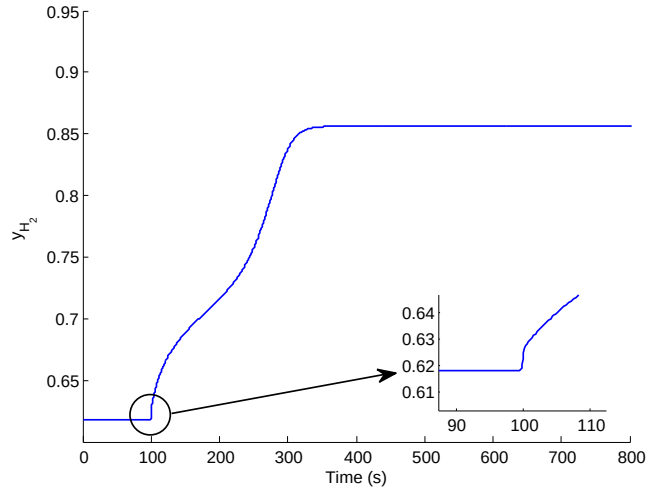

Figure 7.6.6: The transient profile of y_{H_2} for a change in value of R_{load} from 0.003 Ω to 0.00325 Ω around 100 seconds, showing the behaviour of y_{H_2} during the extinction phase.

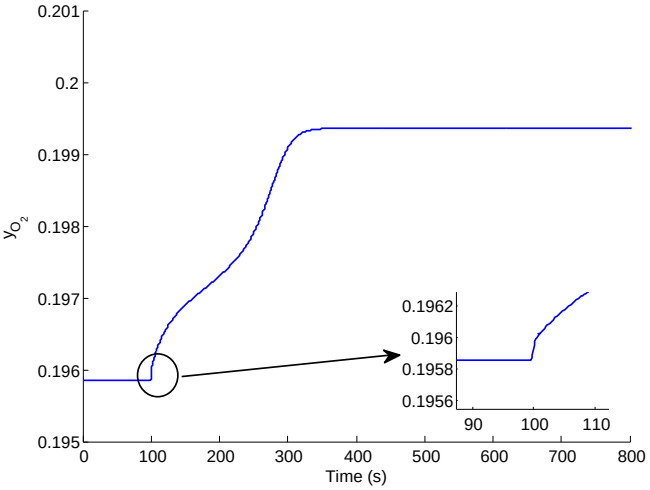

Figure 7.6.7: The transient profile of y_{O_2} for a change in value of R_{load} from 0.003 Ω to 0.00325 Ω around 100 seconds, showing the behaviour of y_{O_2} during the extinction phase.

Figures 7.6.6 and 7.6.7 represent the transient profiles of the mole fractions of Hydrogen and Oxygen respectively. Since there is a significant drop in electrochemical activity during the extinction phase, less Hydrogen and Oxygen is consumed within the electrochemical reactions. Hence, there is an increase in Hydrogen and Oxygen levels within the SOFC during the extinction phase. This also means that less Water is produced from the electrochemical reactions, as less Hydrogen and Oxygen is consumed within the SOFC operating at a lower temperature, resulting in a drop in Water levels during the extinction phase.

7.6.2 Change in R_{load} from 0.00325 Ω to 0.003 Ω

For this particular case, R_{load} is expressed as follows:

$$R_{\text{load}} = 0.00325 - 0.000125 \left\{ 1 + \tanh\left(\frac{t - 100}{0.25} \right) \right\}. \tag{7.14}$$

Since the absolute difference between the solution vector of the dynamic model with the predicted steady-state solution vector is very small at 800 seconds (of order 10^{-10}), this means that the solution to the dynamic model at that time is more or less equal to the predicted steady-state solution at $R_{\text{load}} = 0.00325$ Ω along the un-ignited steady-state branch. Therefore, the initial conditions for this case are equal to the predicted steady-state solution at $R_{\text{load}} = 0.00325$ Ω on the un-ignited steady-state branch.

Figure 7.6.8 shows the expected transition of T_{cell} along the un-ignited steady-state branch (which is zoomed-in) for this case. Comparing this to figure 7.6.1, this shows that once the SOFC reaches the extinction state, the SOFC continues to operate along the un-ignited steady-state branch after a drop in R_{load} below the extinction point (but still above the ignition point), highlighting the fact that there are two stable steady-state branches.

Figure 7.6.9 shows the transient profile of T_{cell} for this case. Since R_{load} is dropped from one value to another, there is a gradual rise in T_{cell} from one steady-state solution to

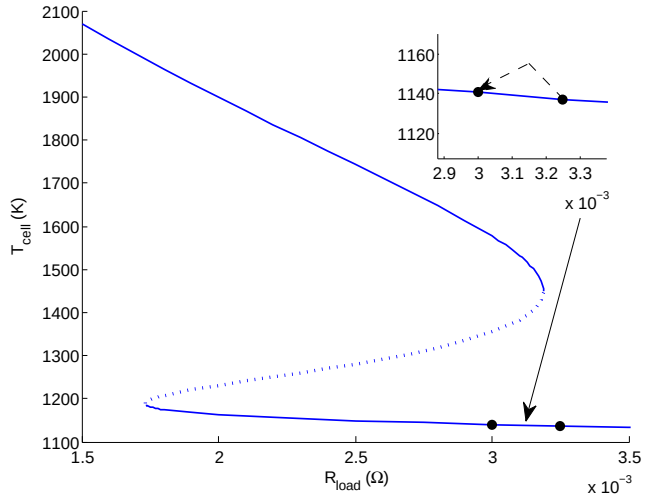

Figure 7.6.8: The steady-state profile of T_{cell} from the base case, showing the expected transition of T_{cell} after a change in the value R_{load} from 0.00325 Ω to 0.003 Ω.

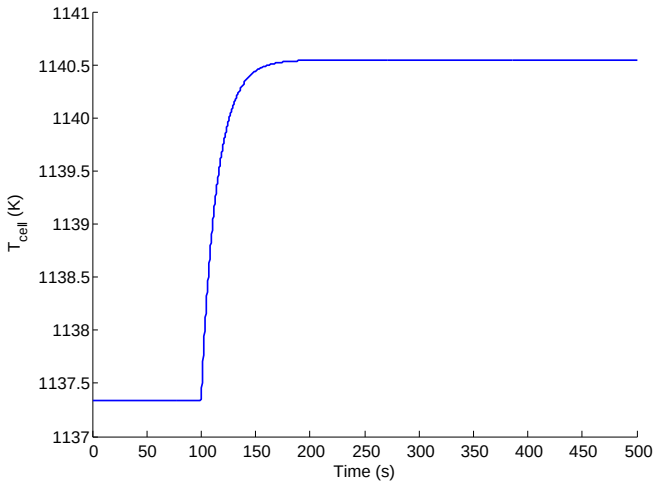

Figure 7.6.9: The transient profile of T_{cell} for a change in the value of R_{load} from 0.00325 Ω to 0.003 Ω around 100 seconds.

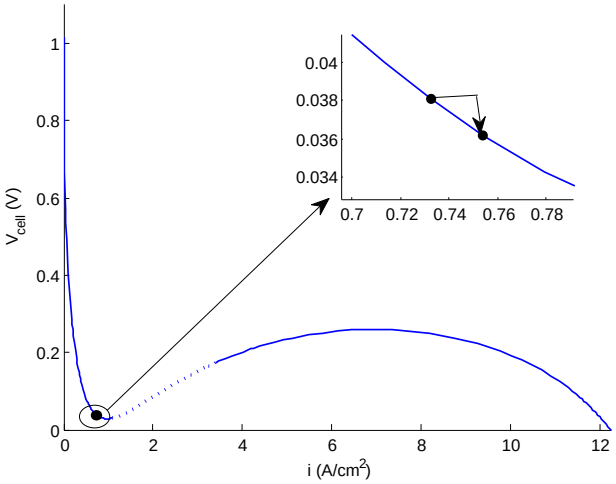

Figure 7.6.10: The V-I profile from the base case, showing the expected transition of V_{cell} after a change in the value of R_{load} from 0.00325 Ω to 0.003 Ω.

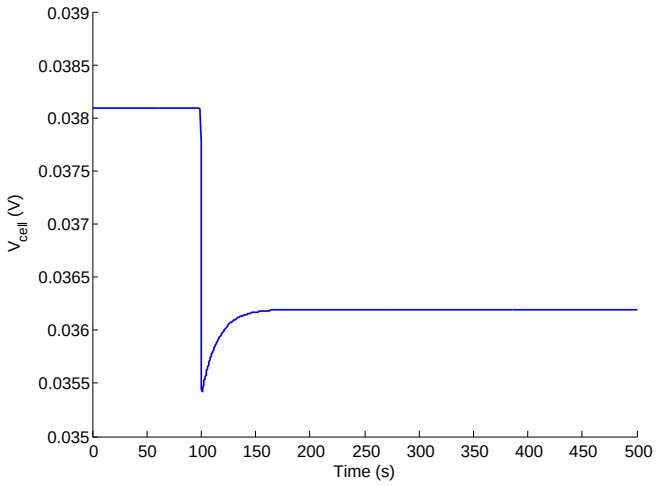

Figure 7.6.11: The transient profile of V_{cell} for a change in the value R_{load} from 0.00325 Ω to 0.003 Ω around 100 seconds.

another. However, the steady-state solution it tends towards is the steady-state solution for $R_{\text{load}} = 0.003\ \Omega$ along the un-ignited steady-state branch, not the ignited steady-state branch. It takes about 400 seconds for T_{cell} to converge towards a new steady-state solution (where the absolute difference between this and the predicted steady-state solution is of the order 10^{-12}). Just like the ignition case, this shows that there are at least two different operating regimes for a Solid Oxide Fuel Cell.

Figures 7.6.10 and 7.6.11 show the expected and actual transition of V_{cell} from one steady-state solution to another for this case respectively. Since the steady-state solutions of V_{cell} for those points of R_{load} are located near the bottom of the un-ignited steady-state branch of the V-I profile, there is just a small overall drop in V_{cell}. Since V_{cell} drops down overall for this case, η_{Ohm} rises slightly towards a new steady-state value for this case.

Since T_{cell} rises slightly for this case, I also rises slightly from around 11.72 A to around 12.07 A after the step change. The small rise in I means that there is a slight drop in Hydrogen and Oxygen levels as more of it is consumed within the SOFC. For both the ignition and extinction case, it has been shown that two different operating regimes for the SOFC occur, and that the ignited and un-ignited steady-state branches look like they are stable steady-state branches.

7.7 Transient behaviour of the SOFC on the unstable steady-state branch

For this section, the transient behaviour of the SOFC will be investigated where the SOFC initially operates at a point on the middle, assumed unstable steady-state branch. The point chosen is $R_{\text{load}} = 0.0025\ \Omega$, where up to three steady-state solutions exist. It located more or less in the middle of the multiplicity region associated with the base case. The initial conditions are equal to the predicted steady-state solutions for that point of R_{load} on the assumed unstable steady-state branch.

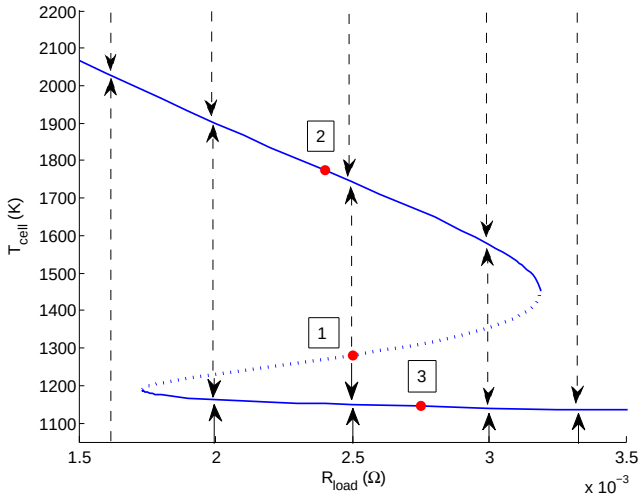

Figure 7.7.1: The steady-state profile of T_{cell} from the base case, showing the expected transition of T_{cell} at any point away from the steady-state branches (as shown by the arrows). Point 1 represents the location of the initial operating temperature at $R_{\text{load}} = 0.0025\ \Omega$; point 2 represents the expected location of T_{cell} after a shift in value of R_{load} from 0.0025 Ω to 0.0024 Ω; point 3 represents the expected location of T_{cell} after a shift in value of R_{load} from 0.0025 Ω to 0.00275 Ω.

Figure 7.7.1 shows the expected transition of T_{cell} at any point on the graph away from the steady-state branches. In the region of R_{load} where three steady-state solutions exist, if T_{cell} is located between the unstable steady-state branch and the ignited, stable steady-state branch, T_{cell} will tend towards the stable, ignited steady-state branch. Similarly, if T_{cell} is located between the unstable steady-state branch and the stable, un-ignited steady-state branch, T_{cell} will tend towards the stable, un-ignited steady-state branch. This was shown earlier in the thesis, in subsection 4.2.2, where for $R_{\text{load}} = 0.0025\ \Omega$, $\dot{T}_{\text{cell}} > 0$ for values of T_{cell} between the steady-state solutions located at the unstable steady-state branch, and the ignited steady-state branch, and $\dot{T}_{\text{cell}} < 0$ for values of T_{cell} between the steady-state solutions located at the unstable steady-state branch, and the un-ignited steady-state branch.

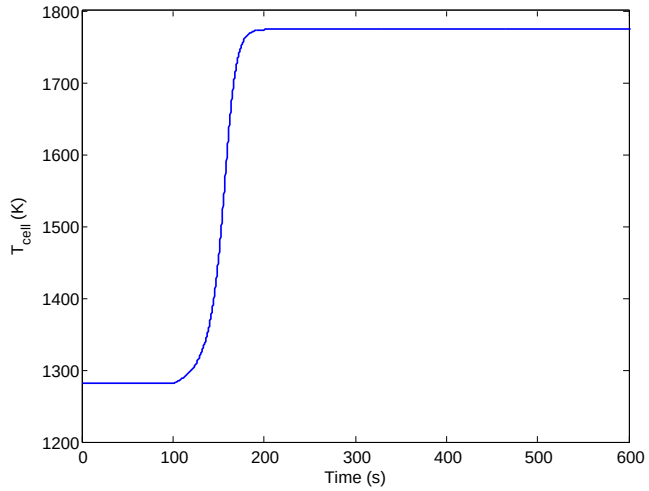

Figure 7.7.2: The transient profile of T_{cell} for a change in the value of R_{load} from 0.0025 Ω to 0.0024 Ω around 100 seconds. The SOFC initially operates on the unstable steady-state branch.

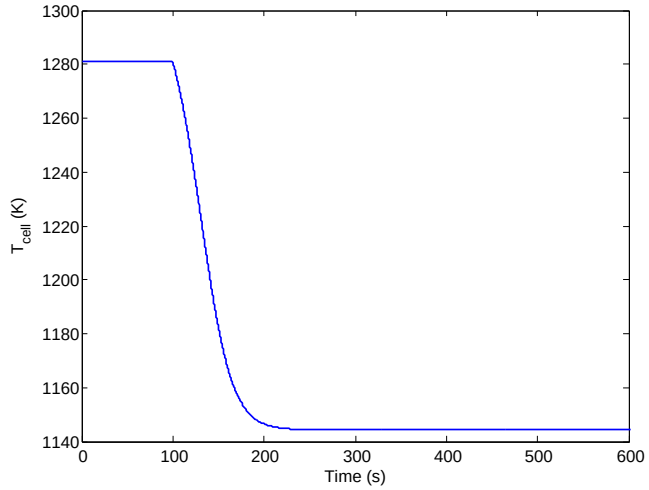

Figure 7.7.3: The transient profile of T_{cell} for a change in the value of R_{load} from 0.0025 Ω to 0.00275 Ω around 100 seconds. The SOFC initially operates on the unstable steady-state branch.

Also shown in figure 7.7.1 are three red points, with one on each branch. Point 1 represents the location of the initial operating cell temperature on the unstable steady-state branch for $R_{\text{load}} = 0.0025\ \Omega$. Point 2 represents the expected value of T_{cell} for a shift in R_{load} from 0.0025 Ω on the unstable steady-state branch to 0.0024 Ω. Point 3 represents the expected value of T_{cell} for a shift in R_{load} from 0.0025 Ω on the unstable steady-state branch to 0.00275 Ω.

The actual change in T_{cell} for both cases is shown in figures 7.7.2 and 7.7.3. If the SOFC initially operates at $R_{\text{load}} = 0.0025\ \Omega$ on the unstable steady-state branch, a decrease in the value of R_{load} from 0.0025 Ω to 0.0024 Ω around 100 seconds results in a rise in T_{cell} towards the predicted steady-state solution on the ignited steady-state branch (as shown in figure 7.7.2). It stops converging just after 250 seconds. For the other case, where R_{load} rises from 0.0025 Ω to 0.00275 Ω around 100 seconds, figure 7.7.3 shows a drop in T_{cell} towards the predicted steady-state value located on the un-ignited steady-state branch. It stops converging around 630 seconds.

The expression of R_{load} for the case corresponding to figure 7.7.2 was

$$R_{\text{load}} = 0.0025 - 0.00005 \left\{ 1 + \tanh\left(\frac{t - 100}{0.25} \right) \right\}, \tag{7.15}$$

while the expression of R_{load} for the case corresponding to figure 7.7.3 was

$$R_{\text{load}} = 0.0025 + 0.000125 \left\{ 1 + \tanh\left(\frac{t - 100}{0.25} \right) \right\}. \tag{7.16}$$

What is noticeable is that when the SOFC operates at any point along the unstable steady-state branch between the ignition and extinction points, a drop in R_{load} results in a rise in the operating temperature towards a steady-state solution on the ignited branch, while a rise in R_{load} results in a drop in T_{cell} towards a steady-state solution on the un-ignited branch. The reason for this is that when R_{load} is dropped from its initial value,

the initial steady-state value of T_{cell} on the unstable steady-state branch is now located in the region between the unstable branch and the ignited steady-state branch for the new value of R_{load}. In that region, $\dot{T}_{\text{cell}} > 0$, which means that T_{cell} will rise up towards a new steady-state solution on the ignited branch. Similarly, if R_{load} is raised from its initial value, the initial value of T_{cell} will lie in the region between the unstable branch and the un-ignited branch for the updated value of R_{load}, where $\dot{T}_{\text{cell}} < 0$. In terms of practical operation of a Solid Oxide Fuel Cell, if the SOFC initially operates at any point on the unstable steady-state branch, it would be best to raise the value of R_{load} to prevent T_{cell} operating at too high a value which would cause irreparable long-term damage to the cell.

7.8 Summary

In this section, the different time-scales within the SOFC, and the transient behaviour of the SOFC under load changes (especially during ignition and extinction) were investigated. Solid Oxide Fuel Cells are multi-time-scale systems. There are a wide range of dynamics to consider within the SOFC, and the time-scales for these dynamics range between an order of magnitude of 10^{-5} seconds to 10^{4} seconds. The time-scales for these dynamics can be split up into three groups. The first group covers short-range time-scales, which include the cell charging time (order 10^{-5} s. Ignored for this case), mass diffusion within the electrode diffusion layer and across the height of the gas channels (10^{-5} s–10^{-3} s), and convection across the length of the gas channels (10^{-4} s–10^{-2} s). The second group covers mid-range time-scales, including cell consumption rates (10^{-1} s), diffusion across the length of the gas channels (10^{0} s), and conduction across the length of the gas channels (10^{0} s–10^{1} s). The third group covers the sole long-term time-scale considered in this model, which is the cell heating time. The time-scales that are actually present in the model mainly include the short-range time-scales plus the cell reactant consumption time-scales. Since the Péclet numbers for heat and mass transfer are large for both heat

and mass transfer in both gas channels, diffusion and conduction across the length of the channel is neglected, hence the conduction and diffusion time-scales across the length of the channel are not present in this model. Also, since the conductivity of the SOFC is not considered in this model, there is no explicit cell heating time-scale present in this model either. More work is needed to clarify the time-scales related to T_{cell}. But since the density and specific heat capacity of the cell are present in the SOFC model, it is likely that any long-term time-scales present in the SOFC is related to the large density and heat capacity of the SOFC. For this model, the absolute difference between the transient solution and the predicted steady-state solution was used to determine how long it took T_{cell} (and the SOFC as a whole) to reach a new steady-state.

Unlike some of the previous work done on the transient behaviour of a Solid Oxide Fuel Cell, where they consider a step-change in either R_{load}, I or V_{cell}, in this chapter, R_{load} was defined as a smooth function of time. It was defined in terms of the tanh function and also included the initial value of R_{load}, the final value of R_{load}, the transition mid-point time, and an extra constant ω (defined in terms of seconds) that determined how quickly R_{load} changed from one value to another. Looking at six different values of ω, the evolution of the SOFC parameters of time was looked into for a change in R_{load} from 10 Ω to 5 Ω along the un-ignited steady-state branch. The values of ω considered were 10 s, 5 s, 2.5 s, 1 s, 0.5 s and 0.25 s. Using the expression of R_{load} given in (7.1), the dynamic SOFC model was solved using the ODE solver *ode15s* over one complete time-interval. The only modification made to this solver was to set up the size of the maximum time-step to prevent any unnecessary large time steps which would affect the accuracy of the profile during the transition from one steady-state value to another.

Looking at the evolution of each SOFC parameter for decreasing values of ω, what became noticeable was that the shape of each transient profile after R_{load} starts to change value could be described in terms of two regions:

1. The first region covered the period of transition of R_{load} from one value to another, in which for $\omega = 0.25$ seconds, only took around 1.5 seconds. Within that time frame, all of the fast dynamics within the SOFC have already occurred. The main SOFC parameters affected by a change in value of R_{load} include all the electrical parameters like I, V_{cell} and all the different cell polarisations, plus the concentrations of Hydrogen, Oxygen and Water in both the TPB and the bulk gas flow (since the consumption/production rates are defined in terms of I), and u_{air} due to the bulk air flow pressure. Also affected for this particular case were the fuel flow based parameters due to a slight rise in fuel concentration brought on by Water entering the fuel channel;

2. The second region covered the longer, more gradual transition towards a new steady-state value. This was mainly due to the solid cell dynamics, which due to its large density and heat capacity, is very sluggish in response to a change in value of R_{load}. The end result being that T_{cell} does not have a sharp rise/drop within the period where R_{load} changes from one value to another. It has a more gradual rise/drop towards a new steady-state solution. Looking at the six different transient profiles for each SOFC parameter, what was noticeable was that the long-term transient behaviour became established when $\omega = 1$ second.

Also looked into was the amount of time taken for T_{cell} (and the SOFC as a whole) to reach a new steady-state solution at $R_{\text{load}} = 5\ \Omega$ for each of the six different profiles. This was done by looking into the absolute difference between the solution of the dynamic model with increasing time and the predicted steady-state solution. With exception of the case where $\omega = 10$ seconds, each profile stopped converging any further around 200 seconds, suggesting that for $\omega = 0.25$ seconds, the transition of most of the SOFC parameters from one steady-state solution to another will take around 100 seconds, as shown by figures 7.3.16 and 7.3.17.

Comparing this model with other equivalent models where a step change in R_{load} is considered, there is not really much of a difference at all in terms of the shape of the transient profiles. If there are any differences in the shape of any of these profiles, it is due to extra dynamics/processes that are considered in other models (such as double-layer capacitance) which may have an effect on the transient behaviour of the SOFC. Especially, comparing these results with the equivalent transient results from [49], the shape of the transient profiles of T_{cell}, I and V_{cell} are very similar.

The transient behaviour of the SOFC was investigated over the ignition phase. This was not only to show how the parameters change during the ignition phase when a hot spot is formed, but to also show that there are at least two different operating regimes within a Solid Oxide Fuel Cell. The transient behaviour of the SOFC was initially investigated for a drop in the value of R_{load} from 0.0018 Ω to 0.0017 Ω around 100 seconds. The actual ignition point for the base case is located at 0.001732375 Ω. The hot spot within the SOFC is formed between 300 and 400 seconds as T_{cell} rises sharply with decreasing η_{Ohm} and increasing I towards a new steady-state solution along the ignited steady-state branch. The conformation that there were at least two different operating regimes was confirmed by another step-change in R_{load} from 0.0017 Ω back to 0.0018 Ω, where the cell parameters do not go back to their original operating values. There is also a clear indication that the un-ignited and ignited steady-state branches are stable.

The same thing was done for the SOFC during the extinction phase to show that at least two different operating regimes exist. For both the ignition and extinction cases, these transient profiles were backed up by steady-state profiles of T_{cell} showing the expected change in T_{cell} before and after the step-change. The extinction phase goes by more quickly than the ignition phase (although it takes a bit longer for the SOFC to operate at a steady-state). This is most likely because the change in T_{cell} during the extinction phase is smaller than the change in T_{cell} during the ignition phase.

Finally, the transient behaviour of the SOFC was investigated when the SOFC initially operates on a point on the middle, assumed unstable steady-state branch. If the SOFC initially operates at any point on the unstable steady-state branch between the ignition and extinction points, a drop in R_{load} would result in a rise in T_{cell} towards a new steady-state solution on the ignited steady-state branch, while a rise in R_{load} would result in a drop in T_{cell} towards a solution on the un-ignited steady-state branch.

Chapter 8

Conclusions and Future Work

8.1 Conclusions

In this thesis, we have investigated the existence of multiple steady-states within a planar SOFC using a more detailed SOFC model. The model builds upon the model from [49] by re-defining the concentration polarisation term η_{conc}, using an expression for the heat-transfer coefficient based on the one given in [52], and allowing the gas flow velocities to vary. Other performance parameters such as fuel utilisation, electrical efficiency and non-dimensional parameters such as the Prandtl number, the Reynolds number and the Péclet number for heat and mass transfer were also considered. The steady-state behaviour of the SOFC was considered for three modes of operation (constant external load, potentiostatic and galvanostatic), and solved in MATLAB using the built-in solver *fsolve*. The dynamic behaviour of the SOFC was considered for a constant external load operation, and was also solved in MATLAB using the IVP solver *ode15s*, which is suitable for a system of DAEs.

In chapter 4, it is seen that up to three steady-state solutions exist for a Solid Oxide Fuel Cell operating under a constant external load. The multiplicity region is located towards lower values of the load resistance R_{load} compared to [47] and [49]. This is because with

the definition of the heat-transfer coefficients given in equations (3.34) and (3.35), a lot more heat is removed by convection, resulting in a steeper heat removal curve. In fact, the values of both heat-transfer coefficients are larger than 25 W/(m^{2}K). The high values for both heat-transfer coefficients is mainly due to the high values of the Reynolds number for both gas flows (especially the air flow). The graphs showing the expected values of $\dot{T}_{\text{cell}}$ at time $t = 0$ s for varying values of cell temperature T_{cell} suggest that for a value of R_{load} where three steady-state solutions exist, the solution of T_{cell} in the middle is unstable while the other two solutions of T_{cell} are stable.

Due to the increase in electrolyte conductivity with increasing T_{cell} as R_{load} approaches the ignition point, cell voltage V_{cell} and power density P_{cell} start to rise as well. A sharper rise in temperature leads to a decrease in activation polarisation (faster activating reactions) and Ohmic resistivity (increasing conductivity of electrolyte), causing V_{cell} to rise. The rise in V_{cell} along with rising current density i causes P_{cell} to rise towards a much larger peak compared to the one along the un-ignited steady-state branch. After ignition, V_{cell} and P_{cell} operate close to their maximum values along the ignited steady-state branch (P_{cell} more so than V_{cell}). The profile for electrical efficiency is very similar to the profile for power density. But it is also heavily influenced by the amount of fuel utilised within the cell. After ignition, fuel utilisation rises up to just over 50%, and electrical efficiency is close to 10%.

After ignition, more fuel is consumed within the SOFC than air. The shape of these profiles, including the mole fraction profiles are very similar to the profile of the cell current I for changes in R_{load}. This highlights the fact that the composition of both gas flows and their individual constituents are heavily influenced by the consumption/production rates, which is directly proportional to I. Both gas flow temperatures rise with decreasing R_{load}. T_{fuel} rises a lot more than T_{air} since extra heat is transferred from the cell to the fuel flow via the enthalpy flux of water. Gas flow velocities do not change a lot along the

un-ignited steady-state branch. However, there is a noticeable rise in both velocities after ignition due to a larger pressure drop across both channels.

Looking at the non-dimensional parameters, the Reynolds number of the air flow is much larger than the fuel flow, but still remains below the critical value for a laminar flow. The fuel flow Reynolds number profile increases along with increasing velocity until R_{load} approaches zero along the ignited steady-state branch, where it is affected by the drop in fuel concentration $C^{\text{b}}_{\text{fuel}}$ along the ignited steady-state branch. The profile of the air flow Reynolds number is affected more by changes in concentration than in velocity. As for the Prandtl numbers, viscous diffusion effects are slightly larger than thermal diffusion effects for both gas flows. But looking at both non-dimensional parameters, the heat-transfer coefficient/convective effects are dominated by the Reynolds number. The Péclet numbers for heat and mass transfer across the length of both gas channels suggest that advection/convection across the length of the channel is more dominant than diffusion/conduction (more so in the air channel). Hence, diffusion and conduction across the length of the channel is not considered in the conservation equations. Also, the Péclet numbers for heat transfer are larger than the Péclet numbers for mass transfer, which suggest that diffusive effects across the length of the gas channel is slightly more important than conductive effects. Diffusive effects are much stronger across the height of the channel rather than the length.

In chapter 5, the effects of different inlet parameters on SOFC performance (and steady-state multiplicity) were investigated. The inlet parameters considered were the inlet gas flow temperatures, the inlet gas flow velocities, and the inlet molar flow rates. Larger inlet gas flow temperatures result in less heat being removed by convection since the gap between T_{cell} and either gas flow temperature in the heat removal term shrinks, reducing the effect of the heat-transfer coefficient.

Reducing the inlet gas flow velocities has a much bigger impact on SOFC performance,

especially in terms of fuel utilisation. Since the inlet molar flow rates are kept fixed, reducing either inlet gas flow velocity increases the concentration level of fuel/air within their respective gas channels, at a lower velocity. This results in an easier consumption of Hydrogen/Oxygen (whose concentration levels go up as well since their inlet mole fractions are kept fixed) within the SOFC over the length of the cell. This in turn raises T_{cell}, raises i, shifts the multiplicity region towards higher values of R_{load}, and leads to more fuel being utilised. For low enough velocities, the multiplicity region disappears. The SOFC is more sensitive to changes in $u_{\text{fuel}}^{\text{in}}$ than $u_{\text{air}}^{\text{in}}$.

As for the inlet molar flow rates, modifying the value has a much bigger impact than the inlet gas flow velocities and temperature in changing the amount of heat removed by convection. Since the inlet gas flow velocities are fixed, increasing either inlet molar flow rate results in a higher concentration of fuel/air entering their respective gas channels at the same inlet velocity, increasing the Reynolds number and subsequently the heat-transfer coefficient. As a result, more heat is removed from the SOFC by convection. Changing $\dot{N}_{\text{fuel}}^{\text{in}}$ has more of an impact on the amount of heat produced then changing $\dot{N}_{\text{air}}^{\text{in}}$ due to the amount of Hydrogen available for consumption. Reducing $\dot{N}_{\text{fuel}}^{\text{in}}$ reduces the amount of Hydrogen available for consumption, hence reduces the amount of heat produced within the SOFC as well as the heat removed. This results in a larger multiplicity region for lower values of R_{load}. Raising $\dot{N}_{\text{fuel}}^{\text{in}}$ also has the same effect with regards to the shift and the size of the multiplicity region, which means that the multiplicity region does not disappear. The main difference is that along the ignited steady-state branch, T_{cell} and i rise up to much higher values since there is still plenty of Hydrogen left for consumption. P_{cell} rises towards a much higher peak. However, the amount of fuel utilised goes down due to the rise in the amount of Hydrogen entering the SOFC, which means that electrical efficiency is not much better than it was before. Changing $\dot{N}_{\text{air}}^{\text{in}}$ only has an impact on the amount of heat removed from the SOFC.

As for the potentiostatic and galvanostatic cases in chapter 6, there are up to three steady-state solutions for the potentiostatic case, and only one for the galvanostatic case. The rise in T_{cell} after ignition is larger for the potentiostatic case than the constant external load case. But, it is not as high as the equivalent potentiostatic cases in both [47] and [49], due to a larger amount of heat removed by convection. As for the multiplicity regions, it is much more difficult to remove the multiplicity regions for the potentiostatic case compared to the constant external load case. This is due to the sluggish rise in the amount of heat produced at low values of T_{cell}, and the larger amount of heat produced by the SOFC at higher temperatures when V_{cell} is dropped. As for the galvanostatic case, setting I as a constant parameter fixes the reaction rates, and removes most of the non-linearity from the model. Since the reaction rates are fixed, it is not influenced by T_{cell} and electrolyte conductivity, which means that no hot spots are formed within the SOFC.

In chapter 7, the transient behaviour of the SOFC under load changes was investigated. Before looking at the transient behaviour of the SOFC, the different time-scales within a Solid Oxide Fuel Cell were covered first. The time-scales of the different dynamics that occur in the SOFC range from an order of magnitude of 10^{-5} seconds to an order of magnitude of 10^{3} seconds. The very quick dynamics include cell charging (which is not considered here), diffusion within the electrodes and across the height of the channels, and convection across the length of the channels. They range from between 10^{-5} seconds to 10^{-2} seconds. The mid-range dynamics include the consumption rate, diffusion across the length of the channels, and conduction across the length of the channels. They range from between 10^{-1} seconds to 10^{1} seconds. The long-term dynamics only include the cell heating time, which is defined in terms of the cell density, the cell conductivity and the heat capacity of the cell. The time-scales which are present in this model however are mainly the short-range time-scales, plus the reactant consumption time-scale. Diffusion and conductivity of both gas flows across the channel, and the cell conductivity is not

considered in this model, which means that the time-scales related to diffusion and conduction across the length of the SOFC, and the time it takes for the SOFC to heat up are not present in this model. Since the density and specific heat capacity of the solid cell component are still present in the SOFC model, the long-term transient behaviour of the SOFC is still affected by these parameters. But more work is needed to determine the relevant time-scales related to T_{cell}.

For the transient calculations in chapter 7, the SOFC was operating under a constant external load. Instead of considering a step-change in R_{load}, R_{load} was defined as a smooth function of time by defining it in terms of the tanh function, as shown in equation (7.1):

$$R_{\text{load}} = R_{\text{load}}^{(0)} + \frac{1}{2}\left[R_{\text{load}}^{(1)} - R_{\text{load}}^{(0)}\right]\left\{1 + \tanh\left(\frac{t-100}{\omega}\right)\right\},$$

where $R_{\text{load}}^{(0)}$ is the initial load resistance value, $R_{\text{load}}^{(1)}$ is the final load resistance value, and ω is a constant (defined in terms of seconds) which determines how quickly R_{load} changes from $R_{\text{load}}^{(0)}$ to $R_{\text{load}}^{(1)}$. The number 100 in the tanh function represents the time of the transition mid-point.

Considering a change in R_{load} from 10 Ω to 5 Ω, the evolution of each SOFC parameter with time was investigated for six different expressions of R_{load} based on six different values of ω (10 s, 5 s, 2.5 s, 1 s, 0.5 s and 0.25 s). This was to observe how the transient profile for each SOFC parameter was developed for decreasing values of ω. What became noticeable was that all the quick dynamics within the SOFC take place within the time it takes for R_{load} to change from 10 Ω to 5 Ω (which, for $\omega = 0.25$ seconds, only takes about 1.5 seconds), and that the long-term transient profile becomes fully developed when $\omega = 1$ second. The constant ω was set as low as possible to capture the effects of the quicker dynamics on the transient behaviour of each SOFC parameter.

For decreasing values of ω, the transient profiles after a change in value of R_{load} could be

split up into two regions: (i) a region covering the transition of R_{load} from $R_{\text{load}}^{(0)}$ to $R_{\text{load}}^{(1)}$. Main parameters affected within this period include the electrical parameters, the mole fractions, and u_{air}; (ii) another region after the transition of R_{load} where the parameters gradually move towards a new steady-state solution. This is mainly influenced by the amount of time it takes T_{cell} to move towards a new steady-state solution, thanks to its large heat capacity. Since cell conductivity was not considered in this model, the amount of time taken for T_{cell} (and the SOFC as a whole) to move towards a new steady-state was investigated by looking at the absolute difference of the solution to the dynamic model with increasing time with the predicted steady-state solution at $R_{\text{load}} = 5\ \Omega$.

Comparing these results with equivalent results from [49] and [67], there is hardly any difference in terms of the shape of the transient profiles, even though R_{load} is not a step-function in this case. Any differences in shape is mainly down to certain dynamics/processes that were considered in other papers (such as double-layer capacitance) that were not considered in this model.

The next case considered was the transient behaviour of the SOFC during ignition. After a change in the value of R_{load} from 0.0018 Ω to 0.0017 Ω around 100 seconds, T_{cell} rises up towards a new value located on the ignited steady-state branch. It takes almost 450 seconds after the step change to approach the new steady-state value. To show that the SOFC is operating in a different steady-state region, another change in value of R_{load} was made from 0.0017 Ω to 0.0018 Ω, with the SOFC operating along the ignited steady-state branch. It is shown that T_{cell} and other cell parameters do not go back to their original steady-state values along the un-ignited steady-state branch for the same value of R_{load} before the SOFC is switched on. This means that there are at least two different operating regimes within a Solid Oxide Fuel Cell.

The same thing was done for the extinction case. It was shown that if T_{cell} drops towards a steady-state value on the un-ignited steady-state branch from the ignited steady-state

branch, it does not go back near its original value along the ignited steady-state branch when R_{load} is dropped back below the extinction point (but above the ignition point). If the SOFC operates along any point on the unstable steady-state branch with initial conditions based on the predicted steady-state solution at that point, a drop in R_{load} would result in the SOFC operating along the ignited steady-state branch, while a rise in R_{load} would result in the SOFC operating along the un-ignited steady-state branch.

8.2 Further Work

In this thesis, the heat-transfer coefficient was approximated using an averaged approximation of the Nusselt number across the length of the SOFC. This approximation is mainly suitable for external flows over a parallel surface [72, p 311]. Since this is a lumped-parameter model, where the length scale L is not very large, this is not a bad approximation of the heat-transfer coefficient. However, since the diffusion time-scale across the height of the channel is slightly smaller than the advection time-scale across the length of the channel, either one of two modifications need to be considered to ensure that the expression of the heat-transfer coefficient used in this model is fully valid. One modification that could be considered would be to decrease the length of the SOFC so that the advection time-scale is smaller than the diffusion time-scale over the height of the gas channel. The other modification that could be considered would be to alter the expression of the heat-transfer coefficient so that it is suitable for an internal flow inside a pipe. This would require an alternative approximation of the Nusselt number based on a flow inside a rectangular duct.

In this thesis it has been shown that there are three different operating regimes within a Solid Oxide Fuel Cell, where two of them are stable, and one is unstable. The next step would be to show mathematically that the un-ignited and ignited steady-state branches are stable, and that the steady-state branch in the middle is unstable. However, the

DAE system considered here is very large, highly coupled and very stiff. Before attempting to determine the stability of the branches mathematically, the model will be non-dimensionalised to determine the more dominant physical regimes in different subsystems. This is with a view towards reducing the size of the model to a size close to or similar to the size of the lumped-parameter model in [47]. If the model in this thesis can be reduced to the size (or close to the size) of the model in [47], then the simplified model will be analysed mathematically to (i) determine the stability of the steady-state branches; (ii) determine the nature of the turning points. This can be done via phase plane analysis, checking the linear stability of the solutions, maybe asymptotic analysis. Another potential route to take would be to move on towards a one-dimensional model of the planar SOFC considered in this thesis. Even though this model has shown that hot spots can exist, which leads to different operating regimes (which has been verified), more investigatory work is needed to determine the nature of the different operating regimes across the length of the SOFC. There has been some work done in [47] with regards to the change in co-existing steady-state profiles over the length of a 1D SOFC, which operates under a constant cell current. But not for a Solid Oxide Fuel Cell operating under a constant external load. Also, we can try to verify whether any more steady-state regimes exist for a 1D SOFC operating under a constant external load, or a constant cell voltage, and whether at least up to three steady-state solutions exist for a 1D SOFC operating under a constant cell current.

Appendix A
Parameter Values of the model

Parameter	Description	Value
L	Cell Length (m)	0.04 [47]
W	Cell Width (m)	0.04 [47]
h^{fuel}	Fuel Channel Height (m)	1×10^{-3} [47]
h^{air}	Air Channel Height (m)	1×10^{-3} [47]
d_{An}	Anode Thickness (m)	1×10^{-4} [71]
d_{Ele}	Electrolyte Thickness (m)	1.8×10^{-4} [71]
d_{Cat}	Cathode Thickness (m)	0.5×10^{-4} [71]
k_{cell}	Thermal Conductivity of the cell (W m^{-2} K^{-1}))	0.7 [47]
$\rho_{\text{cell}} C_{\text{p,cell}}$	Cell density $\times$ Specific Heat Capacity of Cell (J m^{-3} K^{-1})	1×10^{-6} [47]
γ^{An}	Pre-exponential Kinetic Factor (Anode Reaction) (A m^{-2})	5.7×10^{7} [71]
γ^{Cat}	Pre-exponential Kinetic Factor (Cathode Reaction) (A m^{-2})	7×10^{9} [71]
$\theta_{\text{f}}^{\text{An}}$	Transfer Coefficient of forward reaction (Anode)	2 [71]
$\theta_{\text{b}}^{\text{An}}$	Transfer Coefficient of backward reaction (Anode)	1 [71]
$\theta_{\text{f}}^{\text{Cat}}$	Transfer Coefficient of forward reaction (Cathode)	1.4 [71]
$\theta_{\text{b}}^{\text{Cat}}$	Transfer Coefficient of backward reaction (Cathode)	0.6 [71]
β_i	Coefficient of specific electrolyte resistivity (Ω^{-1} m^{-1})	3.34×10^{4} [71]
β_{ii}	Coefficient of specific electrolyte resistivity (K)	1.03×10^{4} [71]
$E_{\text{act,An}}$	Activation Energy of Anode Reaction (J mol^{-1})	140,000 [71]
$E_{\text{act,Cat}}$	Activation Energy of Cathode Reaction (J mol^{-1})	160,000 [71]
Δ_{An}	Anode Diffusion Layer Thickness (m)	1×10^{-5} [49]
Δ_{Aat}	Cathode Diffusion Layer Thickness (m)	1×10^{-5} [49]
ε_{An}	Porosity of Anode	0.5 [58]
ε_{Cat}	Porosity of Cathode	0.5 [58]
τ_{An}	Tortuosity of Anode	3 [58]
τ_{Cat}	Tortuosity of Cathode	3 [58]
δ_{An}	Mean pore radius of the anode (m)	5×10^{-7} [75]
δ_{Cat}	Mean pore radius of the cathode (m)	5×10^{-7} [75]
ν_{H_2}	Diffusional Volume of Hydrogen	7.07 [72]
ν_{O_2}	Diffusional Volume of Oxygen	16.6 [72]
ν_{N_2}	Diffusional Volume of Nitrogen	17.9 [72]
$\nu_{\text{H}_2\text{O}}$	Diffusional Volume of Water	12.7 [72]

Appendix B
Inlet conditions for the cell

Parameter	Description	Value
$T_{\text{air}}^{\text{in}}$	Inlet Air Temperature (K)	1033
$T_{\text{fuel}}^{\text{in}}$	Inlet Fuel Temperature (K)	1033
$\dot{N}_{\text{air}}^{\text{in}}$	Inlet Air Molar Flow Rate (mol s^{-1})	3.8×10^{-2}
$\dot{N}_{\text{fuel}}^{\text{in}}$	Inlet Fuel Molar Flow Rate (mol s^{-1})	1.39×10^{-3}
$u_{\text{air}}^{\text{in}}$	Air Velocity (m s^{-1})	78.98
$u_{\text{fuel}}^{\text{in}}$	Fuel Velocity (m s^{-1})	2.88
$y_{\text{O}_2}^{\text{in}}$	Oxygen Mole Fraction at inlet	0.2
$y_{\text{N}_2}^{\text{in}}$	Nitrogen Mole Fraction at inlet	0.8
$y_{\text{H}_2}^{\text{in}}$	Hydrogen Mole Fraction at inlet	0.9
$y_{\text{H}_2\text{O}}^{\text{in}}$	Water Mole Fraction at inlet	0.1

Appendix C
Performance Parameters

C.1 Fuel Utilisation

Fuel Utilisation is defined as a ratio of the amount of fuel utilised in the SOFC to the maximum available fuel in the fuel cell [25, p. 19]

$$U_f = \frac{\dot{N}_{\mathrm{OX}}}{\dot{N}^{\mathrm{in}}_{\mathrm{fuel}}} = 1 - \frac{\dot{N}^{\mathrm{out}}_{\mathrm{fuel}}}{\dot{N}^{\mathrm{in}}_{\mathrm{fuel}}} \tag{C.1}$$

where $\dot{N}_{\mathrm{OX}} = \dot{N}^{\mathrm{in}}_{\mathrm{fuel}} - \dot{N}^{\mathrm{out}}_{\mathrm{fuel}}$ is the molar flow of the oxidised fuel, and can be defined as the difference between the molar flow at the inlet and the molar flow at the outlet. Fuel utilisation can also be defined within the expression for the molar flow of electrons $\dot{n}_{el}$ within a SOFC [18, pp. 58-59,62],

$$\dot{n}_{el} = n_{el} \cdot U_f \cdot \dot{N}^{\mathrm{in}}_{\mathrm{fuel}}$$

with the number of electrons transferred in the electrochemical reaction $n_{el} = 2$. The electric current I is a linear function of $\dot{n}_{el}$ [18, p. 58],

$$I = -\dot{n}_{el} \cdot F$$

and using the expression of $\dot{n}_{el}$ above, fuel utilisation in a SOFC can be defined in terms of the consumption rate of the fuel (given in terms of Faraday's law in section 3.2) over the inlet fuel molar flow rate [18, p. 65],

$$U_f = \frac{I}{2 \cdot F \cdot \dot{N}^{\mathrm{in}}_{\mathrm{fuel}}}. \tag{C.2}$$

C.2 Efficiency

C.2.1 Thermodynamic Efficiency

The efficiency of a fuel conversion device/reactor is defined as the amount of work done relative to the energy input in the device. In a fuel cell, the work done by the fuel cell

is defined in terms of the Gibbs free energy of the reaction $\Delta^r G$, and the net change in enthalpy produced from the electrochemical reactions $\Delta^r H$. leading to the equation that describes the reversible efficiency of a fuel cell [7, p. 2-13]

$$\eta_{\text{rev}} = \frac{\Delta^r G}{\Delta^r H}. \tag{C.3}$$

In a SOFC where the overall cell reaction is given by (3.3), and H_2O is in the form of steam, the ideal Gibbs free energy of the reaction (at standard conditions) is $\Delta^r G^0 = -228.59$ kJ/mol, and the ideal reaction enthalpy $\Delta^r H^0 = -241.82$ kJ/mol. The thermodynamic, or ideal efficiency of a SOFC is defined in terms of the ideal Gibbs free energy and reaction enthalpy [15, p. 32]

$$\eta_{\text{Thm}} = \frac{\Delta^r G^0}{\Delta^r H^0} \approx 0.945. \tag{C.4}$$

C.2.2 Voltage Efficiency

The reversible, or open circuit voltage is defined in equation (3.8), with the standard electrode potential taken from [58]. At standard conditions, the Nernst potential $E_0 = 1.273 - (2.7645 \times 10^{-4}) \cdot 298.15 \approx 1.19$ V. The voltage efficiency of the cell is defined in terms of the actual voltage over the ideal reversible voltage [15, p. 34]

$$\eta_{\text{Vol}} = \frac{V_{\text{cell}}}{E_0} \approx 0.84 \cdot V_{\text{cell}} \text{ V}^{-1}. \tag{C.5}$$

C.2.3 Electrical Efficiency

The electrical efficiency of the cell is defined as [18, p. 308]

$$\eta_{\text{el}} = \frac{\text{electrical power output}}{\text{Chemical Energy input per unit time}}. \tag{C.6}$$

The chemical energy input per unit time is defined in terms of the reaction enthalpy times the molar flow rate of the fuel flow at the inlet (in accordance with fuel utilisation). The equation for electrical efficiency can be described in terms of equations (C.4), (C.5), and (C.2) [18, p. 308]

$$\eta_{\text{el}} = \eta_{\text{Thm}} \cdot \eta_{\text{Vol}} \cdot U_f \approx 0.794 \frac{V_{\text{cell}} \cdot I}{2 \cdot F \cdot \dot{N}^{\text{in}}_{\text{fuel}}} \text{ V}^{-1}. \tag{C.7}$$

Appendix D
Péclet numbers

To gain a further understanding into the effects of certain gas properties on both gas flows either side of the cell, certain non-dimensional parameters related to both gas flows will also be investigated. These non-dimensional parameters include the Prandtl number, the Reynolds number (both of which are covered in subsection 3.3.3), and the Péclet number for both mass and heat transfer within the cell.

D.1 Péclet number (Mass Transfer)

The Péclet number for mass transfer is defined to be the ratio of the advective transport rate over the diffusive transport rate

$$Pe = \frac{\text{Advective Transport Rate}}{\text{Diffusive Transport Rate}}.$$

The mass transfer Péclet number is defined in terms of the advective time scale T_{Adv} and the diffusive time scale T_{Diff}, where

$$Pe_{\text{M}} = \frac{T_{\text{Diff}}}{T_{\text{Adv}}}. \tag{D.1}$$

T_{Adv} is defined over the length of the cell:

$$T_{\text{Adv}} = \frac{L}{u_j} \quad (j = \text{fuel,air}).$$

However, for the diffusive time scale, we consider two different versions: one for diffusion across the length of the cell, and the other for diffusion across the height of the gas channel (taking account of molar flux into/out of the cell surface). The two different diffusive time scales are

$$T_{\text{Diff,L}} = \frac{L^2}{D_j}, \quad T_{\text{Diff,h}} = \frac{(h^j)^2}{D_j},$$

where D_j is the diffusion coefficient of the fuel/air flow. In the gas channels, this is defined in terms of the binary diffusion coefficient.

Considering diffusion across the length of the cell, the Péclet number for mass transfer in the fuel and air channels are

$$Pe_{\mathrm{ML,fuel}} = \frac{Lu_{\mathrm{fuel}}}{D_{\mathrm{H_2,H_2O}}}; \tag{D.2}$$

$$Pe_{\mathrm{ML,air}} = \frac{Lu_{\mathrm{air}}}{D_{\mathrm{O_2,N_2}}}, \tag{D.3}$$

while the mass transfer Péclet number when diffusion is considered across the height of the cell is

$$Pe_{\mathrm{Mh,fuel}} = \frac{(h^{\mathrm{An}})^2 u_{\mathrm{fuel}}}{LD_{\mathrm{H_2,H_2O}}}; \tag{D.4}$$

$$Pe_{\mathrm{Mh,air}} = \frac{(h^{\mathrm{Cat}})^2 u_{\mathrm{air}}}{LD_{\mathrm{O_2,N_2}}}. \tag{D.5}$$

For advection and diffusion considered across the length of the cell,

- If $Pe_{\mathrm{ML},j} \gg 1$, advection dominates;
- If $Pe_{\mathrm{ML},j} \ll 1$, diffusion dominates.

As for $Pe_{\mathrm{Mh,fuel}}$ and $Pe_{\mathrm{Mh,air}}$, the length scales are different. Hence the advection length scale L can be written as a multiple C of the channel height h^j (which is the same for both the anode-side and cathode-side gas channels), *i.e.* $L = Ch^j$. Therefore, the diffusive time scale can be re-written as $T_{\mathrm{Diff}} = \frac{L^2}{C^2 D_j}$. Substituting it into equations (D.4) and (D.5), we get

$$Pe_{\mathrm{Mh,fuel}} = \frac{Lu_{\mathrm{fuel}}}{C^2 D_{\mathrm{H_2,H_2O}}},$$
$$Pe_{\mathrm{Mh,air}} = \frac{Lu_{\mathrm{air}}}{C^2 D_{\mathrm{O_2,N_2}}}.$$

For both $Pe_{\mathrm{Mh,fuel}}$ and $Pe_{\mathrm{Mh,air}}$,

- If $Pe_{\mathrm{Mh},j} \gg (C^2)$, advection dominates;
- If $Pe_{\mathrm{Mh},j} \ll (C^2)$, diffusion dominates.

In this case, $C = 40$.

D.2 Péclet number (Heat Transfer)

Similar to mass transfer, the Péclet number for heat transfer is the ratio of the convective transfer rate to the conductive transfer rate. It is defined in terms of the convective time scale T_{Conv} (which is the same as the advective time scale), and the conductive time scale T_{Cond}:

$$Pe_{\mathrm{H}} = \frac{T_{\mathrm{Cond}}}{T_{\mathrm{Conv}}} \tag{D.6}$$

where

$$T_{\mathrm{Conv},j} = \frac{L}{u_j}, \quad T_{\mathrm{Cond},j} = \frac{L^2}{\alpha_j} \quad (j = \mathrm{fuel}, \mathrm{air}).$$

Here, α_j represents the thermal diffusivity rate (with the same dimensions as the diffusion coefficient), and for the gas flows, it is defined in terms of the thermal conductivity of the fluid, the molar concentration of the bulk gas flow and the molar heat capacity of the gas flow:

$$\alpha_j = \frac{k_j}{C_j^{\mathrm{b}} C_{\mathrm{p},j}}. \tag{D.7}$$

Since the length scales for both time scales are the same, the heat transfer Péclet numbers for the fuel and air flow are

$$Pe_{\mathrm{H,fuel}} = \frac{L u_{\mathrm{fuel}}}{\alpha_{\mathrm{fuel}}}; \tag{D.8}$$

$$Pe_{\mathrm{H,air}} = \frac{L u_{\mathrm{air}}}{\alpha_{\mathrm{air}}}. \tag{D.9}$$

For both $Pe_{\mathrm{H,fuel}}$ and $Pe_{\mathrm{H,air}}$,

- If $Pe_{\mathrm{H}} \gg 1$, then convective effects dominate;
- If $Pe_{\mathrm{H}} \ll 1$, then conductive effects dominate.

Appendix E
Approximation of Gas properties between 900-2000 K

E.1 Molar Mass, Critical Temperature and Critical Pressure

Gas	**Molar Mass** (kg/mol)	T_C (K)	P_C (Pa)	**Reference**
H_2	2×10^{-3}	33.2	1.32×10^6	[77]
H_2O	18×10^{-3}	647.096	21.94×10^6	[77]
O_2	32×10^{-3}	154.6	5.02×10^6	[77]
N_2	28×10^{-3}	126.7	3.39×10^6	[77]
Air	29×10^{-3}	132.65	3.79×10^6	[77]

E.2 Approximation of Molar Heat Capacity at constant pressure

The expression for the molar heat capacities were taken from the 8th edition of Perry's Chemical Engineering book [78, pp 2-176–2-181], where

$$C_{p,i}(T) = C_i1 + C_i2\left[\frac{C_i3/T}{\sinh(C_i3/T)}\right]^2 + C_i4\left[\frac{C_i5/T}{\cosh(C_i5/T)}\right]^2 \quad (i = H_2, H_2O, O_2, N_2, \text{Air}).$$

The values of C_i1 to C_i5 were taken from Table 2-156, with C_i1, C_i2 and C_i4 being of order 10^5 (not 10^{-5}), C_i3 being of order 10^3 (not 10^{-3}), and C_i5 being of order 10^0. This expression of the molar heat capacity has units J/(kmol·K). These approximations of the molar heat capacity were further approximated by 2nd-order polynomial fit over the temperature region between 900 and 2000 K, using *polyfit* and *polyval* in MATLAB. This is a much nicer way to express the molar heat capacity, especially as there are time derivatives of the molar heat capacity within the dynamic model (equations (F.32) and (F.38)).

Gas	$C_{\mathrm{p},i}(T)$ (J/(mol · K))	Max. Error %	Reference
H_2	$24.9263 + (6.1156 \times 10^{-3})T - (8.3091 \times 10^{-7})T^2$	0.32	[78]
H_2O	$24.5098 + (2.0143 \times 10^{-2})T - (3.3949 \times 10^{-6})T^2$	0.22	[78]
O_2	$28.9417 + (7.6346 \times 10^{-3})T - (1.7098 \times 10^{-6})T^2$	0.23	[78]
N_2	$25.0721 + (9.8711 \times 10^{-3})T - (2.2362 \times 10^{-6})T^2$	0.17	[78]
Air	$25.8534 + (8.9857 \times 10^{-3})T - (1.9411 \times 10^{-6})T^2$	0.17	[78]

E.3 Approximation of dynamic viscosity

The approximation of the dynamic viscosity of individual gas species is based on the Reichenburg method [77, p 2-363], where

$$\mu_i = \frac{A_i T_{\mathrm{r},i}^2}{[1 + 0.36 T_{\mathrm{r},i}(T_{\mathrm{r},i} - 1)]^{1/6}},$$

with $A_i = (1.6104 \times 10^{-10}) M_i^{1/2} P_{\mathrm{C},i}^{2/3} T_{\mathrm{C},i}^{-1/6}$ and $T_{\mathrm{r},i} = T/T_{\mathrm{C},i}$. A first-order polynomial fit was applied to μ_i over the temperature region between 900 and 2000 K.

Gas	$\mu_i(T)$ (Pa · s)	Max. Error %	Reference
H_2	$7.4075 \times 10^{-6} + (1.0441 \times 10^{-8})T$	1.66	[77]
H_2O	$7.8674 \times 10^{-6} + (1.9404 \times 10^{-8})T$	3.04	[77]
O_2	$2.0297 \times 10^{-5} + (2.8141 \times 10^{-8})T$	1.76	[77]
N_2	$1.7290 \times 10^{-5} + (2.3913 \times 10^{-8})T$	1.71	[77]
Air	$1.8322 \times 10^{-5} + (2.5344 \times 10^{-8})T$	1.72	[77]

E.4 Approximation of thermal conductivity

The approximation for k_i is based on the Stiel-Thodos method where

$$k_i = \frac{\mu_i}{M_i}\left[1.30 C_{\mathrm{v},i} + 14644.0 - \frac{2928.8}{T_{\mathrm{r},i}}\right].$$

$C_{\mathrm{v},i}$ represents the molar heat capacity at constant volume, and if the gases are ideal, $C_{\mathrm{p},i}$ and $C_{\mathrm{v},i}$ are related to each other from the following formula: $C_{\mathrm{v},i} = C_{\mathrm{p},i} - R$. A first-order polynomial fit was applied to k_i over the temperature region between 900 and 2000 K.

Gas	$k_i(T)$ (W/(m · K))	Max. Error %	Reference
H_2	$5.2975 \times 10^{-2} + (7.6463 \times 10^{-5})T$	1.69	[77]
H_2O	$3.1367 \times 10^{-3} + (1.6280 \times 10^{-5})T$	3.56	[77]
O_2	$8.4998 \times 10^{-3} + (1.3092 \times 10^{-5})T$	1.91	[77]
N_2	$8.3984 \times 10^{-3} + (1.2661 \times 10^{-5})T$	1.83	[77]
Air	$8.5265 \times 10^{-3} + (1.2910 \times 10^{-5})T$	1.85	[77]

E.5 Approximation of enthalpy

The expression of the molar heat capacity in equation (3.26) is based on the expression in [78], not the polynomial approximation. Once this was solved, a first order polynomial fit was applied to each H_i over the temperature region between 900 and 2000 K.

Gas	$H_i(T)$ (J/mol)	**Max. Error** %	**Reference**
H_2	$-1.1517 \times 10^4 + 31.9957T$	2.20	[7, p 2-2],[78]
H_2O	$-2.6273 \times 10^5 + 46.3697T$	0.50	[7, p 2-2],[78]
O_2	$-1.3749 \times 10^4 + 36.3117T$	1.58	[7, p 2-2],[78]
N_2	$-1.3256 \times 10^4 + 34.5459T$	2.12	[7, p 2-2],[78]
Air	$-1.3291 \times 10^4 + 34.6819T$	2.06	[7, p 2-2],[78]

Appendix F
Steady-state and dynamic model

F.1 Steady-State Models

F.1.1 Constant External Load

Constant Parameter: R_{load}. ($V_{\text{cell}} = IR_{\text{load}}$ by **Ohm's Law**)

$$\mathbf{x}^{\mathrm{T}} = [I, \eta_{\text{act}}^{\text{An}}, \eta_{\text{act}}^{\text{Cat}}, T_{\text{cell}}, p_{\text{O}_2}^{\text{tpb}}, C_{\text{air}}^{\text{b}}, y_{\text{O}_2}, T_{\text{air}}, u_{\text{air}}, p_{\text{H}_2}^{\text{tpb}}, p_{\text{H}_2\text{O}}^{\text{tpb}}, C_{\text{fuel}}^{\text{b}}, y_{\text{H}_2}, T_{\text{fuel}}, u_{\text{fuel}}]$$

Steady-state model:

1. **Cell Current**

$$\begin{aligned} f_1(\mathbf{x}) = x_1 R_{\text{load}} - \Big\{ & 1.273 - (2.7645 \times 10^{-4}) x_4 \\ & - \frac{Rx_4}{2F} \log\left(\frac{(1 - x_{13})}{x_{13}} \left(\frac{p_0}{x_7 x_6 R x_8} \right)^{\frac{1}{2}} \right) \Big\} \\ & + x_2 + x_3 + \frac{1}{\beta_i} \exp\left(\frac{\beta_{ii}}{x_4} \right) d_{\text{Ele}} \left(\frac{x_1}{LW} \right) + \frac{Rx_4}{2F} \log\left(1 + \frac{x_1 R x_4 \Delta_{\text{An}}}{2LWF x_{11} D_{\text{eff,An}}} \right) \\ & - \frac{Rx_4}{2F} \log\left(1 - \frac{x_1 R x_4 \Delta_{\text{An}}}{2LWF x_{10} D_{\text{eff,An}}} \right) \\ & - \frac{Rx_4}{4F} \log\left(1 - \left(1 - \frac{x_5}{p_0} \right) \frac{x_1 R x_4 \Delta_{\text{An}}}{4LWF x_5 D_{\text{eff,Cat}}} \right) \end{aligned} \tag{F.1}$$

2. **Anode Activation Polarisation**

$$\begin{aligned} f_2(\mathbf{x}) = \frac{x_1}{LW} - \gamma^{\text{An}} \left(\frac{x_{10}}{p_0} \right) \left(\frac{x_{11}}{p_0} \right) \exp\left(-\frac{E_{\text{act,An}}}{Rx_4} \right) \Big\{ & \exp\left(\theta_{\text{f}}^{\text{An}} \frac{F}{Rx_4} x_2 \right) \\ & - \exp\left(-\theta_{\text{b}}^{\text{An}} \frac{F}{Rx_4} x_2 \right) \Big\} \end{aligned} \tag{F.2}$$

3. **Cathode Activation Polarisation**

$$f_3(\mathbf{x}) = \frac{x_1}{LW} - \gamma^{\mathrm{Cat}} \left(\frac{x_5}{p_0}\right)^{0.25} \exp\left(-\frac{E_{\mathrm{act,Cat}}}{Rx_4}\right) \left\{\exp\left(\theta_{\mathrm{f}}^{\mathrm{Cat}} \frac{F}{Rx_4} x_3\right) - \exp\left(-\theta_{\mathrm{b}}^{\mathrm{Cat}} \frac{F}{Rx_4} x_3\right)\right\} \tag{F.3}$$

4. **Cell Temperature**

$$\begin{aligned} f_4(\mathbf{x}) = {} & (a_{\mathrm{H_2}} + b_{\mathrm{H_2}} x_{14}) \frac{D_{\mathrm{eff,H_2}}}{\Delta_{\mathrm{An}}} \left[x_{13}x_{12} - \frac{x_{10}}{Rx_4}\right] + (a_{\mathrm{O_2}} + b_{\mathrm{O_2}} x_8) \frac{D_{\mathrm{eff,O_2}}}{\Delta_{\mathrm{Cat}}} \left[x_7 x_6 - \frac{x_5}{Rx_4}\right] \\ & - (a_{\mathrm{H_2O}} + b_{\mathrm{H_2O}} x_4) \frac{D_{\mathrm{eff,H_2O}}}{\Delta_{\mathrm{An}}} \left[\frac{x_{11}}{Rx_4} - (1 - x_{13})x_{12}\right] - R_{\mathrm{load}} \left(\frac{x_1^2}{LW}\right) \\ & - 0.664 \frac{k_{\mathrm{fuel}}}{L} \left(\frac{C_{\mathrm{p,fuel}}^{\mathrm{S}} \mu_{\mathrm{fuel}}}{k_{\mathrm{fuel}}}\right)^{\frac{1}{3}} \left(\frac{x_{12}(x_{13}M_{\mathrm{H_2}} + (1 - x_{13})M_{\mathrm{H_2O}})x_{15}L}{\mu_{\mathrm{fuel}}}\right)^{\frac{1}{2}} (x_4 - x_{14}) \\ & - 0.664 \frac{k_{\mathrm{air}}}{L} \left(\frac{C_{\mathrm{p,air}}^{\mathrm{S}} \mu_{\mathrm{air}}}{k_{\mathrm{air}}}\right)^{\frac{1}{3}} \left(\frac{M_{\mathrm{air}} x_6 x_9 L}{\mu_{\mathrm{air}}}\right)^{\frac{1}{2}} (x_4 - x_8) \end{aligned} \tag{F.4}$$

5. **Oxygen TPB partial pressure**

$$f_5(\mathbf{x}) = \frac{D_{\mathrm{eff,O_2}}}{\Delta_{\mathrm{Cat}}} \left[x_7 x_6 - \frac{x_5}{Rx_4}\right] - \frac{1}{4F} \left(\frac{x_1}{LW}\right) \tag{F.5}$$

6. **Air Concentration**

$$f_6(\mathbf{x}) = \dot{N}_{\mathrm{air}}^{\mathrm{in}} - x_9 x_6 W h^{\mathrm{air}} - \frac{D_{\mathrm{eff,O_2}}}{\Delta_{\mathrm{Cat}}} \left[x_7 x_6 - \frac{x_5}{Rx_4}\right] LW \tag{F.6}$$

7. **Oxygen Mole Fraction**

$$f_7(\mathbf{x}) = \dot{N}_{\mathrm{air}}^{\mathrm{in}} y_{\mathrm{O_2}}^{\mathrm{in}} - x_9 x_6 x_7 W h^{\mathrm{air}} - \frac{D_{\mathrm{eff,O_2}}}{\Delta_{\mathrm{Cat}}} \left[x_7 x_6 - \frac{x_5}{Rx_4}\right] LW \tag{F.7}$$

8. **Air Temperature**

$$\begin{aligned} f_8(\mathbf{x}) = {} & \dot{N}_{\mathrm{air}}^{\mathrm{in}} (a_{\mathrm{O_2}} + b_{\mathrm{O_2}} T_{\mathrm{air}}^{\mathrm{in}}) - x_9 x_6 (a_{\mathrm{O_2}} + b_{\mathrm{O_2}} x_8) W h^{\mathrm{air}} \\ & - (a_{\mathrm{O_2}} + b_{\mathrm{O_2}} x_8) \frac{D_{\mathrm{eff,O_2}}}{\Delta_{\mathrm{Cat}}} \left[x_7 x_6 - \frac{x_5}{Rx_4}\right] LW \\ & + 0.664 \frac{k_{\mathrm{air}}}{L} \left(\frac{C_{\mathrm{p,air}}^{\mathrm{S}} \mu_{\mathrm{air}}}{k_{\mathrm{air}}}\right)^{\frac{1}{3}} \left(\frac{M_{\mathrm{air}} x_6 x_9 L}{\mu_{\mathrm{air}}}\right)^{\frac{1}{2}} (x_4 - x_8) LW \end{aligned} \tag{F.8}$$

9. **Air Velocity**

$$f_9(\mathbf{x}) = \dot{N}^{\text{in}}_{\text{air}} u^{\text{in}}_{\text{air}} - x_6 x_9^2 W h^{\text{air}} + \frac{\dot{N}^{\text{in}}_{\text{air}} R T^{\text{in}}_{\text{air}}}{M_{\text{air}} u^{\text{in}}_{\text{air}}} - \frac{x_6 R x_8}{M_{\text{air}}} W h^{\text{air}} \\ \frac{M_{\text{O}_2}}{M_{\text{air}}} \cdot \frac{D_{\text{eff,O}_2}}{\Delta_{\text{Cat}}} \left[x_7 x_6 - \frac{x_5}{R x_4} \right] x_9 LW \tag{F.9}$$

10. **Hydrogen TPB partial pressure**

$$f_{10}(\mathbf{x}) = \frac{D_{\text{eff,H}_2}}{\Delta_{\text{An}}} \left[x_{13} x_{12} - \frac{x_{10}}{R x_4} \right] - \frac{1}{2F} \left(\frac{x_1}{LW} \right) \tag{F.10}$$

11. **Water TPB partial pressure**

$$f_{11}(\mathbf{x}) = \frac{1}{2F} \left(\frac{x_1}{LW} \right) - \frac{D_{\text{eff,H}_2\text{O}}}{\Delta_{\text{An}}} \left[\frac{x_{11}}{R x_4} - (1 - x_{13}) x_{12} \right] \tag{F.11}$$

12. **Fuel Concentration**

$$f_{12}(\mathbf{x}) = \dot{N}^{\text{in}}_{\text{fuel}} - x_{15} x_{12} W h^{\text{fuel}} + \left\{ \frac{D_{\text{eff,H}_2\text{O}}}{\Delta_{\text{An}}} \left[\frac{x_{11}}{R x_4} - (1 - x_{13}) x_{12} \right] \right. \\ \left. - \frac{D_{\text{eff,H}_2}}{\Delta_{\text{An}}} \left[x_{13} x_{12} - \frac{x_{10}}{R x_4} \right] \right\} LW \tag{F.12}$$

13. **Hydrogen Mole Fraction**

$$f_{13}(\mathbf{x}) = \dot{N}^{\text{in}}_{\text{fuel}} y^{\text{in}}_{\text{H}_2} - x_{15} x_{12} x_{13} W h^{\text{fuel}} - \frac{D_{\text{eff,H}_2}}{\Delta_{\text{An}}} \left[x_{13} x_{12} - \frac{x_{10}}{R x_4} \right] LW \tag{F.13}$$

14. **Fuel Temperature**

$$f_{14}(\mathbf{x}) = \dot{N}^{\text{in}}_{\text{fuel}} [y^{\text{in}}_{\text{H}_2} (a_{\text{H}_2} + b_{\text{H}_2} T^{\text{in}}_{\text{fuel}}) + y^{\text{in}}_{\text{H}_2\text{O}} (a_{\text{H}_2\text{O}} + b_{\text{H}_2\text{O}} T^{\text{in}}_{\text{fuel}})] \\ - x_{15} x_{12} [x_{13} (a_{\text{H}_2} + b_{\text{H}_2} x_{14}) + (1 - x_{13}) (a_{\text{H}_2\text{O}} + b_{\text{H}_2\text{O}} x_{14})] W h^{\text{fuel}} \\ + 0.664 \frac{k_{\text{fuel}}}{L} \left(\frac{C^{\text{S}}_{\text{p,fuel}} \mu_{\text{fuel}}}{k_{\text{fuel}}} \right)^{\frac{1}{3}} \left(\frac{x_{12} (x_{13} M_{\text{H}_2} + (1 - x_{13}) M_{\text{H}_2\text{O}}) x_{15} L}{\mu_{\text{fuel}}} \right)^{\frac{1}{2}} (x_4 - x_{14}) LW \\ + \left\{ (a_{\text{H}_2\text{O}} + b_{\text{H}_2\text{O}} x_4) \frac{D_{\text{eff,H}_2\text{O}}}{\Delta_{\text{An}}} \left[\frac{x_{11}}{R x_4} - (1 - x_{13}) x_{12} \right] \right. \\ \left. - (a_{\text{H}_2} + b_{\text{H}_2} x_{14}) \frac{D_{\text{eff,H}_2}}{\Delta_{\text{An}}} \left[x_{13} x_{12} - \frac{x_{10}}{R x_4} \right] \right\} LW \tag{F.14}$$

15. **Fuel Velocity**

$$\begin{aligned} f_{15}(\mathbf{x}) = {} & M_{\mathrm{H_2}}[\dot{N}^{\mathrm{in}}_{\mathrm{fuel}} y^{\mathrm{in}}_{\mathrm{H_2}} u^{\mathrm{in}}_{\mathrm{fuel}} - x_{13}x_{12}x_{15}^2 W h^{\mathrm{fuel}}] \\ & + M_{\mathrm{H_2O}}[\dot{N}^{\mathrm{in}}_{\mathrm{fuel}} y^{\mathrm{in}}_{\mathrm{H_2O}} u^{\mathrm{in}}_{\mathrm{fuel}} - (1-x_{13})x_{12}x_{15}^2 W h^{\mathrm{fuel}}] \\ & + \frac{\dot{N}^{\mathrm{in}}_{\mathrm{fuel}} R T^{\mathrm{in}}_{\mathrm{fuel}}}{u^{\mathrm{in}}_{\mathrm{fuel}}} - x_{12}Rx_{14}Wh^{\mathrm{fuel}} + M_{\mathrm{H_2O}} \frac{D_{\mathrm{eff,H_2O}}}{\Delta_{\mathrm{An}}} \left[\frac{x_{11}}{Rx_4} \right. \\ & \left. - (1-x_{13})x_{12} \right] x_{15} LW - M_{\mathrm{H_2}} \frac{D_{\mathrm{eff,H_2}}}{\Delta_{\mathrm{An}}} \left[x_{13}x_{12} - \frac{x_{10}}{Rx_4} \right] x_{15} LW \end{aligned} \tag{F.15}$$

F.1.2 Constant Cell Voltage

Constant Parameter: V_{cell}.

$$\mathbf{x}^{\mathrm{T}} = [I, \eta^{\mathrm{An}}_{\mathrm{act}}, \eta^{\mathrm{Cat}}_{\mathrm{act}}, T_{\mathrm{cell}}, p^{\mathrm{tpb}}_{\mathrm{O_2}}, C^{\mathrm{b}}_{\mathrm{air}}, y_{\mathrm{O_2}}, T_{\mathrm{air}}, u_{\mathrm{air}}, p^{\mathrm{tpb}}_{\mathrm{H_2}}, p^{\mathrm{tpb}}_{\mathrm{H_2O}}, C^{\mathrm{b}}_{\mathrm{fuel}}, y_{\mathrm{H_2}}, T_{\mathrm{fuel}}, u_{\mathrm{fuel}}]$$

1. **Cell Current**

$$\begin{aligned} f_1(\mathbf{x}) = {} & V_{\mathrm{cell}} - \Big\{ 1.273 - (2.7645 \times 10^{-4}) x_4 \\ & - \frac{Rx_4}{2F} \log \left(\frac{(1-x_{13})}{x_{13}} \left(\frac{p_0}{x_7 x_6 R x_8} \right)^{\frac{1}{2}} \right) \Big\} \\ & + x_2 + x_3 + \frac{1}{\beta_i} \exp\left(\frac{\beta_{ii}}{x_4} \right) d_{\mathrm{Ele}} \left(\frac{x_1}{LW} \right) + \frac{Rx_4}{2F} \log \left(1 + \frac{x_1 R x_4 \Delta_{\mathrm{An}}}{2LWF x_{11} D_{\mathrm{eff,An}}} \right) \\ & - \frac{Rx_4}{2F} \log \left(1 - \frac{x_1 R x_4 \Delta_{\mathrm{An}}}{2LWF x_{10} D_{\mathrm{eff,An}}} \right) \\ & - \frac{Rx_4}{4F} \log \left(1 - \left(1 - \frac{x_5}{p_0} \right) \frac{x_1 R x_4 \Delta_{\mathrm{An}}}{4LWF x_5 D_{\mathrm{eff,Cat}}} \right) \end{aligned} \tag{F.16}$$

2. **Anode Activation Polarisation**: See equation (F.2).

3. **Cathode Activation Polarisation**: See equation (F.3).

4. **Cell Temperature**

$$
\begin{aligned}
f_4(\mathbf{x}) = {} & (a_{\mathrm{H_2}} + b_{\mathrm{H_2}} x_{14}) \frac{D_{\mathrm{eff,H_2}}}{\Delta_{\mathrm{An}}} \left[x_{13} x_{12} - \frac{x_{10}}{R x_4} \right] + (a_{\mathrm{O_2}} + b_{\mathrm{O_2}} x_8) \frac{D_{\mathrm{eff,O_2}}}{\Delta_{\mathrm{Cat}}} \left[x_7 x_6 - \frac{x_5}{R x_4} \right] \\
& - (a_{\mathrm{H_2O}} + b_{\mathrm{H_2O}} x_4) \frac{D_{\mathrm{eff,H_2O}}}{\Delta_{\mathrm{An}}} \left[\frac{x_{11}}{R x_4} - (1 - x_{13}) x_{12} \right] - V_{\mathrm{cell}} \left(\frac{x_1}{LW} \right) \\
& - 0.664 \frac{k_{\mathrm{fuel}}}{L} \left(\frac{C^{\mathrm{S}}_{\mathrm{p,fuel}} \mu_{\mathrm{fuel}}}{k_{\mathrm{fuel}}} \right)^{\frac{1}{3}} \left(\frac{x_{12}(x_{13} M_{\mathrm{H_2}} + (1 - x_{13}) M_{\mathrm{H_2O}}) x_{15} L}{\mu_{\mathrm{fuel}}} \right)^{\frac{1}{2}} (x_4 - x_{14}) \\
& - 0.664 \frac{k_{\mathrm{air}}}{L} \left(\frac{C^{\mathrm{S}}_{\mathrm{p,air}} \mu_{\mathrm{air}}}{k_{\mathrm{air}}} \right)^{\frac{1}{3}} \left(\frac{M_{\mathrm{air}} x_6 x_9 L}{\mu_{\mathrm{air}}} \right)^{\frac{1}{2}} (x_4 - x_8) \qquad \text{(F.17)}
\end{aligned}
$$

5. **Oxygen TPB partial pressure**: See equation (F.5).
6. **Air Concentration**: See equation (F.6).
7. **Oxygen Mole Fraction**: See equation (F.7).
8. **Air Temperature**: See equation (F.8).
9. **Air Velocity**: See equation (F.9).
10. **Hydrogen TPB partial pressure**: See equation (F.10).
11. **Water TPB partial pressure**: See equation (F.11).
12. **Fuel Concentration**: See equation (F.12).
13. **Hydrogen Mole Fraction**: See equation (F.13).
14. **Fuel Temperature**: See equation (F.14).
15. **Fuel Velocity**: See equation (F.15).

F.1.3 Constant Cell Current

Constant Parameter: I.

$$
\mathbf{x}^{\mathrm{T}} = [V_{\mathrm{cell}}, \eta^{\mathrm{An}}_{\mathrm{act}}, \eta^{\mathrm{Cat}}_{\mathrm{act}}, T_{\mathrm{cell}}, p^{\mathrm{tpb}}_{\mathrm{O_2}}, C^{\mathrm{b}}_{\mathrm{air}}, y_{\mathrm{O_2}}, T_{\mathrm{air}}, u_{\mathrm{air}}, p^{\mathrm{tpb}}_{\mathrm{H_2}}, p^{\mathrm{tpb}}_{\mathrm{H_2O}}, C^{\mathrm{b}}_{\mathrm{fuel}}, y_{\mathrm{H_2}}, T_{\mathrm{fuel}}, u_{\mathrm{fuel}}]
$$

1. **Cell Voltage**

$$
\begin{aligned}
f_1(\mathbf{x}) = x_1 - \Big\{ & 1.273 - (2.7645 \times 10^{-4}) x_4 \\
& - \frac{R x_4}{2F} \log \left(\frac{(1 - x_{13})}{x_{13}} \left(\frac{p_0}{x_7 x_6 R x_8} \right)^{\frac{1}{2}} \right) \Big\} \\
& + x_2 + x_3 + \frac{1}{\beta_i} \exp \left(\frac{\beta_{ii}}{x_4} \right) d_{\mathrm{Ele}} \left(\frac{I}{LW} \right) + \frac{R x_4}{2F} \log \left(1 + \frac{I R x_4 \Delta_{\mathrm{An}}}{2LWF x_{11} D_{\mathrm{eff,An}}} \right) \\
& - \frac{R x_4}{2F} \log \left(1 - \frac{I R x_4 \Delta_{\mathrm{An}}}{2LWF x_{10} D_{\mathrm{eff,An}}} \right) \\
& - \frac{R x_4}{4F} \log \left(1 - \left(1 - \frac{x_5}{p_0} \right) \frac{I R x_4 \Delta_{\mathrm{An}}}{4LWF x_5 D_{\mathrm{eff,Cat}}} \right)
\end{aligned} \tag{F.18}
$$

2. **Anode Activation Polarisation**

$$
\begin{aligned}
f_2(\mathbf{x}) = \frac{I}{LW} - \gamma^{\mathrm{An}} \left(\frac{x_{10}}{p_0} \right) \left(\frac{x_{11}}{p_0} \right) \exp \left(- \frac{E_{\mathrm{act,An}}}{R x_4} \right) \Big\{ & \exp \left(\theta_{\mathrm{f}}^{\mathrm{An}} \frac{F}{R x_4} x_2 \right) \\
& - \exp \left(- \theta_{\mathrm{b}}^{\mathrm{An}} \frac{F}{R x_4} x_2 \right) \Big\}
\end{aligned} \tag{F.19}
$$

3. **Cathode Activation Polarisation**

$$
\begin{aligned}
f_3(\mathbf{x}) = \frac{I}{LW} - \gamma^{\mathrm{Cat}} \left(\frac{x_5}{p_0} \right)^{0.25} \exp \left(- \frac{E_{\mathrm{act,Cat}}}{R x_4} \right) \Big\{ & \exp \left(\theta_{\mathrm{f}}^{\mathrm{Cat}} \frac{F}{R x_4} x_3 \right) \\
& - \exp \left(- \theta_{\mathrm{b}}^{\mathrm{Cat}} \frac{F}{R x_4} x_3 \right) \Big\}
\end{aligned} \tag{F.20}
$$

4. **Cell Temperature**

$$
\begin{aligned}
f_4(\mathbf{x}) = & (a_{\mathrm{H_2}} + b_{\mathrm{H_2}} x_{14}) \frac{D_{\mathrm{eff,H_2}}}{\Delta_{\mathrm{An}}} \left[x_{13} x_{12} - \frac{x_{10}}{R x_4} \right] + (a_{\mathrm{O_2}} + b_{\mathrm{O_2}} x_8) \frac{D_{\mathrm{eff,O_2}}}{\Delta_{\mathrm{Cat}}} \left[x_7 x_6 - \frac{x_5}{R x_4} \right] \\
& - (a_{\mathrm{H_2O}} + b_{\mathrm{H_2O}} x_4) \frac{D_{\mathrm{eff,H_2O}}}{\Delta_{\mathrm{An}}} \left[\frac{x_{11}}{R x_4} - (1 - x_{13}) x_{12} \right] - x_1 \left(\frac{I}{LW} \right) \\
& - 0.664 \frac{k_{\mathrm{fuel}}}{L} \left(\frac{C_{\mathrm{p,fuel}}^{\mathrm{S}} \mu_{\mathrm{fuel}}}{k_{\mathrm{fuel}}} \right)^{\frac{1}{3}} \left(\frac{x_{12} (x_{13} M_{\mathrm{H_2}} + (1 - x_{13}) M_{\mathrm{H_2O}}) x_{15} L}{\mu_{\mathrm{fuel}}} \right)^{\frac{1}{2}} (x_4 - x_{14}) \\
& - 0.664 \frac{k_{\mathrm{air}}}{L} \left(\frac{C_{\mathrm{p,air}}^{\mathrm{S}} \mu_{\mathrm{air}}}{k_{\mathrm{air}}} \right)^{\frac{1}{3}} \left(\frac{M_{\mathrm{air}} x_6 x_9 L}{\mu_{\mathrm{air}}} \right)^{\frac{1}{2}} (x_4 - x_8)
\end{aligned} \tag{F.21}
$$

5. **Oxygen TPB partial pressure**

$$f_5(\mathbf{x}) = \frac{D_{\text{eff},\text{O}_2}}{\Delta_{\text{Cat}}}\left[x_7 x_6 - \frac{x_5}{R x_4}\right] - \frac{1}{4F}\left(\frac{I}{LW}\right) \tag{F.22}$$

6. **Air Concentration**: See equation (F.6).
7. **Oxygen Mole Fraction**: See equation (F.7).
8. **Air Temperature**: See equation (F.8).
9. **Air Velocity**: See equation (F.9).
10. **Hydrogen TPB partial pressure**

$$f_{10}(\mathbf{x}) = \frac{D_{\text{eff},\text{H}_2}}{\Delta_{\text{An}}}\left[x_{13} x_{12} - \frac{x_{10}}{R x_4}\right] - \frac{1}{2F}\left(\frac{I}{LW}\right) \tag{F.23}$$

11. **Water TPB partial pressure**

$$f_{11}(\mathbf{x}) = \frac{1}{2F}\left(\frac{I}{LW}\right) - \frac{D_{\text{eff},\text{H}_2\text{O}}}{\Delta_{\text{An}}}\left[\frac{x_{11}}{R x_4} - (1 - x_{13}) x_{12}\right] \tag{F.24}$$

12. **Fuel Concentration**: See equation (F.12).
13. **Hydrogen Mole Fraction**: See equation (F.13).
14. **Fuel Temperature**: See equation (F.14).
15. **Fuel Velocity**: See equation (F.15).

F.2 Dynamic Model

We consider the dynamic model of a SOFC operating under a constant external load.

$$\mathbf{x}^{\text{T}} = [I, \eta_{\text{act}}^{\text{An}}, \eta_{\text{act}}^{\text{Cat}}, T_{\text{cell}}, p_{\text{O}_2}^{\text{tpb}}, C_{\text{air}}^{\text{b}}, y_{\text{O}_2}, T_{\text{air}}, u_{\text{air}}, p_{\text{H}_2}^{\text{tpb}}, p_{\text{H}_2\text{O}}^{\text{tpb}}, C_{\text{fuel}}^{\text{b}}, y_{\text{H}_2}, T_{\text{fuel}}, u_{\text{fuel}}]$$

1. **Cell Current**

$$
\begin{aligned}
0 = x_1 R_{\text{load}} - \Big\{ & 1.273 - (2.7645 \times 10^{-4}) x_4 \\
& - \frac{R x_4}{2F} \log \left(\frac{(1 - x_{13})}{x_{13}} \left(\frac{p_0}{x_7 x_6 R x_8} \right)^{\frac{1}{2}} \right) \Big\} \\
& + x_2 + x_3 + \frac{1}{\beta_i} \exp \left(\frac{\beta_{ii}}{x_4} \right) d_{\text{Ele}} \left(\frac{x_1}{LW} \right) + \frac{R x_4}{2F} \log \left(1 + \frac{x_1 R x_4 \Delta_{\text{An}}}{2LWF x_{11} D_{\text{eff,An}}} \right) \\
& - \frac{R x_4}{2F} \log \left(1 - \frac{x_1 R x_4 \Delta_{\text{An}}}{2LWF x_{10} D_{\text{eff,An}}} \right) \\
& - \frac{R x_4}{4F} \log \left(1 - \left(1 - \frac{x_5}{p_0} \right) \frac{x_1 R x_4 \Delta_{\text{An}}}{4LWF x_5 D_{\text{eff,Cat}}} \right)
\end{aligned} \tag{F.25}
$$

2. **Anode Activation Polarisation**

$$
\begin{aligned}
0 = \frac{x_1}{LW} - \gamma^{\text{An}} \left(\frac{x_{10}}{p_0} \right) \left(\frac{x_{11}}{p_0} \right) \exp \left(- \frac{E_{\text{act,An}}}{R x_4} \right) \Big\{ & \exp \left(\theta_{\text{f}}^{\text{An}} \frac{F}{R x_4} x_2 \right) \\
& - \exp \left(- \theta_{\text{b}}^{\text{An}} \frac{F}{R x_4} x_2 \right) \Big\}
\end{aligned} \tag{F.26}
$$

3. **Cathode Activation Polarisation**

$$
\begin{aligned}
0 = \frac{x_1}{LW} - \gamma^{\text{Cat}} \left(\frac{x_5}{p_0} \right)^{0.25} \exp \left(- \frac{E_{\text{act,Cat}}}{R x_4} \right) \Big\{ & \exp \left(\theta_{\text{f}}^{\text{Cat}} \frac{F}{R x_4} x_3 \right) \\
& - \exp \left(- \theta_{\text{b}}^{\text{Cat}} \frac{F}{R x_4} x_3 \right) \Big\}
\end{aligned} \tag{F.27}
$$

4. **Cell Temperature**

$$
\begin{aligned}
\dot{x_4} = [(d_{\text{An}} + d_{\text{Ele}} + d_{\text{Cat}}) \rho_{\text{cell}} C_{\text{p,cell}}]^{-1} \Big\{ & (a_{\text{H}_2} + b_{\text{H}_2} x_{14}) \frac{D_{\text{eff,H}_2}}{\Delta_{\text{An}}} \left[x_{13} x_{12} - \frac{x_{10}}{R x_4} \right] \\
& + (a_{\text{O}_2} + b_{\text{O}_2} x_8) \frac{D_{\text{eff,O}_2}}{\Delta_{\text{Cat}}} \left[x_7 x_6 - \frac{x_5}{R x_4} \right] \\
& - (a_{\text{H}_2\text{O}} + b_{\text{H}_2\text{O}} x_4) \frac{D_{\text{eff,H}_2\text{O}}}{\Delta_{\text{An}}} \left[\frac{x_{11}}{R x_4} - (1 - x_{13}) x_{12} \right] - R_{\text{load}} \left(\frac{x_1^2}{LW} \right) \\
& - 0.664 \frac{k_{\text{fuel}}}{L} \left(\frac{C_{\text{p,fuel}}^{\text{S}} \mu_{\text{fuel}}}{k_{\text{fuel}}} \right)^{\frac{1}{3}} \left(\frac{x_{12} (x_{13} M_{\text{H}_2} + (1 - x_{13}) M_{\text{H}_2\text{O}}) x_{15} L}{\mu_{\text{fuel}}} \right)^{\frac{1}{2}} (x_4 - x_{14}) \\
& - 0.664 \frac{k_{\text{air}}}{L} \left(\frac{C_{\text{p,air}}^{\text{S}} \mu_{\text{air}}}{k_{\text{air}}} \right)^{\frac{1}{3}} \left(\frac{M_{\text{air}} x_6 x_9 L}{\mu_{\text{air}}} \right)^{\frac{1}{2}} (x_4 - x_8) \Big\}
\end{aligned} \tag{F.28}
$$

5. **Oxygen TPB partial pressure**

$$\dot{x_5} = \frac{x_5}{x_4}\dot{x_4} + \frac{Rx_4}{\Delta_{\text{Cat}}}\left\{\frac{D_{\text{eff,O}_2}}{\Delta_{\text{Cat}}}\left[x_7x_6 - \frac{x_5}{Rx_4}\right] - \frac{1}{4F}\left(\frac{x_1}{LW}\right)\right\} \tag{F.29}$$

6. **Air Concentration**

$$\dot{x_6} = \frac{1}{LWh^{\text{air}}}\left\{\dot{N}^{\text{in}}_{\text{air}} - x_9x_6Wh^{\text{air}} - \frac{D_{\text{eff,O}_2}}{\Delta_{\text{Cat}}}\left[x_7x_6 - \frac{x_5}{Rx_4}\right]LW\right\} \tag{F.30}$$

7. **Oxygen Mole Fraction**

$$\dot{x_7} = -\frac{x_7}{x_6}\dot{x_6} - \frac{1}{LWh^{\text{air}}x_6}\left\{\dot{N}^{\text{in}}_{\text{air}}y^{\text{in}}_{\text{O}_2} - x_9x_6x_7Wh^{\text{air}} - \frac{D_{\text{eff,O}_2}}{\Delta_{\text{Cat}}}\left[x_7x_6 - \frac{x_5}{Rx_4}\right]LW\right\} \tag{F.31}$$

8. **Air Temperature**

$$\begin{aligned}\dot{x_8} = &-\frac{x_8}{x_6}\dot{x_6} - \frac{x_8}{C_{\text{p,air}}}\dot{C}_{\text{p,air}} \\ &+ \frac{1}{LWh^{\text{air}}C_{\text{p,air}}x_6}\left\{\dot{N}^{\text{in}}_{\text{air}}(a_{\text{O}_2} + b_{\text{O}_2}T^{\text{in}}_{\text{air}}) - x_9x_6(a_{\text{O}_2} + b_{\text{O}_2}x_8)Wh^{\text{air}}\right. \\ &- (a_{\text{O}_2} + b_{\text{O}_2}x_8)\frac{D_{\text{eff,O}_2}}{\Delta_{\text{Cat}}}\left[x_7x_6 - \frac{x_5}{Rx_4}\right]LW \\ &\left.+ 0.664\frac{k_{\text{air}}}{L}\left(\frac{C^{\text{S}}_{\text{p,air}}\mu_{\text{air}}}{k_{\text{air}}}\right)^{\frac{1}{3}}\left(\frac{M_{\text{air}}x_6x_9L}{\mu_{\text{air}}}\right)^{\frac{1}{2}}(x_4 - x_8)LW\right\}\end{aligned} \tag{F.32}$$

9. **Air Velocity**

$$\begin{aligned}\dot{x_9} = &-\frac{x_9}{x_6}\dot{x_6} + \frac{1}{LWh^{\text{air}}x_6}\left\{\dot{N}^{\text{in}}_{\text{air}}u^{\text{in}}_{\text{air}} - x_6x_9^2Wh^{\text{air}} + \frac{\dot{N}^{\text{in}}_{\text{air}}RT^{\text{in}}_{\text{air}}}{M_{\text{air}}u^{\text{in}}_{\text{air}}} - \frac{x_6Rx_8}{M_{\text{air}}}Wh^{\text{air}}\right. \\ &\left.\frac{M_{\text{O}_2}}{M_{\text{air}}}\cdot\frac{D_{\text{eff,O}_2}}{\Delta_{\text{Cat}}}\left[x_7x_6 - \frac{x_5}{Rx_4}\right]x_9LW\right\}\end{aligned} \tag{F.33}$$

10. **Hydrogen TPB partial pressure**

$$\dot{x_{10}} = \frac{x_{10}}{x_4}\dot{x_4} + \frac{Rx_4}{\Delta_{\text{An}}}\left\{\frac{D_{\text{eff,H}_2}}{\Delta_{\text{An}}}\left[x_{13}x_{12} - \frac{x_{10}}{Rx_4}\right] - \frac{1}{2F}\left(\frac{x_1}{LW}\right)\right\} \tag{F.34}$$

11. **Water TPB partial pressure**

$$\dot{x_{11}} = \frac{x_{11}}{x_4}\dot{x_4} + \frac{Rx_4}{\Delta_{\text{An}}}\left\{\frac{1}{2F}\left(\frac{x_1}{LW}\right) - \frac{D_{\text{eff,H}_2\text{O}}}{\Delta_{\text{An}}}\left[\frac{x_{11}}{Rx_4} - (1 - x_{13})x_{12}\right]\right\} \tag{F.35}$$

12. **Fuel Concentration**

$$\dot{x_{12}} = \frac{1}{LWh^{\text{fuel}}}\left\{\dot{N}^{\text{in}}_{\text{fuel}} - x_{15}x_{12}Wh^{\text{fuel}} + \frac{D_{\text{eff,H}_2\text{O}}}{\Delta_{\text{An}}}\left[\frac{x_{11}}{Rx_4} - (1-x_{13})x_{12}\right]LW \right.$$
$$\left. - \frac{D_{\text{eff,H}_2}}{\Delta_{\text{An}}}\left[x_{13}x_{12} - \frac{x_{10}}{Rx_4}\right]LW\right\} \tag{F.36}$$

13. **Hydrogen Mole Fraction**

$$\dot{x_{13}} = -\frac{x_{13}}{x_{12}}\dot{x_{12}} + \frac{1}{LWh^{\text{fuel}}x_{12}}\left\{\dot{N}^{\text{in}}_{\text{fuel}}y^{\text{in}}_{\text{H}_2} - x_{15}x_{12}x_{13}Wh^{\text{fuel}}\right.$$
$$\left. - \frac{D_{\text{eff,H}_2}}{\Delta_{\text{An}}}\left[x_{13}x_{12} - \frac{x_{10}}{Rx_4}\right]LW\right\} \tag{F.37}$$

14. **Fuel Temperature**

$$\begin{aligned}\dot{x_{14}} = &-\frac{x_{14}}{x_{12}}\dot{x_{12}} - \frac{x_{14}}{C_{\text{p,fuel}}}\dot{C}_{\text{p,fuel}} \\ &+ \frac{1}{LWh^{\text{fuel}}C_{\text{p,fuel}}x_{12}}\left\{\dot{N}^{\text{in}}_{\text{fuel}}[y^{\text{in}}_{\text{H}_2}(a_{\text{H}_2} + b_{\text{H}_2}T^{\text{in}}_{\text{fuel}}) + y^{\text{in}}_{\text{H}_2\text{O}}(a_{\text{H}_2\text{O}} + b_{\text{H}_2\text{O}}T^{\text{in}}_{\text{fuel}})]\right. \\ &- x_{15}x_{12}[x_{13}(a_{\text{H}_2} + b_{\text{H}_2}x_{14}) + (1-x_{13})(a_{\text{H}_2\text{O}} + b_{\text{H}_2\text{O}}x_{14})]Wh^{\text{fuel}} \\ &+ 0.664\frac{k_{\text{fuel}}}{L}\left(\frac{C^{\text{S}}_{\text{p,fuel}}\mu_{\text{fuel}}}{k_{\text{fuel}}}\right)^{\frac{1}{3}}\left(\frac{x_{12}(x_{13}M_{\text{H}_2} + (1-x_{13})M_{\text{H}_2\text{O}})x_{15}L}{\mu_{\text{fuel}}}\right)^{\frac{1}{2}}(x_4 - x_{14})LW \\ &+ (a_{\text{H}_2\text{O}} + b_{\text{H}_2\text{O}}x_4)\frac{D_{\text{eff,H}_2\text{O}}}{\Delta_{\text{An}}}\left[\frac{x_{11}}{Rx_4} - (1-x_{13})x_{12}\right]LW \\ &\left. - (a_{\text{H}_2} + b_{\text{H}_2}x_{14})\frac{D_{\text{eff,H}_2}}{\Delta_{\text{An}}}\left[x_{13}x_{12} - \frac{x_{10}}{Rx_4}\right]LW\right\}\end{aligned} \tag{F.38}$$

15. **Fuel Velocity**

$$\begin{aligned}\dot{x_{15}} = &-\frac{x_{15}}{x_{12}}\dot{x_{12}} - \frac{x_{15}}{(x_{13}M_{\text{H}_2} + (1-x_{13})M_{\text{H}_2\text{O}})}(M_{\text{H}_2} - M_{\text{H}_2\text{O}})\dot{x_{13}} \\ &+ [LWh^{\text{fuel}}(x_{13}M_{\text{H}_2} + (1-x_{13})M_{\text{H}_2\text{O}})x_{12}]^{-1}\left\{M_{\text{H}_2}[\dot{N}^{\text{in}}_{\text{fuel}}y^{\text{in}}_{\text{H}_2}u^{\text{in}}_{\text{fuel}} - x_{13}x_{12}x_{15}^2Wh^{\text{fuel}}]\right. \\ &+ M_{\text{H}_2\text{O}}[\dot{N}^{\text{in}}_{\text{fuel}}y^{\text{in}}_{\text{H}_2\text{O}}u^{\text{in}}_{\text{fuel}} - (1-x_{13})x_{12}x_{15}^2Wh^{\text{fuel}}] \\ &+ \frac{\dot{N}^{\text{in}}_{\text{fuel}}RT^{\text{in}}_{\text{fuel}}}{u^{\text{in}}_{\text{fuel}}} - x_{12}Rx_{14}Wh^{\text{fuel}} + M_{\text{H}_2\text{O}}\frac{D_{\text{eff,H}_2\text{O}}}{\Delta_{\text{An}}}\left[\frac{x_{11}}{Rx_4} - (1-x_{13})x_{12}\right]x_{15}LW \\ &\left. - M_{\text{H}_2}\frac{D_{\text{eff,H}_2}}{\Delta_{\text{An}}}\left[x_{13}x_{12} - \frac{x_{10}}{Rx_4}\right]x_{15}LW\right\}\end{aligned} \tag{F.39}$$

Appendix G
Ignition and extinction values

G.1 Base Case (Constant R_{load})

Ignition point: $R_{\text{load}} = 0.001732375\ \Omega$; Extinction point: $R_{\text{load}} = 0.00318746\ \Omega$

Parameter	Ignition Point	After Ignition	Extinction Point	After Extinction
I (A)	17.58234	138.5950	54.54869	11.80169
$\eta_{\text{act}}^{\text{An}}$ (V)	0.379528	0.262392	0.340785	0.382233
$\eta_{\text{act}}^{\text{Cat}}$ (V)	0.234094	0.021742	0.134090	0.247505
T_{cell} (K)	1189.5370	1987.8753	1450.6279	1138.0996
$p_{\text{O}_2}^{\text{tpb}}$ (Pa)	22712.401	30301.622	25603.825	22047.375
$C_{\text{air}}^{\text{b}}$ (mol/m^3)	11.87396	11.13044	11.62298	11.92439
y_{O_2}	0.199040	0.192368	0.197013	0.199356
T_{air} (K)	1046.1698	1114.6538	1068.3207	1041.8318
u_{air} (m/s)	79.91108	84.54495	81.43060	79.60455
$p_{\text{H}_2}^{\text{tpb}}$ (Pa)	90610.095	43827.634	78764.868	91742.363
$p_{\text{H}_2\text{O}}^{\text{tpb}}$ (Pa)	18653.306	80139.063	36725.914	15876.780
$C_{\text{fuel}}^{\text{b}}$ (mol/m^3)	11.01866	7.32427	9.49432	11.35326
y_{H_2}	0.834450	0.383295	0.696633	0.856001
T_{fuel} (K)	1131.1853	1701.7571	1312.7994	1097.8470
u_{fuel} (m/s)	3.153741	4.744503	3.660083	3.060794
$y_{\text{H}_2\text{O}}$	0.165550	0.616705	0.303367	0.143999
i (A/cm^2)	1.098896	8.662187	3.409293	0.737606
V_{cell} (V)	0.030459	0.240099	0.173872	0.037617
P_{cell} (W/cm^2)	0.033471	2.079778	0.592780	0.027747
η_{Ohm} (V)	0.341166	0.083064	0.222763	0.338681
η_{conc} (V)	0.00093736	0.00560685	0.00224854	0.00067974
U_f	0.065550	0.516705	0.203367	0.043999
η_{Vol}	0.025584	0.201666	0.146040	0.031596
η_{el}	0.001585	0.098497	0.028074	0.001314

G.2 Base Case (Constant V_{cell})

Ignition point: $V_{\text{cell}} = 0.028517$ V; Extinction point: $V_{\text{cell}} = 0.2595521$ V

Parameter	Ignition Point	After Ignition	Extinction Point	After Extinction
I (A)	15.48993	192.6729	111.2654	3.25502
$\eta_{\text{act}}^{\text{An}}$ (V)	0.380957	0.217821	0.286979	0.360857
$\eta_{\text{act}}^{\text{Cat}}$ (V)	0.239500	0.004160	0.042283	0.231223
T_{cell} (K)	1171.4128	2589.8978	1794.8496	1057.0687
$p_{\text{O}_2}^{\text{tpb}}$ (Pa)	22481.534	36031.790	28629.891	20957.743
$C_{\text{air}}^{\text{b}}$ (mol/m^3)	11.89169	10.61025	11.30405	12.00446
y_{O_2}	0.199154	0.189350	0.193884	0.199822
T_{air} (K)	1044.6403	1168.0987	1097.8740	1035.0175
u_{air} (m/s)	79.80333	88.35976	83.40306	79.11968
$p_{\text{H}_2}^{\text{tpb}}$ (Pa)	91058.173	19355.549	55660.928	92797.764
$p_{\text{H}_2\text{O}}^{\text{tpb}}$ (Pa)	17645.934	111932.25	65519.698	11838.119
$C_{\text{fuel}}^{\text{b}}$ (mol/m^3)	11.13540	5.88239	7.97152	11.89980
y_{H_2}	0.842251	0.181683	0.485184	0.887865
T_{fuel} (K)	1119.3258	2118.8837	1563.5821	1047.4254
u_{fuel} (m/s)	3.120677	5.907461	4.359269	2.920218
$y_{\text{H}_2\text{O}}$	0.157749	0.818317	0.514816	0.112135
i (A/cm^2)	0.968120	12.042059	6.954085	0.203439
P_{cell} (W/cm^2)	0.027608	0.343403	1.804947	0.052803
η_{Ohm} (V)	0.343653	0.034627	0.116420	0.186936
η_{conc} (V)	0.00084761	0.01205904	0.00427558	0.00021859
U_f	0.057749	0.718317	0.414816	0.012135
η_{Vol}	0.023952	0.023952	0.218005	0.218005
η_{el}	0.001307	0.016263	0.085481	0.002501

Appendix H
Dynamic Behaviour Results

H.1 R_{load} changes from 10 Ω to 5 Ω

$$R_{\text{load}} = 10 - 2.5\left[1 + \tanh\left(\frac{t-100}{0.25}\right)\right]$$

Time Interval: $t \in [0, 300]$
Maximum Time Step: 0.35 seconds.

Parameter	Initial Conditions	Solution at 300 s	Predicted Solution at 5 Ω
I (A)	0.078996627189957	0.146551703650899	0.146551703650899
$\eta_{\text{act}}^{\text{An}}$ (V)	0.209110208145408	0.236337170972953	0.236337170972953
$\eta_{\text{act}}^{\text{Cat}}$ (V)	0.044875351501756	0.069836722374867	0.069836722374866
T_{cell} (K)	1033.283365170577	1033.586253137498	1033.586253137498
$p_{\text{O}_2}^{\text{tpb}}$ (Pa)	20663.48157913932	20666.04490359147	20666.04490359148
$C_{\text{air}}^{\text{b}}$ (mol/m^3)	12.028081552920842	12.027781500933944	12.027781500933942
y_{O_2}	0.199995690791713	0.199992005674832	0.199992005674832
T_{air} (K)	1033.023650486957	1033.048967951577	1033.048967951577
u_{air} (m/s)	78.981413508293855	78.983019999154578	78.983019999154592
$p_{\text{H}_2}^{\text{tpb}}$ (Pa)	93247.16928925419	93230.94179612339	93230.94179612339
$p_{\text{H}_2\text{O}}^{\text{tpb}}$ (Pa)	10397.53931207724	10427.16517094632	10427.16517094633
$C_{\text{fuel}}^{\text{b}}$ (mol/m^3)	12.064012257026722	12.061916961781078	12.061916961781071
y_{H_2}	0.899705487350925	0.899453630718120	0.899453630718120
T_{fuel} (K)	1033.167824515076	1033.347297156850	1033.347297156851
u_{fuel} (m/s)	2.880467895725135	2.880968266495906	2.880968266495907
$y_{\text{H}_2\text{O}}$	0.100294512649075	0.100546369281880	0.100546369281880
V_{cell} (V)	0.789966271899567	0.732758518254496	0.732758518254497
η_{Ohm} (V)	0.005677527753026	0.010502022659313	0.010502022659313

H.2 R_{load} changes from 0.0018 Ω to 0.0017 Ω

$$R_{\text{load}} = 0.0018 - 0.00005\left[1 + \tanh\left(\frac{t-100}{0.25}\right)\right]$$

Time Interval: $t \in [0, 1000]$
Maximum Time Step: 0.3 seconds.

Parameter	Initial Conditions	Solution at 1000 s	Predicted Solution at 0.0017 Ω
I (A)	15.886073281559185	139.9940981962565	139.9940981962565
$\eta_{\text{act}}^{\text{An}}$ (V)	0.380715301087691	0.261136995725900	0.261136995725900
$\eta_{\text{act}}^{\text{Cat}}$ (V)	0.238509378474801	0.020969575337276	0.020969575337276
T_{cell} (K)	1174.886519096612	1998.857984360721	1998.857984360721
$p_{\text{O}_2}^{\text{tpb}}$ (Pa)	22526.08382290480	30399.10791519401	30399.10791519400
$C_{\text{air}}^{\text{b}}$ (mol/m^3)	11.888290482556791	11.120662640554253	11.120662640554256
y_{O_2}	0.199132491283600	0.192289867004643	0.192289867004643
T_{air} (K)	1044.933356171751	1115.613542877934	1115.613542877934
u_{air} (m/s)	79.824004189646928	84.611110465969801	84.611110465969787
$p_{\text{H}_2}^{\text{tpb}}$ (Pa)	90976.47269077871	43212.93703569740	43212.93703569743
$p_{\text{H}_2\text{O}}^{\text{tpb}}$ (Pa)	17836.47137360906	80906.29578752519	80906.29578752519
$C_{\text{fuel}}^{\text{b}}$ (mol/m^3)	11.112930593706908	7.290944305362820	7.290944305362823
y_{H_2}	0.840774059703770	0.378078568904711	0.378078568904711
T_{fuel} (K)	1121.589438917897	1709.534513448058	1709.534513448058
u_{fuel} (m/s)	3.126987944987115	4.766186456045179	4.766186456045176
$y_{\text{H}_2\text{O}}$	0.159225940296230	0.621921431095289	0.621921431095289
V_{cell} (V)	0.028594931906807	0.237989966933636	0.237989966933636
η_{Ohm} (V)	0.343397618763600	0.081547418981714	0.081547418981714

H.3 R_{load} changes from 0.0017 Ω to 0.0018 Ω

$$R_{\text{load}} = 0.0018 - 0.00005 \left[1 + \tanh\left(\frac{t - 100}{0.25}\right)\right]$$

Time Interval: $t \in [0, 300]$
Maximum Time Step: 0.25 seconds.

Parameter	Initial Conditions	Solution at 300 s	Predicted Solution at 0.0018 Ω
I (A)	139.9940981962565	135.6456606861717	135.6456606861718
$\eta_{\text{act}}^{\text{An}}$ (V)	0.261136995725900	0.265040169032996	0.265040169032996
$\eta_{\text{act}}^{\text{Cat}}$ (V)	0.020969575337276	0.023446033102421	0.023446033102421
T_{cell} (K)	1998.857984360721	1965.150678488519	1965.150678488519
$p_{\text{O}_2}^{\text{tpb}}$ (Pa)	30399.10791519400	30100.81871478345	30100.81871478345
$C_{\text{air}}^{\text{b}}$ (mol/m^3)	11.120662640554256	11.150695396248482	11.150695396248482
y_{O_2}	0.192289867004643	0.192531591648136	0.192531591648136
T_{air} (K)	1115.613542877934	1112.669843201027	1112.669843201027
u_{air} (m/s)	84.611110465969787	84.408483957811171	84.408483957811157
$p_{\text{H}_2}^{\text{tpb}}$ (Pa)	43212.93703569743	45120.59793190058	45120.59793190058
$p_{\text{H}_2\text{O}}^{\text{tpb}}$ (Pa)	80906.29578752519	78528.44627353722	78528.44627353725
$C_{\text{fuel}}^{\text{b}}$ (mol/m^3)	7.290944305362823	7.394312039759212	7.394312039759213
y_{H_2}	0.378078568904711	0.394290271808859	0.394290271808859
T_{fuel} (K)	1709.534513448058	1685.636454226757	1685.636454226757
u_{fuel} (m/s)	4.766186456045176	4.699558229778412	4.699558229778411
$y_{\text{H}_2\text{O}}$	0.621921431095289	0.605709728191141	0.605709728191141
V_{cell} (V)	0.237989966933636	0.244162189235109	0.244162189235109
η_{Ohm} (V)	0.081547418981714	0.086316127772833	0.086316127772833

H.4 R_{load} changes from 0.003 Ω to 0.00325 Ω

$$R_{\text{load}} = 0.003 + 0.000125\left[1 + \tanh\left(\frac{t-100}{0.25}\right)\right]$$

Time Interval: $t \in [0, 1100]$
Maximum Time Step: 0.25 seconds.

Parameter	Initial Conditions	Solution at 1100 s	Predicted Solution at 0.00325 Ω
I (A)	75.627419289518230	11.719664830834226	11.719664830833896
$\eta_{\text{act}}^{\text{An}}$ (V)	0.319840521162637	0.382234798257955	0.382234798257955
$\eta_{\text{act}}^{\text{Cat}}$ (V)	0.090616963275105	0.247647765882359	0.247647765882360
T_{cell} (K)	1577.317683159802	1137.338972830316	1137.338972830313
$p_{\text{O}_2}^{\text{tpb}}$ (Pa)	26768.82696748787	22037.32337339917	22037.32337339912
$C_{\text{air}}^{\text{b}}$ (mol/m^3)	11.504111788579085	11.925135247621315	11.925135247621316
y_{O_2}	0.195853217853353	0.199360193008720	0.199360193008720
T_{air} (K)	1079.147841876850	1041.767751424911	1041.767751424911
u_{air} (m/s)	82.153329780043251	79.600005923200300	79.600005923200300
$p_{\text{H}_2}^{\text{tpb}}$ (Pa)	70505.57291464109	91755.92591509178	91755.92591509181
$p_{\text{H}_2\text{O}}^{\text{tpb}}$ (Pa)	47245.92532007763	15837.54642579272	15837.54642579257
$C_{\text{fuel}}^{\text{b}}$ (mol/m^3)	8.870856611267719	11.358286179368038	11.358286179368065
y_{H_2}	0.618048321935015	0.856307127805551	0.856307127805553
T_{fuel} (K)	1405.065400559853	1097.361556913606	1097.361556913603
u_{fuel} (m/s)	3.917321801353515	3.059440434167107	3.059440434167099
$y_{\text{H}_2\text{O}}$	0.381951678064985	0.143692872194449	0.143692872194447
V_{cell} (V)	0.226882257868555	0.038088910700211	0.038088910700210
η_{Ohm} (V)	0.174606381687557	0.338369097484708	0.338369097484709

H.5 R_{load} changes from 0.00325 Ω to 0.003 Ω

$$R_{\text{load}} = 0.00325 - 0.000125\left[1 + \tanh\left(\frac{t-100}{0.25}\right)\right]$$

Time Interval: $t \in [0, 500]$
Maximum Time Step: 0.25 seconds.

Parameter	Initial Conditions	Solution at 500 s	Predicted Solution at 0.003 Ω
I (A)	11.719664830833830	12.065989166338928	12.065989166339312
$\eta_{\text{act}}^{\text{An}}$ (V)	0.382234798257956	0.382217894876812	0.382217894876811
$\eta_{\text{act}}^{\text{Cat}}$ (V)	0.247647765882360	0.247030112691648	0.247030112691647
T_{cell} (K)	1137.338972830312	1140.544818298306	1140.544818298311
$p_{\text{O}_2}^{\text{tpb}}$ (Pa)	22037.32337339912	22079.65019911617	22079.65019911623
$C_{\text{air}}^{\text{b}}$ (mol/m^3)	11.925135247621322	11.921982720714366	11.921982720714364
y_{O_2}	0.199360193008720	0.199341270694263	0.199341270694263
T_{air} (K)	1041.767751424911	1042.037844174917	1042.037844174917
u_{air} (m/s)	79.600005923200271	79.619172813984036	79.619172813984051
$p_{\text{H}_2}^{\text{tpb}}$ (Pa)	91755.92591509187	91698.15269345749	91698.15269345751
$p_{\text{H}_2\text{O}}^{\text{tpb}}$ (Pa)	15837.54642579252	16003.23267203180	16003.23267203197
$C_{\text{fuel}}^{\text{b}}$ (mol/m^3)	11.358286179368074	11.337131239116790	11.337131239116768
y_{H_2}	0.856307127805553	0.855015972713025	0.855015972713024
T_{fuel} (K)	1097.361556913602	1099.409211808313	1099.409211808315
u_{fuel} (m/s)	3.059440434167097	3.065149310444709	3.065149310444714
$y_{\text{H}_2\text{O}}$	0.143692872194447	0.144984027286975	0.144984027286976
V_{cell} (V)	0.038088910700210	0.036197967499017	0.036197967499018
η_{Ohm} (V)	0.338369097484710	0.339612255168453	0.339612255168452

H.6 R_{load} changes from 0.0025 Ω on the unstable steady-state branch to 0.0024 Ω

$$R_{\text{load}} = 0.0025 - 0.00005 \left[1 + \tanh\left(\frac{t - 100}{0.25}\right)\right]$$

Time Interval: $t \in [0, 1000]$
Maximum Time Step: 0.25 seconds.

Parameter	Initial Conditions	Solution at 1000 s	Solution at 0.0024 Ω on ignited branch
I (A)	29.114618527804751	108.0371627942187	108.0372389788058
$\eta_{\text{act}}^{\text{An}}$ (V)	0.368248864315076	0.289895151196486	0.289895182914735
$\eta_{\text{act}}^{\text{Cat}}$ (V)	0.201239308867622	0.045524850128934	0.045524373050253
T_{cell} (K)	1280.833786117933	1774.090027449658	1774.090086015520
$p_{\text{O}_2}^{\text{tpb}}$ (Pa)	23814.18790369147	28453.58077622723	28453.57839165904
$C_{\text{air}}^{\text{b}}$ (mol/m^3)	11.785257277475377	11.322936449674316	11.322936399172940
y_{O_2}	0.198408668252290	0.194062947259966	0.194062943079481
T_{air} (K)	1053.890840400138	1096.078836986938	1096.078841778903
u_{air} (m/s)	80.449159717260883	83.282432143834114	83.282432085688427
$p_{\text{H}_2}^{\text{tpb}}$ (Pa)	87545.59192918314	57036.03259628048	57035.99491620659
$p_{\text{H}_2\text{O}}^{\text{tpb}}$ (Pa)	24240.42652074413	63832.61796984557	63832.65290679370
$C_{\text{fuel}}^{\text{b}}$ (mol/m^3)	10.450868476414119	8.048865357936984	8.048864729643762
y_{H_2}	0.791455828755561	0.497219384427228	0.497219089190791
T_{fuel} (K)	1192.641801673352	1548.557126169842	1548.557231006680
u_{fuel} (m/s)	3.325082511412807	4.317378668586910	4.317379054963694
$y_{\text{H}_2\text{O}}$	0.208544171244439	0.502780615572772	0.502780910809209
V_{cell} (V)	0.072786546319512	0.259289190706125	0.259289373549134
η_{Ohm} (V)	0.304758347845648	0.120893575034460	0.120893637114584

H.7 R_{load} changes from 0.0025 Ω on the unstable steady-state branch to 0.00275 Ω

$$R_{\text{load}} = 0.0025 + 0.000125 \left[1 + \tanh\left(\frac{t - 100}{0.25}\right)\right]$$

Time Interval: $t \in [0, 1000]$
Maximum Time Step: 0.25 seconds.

Parameter	Initial Conditions	Solution at 1000 s	Solution at 0.00275 Ω on un-ignited branch
I (A)	29.114618527804751	12.472099051532359	12.472099051532004
$\eta_{\text{act}}^{\text{An}}$ (V)	0.368248864315076	0.382166315333891	0.382166315333892
$\eta_{\text{act}}^{\text{Cat}}$ (V)	0.201239308867622	0.246263410248033	0.246263410248034
T_{cell} (K)	1280.833786117933	1144.284939788271	1144.284939788267
$p_{\text{O}_2}^{\text{tpb}}$ (Pa)	23814.18790369147	22128.89752202547	22128.89752202543
$C_{\text{air}}^{\text{b}}$ (mol/m^3)	11.785257277475377	11.918306374641221	11.918306374641228
y_{O_2}	0.198408668252290	0.199319080704246	0.199319080704246
T_{air} (K)	1053.890840400138	1042.352995045741	1042.352995045741
u_{air} (m/s)	80.449159717260883	79.641525074627751	79.641525074627708
$p_{\text{H}_2}^{\text{tpb}}$ (Pa)	87545.59192918314	91628.72385067759	91628.72385067763
$p_{\text{H}_2\text{O}}^{\text{tpb}}$ (Pa)	24240.42652074413	16197.64265697356	16197.64265697339
$C_{\text{fuel}}^{\text{b}}$ (mol/m^3)	10.450868476414119	11.312498713745084	11.312498713745107
y_{H_2}	0.791455828755561	0.853501927084009	0.853501927084010
T_{fuel} (K)	1192.641801673352	1101.803123672272	1101.803123672270
u_{fuel} (m/s)	3.325082511412807	3.071823553692654	3.071823553692648
$y_{\text{H}_2\text{O}}$	0.208544171244439	0.146498072915991	0.146498072915990
V_{cell} (V)	0.072786546319512	0.034298272391714	0.034298272391713
η_{Ohm} (V)	0.304758347845648	0.340832327508376	0.340832327508376

List of References

[1] A. B. Stambouli and E. Traversa, "Solid oxide fuel cells (sofcs): a review of an environmentally clean and efficient source of energy," *Renewable and Sustainable Energy Reviews*, vol. 6, pp. 433–455, October 2002.

[2] J. Andujar and F. Segura, "Fuel cells: History and updating. a walk along two centuries," *Renewable and Sustainable Energy Reviews*, vol. 13, pp. 2309–2322, December 2009.

[3] W. Grove, "On voltaic series and the combination of gases by platinum," *The London and Edinburgh philosophical magazine and journal of science*, vol. 14, no. 86, pp. 127–130, 1839.

[4] P. Grimes, "Historical pathways for fuel cells - The new electric century," *IEEE Aerospace and Electronic Systems Magazine*, vol. 15, pp. 7–10, December 2000.

[5] U. Bossel and E. F. C. Forum, *The Birth of the Fuel Cell, 1835-1845: Including the First Publication of the Complete Correspondence from 1839 to 1868 Between Christian Friedrich Schoenbein (discoverer of the Fuel Cell Effect) and William Robert Grove (inventor of the Fuel Cell).* European Fuel Cell Forum, 2000.

[6] A. Appleby, "From Sir William Grove to today - Fuel-Cells and the future," *Journal of Power Sources*, vol. 29, pp. 3–11, January 1990.

[7] I. EG&G Technical Services, *Fuel Cell Handbook (Seventh Edition).* Morgantown, West Virginia: US Department of Energy, 2004.

[8] J.-H. Wee, "Applications of proton exchange membrane fuel cell systems," *Renewable and Sustainable Energy Reviews*, vol. 11, pp. 1720–1738, October 2007.

[9] E. E. Ltd, "Post-2014 london hydrogen activity: Options assessment." `http://www.hydrogenlondon.org/wp-content/uploads/2013/10/HydrogenBuses-Post-2014-221012.pdf`, 2012.

[10] F. C. Bulletin, "First {UK} integrated hydrogen transport system in london, {SE}," *Fuel Cells Bulletin*, vol. 2013, pp. 8 – 9, February 2013.

[11] Hyundai, "Hyundai ix35 hydrogen fuel cell vehicle." http://www.hyundai.co.uk/about-us/environment/hydrogen-fuel-cell, 2015.

[12] F. C. Bulletin, "European officials to drive leased hyundai ix35 fuel cell vehicle," *Fuel Cells Bulletin*, vol. 2011, p. 2, October 2011.

[13] Toyota, "Toyota mirai-the turning point." http://www.toyota.com/mirai/fcv.html, 2015.

[14] F. C. Bulletin, "Toyota, honda get ready to launch their {FCVs}," *Fuel Cells Bulletin*, vol. 2014, p. 1, November 2014.

[15] J. Laramie and A. Dicks, *Fuel Cell Systems Explained*. Chichester, West Sussex: John Wiley & Sons Ltd., 2003.

[16] F. C. Today, "Afc." http://www.fuelcelltoday.com/technologies/afc, 2015.

[17] W. N. N. Heraeus, "ber die elektrolytische leitung fester krper bei sehr hohen temperaturen," *Zeitschrift fur Elektrochemie*, vol. 6, pp. 41–43, July 1899.

[18] K. Kendall and S. C. Singhal, *High Temperature Solid Oxide Fuel Cells: Fundamentals, Design and Applications*. The Boulevard, Langford Lane, Kidlington, Oxford, OX5 1GB, UK: Elsevier Ltd., 2008.

[19] C. Wagner, "The mechanism of electric supply lines in neon lamps," *Naturwissenschaften*, vol. 31, pp. 265–268, 1943.

[20] E. Baur and H. Preis, "Uber brennstoff-ketten mit festleitern," *Zeitschrift fur Elektrochemie*, vol. 43, pp. 727–732, September 1937.

[21] K. Kiukkola and C. Wagner, "Measurements On Galvanic Cells Involving Solid Electrolytes," *Journal of the Electrochemical Society*, vol. 104, no. 6, pp. 379–387, 1957.

[22] S. C. Singhal, "Solid oxide fuel cells, history," in *Encyclopedia of Applied Electrochemistry* (G. Kreysa, K. ichiro Ota, and R. F. Savinell, eds.), pp. 2008–2018, Springer New York, 2014.

[23] J. Weissbart and R. Ruka, "A Solid Electrolyte Fuel Cell," *Journal of the Electrochemical Society*, vol. 109, no. 8, pp. 723–726, 1962.

[24] A. J. Jacobson, "Materials for Solid Oxide Fuel Cells," *Chemistry of Materials*, vol. 22, pp. 660–674, February 2010.

[25] R. Bove and S. Ubertini, *Modeling Solid Oxide Fuel Cells*. Springer, 2008.

[26] S. Singhal, "Science and technology of solid-oxide fuel cells," *MRS Bulletin*, vol. 25, pp. 16–21, March 2000.

[27] K. S. Howe, G. J. Thompson, and K. Kendall, "Micro-tubular solid oxide fuel cells and stacks," *Journal of Power Sources*, vol. 196, pp. 1677–1686, February 2011.

[28] W. Zhu and S. Deevi, "Development of interconnect materials for solid oxide fuel cells," *Materials Science and Engineering A-Structural Materials Properties Microstrcture and Processing*, vol. 348, pp. 227–243, May 2003.

[29] E. E. US Department of Energy and F. C. T. P. Renewable Energy, "Comparison of fuel cell technologies." `http://www1.eere.energy.gov/hydrogenandfuelcells/fuelcells/pdfs/fc_comparison_chart.pdf`, 2011.

[30] N. Q. Minh, "Solid oxide fuel cell technology-features and applications," *Solid State Ionics*, vol. 174, pp. 271–277, October 2004.

[31] W. Bujalski, C. M. Dikwal, and K. Kendall, "Cycling of three solid oxide fuel cell types," *Journal of Power Sources*, vol. 171, pp. 96–100, September 2007.

[32] L. Liu, G.-Y. Kim, and A. Chandra, "Modeling of thermal stresses and lifetime prediction of planar solid oxide fuel cell under thermal cycling conditions," *Journal of Power Sources*, vol. 195, pp. 2310–2318, April 2010.

[33] Protonex, "Products." `http://www.protonex.com/products/`, 2015.

[34] Delphi, "Solid oxide fuel cell technology." `http://www.delphi.com/manufacturers/auto/fuelcells`, 2015.

[35] Callux, "Callux, practical tests for fuel cells in a domestic setting." `http://www.callux.net/home.English.html`, 2015.

[36] J. L. G. Association, "Appliances." `http://www.j-lpgas.gr.jp/en/appliances/`, 2015.

[37] W. G. Colella, S. H. Schneider, D. M. Kammen, A. Jhunjhunwala, and N. Teo, "Optimizing the design and deployment of stationary combined heat and power fuel cell systems for minimum costs and emissions-part i: Model design," *Journal of Fuel Cell Science and Technology*, vol. 8, pp. 021001–1–0121001–13, April 2011.

[38] B. Energy, "What is an energy server." `http://www.bloomenergy.com/fuel-cell/energy-server/`, 2014.

[39] F. Energy, "Products and services." `http://www.fuelcellenergy.com/products-services/products/`, 2013.

[40] B. V. Consultants, "Fuel cell & industry and patent overview 2015." `http://www.hgf.com/media/438442/Fuel-Cell-Report-2015-HGF-and-BV.pdf`, 2015.

[41] M. Bavarian, M. Soroush, I. G. Kevrekidis, and J. B. Benziger, "Mathematical modelling, steady-state and dynamic behaviour, and control of fuel cells: A review," *Industrial & Engineering Chemistry Research*, vol. 49, pp. 7922–7950, September 2010.

[42] B. Huang, Y. Qi, and M. Murshed, "Solid oxide fuel cell: Perspective of dynamic modeling and control," *Journal of Process Control*, vol. 21, pp. 1426–1437, December 2011.

[43] R. Bove and S. Ubertini, "Modeling solid oxide fuel cell operation: Approaches, techniques and results," *Journal of Power Sources*, vol. 159, pp. 543–559, September 2006.

[44] S. A. Hajimolana, M. A. Hussain, W. M. A. W. Daud, M. Soroush, and A. Shamiri, "Mathematical modeling of solid oxide fuel cells: A review," *Renewable & Sustainable Energy Reviews*, vol. 15, pp. 1893–1917, May 2011.

[45] P. Debenedetti and C. Vayenas, "Steady-state analysis of high temperature fuel cells," *Chemical Engineering Science*, vol. 38, pp. 1817–1829, November 1983.

[46] C. van Heerden, "The character of the stationary state of exothermic processes," *Chemical Engineering Science*, vol. 8, no. 1–2, pp. 133–145, 1956.

[47] M. Mangold, M. Krasnyk, and K. Sundmacher, "Theoretical investigation of steady-state multiplicities in solid oxide fuel cells," *Journal of Applied Electrochemistry*, vol. 36, pp. 265–275, March 2006.

[48] A. Mangold, A. Krasnyk, and K. Sundmacher, "Nonlinear analysis of current instabilities in high temperature fuel cells," *Chemical Engineering Science*, vol. 59, pp. 4869–4877, Nov-Dec 2004.

[49] M. Bavarian and M. Soroush, "Steady-state multiplicity in a solid oxide fuel cell: Practical considerations," *Chemical Engineering Science*, vol. 67, pp. 2–14, January 2012.

[50] M. Bavarian and M. Soroush, "Mathematical modeling and steady-state analysis of a proton-conducting solid oxide fuel cell," *Journal of Process Control*, vol. 22, pp. 1521–1530, September 2012.

[51] M. Bavarian, M. Soroush, I. G. Kevrekidis, and J. B. Benziger, "Mathematical modeling and steady-state analysis of a co-ionic-conducting solid oxide fuel cell," *2012 American Control Conference (ACC)*, pp. 4269–4274, June 2012.

[52] M. Bavarian, M. Soroush, I. G. Kevrekidis, and J. B. Benziger, "Modeling and bifurcation analysis of a coionic conducting solid oxide fuel cell," *Industrial and Chemical Engineeing Research*, vol. 52, pp. 3165–3177, March 2013.

[53] J. D. Sands, "Current oscillations arising from nonlinear chemical dynamics in solid oxide fuel cells." July 2015.

[54] J. D. Sands, D. J. Needham, and J. Uddin, "Nonlinear Oscillatory Dynamics in Solid Oxide Fuel Cells," in *Solid Oxide Fuel Cells 13 (SOFC-XIII)* (Kawada, T and Singhal, SC, ed.), vol. 57 of *ECS Transactions*, pp. 2617–2626, 2013.

[55] J. D. Sands, J. Uddin, and D. J. Needham, "A fundamental model exhibiting nonlinear oscillatory dynamics in solid oxide fuel cells-the effects of fuel stream humidification," *Quarterly Journal of Mechanics and Applied Mathematics*, vol. 69, pp. 83–113, FEB 2016.

[56] P. M. Aguiar, C. S. Adjiman, and N. P. Brandon, "Anode-supported intermediate temperature direct internal reforming solid oxide fuel cell. i: model-based steady-state performance," *Journal of Power Sources*, vol. 138, pp. 120–136, November 2004.

[57] P. Iora, P. M. Aguiar, C. S. Adjiman, and N. P. Brandon, "Comparison of two it dir-sofc models: Impact of variable thermodynamic, physical, and flow properties. steady-state and dynamic analysis," *Chemical Engineering Science*, vol. 60, pp. 2963–2975, June 2005.

[58] S. Campanari and P. Iora, "Definition and sensitivity analysis of a finite volume sofc model for a tubular cell geometry," *Journal of Power Sources*, vol. 132, pp. 113–126, May 2004.

[59] E. Achenbach, "3-dimensional and time-dependent simulation of a planar solid oxide fuel cell stack," *Journal of Power Sources*, vol. 49, pp. 333–348, April 1994.

[60] E. Achenbach, "Response of a solid oxide fuel cell to load change," *Journal of Power Sources*, vol. 57, pp. 105–109, September–December 1995.

[61] D. Hall and R. Colclaser, "Transient modeling and simulation of a tubular solid oxide fuel cell," *IEEE Transactions on Energy Conversion*, vol. 14, pp. 749–753, September 1999.

[62] J. Padullés, G. Ault, and J. McDonald, "An integrated sofc plant dynamic model for power systems simulation," *Journal of Power Sources*, vol. 86, pp. 495–500, March 2000.

[63] K. Sedghisigarchi and A. Feliachi, "Dynamic and transient analysis of power distribution systems with fuel cells-part i: Fuel-cell dynamic model," *IEEE Transactions on Energy Conversion*, vol. 19, pp. 423–428, June 2004.

[64] D. F. Cheddie and N. D. Munroe, "A dynamic 1d model of a solid oxide fuel cell for real time simulation," *Journal of Power Sources*, vol. 171, pp. 634–643, September 2007.

[65] Y. Qi, B. Huang, and K. Chuang, "Dynamic modeling of solid oxide fuel cell: The effect of diffusion and inherent impedance," *Journal of Power Sources*, vol. 150, pp. 32–47, October 2005.

[66] E. N. Fuller, P. D. Schettler, and J. C. Giddings, "New method for prediction of binary gas-phase diffusion coefficients," *Industrial and Engineering Chemistry*, vol. 58, pp. 18–27, May 1966.

[67] Y. Qi, B. Huang, and J. Luo, "Dynamic modeling of a finite volume of a solid oxide fuel cell: The effect of transport dynamics," *Chemical Engineering Science*, vol. 61, pp. 6057–6076, September 2006.

[68] K. Ahmed and K. Foger, "Kinetics of internal steam reforming of methane on ni/ysz-based anodes for solid oxide fuel cells," *Catalysis Today*, vol. 63, pp. 479–487, December 2000.

[69] Y. Qi, B. Huang, and J. Luo, "1-d dynamic modeling of sofc with analytical solution for reacting gas-flow problem," *AICHE Journal*, vol. 54, pp. 1537–1553, June 2008.

[70] E. S. Staff, *Fuel Cell Handbook (Fifth Edition)*. US Department of Energy, 2000.

[71] P. Costamagna and K. Honegger, "Modeling at solid oxide heat exchanger integrated stacks and simulation at high fuel utilization," *Journal of the Electrochemical Society*, vol. 145, pp. 3995–4007, November 1998.

[72] J. R. Welty, C. E. Wicks, R. E. Wilson, and G. L. Rorrer, *Fundamentals of Momentum, Heat, and Mass Transfer*. John Wiley and Sons, Inc., 5th ed., 2008.

[73] R. Gemmen and C. Johnson, "Effect of load transients on SOFC operation-current reversal on loss of load," *Journal of Power Sources*, vol. 144, pp. 152–164, Jun 1 2005.

[74] G. Le Bas, *The Molecular Volumes of Liquid Chemical Compounds, from the Point of View of Kopp*. Longmans, Green, 1915.

[75] S. Chan, K. Khor, and Z. Xia, "A complete polarization model of a solid oxide fuel cell and its sensitivity to the change of cell component thickness," *Journal of Power Sources*, vol. 93, pp. 130–140, February 2001.

[76] D. Bhattacharyya and R. Rengaswamy, "A review of solid oxide fuel cell (sofc) dynamic models," *Industrial & Engineering Chemistry Research*, vol. 48, no. 13, pp. 6068–6086, 2009.

[77] R. Perry, D. W. Green, and J. O. Maloney, *Perry's Chemical Engineers' Handbook*. No. v. 7, pt. 1997 in McGraw-Hill international editions / Chemical engineering series, McGraw-Hill, 1997.

[78] D. Green and R. Perry, *Perry's Chemical Engineers' Handbook, Eighth Edition.* McGraw Hill professional, McGraw-Hill Education, 2007.